PERGAMON

Progress in Surface Science 60 (1999) 89–257

Progress in SURFACE SCIENCE

Review paper

Structures and electronic transport on silicon surfaces

Shuji Hasegawa[a, b,*], Xiao Tong[a], Sakura Takeda[a], Norio Sato[a], Tadaaki Nagao[a, b]

[a]*Department of Physics, School of Science, University of Tokyo, Hongo, Bunkyo-ku, Tokyo, 113-0033, Japan*

[b]*Core Research for Evolutional Science and Technology (CREST), The Japan Science and Technology Corporation (JST), Kawaguchi Center Bldg, Hon-cho 4-1-8, Kawaguchi, Saitama, 332-0012, Japan*

Abstract

By utilizing a variety of surface superstructures formed on silicon surfaces and atomic layers grown on them, close correlations between the atomic-scale structures and electrical conduction phenomena at the surfaces have been revealed. State-of-art techniques for analyzing and controlling atomic/electronic structures of surfaces are leading to an understanding of the novel electronic transport properties at surfaces. For example, the electrical conduction through surface-state bands, which are inherent in the surface superstructure, has been confirmed in in-situ measurements. An important phenomenon has also been found, where adatoms donate carriers into the surface-state band, resulting in a remarkable enhancement in electrical conductance. The nucleation of the adatoms diminishes such a doping effect. Furthermore, electrical conduction through atomic layers grown on the surfaces, whose growth structures are sensitive to the substrate surface structures, will be also discussed. In this review, we emphasize that the surface electronic transport properties are closely related to the atomic structures and atomistic dynamics on surfaces. The ultimate two-dimensional electron systems, consisting of the surface-state bands and grown atomic layers, are expected to provide a new stage in surface physics, as well as a precursory stage leading to atomic-scale electronics devices.

* Corresponding author.
E-mail address: shuji@surface.phys.s.u-tokyo.ac.jp (S. Hasegawa)

0079-6816/99/$ - see front matter
PII: S0079-6816(99)00008-8

Nomenclature

AC	Alternating Current
AES	Auger Electron Spectroscopy
ARUPS	Angle-Resolved Ultraviolet Photoelectron Spectroscopy
ARPES	Angle-Resolved Photo-Emission Spectroscopy
CBM	Conduction-Band Minimum
DAS	Dimer-Adatom-Stacking fault
DC	Direct Current
DOS	Density of States
EELS	Electron-Energy-Loss Spectroscopy
FWHM	Full Width of Half Maximum
HCT	Honeycomb-Chained Triangles
IPES	Inverse Photoemission Spectroscopy
IV	Intensity-Voltage
LEED	Low-Energy Electron Diffraction
ML	Mono Layer
MESFET	MEtal-Semiconductor Field-Effect Transistor
MISFET	Metal-Insulator-Semiconductor Field-Effect Transistor
RHEED	Reflection-High-Energy Electron Diffraction
RBS	Rutherford Backscattering Spectroscopy
RT	Room Temperature
SEM	Scanning Electron Microscopy
STM	Scanning Tunneling Microscopy
STS	Scanning Tunneling Spectroscopy
TED	Transmission Electron Diffraction
TV	Television
UHV	Ultra-High Vacuum
UPS	Ultra-violet Photoelectron Spectroscopy
UV	Ultra Violet
VBM	Valence-Band Maximum
XPS	X-ray Photoelectron Spectroscopy
2D	two Dimension(al)
2DAG	two-Dimensional Adatom Gas
3D	three Dimension(al)

Contents

1. Introduction

1.1. Surface superstructures and two-dimensional electron systems

While some metal surfaces have been intensively studied in relation to catalysis for a long time, semiconductor surfaces, especially silicon ones, are another major target in surface science, because of their importance in device applications and fundamental physics. Severe atomic rearrangements (*reconstructions*) frequently occur on semiconductors to lower the surface energies on clean as well as adlayered surfaces. For lack of symmetry in a direction normal to the surface, the reconstructions produce quite a large variety of peculiar periodic atomic arrangements, i.e., *surface superstructures*, which are not expected in the bulk. In addition to superstructures formed on clean surfaces, more than 300 kinds of "adsorbate-induced surface superstructures" have been found on silicon. Detailed investigations of the atomic and electronic structures of the respective surfaces have been widely carried out all over the world. A large monograph entitled

Surface Phases on Silicon [1] compiles all the data on the subject from various sources.

However, there is a very limited number of studies for answering simple questions—what special properties do we actually have from such surface superstructures? Are there any electric, magnetic, or optical properties at surfaces, which are not exhibited in the bulk? Expectations for novel properties, and the resulting electronics devices, are the driving forces for research on semiconductor surfaces. However, since structural/chemical analyses, and their controls, are not easy to perform (therefore, they are interesting!), the properties of surfaces are seldom investigated by relating them to the atomic-scale structures.

By utilizing a variety of the surface superstructures on silicon surfaces, we have studied how the arrangements of atoms in only one or two atomic layers on the topmost surfaces actually affect the electronic transport properties [2–23]. Recalling the history of modern surface physics, the electrical conduction near semiconductor surfaces has been one of the most important subjects since the discovery of transistors in 1950 s [24]. However, this subject does not seem to be treated in the main stream of modern surface science, where structural controls and analyses on atomic scales are the main concerns. Instead, electronic transport properties near semiconductor surfaces have been major themes in mesoscopic and device physics, where the arrangements and bondings of individual atoms near surfaces are virtually of no interest, since the atomic-scale structures were not believed to play any important roles in the transport properties, because the de Broglie wavelengths of the charge carriers are much larger than atomic dimensions. However, we intend to correlate the properties with the surface atomic structures, which we believe is interesting and important for physics, as well as for nanometer-scale device performance.

In fact, we have succeeded for the first time to confirm experimentally the electrical conduction through a surface-state band inherent in the surface superstructures on silicon [11,12,14,18], which clearly demonstrates the close correlation between the electrical properties and atomic structures. This type of conduction must be distinguished from the conventional surface electrical conduction via the surface space-charge layer. The new type of conduction, through surface-state bands, is due to an inherently *two-dimensional* (2D) electron system localized in the topmost surface atomic layers, while the conventional 2D electron system is made of bulk-state electrons confined in space-charge layers by band bending near surfaces or heterojunctions.

As is well-known, conventional 2D electron systems have provided us with a marvelous variety of phenomena, such as the quantum Hall effect, charge-density waves and high-critical-temperature superconductivity. Such 2D electron systems are formed near semiconductor interfaces or surfaces, and in intrinsic 2D crystals (layered crystals) likes MoS_2 or $YBa_2Cu_3\ O_{9-y}$. Here, however, we discuss the novel 2D electron system composed of surface-states bands inherent in the surface superstructures on semiconductors, which is quite different from the bulk states in semiconductors. The *thickness* of this 2D electron system is as thin as a monatomic layer, which is much thinner than that at the conventional 2D electron

system. Therefore, we can expect some novel properties from the 2D electron system in the surface-state bands, when correlated with surface structural modifications on the atomic scales.

For example, it has been found that individual adatoms on a surface, which form a *2D adatom gas* phase, donate carriers into a surface-state band, resulting in a remarkable enhancement of the conductance [8,14]. Nucleation of the adatom gas into microcrystals diminishes the carrier-doping effect. Such a phenomenon occurs only on surfaces, and can be probed by sophisticated modern surface science techniques. Conversely, from these findings, we see that the measurements of surface electrical conduction may become a useful method for monitoring the surface atom dynamics in real time, which are difficult to be observed directly by any microscopies or diffraction/scattering methods.

In this review article, we intend to describe systematically our studies, together with related reports from other groups, on the surface electrical conduction which depends decisively on the atomic-scale structures of the surfaces and their dynamical changes.

In the rest of this section, two examples of surface superstructures, Si(111)-7×7 and Si(111)-$\sqrt{3} \times \sqrt{3}$-Ag, are given to illustrate the correlation between the atomic-scale structures and the electronic transport properties of the surfaces. In Section 2, the fundamentals of electrical conduction near semiconductor surfaces are given, on which the following sections are based. In Section 3, we briefly introduce our experimental methods for investigating the atomic structures, electronic states, and electronic transport properties of surfaces. The following sections are devoted to the case studies of Ag adsorption (Section 4), adsorptions of monovalent atoms on the $\sqrt{3} \times \sqrt{3}$-Ag surface (Section 5), Au adsorption (Section 6), and In adsorption (Section 7) on Si(111) surfaces. Section 8 provides the concluding remarks, including a summary of the present status and future prospects.

1.2. Surface-state bands

1.2.1. Si(111)-7×7 and -$\sqrt{3} \times \sqrt{3}$-Ag superstructures

Let us introduce surface superstructures and surface-state bands by using the Si surfaces as an example. Fig. 1 displays a series of *ultrahigh-vacuum* (UHV) *reflection-high-energy electron diffraction* (RHEED) patterns showing a structural transformation from a clean Si(111)-7×7 structure (a) to a $\sqrt{3} \times \sqrt{3}$-Ag structure (c) by depositing Ag at a substrate temperature of 450°C. The fine spots in (a) come from the 7×7 superstructure (*superlattice reflections*), while the strong spots (*fundamental reflections*) originate from the diamond-type crystal structure of the bulk. The details of the RHEED patterns will be described in Section 3.1.1. With a Ag adsorption of amount of about 0.5 ML (*monolayer*, 1 ML = the number density of Si atoms in the topmost layer of the (111) face), as shown in Fig. 1(b), the 7×7-superlattice reflections are slightly weakened, instead, streaky reflections appear indicating a $\sqrt{3} \times \sqrt{3}$ periodicity. At a Ag coverage of 1 ML (c), the 7×7

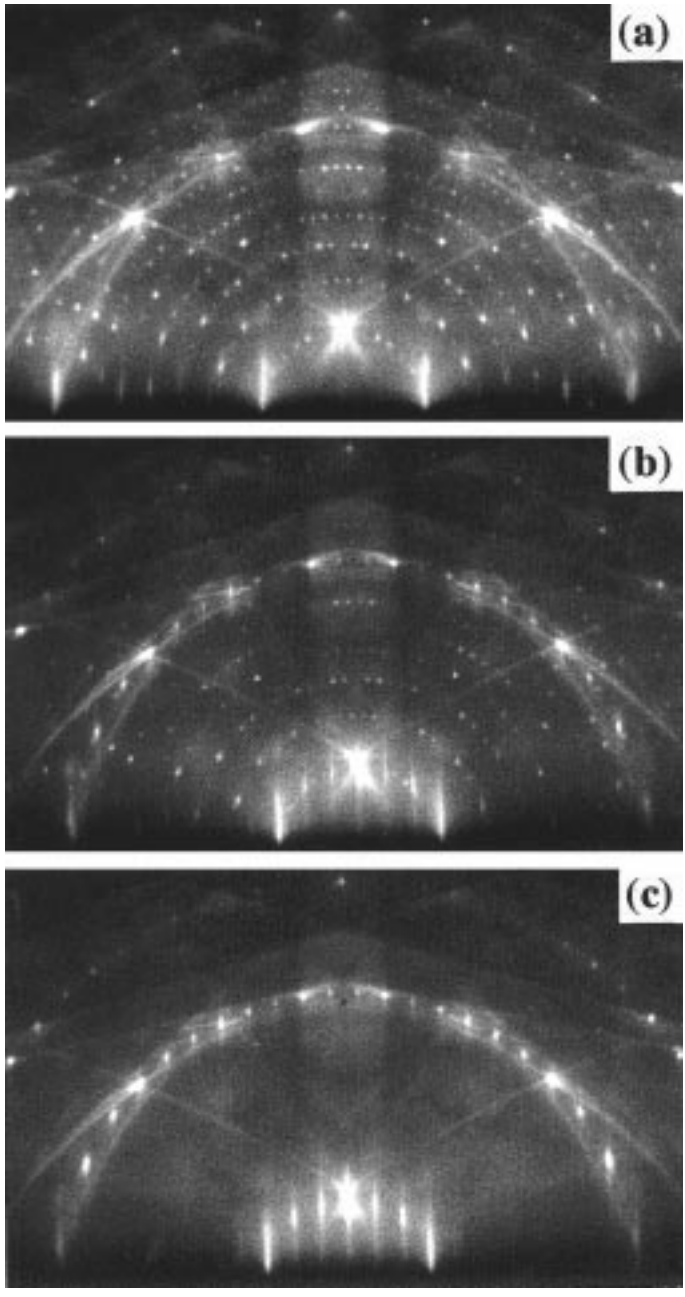

Fig. 1. Ultrahigh-vacuum reflection-high-energy electron diffraction (RHEED) patterns showing a structural transformation from (a) the clean Si(111)-7 × 7 to (c) the $\sqrt{3} \times \sqrt{3}$-Ag structure by Ag deposition at a substrate temperature of 450°C. Ag coverages are (b) 0.5 ML and (c) 1 ML. The electron beam energy is 15 keV, the glancing angle is 3.1° in $[11\bar{2}]$ incidence.

spots completely disappear, and the $\sqrt{3} \times \sqrt{3}$ streaks attain the maximum intensity; the surface fully converts into the $\sqrt{3} \times \sqrt{3}$-Ag superstructure.

The process of this structural conversion is also observed in real space by UHV-*scanning electron microscopy* (SEM) as shown in Fig. 2. The details of SEM will be explained in Section 3.1.2. The surface is composed of large areas of flat terraces and step bunches of around ten-atomic steps as seen in (a). The adsorbed Ag atoms initially nucleate at the monatomic step edges on the flat terraces (see (b)), where the atomic arrangement converts into a $\sqrt{3} \times \sqrt{3}$-Ag superstructures from the clean 7×7 structure. The brighter areas are the $\sqrt{3} \times \sqrt{3}$-Ag domains and the darker ones the 7×7 domains. With increase of Ag coverage, the brighter areas grow and, finally, the whole surface is covered by the $\sqrt{3} \times \sqrt{3}$-Ag superstructure by 1 ML Ag adsorption (see (h)). Thus, the emission yield of secondary electrons is quite different, depending on the surface superstructures of the topmost layers, due to a change in surface electronic states.

Fig. 3(a) is a *scanning tunneling micrograph* (STM) showing a surface with a mixture of the 7×7 and $\sqrt{3} \times \sqrt{3}$-Ag domains [25], which may correspond to the situation in Fig. 2(e). The difference in atomic corrugations is clearly seen in the domains of the respective superstructures. Schematic illustrations of their atomic arrangements are also shown in Figs. 3(b) and (c). After a quarter of a century of controversy, the 7×7 reconstruction is now solved as a so-called *dimer-adatom-stacking fault* (DAS) structure (Fig. 3(b)) [26]. Reviews on this surface are given, for example, in Refs. [32] and [5]. The lozenge of the 7×7-unit cell has corner holes, which are connected to each other by chains of *dimers*. This unit cell is regarded as containing two triangles separated by the dimer chains. Each triangle has six *adatoms* (the biggest open circles) and three *rest atoms* (the circles with crosses), arranged locally in a 2×2 periodicity. The left and right triangles have the opposite stacking sequences; the left-hand side has a stacking fault (*faulted half*), while the right does not (*unfaulted half*). The structure has 19 dangling bonds, which is a significant reduction in the number of unpaired electrons from 49 at an ideal unreconstructed (111) surface. This leads to a decrease of the total energy, which is, however, balanced against an energy increase caused by large angular strains of unusual bondings, such as dimers and adatoms. The reduction of the energy from the ideal unrelaxed surface was theoretically estimated to be 0.36 eV [33] or 0.40 eV [34] per 1×1 unit.

The $\sqrt{3} \times \sqrt{3}$-Ag structure is also clarified by a so-called *honeycomb-chained triangles* (HCT) structure (Fig. 3(c)) [35,36]. The topmost Si atoms make trimers, and the Ag atoms make bonds with the Si atoms, remaining no dangling bonds. The Ag atoms also make triangles, but, without bonding each other. The $\sqrt{3} \times \sqrt{3}$-unit contains three Ag atoms. So the number of valence electrons in the unit cell is even, three from Ag atoms and nine from the dangling bonds of three Si atoms, as is consistent with the semiconducting character of its surface-electronic structure, as mentioned below, which is in contrast to the metallic nature of the Si(111)-7×7 surface.

By comparing the 7×7 clean surface with the $\sqrt{3} \times \sqrt{3}$-Ag structure, we see

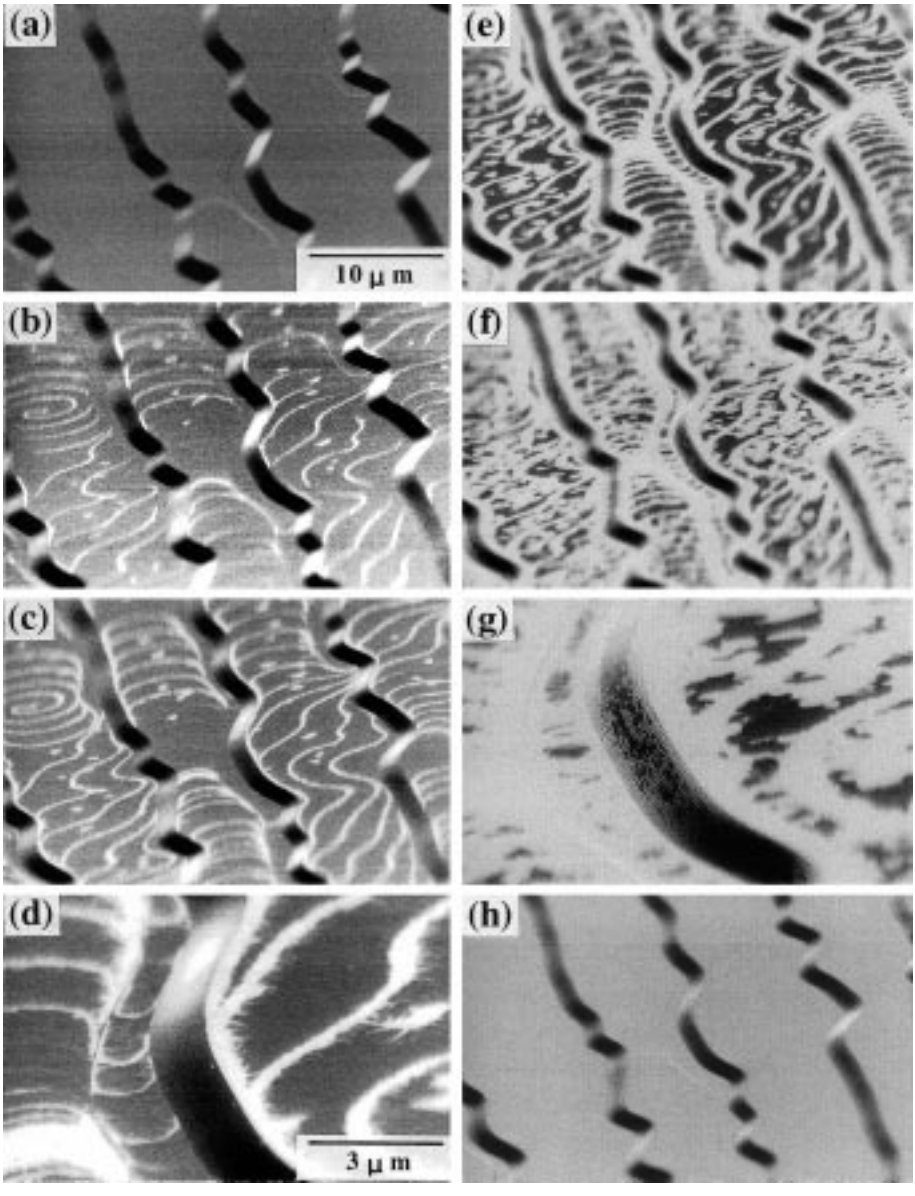

Fig. 2. Ultrahigh-vacuum scanning electron micrographs showing a structural transformation from (a) the clean Si(111)-7 × 7 structure to (h) the $\sqrt{3} \times \sqrt{3}$-Ag structure during Ag deposition at a substrate temperature of 450°C. The brighter areas in (b)–(g) correspond to the $\sqrt{3} \times \sqrt{3}$-Ag domains. The electron beam irradiates the surface at a grazing incidence (about 80° from the surface normal) so that the step bunches are exaggerated.

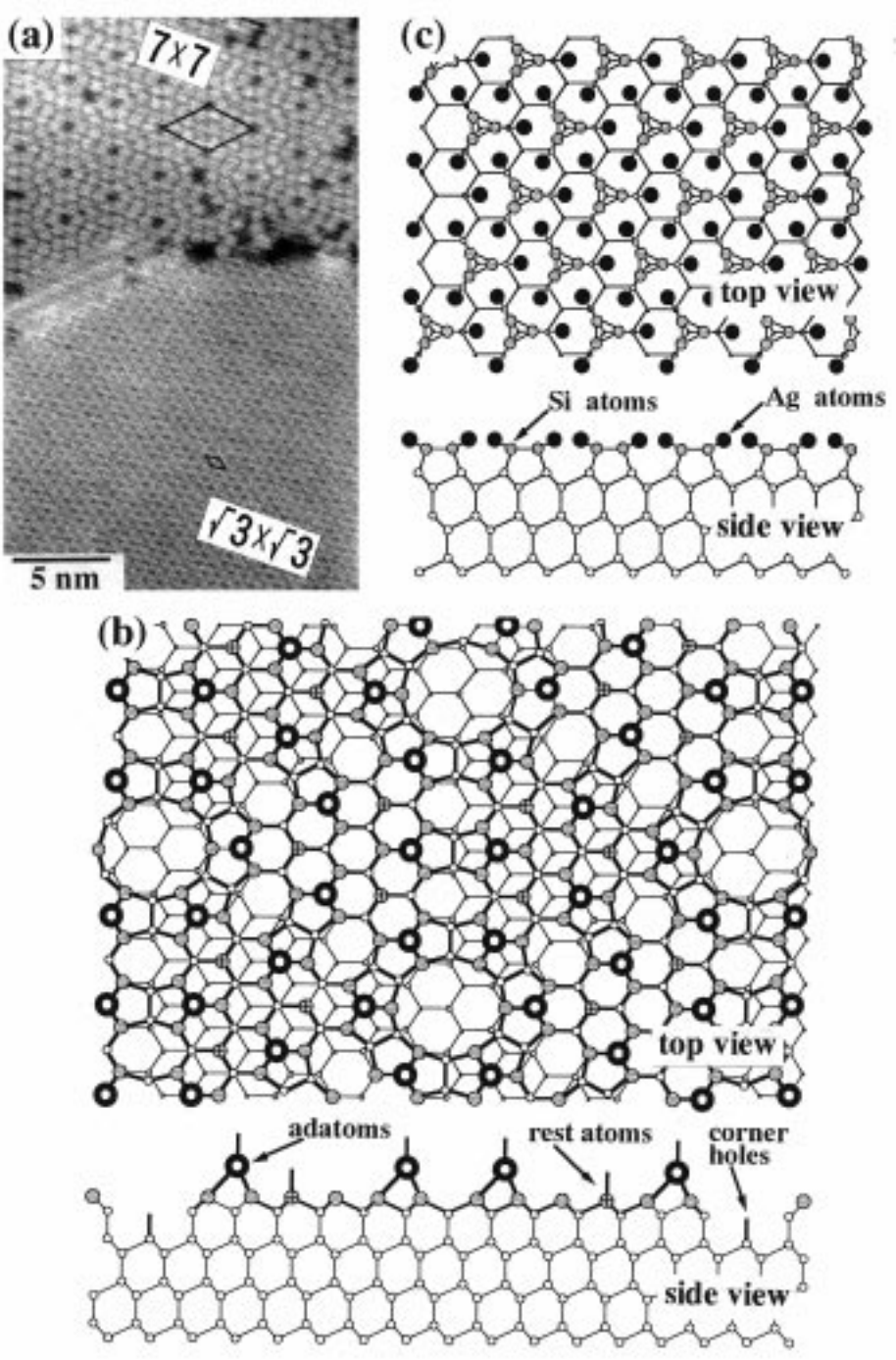

Fig. 3. (a) An ultrahigh vacuum scanning tunneling micrograph showing a mixture of the clean 7×7 and the $\sqrt{3} \times \sqrt{3}$-Ag domains. Reproduced with permission from Ref. [25]. (b) and (c) Schematics of atomic arrangements of the respective surface structures (upper: plan view, lower: sectional view).

that the atoms in only two or three atomic layers on the topmost surface are totally rearranged. Then, what changes occur in electronic states?

1.2.2. Electronic structures

Using an energy diagram, schematically shown in Fig. 4, electronic changes on the surface are qualitatively described. The sp^3 hybrid orbitals are less stable than atomic orbitals $(3s)^2(3p)^2$ for an isolated Si atoms. But, by interacting with neighboring Si atoms, the hybrid orbitals split into a bonding and an anti-bonding orbitals, where the electrons accommodated in the bonding level are much stabler than the initial state of isolated atoms. When many atoms are arranged periodically in a crystal, the bonding and anti-bonding levels are broadened into valence and conduction bands, respectively, between which an energy gap opens up. This is the electronic structure in bulk. Then, what happens at the surface? There are no pairing atoms on the vacuum side for the topmost atomic layer on the surface. So one of the hybrid orbitals remains as a *dangling bond* on each atom, whose energy level may be located between those of the bonding and anti-bonding levels to form a *Shockley-type* surface electronic state. Actually, the energy level of the dangling-bond state on the clean Si(111)-7 × 7 surface is always located around the middle of the band gap. Although this 7 × 7 reconstruction markedly reduces the number of dangling bonds, compared to an ideally

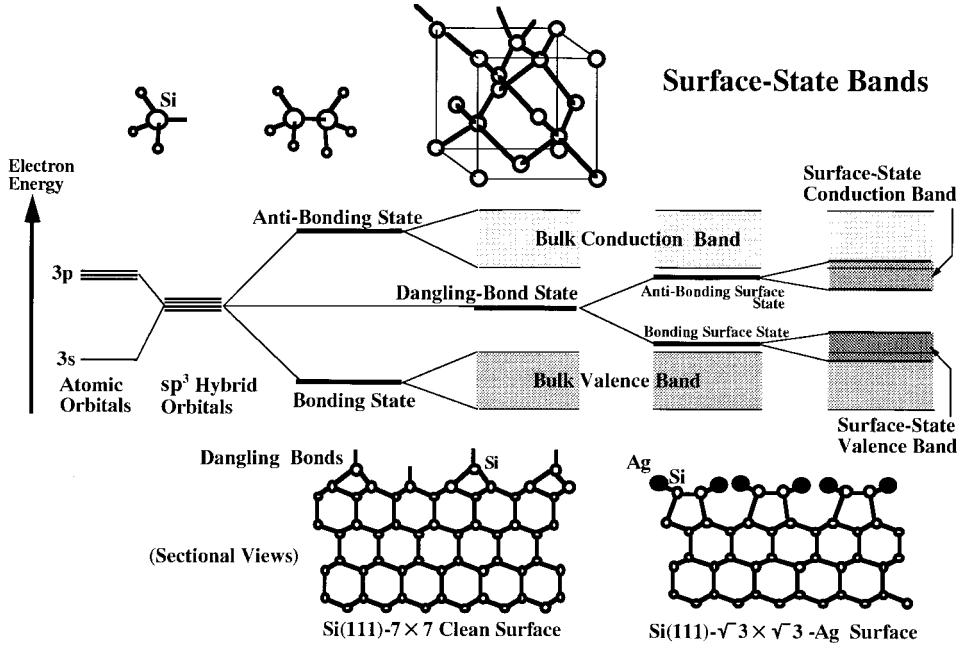

Fig. 4. A schematic illustration of energy diagram of atoms, molecules, and also in bulk and at surface of a silicon crystal.

truncated (111) surface, there still remain some of them. The dangling-bond state on each *adatom* on the topmost layer has an unpaired electron, resulting in a half-filled, therefore *metallic*, surface-state band, that is detected by *angle-resolved ultraviolet photoelectron spectroscopy* (ARUPS), denoted "S_1" in a 2D band dispersion diagram of Fig. 5(a). Such a surface state is always detected at the *Fermi level* (E_F) at any emission angle, indicating *Fermi-level pinning* due to its high density of states. The band is almost flat, and has negligible dispersion,

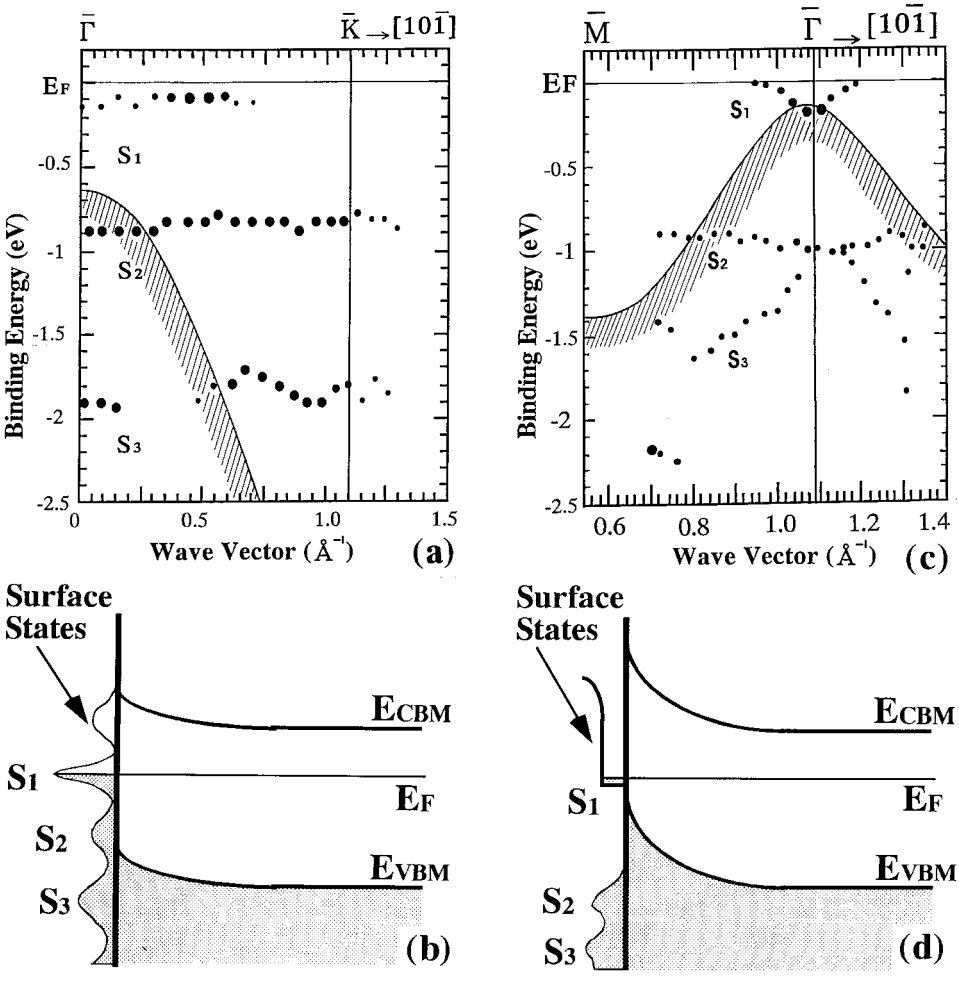

Fig. 5. (a) and (b) Si(111)-7 × 7 clean surface and (c) and (d) Si(111)-$\sqrt{3} \times \sqrt{3}$-Ag surface. (a) and (c) 2D band dispersion diagrams of surface states determined by ARUPS. $\bar{\Gamma}$ and $\bar{K}$ in (a), and $\bar{\Gamma}$ and $\bar{M}$ in (c) are symmetric points in the 1 × 1 and $\sqrt{3} \times \sqrt{3}$ surface Brillouin zones, respectively. The projected band structures of the bulk states are also included by curves with hatching. (b) and (d) Schematics of band diagrams showing surface states and surface space-charge layers. E_{VBM}: valence-band maximum, E_{CBM}: conduction-band minimum, E_F: Fermi level.

because the overlap integral between the neighboring dangling-bond states is so small that the electrons in this state are almost localized on the respective *adatoms*. This is reasonable when one considers that the distance between the neighboring *adatoms* is so large, viz., 0.768 nm, twice the fundamental unit-cell length, and that this state has a character of p_z-like orbitals (z-direction is perpendicular to the surface). Therefore, electrical conductivity parallel to the surface through this dangling-bond-state band is not expected to be very high, in spite of its metallic nature. In fact, there are some experimental results suggesting a low or negligible DC conductance through the dangling-bond state [27–29]. On the other hand, the E_F at this surface is always located around the middle of the band gap (pinned at the S_1-surface state), irrespective of the doping type and concentration in the bulk crystal [30,31], so that the surface space-charge layer beneath the 7×7 surface is always a *depletion layer* (Fig. 5(b)). Therefore, the electrical conduction through the surface space-charge layer is low, too.

When foreign atoms, e.g., Ag, adsorb on the surface, the dangling bonds are saturated by making covalent bonds with the adatoms, resulting in a splitting of the dangling-bond state into a pair of bonding and anti-bonding states (Fig. 4). These energy levels may be quite different from the bulk states because of the different situations at the surface. If the interaction between the neighboring adatoms is strong enough, the bonding and anti-bonding levels at surface will become bands, namely, the so-called a *surface-state valence band* and a *surface-state conduction band*, respectively. These surface-state bands are inherently two-dimensional, being restricted to almost only the topmost atomic layer. Electrons in these bands can be mobile along the surface, so that they can contribute to electronic transport. Let us give an example by using the Si(111)-$\sqrt{3} \times \sqrt{3}$-Ag structure. The Ag atoms in this phase make covalent bonds with the substrate Si atoms, leaving no dangling bonds on the surface. Thus, an energy gap opens up between the anti-bonding and bonding states of Si–Ag bonds [37]. The respective surface states are broadened into bands, due to the interaction between the neighboring Si–Ag bonds, which is a semiconductor-like surface electronic structure. These surface-state conduction and valence bands are observed in ARUPS measurements, denoted as "S_1" and "S_2", respectively, in Fig. 5(c). But we notice a peculiar feature in the band-dispersion diagram; a part of the anti-bonding-state band S_1 is observed below E_F, so that some electrons are trapped in this band, which is observed only in a narrow range of wavevectors around the $\bar{\Gamma}$ point and is highly upward-dispersive [38]. Thus, this state has an extended electron wavefunction in contrast to the localized S_1-dangling-bond state at the 7×7 surface in Fig. 5(a), and therefore resembles a degenerate n-type semiconductor. Moreover, the S_1 state on the $\sqrt{3} \times \sqrt{3}$-Ag surface is found to have a character of $p_{x,y}$ orbitals [15], and is thus expected to have a higher electrical conductance, due to the excess electrons accumulated in the *surface-state conduction band* S_1, in spite of its semiconducting nature. These characters of the surface electronic structure are independent of the bulk doping type and concentration. According to first-principle calculations [39,40], the local density of states of the S_1 surface-state band has a maximum at the centers of Ag triangles

in the *Honeycomb-Chained Triangles* HCT framework (Fig. 3), which is confirmed by bias-dependent *scanning tunneling microscopy* (STM) observations [41]. Therefore, by recalling the high dispersion of this band, the electrons can be expected to travel via the Ag-triangle centers, resulting in a high conductance. It is also experimentally confirmed that the surface E_F is always located near the valence-band maximum [42,38], so that the bulk bands near the surface strongly bend upwards, as shown in Fig. 5(d). The surface space-charge layer is thus a *hole-accumulation* one and is highly conductive.

In this way, the surface-state bands (and also surface space-charge layers) are characteristic to the respective surface superstructures, which will provide interesting playgrounds for studies of electronic transport properties of the novel 2D electron systems.

2. Electrical conduction at semiconductor surfaces

2.1. Fundamentals of electronic transport

Since detailed and general descriptions of electrical conduction in crystals can be found in standard textbooks on solid-state physics [43] and semiconductors [44,45], the present discussion is limited to some of their fundamental concepts, which are useful for the discussions in the following sections.

2.1.1. Free electron model

In the Drude formula, the electrical conductivity σ[S/cm] for *three-dimensional* (3D) systems, or sheet conductance σ[S/□] for 2D systems is given by

$$\sigma = ne\mu, \tag{1}$$

where n[cm^{-3} for 3D, cm^{-2} for 2D] is the carrier concentration, $e(=1.60219\times10^{-19}$C), the elementary charge, and μ[cm^2/Vs], the carrier mobility. (The unit of sheet conductance S/□ means the conductance per arbitrary sizes of squares on the surface; the values of sheet conductance are independent of the sizes.) Hence, when the conductivity changes are detected, one should consider changes in both of n and μ.

2.1.1.1. Carrier mobility. The mobility is expressed by

$$\mu = \frac{e}{m^*}\langle\tau\rangle, \tag{2}$$

where m^* is an effective mass of the carriers, which is generally different from the free-electron mass m_0, because of the crystal field through which the carriers move. The sign of the mobility is defined negative for electrons and positive for holes. $<\tau>$ is the average momentum relaxation time, which is of the order of the collision time τ_c, i.e., a mean free time between collisions of the carriers with

vibrating atoms of the crystal lattices or impurities. The drift velocity v_d of the carriers, with which the current density j is given by $j = nev_d$, will decrease exponentially in a time $<\tau>$, after turning off the electric field (though $<\tau>$ is too short for us to be able to observe it directly). A typical value of $<\tau>$, which in certain simple cases is essentially the inverse vibration frequency of crystal atoms, has an order of magnitude value of 10^{-13}sec, which yields a mobility of about 2000 cm^2/Vs from (2) by assuming an effective mass of 0.1 m_0. Thus, when a voltage of 1 V is applied between the ends of a sample of 1 cm length, the carriers move with a speed of 2000 cm/s. Such an estimated value of the mobility agrees, within an order of magnitude, with the observed mobilities of electrons and holes, 1500 cm^2/Vs and 450 cm^2/Vs respectively, in lightly doped silicon crystals at *room temperature* (RT).

Carriers are scattered in the bulk by phonons and defects (impurities), which determine their mobilities, while near surfaces/interfaces, as described in the next subsection, additional scatterings occur that lead to a further reduction in mobility.

The effective mass m^* is obtained from the energy dispersion curves $E(k)$ of the conduction or valence band by

$$m^* = \hbar^2 \left(\frac{d^2 E}{dk^2} \right)^{-1}, \tag{3}$$

where $\hbar$ is Planck's constant divided by 2π, and k is the wavenumber. So, once one obtains the band dispersion by, e.g., photoemission spectroscopy, m^* can be estimated from its curvature. An almost flat band, as the S_1-surface state on the 7 $\times$ 7 surface (see Fig. 5(a)), means a very large value of m^*, while a highly dispersive band, such as the S_1-surface state on the $\sqrt{3} \times \sqrt{3}$-Ag (see Fig. 5(c)), has a small m^*. Logitudinal and transverse effective masses of electrons in bulk silicon are $m^*_l = 0.98\ m_0$ and $m^*_t = 0.19\ m_0$, respectively, because of its crystal anisotropy, while $m^*_{lh} = 0.043\ m_0$ and $m^*_{hh} = 0.32\ m_0$ for light and heavy holes, respectively.

2.1.1.2. Carrier concentration. Some useful relations are derived here for metallic systems, using the concept of a Fermi surface. For 3D free-electron systems, the electron concentration n is calculated using the Fermi sphere;

$$n = \frac{2}{(2\pi)^3} \int_{|\mathbf{k}| < k_F} d\mathbf{k}, \tag{4}$$

where the integral is carried out inside the Fermi sphere (k_F being the Fermi wavenumber), because two quantum states exist per a volume $(2\pi)^3$ in k space by including spin degeneracy. Therefore, using the surface area of the Fermi sphere $S_F (= 4\pi k_F^2)$,

$$n = \frac{k_F^3}{3\pi^2} = \frac{1}{3\pi^2} \left(\frac{S_F}{4\pi} \right)^{3/2}, \tag{5}$$

so that the conductivity in Eq. (1) can be expressed as

$$\sigma = \frac{e^2 \ell}{6\pi^2 \hbar} S_F, \tag{6}$$

where ℓ is a mean free path given by $\ell = v_F < \tau >$ with the Fermi velocity $v_F = (\hbar k_F)/m^*$. For a 3D Ag crystal, where $m^* \sim m_0$ and $n = 5.8 \times 10^{22}$ cm^{-3}, for example, $k_F = 12$ nm^{-1}, $v_F = 1.4 \times 10^8$ cm/s, the Fermi wavelength $\lambda_F = 2\pi/k_F = 0.52$ nm, and the Fermi energy $E_F = \hbar^2 k_F^2/2 \ m^* = 5.5$ eV. Since $< \tau >$ is of the order of 10^{-13}–10^{-14}sec, the mean free path $\ell = 14$–140 nm, and $\mu = 18$–180 cm^2/Vs.

The electron concentration in Eq. (5) is generally given in terms of the *density of states* (DOS) $N(E)$;

$$n = \int_0^\infty f(E) N(E) \mathrm{d}E, \tag{7}$$

where the Fermi-Dirac distribution function $f(E)$ is already approximated in Eq. (4) by the step function

$$f(E) = \frac{1}{\exp\left[(E - E_F)/k_B T\right] + 1} \simeq \begin{cases} 1 & (E \leqslant E_F) \\ 0 & (E > E_F) \end{cases}, \tag{8}$$

k_B being the Boltzmann constant and T the absolute temperature. The approximation Eq. (8) is frequently used for metallic systems, especially at low temperatures (RT is in many cases low enough for the approximation). $N(E)$ for 3D free-electron systems is given by

$$N(E) = \frac{1}{2\pi^2} \left(\frac{2m^*}{\hbar^2} \right)^{3/2} E^{1/2}. \tag{9}$$

By inserting Eqs. (8) and (9) into Eq. (7), we again obtain Eq. (5). Similarly, for 2D free-electron systems, S_F should be the circumference of the Fermi disk ($S_F = 2\pi k_F$), so that

$$\sigma = \frac{e^2 \ell}{2\pi h} S_F, \tag{10}$$

because

$$n = \frac{2}{(2\pi)^2} \int_{|\mathbf{k}| < k_F} \mathrm{d}\mathbf{k} = \frac{k_F^2}{2\pi} = \frac{S_F}{(2\pi)^3}, \tag{11}$$

where the integral is carried out inside the Fermi disk.

By assuming $n = 7.8 \times 10^{14}$ cm^{-2} (atom number density of the topmost surface of a bulk-truncated Si(111)) and $m^* = 0.1 \ m_0$, then $k_F = 7.0$ nm^{-1}, $v_F = 8.1 \times 10^8$ cm/s, $\lambda_F = 0.9$ nm, $E_F = 19$ eV, $\ell = 81 \sim 810$ nm, and $\mu = 180 \sim 1800$ cm^2/Vs.

For 2D free-electron systems, the DOS

$$N(E) = \frac{m^*}{\pi\hbar^2} \tag{12}$$

is a constant value independent of energy E, which is in sharp contrast to Eq. (9) for 3D systems. Eq. (11) can also be obtained via Eqs. (7), (8) and (12).

2.1.2. Semiconductor statistics

In the above, only metals or degenerate semiconductors have been treated, where the Fermi–Dirac distribution function can be approximated by the step function Eq. (8). However, for intrinsic and lightly/moderately doped semiconductors, such an approximation fails, because E_F is located in the band-gap, so that the tail of the Fermi–Dirac distribution, far from E_F, plays important roles in determining the carrier concentrations. In such cases, the Fermi–Dirac distribution is frequently replaced by the Boltzmann distribution

$$f_e(E) \simeq \exp\big[-(E - E_F)/k_B T\big], \tag{13}$$

which is used for the conduction electrons, when E_F lies more than several $k_B T$below the bottom of the conduction band. The distribution of the conduction holes in the valence band is similarly approximated by

$$f_h(E) \simeq \exp\big[-(E\_F - E)/k_B T\big], \tag{14}$$

when E_F lies more than several $k_B T$ above the top of the valence band. The energy of the conduction electrons (holes) near the bottom (top) of the conduction (valence) band can be approximated by

$$E_e(k) = E_c + \frac{\hbar^2 k^2}{2m_e^*},\ E_h(k) = E_v - \frac{\hbar^2 k^2}{2m_h^*}, \tag{15}$$

where E_c and E_v are the energies at the bottom and top of the respective bands, and m^*_e and m^*_h are the effective masses of the respective carriers. The respective DOS in 3D systems, corresponding to Eq. (9) are then given by

$$N_e(E) = \frac{1}{2\pi^2}\left(\frac{2m_e^*}{\hbar^2}\right)^{3/2}(E - E_c)^{1/2}, \tag{16}$$

$$N_h(E) = \frac{1}{2\pi^2}\left(\frac{2m_h^*}{\hbar^2}\right)^{3/2}(E_v - E)^{1/2}. \tag{17}$$

Hence, the concentrations of the conduction electrons n and holes p are obtained via Eq. (7) as,

$$n = \int_{E_c}^{\infty} f_e(E) N_e(E)\mathrm{d}E \simeq N_c \exp\left(\frac{E_F - E_c}{k_B T}\right), \tag{18}$$

$$p = \int_{-\infty}^{E_v} f_h(E) N_h(E) \mathrm{d}E \simeq N_v \exp\left(\frac{E_v - E_F}{k_B T}\right), \tag{19}$$

respectively, where

$$N_c = 2\left(\frac{m_e^* k_B T}{2\pi\hbar^2}\right)^{3/2}, \; N_v = 2\left(\frac{m_h^* k_B T}{2\pi\hbar^2}\right)^{3/2} \tag{20}$$

are the effective DOS in the conduction and valence bands, respectively. These equations tell us that the carriers are dominated by the conduction electrons (n-type semiconductors) when E_F is located near E_c (see Eqs. (18) and (19) with $(E_F - E_c)/k_B T \sim 0$ and $(E_F - E_v)/k_B T >> 1$), while the conduction holes are the majority carrier (p-type semiconductors) when E_F lies near E_v ($(E_c - E_F)/k_B T >> 1$ and $(E_v - E_F)/k_B T \sim 0$). The E_F position is determined through the *charge neutrality condition* among the mobile carriers and ionized impurities (donors and acceptors). By introducing donors, which tend to be positive ions, by providing electrons into the conduction band, the E_F position will be raised towards E_c, while acceptors will become negative ions by taking electrons away from the valence band to leave holes therein, resulting in a downward shift of E_F towards E_v. In pure or intrinsic semiconductors, the concentrations of electrons and holes are equal, which means E_F lies around the middle of the band-gap. Even in doped (extrinsic) semiconductors, when the temperature is high enough, the carriers are dominated by the conduction electrons and holes thermally excited between the valence and conduction bands, so that the concentrations of electrons and holes are almost equal, so E_F is again located around the middle of the band gap. In this way, the carrier concentrations in the bulk are determined by the E_F position, which is controlled by impurity doping and temperature only. Near the surface, however, as described in the next subsection, additional considerations are needed to determine the carrier concentrations.

2.2. Near semiconductor surfaces

When two electric leads are connected to a surface of a semiconductor crystal and a voltage is applied between them, most of the current flows in the interior bulk of the semiconductor in the majority of cases. However, under certain conditions, the current passes preferentially near the surface. The electrical conductivity $\Delta\sigma$ near the surface can be different from that in the bulk, because of the different values of the carrier concentrations and mobilities near the surface.

When one measures the electrical sheet conductance g[S/□] of a square piece of arbitrary side length and thickness d[cm], g contains contributions from the bulk and the surface;

$$g = g_0 + \Delta\sigma, \tag{21}$$

where g_0 [S/□] is the bulk contribution $g_0 = \sigma_B \cdot d$ (σ_B [S/cm] is the bulk conductivity), and $\Delta\sigma$[S/□] is the extra contribution from the surface region.

The excess (or suppressed) conductivity near the surface is due to: (a) *band-bending* at the sub-surface region (a *surface space-charge layer*) $\Delta\sigma_{SC}$, (b) surface-state bands inherent in the surface superstructures $\Delta\sigma_{SS}$, and (c) conductive atomic layers (or thin films) grown on the surface $\Delta\sigma_{AL}$. Even if one measures the surface conductivity $\Delta\sigma$, it may be a sum of these three contributions; $\Delta\sigma = \Delta\sigma_{SC} + \Delta\sigma_{SS} + \Delta\sigma_{A\,L}$. Each contribution is explained below in more detail.

In order to extract only the surface contribution $\Delta\sigma$ from the measured conductance g, the conductance changes should be measured in situ in *ultra-high vacuum* UHV during the modifications of the surfaces in a controlled manner in which the bulk conductance g_0 does not change. Then, we can say that the *changes* in measured conductance come *only* from the surface region. To do this, we have used the following three methods:

1. Adsorption of (foreign) atoms. Adatoms can have excess charges, bringing about band-bending below the surface, or can induce a new surface superstructure that generates completely different surface electronic states.
2. Application of external electric field (*surface-field effect*). The field applied normal to the surface can penetrate into the semiconductor, giving rise to band-bending. But the field can be screened, to prevent its penetration, by metallic surface states, if any.
3. Irradiation with light. Excitation and re-combination of carriers near the surface can proceed via the surface states, especially for irradiation of light of less than the bulk band-gap energy.

These three kinds of perturbations are effective in modulating only the surface conductance, remaining the bulk conductivity almost unchanged. Because of limited space, only the first method is discussed here; the latter two approaches are reviewed elsewhere.

2.2.1. Conduction through surface space-charge layers

When space-charge layers are formed at surfaces or interfaces of semiconductors, the carrier concentrations in the layers are different from those in the deep bulk, thus resulting in changes of conductivity through the layers. The followings are three kinds of origins for formation of the surface space-charge layers (or for making the bands bend) (see Fig. 6)

1. External electric field: When an electric field is applied normal to the semiconductor surface, the field penetrates the sub-surface region, which causes a band bending under the surface, because the carrier concentration in semiconductors is not large enough to screen the field just at the surface. For example, consider a parallel-plate capacitor consisted of a metal plate and a semiconductor plate, as shown in Fig. 6(a). When the metal plate is positively (negatively) biased, the bands in the semiconductor bend downward (upward), while the bands in the metal hardly bend, due to the much higher carrier

concentrations in it. So excess conduction electrons (holes) can be accumulated at the space-charge layer thus formed under the semiconductor surface. The controllability of the carrier concentrations, and the resulting changes in electrical conductivity parallel to the surface through the space-charge layer is the basis of *metal-insulator-semiconductor type field-effect transistors* (MISFET).

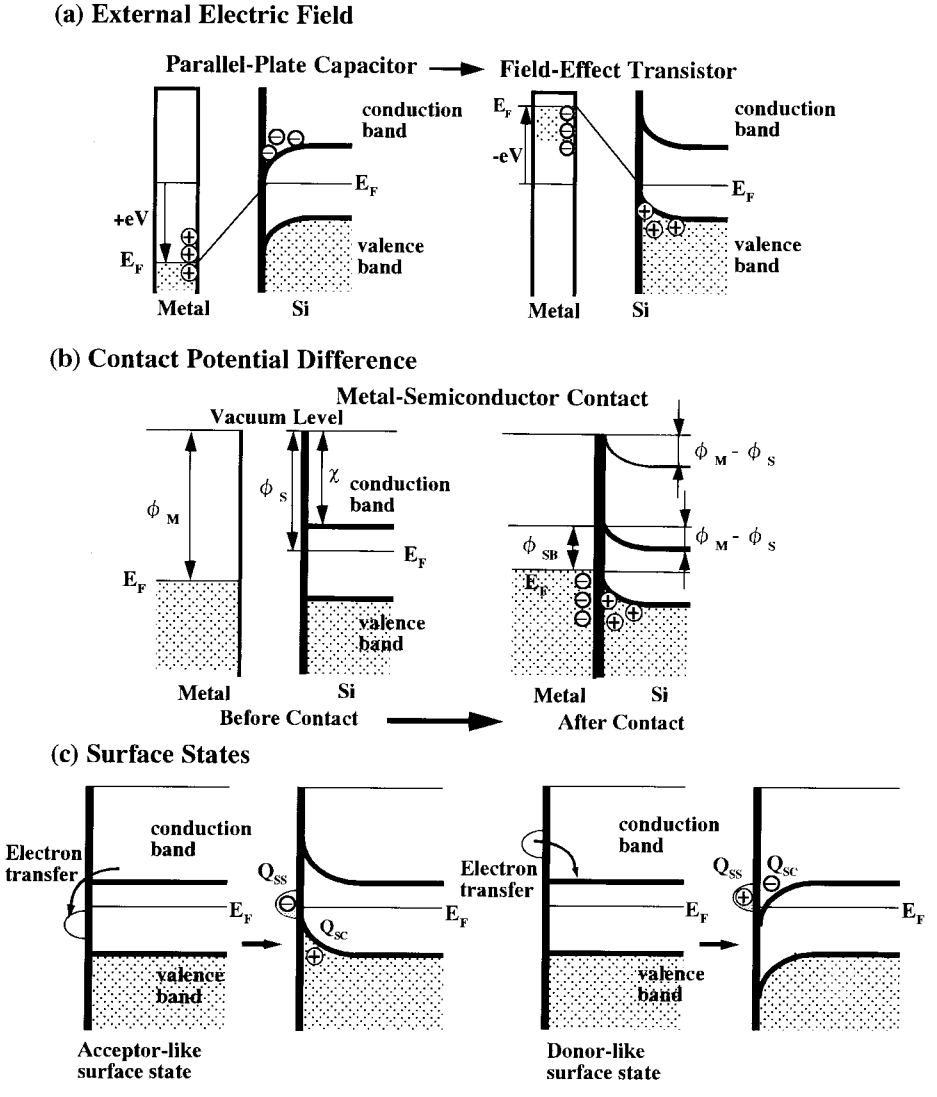

Fig. 6. Origins of the surface space-charge layer. (a) External electric field, (b) contact potential difference, and (c) surface states.

If some surface electronic states exist on the semiconductor surface, the external electric field will be more or less screened by making the surface states charged, so that the characteristics of conductivity vs bias (gate) voltage will change, depending on the energy distribution of the surface states.

2. Contact potential difference: When two materials of different work functions are in contact with each other, some electrons will transfer from the material of a lower work function to that of a higher work function to align the respective Fermi levels. This results in a difference between the respective vacuum levels, or potential difference. Fig. 6(b) shows an example of a contact between a metal and a semiconductor. Since the work function of the metal ϕ_M is larger than that of the semiconductor ϕ_S, in this case, some electrons move from the semiconductor side to the metal side after contact, which makes the metal negatively charged and the semiconductor positively charged, to produce a *contact potential difference*. The potential difference can be sustained on the metal side by the excess negative charges induced just at the interface, because of its large carrier concentration, while, on the semiconductor side, the potential gradually changes because the excess positive charges must be distributed in a much thicker layer (space-charge layer) from the interface, due to its much lower carrier concentration. Hence, the bands bend in the semiconductor side, as shown in Fig. 6(b). The conductivity through the space-charge layer parallel to the interface can be controlled by changing the voltage applied to the metal side, by inducing changes in the band-bending and the resulting carrier concentrations in the space-charge layer of the semiconductor, which is the basis of *metal-semiconductor field effect transistors* (MESFET). The electrons experience a *Schottky barrier* $\phi_{SB} = \phi_M - \chi$, when they pass through the interface from the metal side (χ being the electron affinity of the semiconductor), while the electrons feel an potential barrier $\phi_M - \phi_S$ when they flow from the semiconductor side.
3. Surface states: Surface states can be charged when their neutrality level does not coincide with the Fermi level. When some electrons are transferred from the bulk into the surface states, making them negatively charged, we call them *acceptor-type surface states*. When surface states are positively charged by donating electrons into the bulk, we call them *donor-type surface states* (Fig. 6(c)). The excess charges induced in the bulk are accumulated in the surface space-charge layer. Then, in order to maintain the charge neutrality condition

$$Q_{SS} + Q_{SC} = 0, \tag{22}$$

the bands should bend in the sub-surface region, where Q_{SS} and Q_{SC} are the charges in the surface states and the surface space-charge layer, respectively. When acceptor (donor)-type surface states are created, the bands bend upward (downward) as shown in Fig. 6(c) to induce excess holes (electrons) for counterbalancing the surface-state charge. Therefore, even if the charges in the surface states are not mobile, the surface state

can induce the changes in conductance parallel to the surface through the space-charge layer.

2.2.1.1. Calculating space-charge-layer conductance $\Delta\sigma_{SC}$. Once the surface space-charge layer is created, the excess carrier concentrations accumulated in the surface space-charge layer can be calculated by solving the Poisson's equation, when the magnitude of the band-bending is known [46–48]. Notations for the calculations are given in Fig. 7. The calculations are essentially 1D, with the normal to the surface in the z-direction; its positive direction is set toward the deep bulk from the surface at $z=0$, and the vacuum is in the $z<0$ region. The vertical axis in Fig. 7 indicates the electron energy; we have a forbidden energy gap between the valence and conduction bands. We call a mid-gap level $E_i(z)$, which is the center of the band gap, and changes according to the band-bending as a function of z. The Fermi level E_F is horizontal and independent of z. Whence, the potential variation (band-bending) near the surface is expressed as

$$\Phi(z) = \frac{1}{e}(E_F - E_i(z)), \tag{23}$$

so Poisson's equation is written as

$$\frac{d^2\Phi(z)}{d^2z} = -\frac{\rho(z)}{\varepsilon}, \tag{24}$$

where ε is the dielectric constant of the semiconductor. The charge density $\rho(z)$ is given by

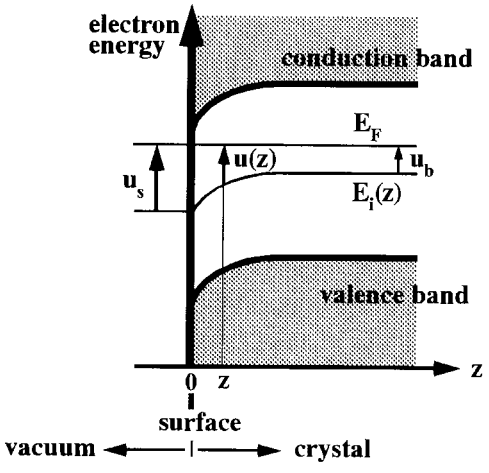

Fig. 7. Notations for calculating the carrier concentrations in the surface space-charge layer.

$$\rho(z) = e\{N_D - N_A + p(z) - n(z)\}, \tag{25}$$

where N_D and N_A are the densities of ionized donors and acceptors, and $p(z)$ and $n(z)$ are the concentrations of the conduction holes and electrons, respectively. The former two charges are static charges, while the latter are mobile and contribute to the electrical conduction through the surface space-charge layer. In the deep bulk $z \to \infty$, $n(z)$ and $p(z)$ should be equal to n_b and p_b, the concentrations of the conduction electrons and holes in the bulk, respectively, which, in turn, should be equal to N_D and N_A, by assuming nondegenerate semiconductors in which the dopants are completely ionized. According to the Fermi statistics Eqs. (18) and (19), and using a dimensionless quantity $u(z) = e\Phi(z)/k_BT = \{E_F - E_i(z)\}/k_BT$, the respective carrier densities are given by

$$n(z) = n_i e^{u(z)},\ p(z) = n_i e^{-u(z)}, \tag{26}$$

especially in the deep bulk,

$$N_D = n_b = n(z \to \infty) = n_i e^{u_b},\ N_A = p_b = p(z \to \infty) = n_i e^{-u_b}, \tag{27}$$

where n_i is the intrinsic carrier concentration, which via Eq. (20) is

$$n_i = N_c e^{-E_g/2k_BT} = N_v e^{-E_g/2k_BT} = 2\left(\frac{m^* k_B T}{2\pi\hbar^2}\right)^{3/2} e^{-E_g/2k_BT}, \tag{28}$$

by assuming $m^*_e = m^*_h \equiv m^*$ for simplicity, and E_g is the band-gap energy $E_c - E_v$. We have defined $u_b \equiv u(z \to \infty)$, which is positive for n-type semiconductors (Fig. 7), and negative for p-type. At the surface, $u_s \equiv u(z \to 0)$, which is different from u_b in band-bending situations, but equals u_b under the flat-band condition. Poisson's equation (Eq. 24) is now rewritten as

$$\frac{d^2\Phi(z)}{dz^2} = -\frac{2en_i}{\varepsilon}\{\sinh(u_b) - \sinh(u(z))\}. \tag{29}$$

By integrating once, we can obtain analytically the first derivative of potential $d\Phi(z)/dz$, which is equal to the electric field,

$$\frac{d\Phi(z)}{dz} = \sqrt{\frac{2n_i k_B T}{\varepsilon}} F(u(z), u_b), \tag{30}$$

where a function $F(u(z), u_b)$ is defined by

$$F(u, u_b) = \sqrt{2}\{(u_b - u)\sinh(u_b) - \cosh(u_b) + \cosh(u)\}^{1/2}. \tag{31}$$

As a result, we obtain the excess-electron concentration $\Delta n[\mathrm{cm}^{-2}]$ accumulated in the surface space-charge layer as

$$\Delta n \equiv \int_0^\infty \{n(z) - n_b\} dz = n_i L_D \int_{u_s}^{u_b} \frac{e^u - e^{u_b}}{F(u, u_b)} du, \tag{32}$$

where the Debye length $L_D=(\varepsilon k_B T/2e^2 n_i)^{1/2}$. The last term is obtained by changing the integration by z to that by u, using a relation $du/dz=(e/k_B T)\ (d\Phi/dz)$. The excess-hole concentration is similarly given by

$$\Delta p \equiv \int_0^{\infty} \{p(z)-p_b\}dz = n_i L_D \int_{u_s}^{u_b} \frac{e^{-u}-e^{-u_b}}{F(u,u_b)}du. \tag{33}$$

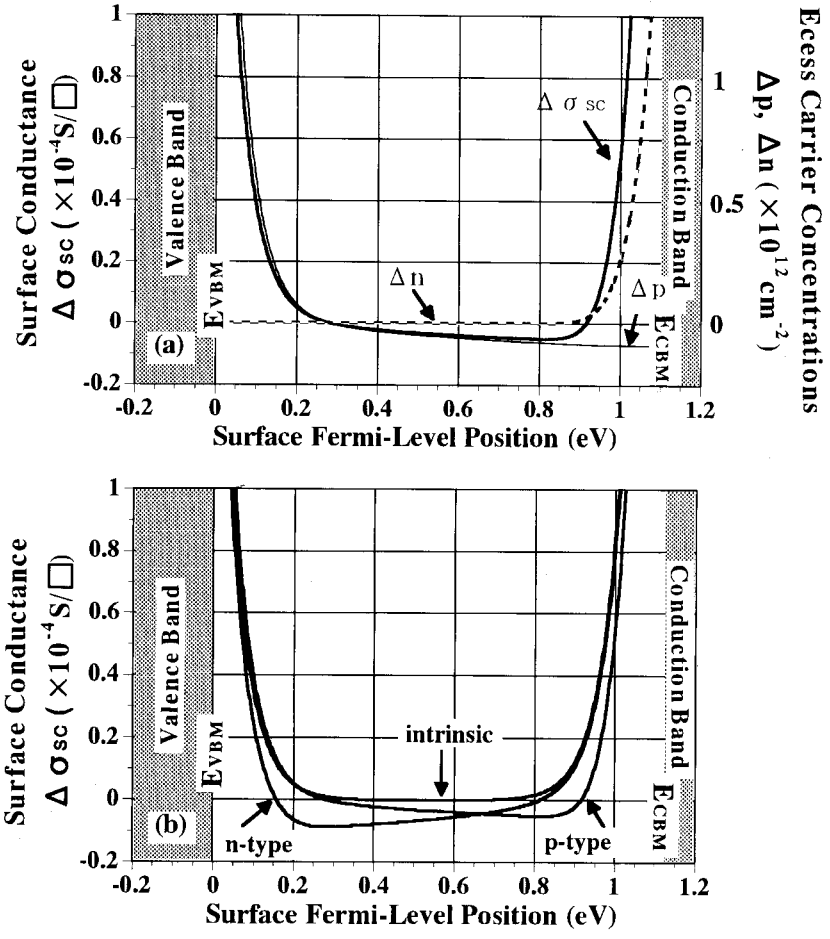

Fig. 8. (a) The excess conductance $\Delta\sigma_{SC}$ through the surface space-charge layer (bold solid line), and the excess carrier concentrations Δn (dashed line) and Δp (thin solid line), calculated as a function of the surface-E_F position for a p-type Si crystal of 20 Ωcm resistivity at RT. The $\Delta\sigma_{SC}$ under the flat-band condition (under which the surface E_F coincides with the bulk E_F) is defined as zero, because no excess or depleted carriers are accumulated near surface (the carrier concentrations are same as in deep bulk). (b) The excess conductance $\Delta\sigma_{SC}$ through the surface space-charge layer, calculated as a function of the surface-E_F position for n-, p-type Si crystals of 20 Ωcm resistivity and an intrinsic one at RT. Courtesy of Mr K. Tsuchie.

Finally, the excess conductance $\Delta\sigma_{SC}$ through the surface space-charge layer is given by multiplying the carrier mobilities with the excess carrier concentrations;

$$\Delta\sigma_{SC} = e(\mu_n \Delta n + \mu_p \Delta p), \tag{34}$$

where μ_n and μ_p [cm^2/Vs] are the mobilities of electrons and holes in the layer. These mobilities should be the same as in the bulk, unless the band-bending is not so steep, but they should be reduced under steep band-bending conditions, due to carrier scatterings by the surface and interface.

$\Delta\sigma_{SC}$, obtained in this way is shown in Fig. 8 as a function of the surface E_F position (or u_s) within the band-gap, together with Δn and Δp.

2.2.1.2. Accumulation, depletion, and inversion layers. When the surface E_F is located near the bulk valence-band maximum E_{VBM}, the bands bend upwards, so that the surface space-charge layer becomes a hole-accumulation layer, where the excess holes are induced into the bulk valence band, resulting in conductivity enhancement. Conversely, when the surface E_F is located near the bulk conduction-band minimum E_{CBM}, the bands bend downwards, so that the surface space-charge layer becomes an electron-accumulation layer, where the excess conduction electrons are induced into the bulk conduction band, again, resulting in conductivity enhancement. If we include the carrier-scattering effect at the surface, which results in the reduction of their mobilities, the calculated curve of $\Delta\sigma_{SC}$ will rise less steeply at both ends of the band-gap. Between these extremes, i.e., when the surface E_F is located around the middle of the band-gap, the surface space-charge layer is a depletion layer, where the carriers are depleted from the region near the surface, so that the conductivity is low.

In order to confirm experimentally the electrical conduction through the surface-state bands $\Delta\sigma_{SS}$ and/or through the grown-atomic layers $\Delta\sigma_{AL}$ mentioned below, we should evaluate and subtract the contribution of the surface space-charge-layer conduction $\Delta\sigma_{SC}$ from the measured surface conductance $\Delta\sigma$; $\Delta\sigma_{SS} + \Delta\sigma_{AL} = \Delta\sigma - \Delta\sigma_{SC}$. For evaluating the band-bending and the resulting excess conductance through the surface space-charge $\Delta\sigma_{SC}$, we should know the E_F position at surface or u_s in Eqs. (32) and (33). (u_b is uniquely determined by the bulk-dopant concentration.) *X-ray photoemission spectroscopy* (XPS) and also *ultraviolet photoemission spectroscopy* (UPS), under proper conditions, are applicable for this purpose, as mentioned in Section 3. A surface inversion layer (a special case of the surface space-charge layer in which the minority carriers dominate in the layer) which is electrically isolated from the bulk interior by the neighboring depletion layer, has been an area for a huge amount of study on 2D electron systems [56]. The carriers confined in the inversion layer can be regarded as a 2D free-electron gas, because they can move freely only along the surface. In the direction normal to the surface, the energy levels are quantized because of the narrow confining potential between the depletion layer under the surface and the barrier potential to the vacuum. Such a 2D free-electron gas is also formed at the heterojunctions, such as GaAs/GaAlAs, where the bands bend steeply enough to

generate an inversion layer. These systems show various interesting phenomena such as the famous quantum Hall effects and various magnetoresistance effects, and are also utilized in studies of the so-called *mesoscopic physics*, by combining them with micro-lithography techniques [57].

2.2.2. Conduction through surface-state bands

Two-dimensional bands are formed due to surface superstructures. The electrons in these bands should be mobile along the surface, just as the electrons in the 3D bulk bands, so that they can contribute to electrical conduction parallel to the surface. Its conductivity is directly dependent on the nature of the surface-state band (metallic or semiconducting) and the effective mass of the carriers therein.

Adatoms on semiconductor surfaces, with an exception of rare-gas atoms, form chemical bonds (partially ionic covalent bonds in general) with surface atoms of the substrate. When the coverage of the adatoms is small enough to be sparsely distributed on the surface, such adatoms may be described as interacting only with their nearest-neighbor substrate atoms. Such a localized model treats adatoms as a form of isolated heteropolar molecules with the substrate atoms [49]. The bonding and anti-bonding energy levels of such a *surface molecule* may be described as discrete surface states of donor and acceptor type, respectively (see Fig. 4), because there is no interaction among the adatoms. However, as the adatom coverage increases up to nearly a ML, interactions among the adatoms have to be considered in many cases. Especially, when the adatoms arrange periodically to form surface superstructures, the energy levels of the surface states become 2D bands. The electron wavefunctions in the bands may be extended, so that the electrons are mobile along the surface.

2.2.2.1. 2D Bloch states. The surface states on (111) faces of noble metals (Au, Ag, Cu), and also the Si(111)-$\sqrt{3}\times\sqrt{3}$-Ag surface as described in Section 1.2, are free-electron-like; their bands show an almost isotropic parabolic dispersion with a positive effective mass m^* and energy minimum E_0 at the $\bar{\Gamma}$ point in the surface Brillouin zone [55]. The energy of such a band is given by [58]

$$E = E_0 + \frac{\hbar^2\left(k_x^2 + k_y^2\right)}{2m^*}, \tag{35}$$

while the corresponding wave function is the 2D Bloch wave

$$\psi = \mathrm{e}^{ik_x x + ik_y y} \cdot u(x,y) \cdot f(z), \tag{36}$$

where $u(x,y)$ is the appropriate cell function. $f(z)$ represents the z-dependence of the surface state, whose most simple expression is $f(z) = \exp(-\int_0^z \mu(E,k_x,k_y)\mathrm{d}z)$, an exponential with a decay constant μ, indicating the decay of the surface state perpendicular to the surface into the bulk. In general, the wavefunction in the z-direction has discrete energy levels $(E_0,E_1,E_2,\ldots)$, because of the narrow confinement within only ML thicknesses. On the (x,y) plane parallel to the surface, the elec-

trons move freely, so that the surface state can be considered as a truly 2D electron system, whose DOS is given by Eq. (12) (see Figs. 9(a) and (b)). This situation is similar to the 2D electron systems confined in an inversion layer beneath

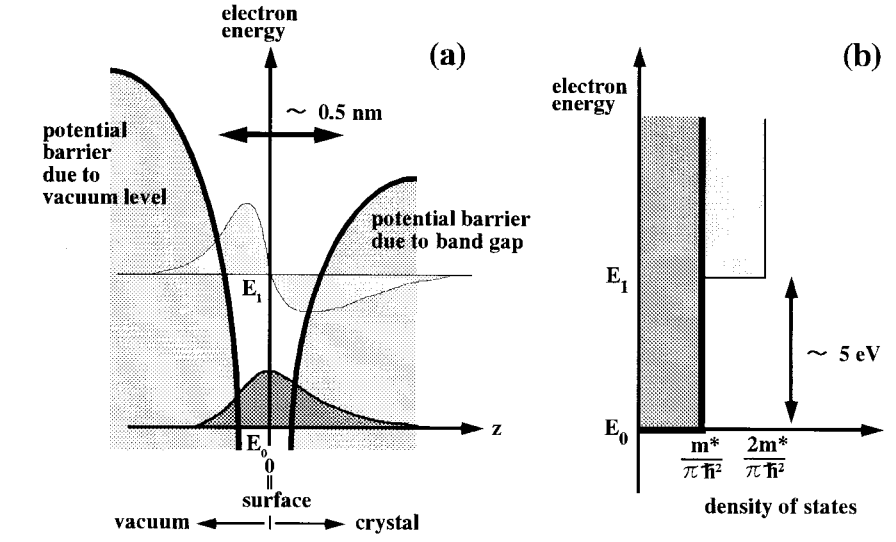

2D electrons in a surface state

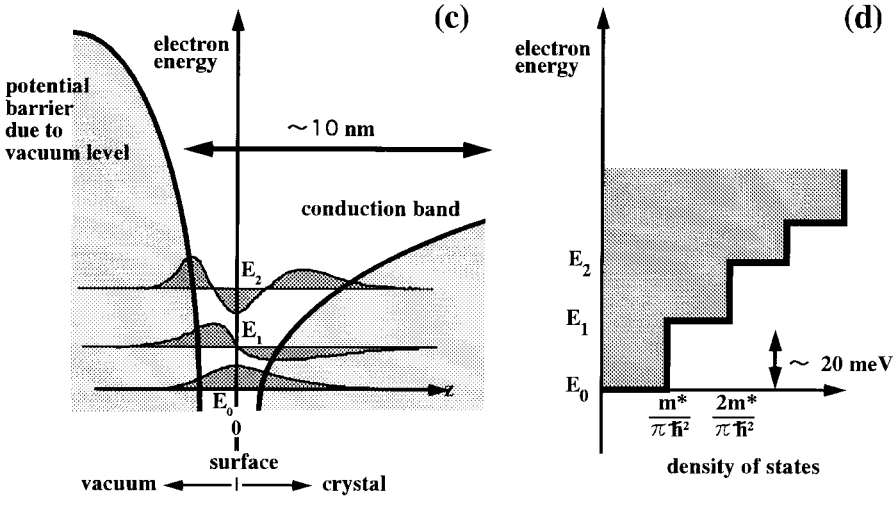

2D electrons in a surface inversion layer

Fig. 9. Two-dimensional free electron system (a) and (b) in a surface state, and (c) and (d) in a surface inversion layer. (a) and (c) Schematics of the z-components of the wavefunctions, and (b) and (d) density of states.

the surface, as described in the previous subsection (Figs. 9(c) and (d)). The differences between the surface-state 2D electron system and that in the inversion layer may be: (a) the width of the confining potential and (b) the cell function $u(x,y)$ in Eq. (36). Much narrower widths of the confining potential for the surface states, around a monatomic thick, compared with those in the surface space-charge layer, around 10 nm thick, result in much larger energy spacing $E_1 - E_0$ between the discrete energy levels of the z-component of the wavefunciton $f(z)$ (see Fig. 9(b)). So we have only to consider its ground state for the surface states, even at RT, while the higher energy levels will be frequently involved in the phenomena at the inversion-layer 2D electron systems, even at low temperatures (Fig. 9(d)). The cell function $u(x,y)$ in Eq. (36) can be totally different from superstructure to superstructure on the surface, which also contrasts to the 2D electron systems in the space-charge layer in which the variation of the crystal potential parallel to the surface is not explicitly considered, so that $u(x,y)$ would not depend on the position (x,y).

2.2.2.2. Experimental challenges to detect surface-state conduction. Until recently, there has been no definite experimental evidence for the surface-state conduction. The first attempt to measure the surface-state conductance of the Si(111)-7 × 7 clean surface was done using *electron-energy-loss spectroscopy* (EELS) by Persson and Demuth [50]. They analyzed quasielastic peaks in EELS spectra and obtained the value of surface-state conductance in AC mode to be of the order of 10^{-5}S/□, which is much larger than DC ones estimated in the reports mentioned below. However, their results show a metallic character of the surface state; the surface resistance increases linearly with temperature.

Hasegawa (Y.) et al. [51] suggested that the electrical conduction through the dangling-bond state on the Si(111)-7 × 7 clean surface is detected as an excess leakage current through a nanometer-scale point contact between the STM tip and the silicon surface. Fig. 10(a) shows the current vs voltage curves measured during an approach of the tip toward to the 7 × 7 surface of *p*-type and *n*-type substrates, respectively. The number on each curve is the displacement of the tip from the tunneling position; larger numbers indicate smaller gap distances. Under tunneling conditions, at the tip displacements between 1.0 to 4.0 Å, the I–V curves are similar on both of *p*- and *n*-type wafers. But, as the tip approaches further to the sample surface, the curves show different behaviors; opposite rectifications are observed, which indicates a Schottky barrier formation between the tip (metal) and the Si surface. But the conductance at $V=0$ at contact is measured to be the same for both wafers, viz., of the order of 10^{-6} S, much larger than that expected from the Schottky barrier (i.e., less than 10^{-12} S). They attribute this large *leak conductance* to the surface-state conductance. Fig. 10(b) shows the leak conductance measured from the I–V curves at $V=0$ as a function of tip displacement toward Au surface, the clean Si(111)-7 × 7 and Si(100)-2 × 1 surfaces, respectively. In a tunneling regime, where the gap is larger, the conductance increases exponentially with a decrease of the gap distance (forward displacement of the tip). When the tip comes contact into the sample surfaces, the conductances

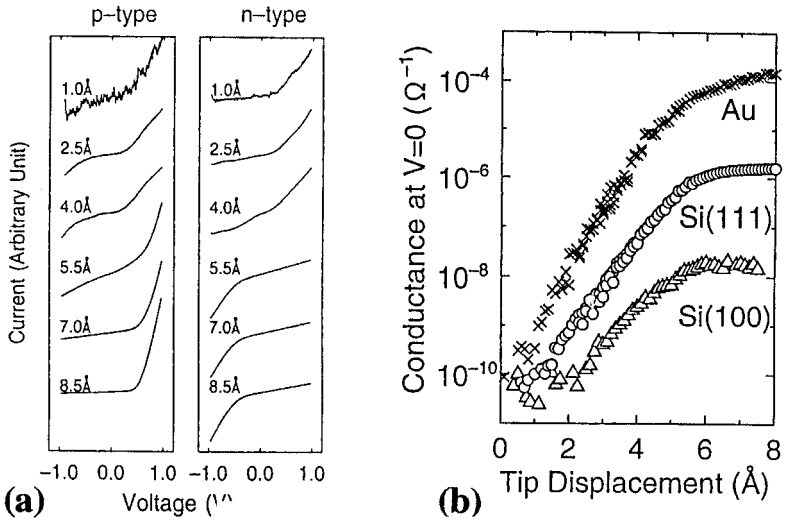

Fig. 10. (a) Current vs voltage spectra measured during STM-tip approaching toward the Si(111)-7 × 7 clean surface on *p*-type and *n*-type substrates. (b) Conductance at $V=0$ in the spectra like (a) as a function of tip displacement toward the Si(111)-7 × 7 surface, Si(100)-2 × 1 surface, and polycrystalline Au surface, respectively. Reproduced with permission from Ref. [51].

show saturation; the saturated values are different, depending on the surfaces. The 7 × 7 surface shows a larger conductance than the 2 × 1 surface, while its value is found to decrease by adsorption of oxygen onto the 7 × 7 surface; oxygen saturates the dangling bonds and reduces the DOS at E_F. These measurements suggest that excess leak conductance via the Schottky contact between the STM tip and the clean 7 × 7 surface is due to current paths parallel to the surface, i.e., the surface-state conductance through the metallic dangling-bond state. Its conductance is estimated at around 1 μS/□.

Another STM approach to detect the surface-state conductivity on the 7 × 7 clean surface has been carried out by Heike et al. [29]. They first fabricated circular insulating trenches on the 7 × 7 surface, as in Figs. 11(a) and (b), by applying a relatively high bias voltage with high tunneling current in the STM. After that, they observed the structured surface in the conventional STM mode. In an empty-state image, as in Fig. 11(b), the apparent height of the area inside the circle is observed to be lower than outside by around 0.1 nm, while in a filled-state image of Fig. 11(a), the heights are almost the same both inside and outside of the circle. They interpreted this phenomenon in terms of a Schottky barrier between the dangling-bond surface state and the bulk state (Fig. 11(c)). In imaging the empty states, the electrons tunnel into the dangling-bond surface state from the tip, and then travel laterally through the surface state along the surface for a while, and finally flow into the bulk conduction band. But when the area is surrounded by a insulating trench, the tunneled electrons *leak* out of the circle through a large leakage resistance of the trench, when the tip is positioned inside

it, and also leak into the bulk state through another large resistance, due to the above-mentioned Schottky barrier between the surface and bulk states. Therefore, a large voltage drop is generated between the inside of the circle and the bulk, resulting in a reduction of the effective bias voltage across the tunneling gap between the tip and sample. As a result, the tip approaches the surface to maintain the constant tunneling current, which means that a lower apparent height is observed in the topographic images. On the other hand, in filled-state imaging, the tunneling electrons are easily transferred from the bulk valence band into the surface state, because the Schottky barrier is forward biased, so that

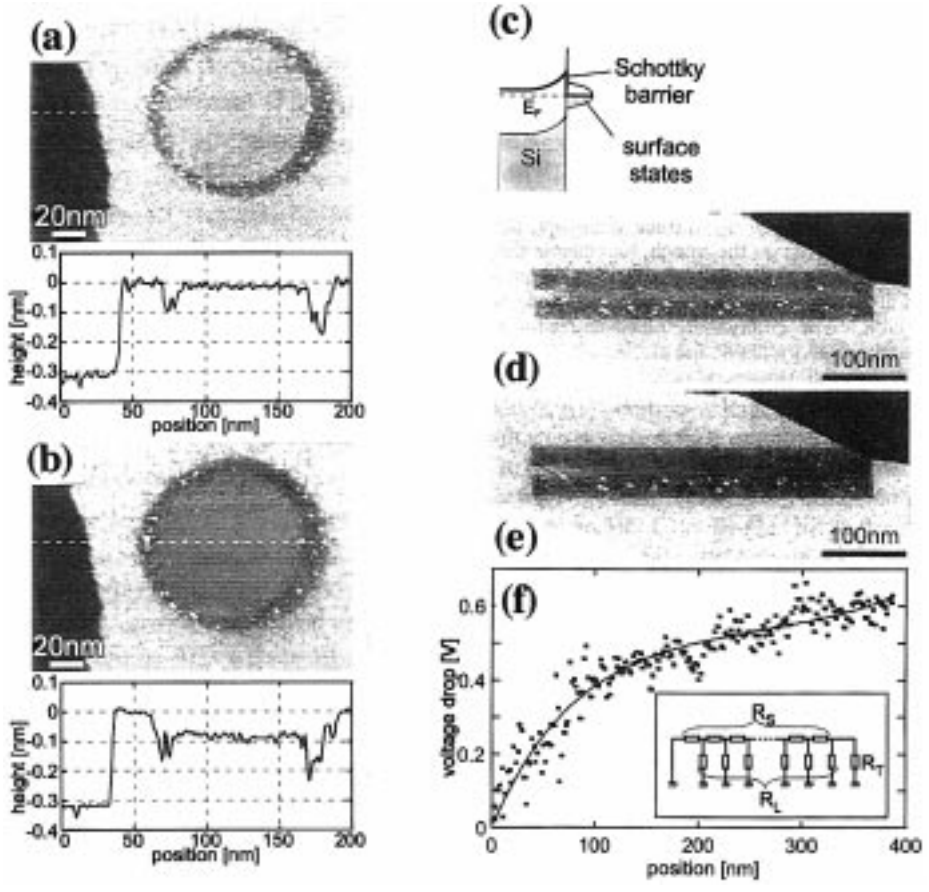

Fig. 11. (a) Filled-state and (b) empty-state STM images of an STM-patterned circle surrounded by an insulating trench, and the corresponding cross sections. (c) A schematic energy band diagram of the natural Schottky barrier between the surface states and the bulk states. (d) Filled-state and (e) empty-state STM images of a STM-patterned half-closed tape-shaped structure surrounded by an insulating trench. (f) Voltage drop along the tape structure in the empty-state image (e). The solid line is a calculated voltage drop using an equivalent electrical circuit model shown in the inset. Reproduced with permission from Ref. [29].

voltage drops, as in the empty-state imaging, are negligibly involved. When a half-closed tape-shaped pattern, surrounded by the same insulating trench, is made as in Fig. 11(d) and (e), the apparent height of the surface inside the tape in the empty-state image in (e) becomes lower (by approximately 0.2 nm), as the STM tip approaches the closed-end of the tape. This is because the current path through the surface state is essentially restricted to along the tape, when the tip is positioned inside the tape so that a voltage drop occurs due to a finite resistance of the surface state, as shown in Fig. 11(f). By comparing this voltage drop along the tape with the calculated one, using an equivalent-electrical-circuit model (shown in the inset), they deduced the sheet conductance of the dangling-bond surface state on the 7×7 structure to be 8.7×10^{-9} S/□, which is much smaller than those of Hasegawa (Y.) et al. [51] and AC conductance of Persson and Demuth [50]. Heike et al. [29] suggest that the discrepancy arises from the measurement methods; the method of Hasegawa (Y.) et al. should involve the conductance through the surface space-charge layer, as well as through the surface states.

The first direct experimental evidence for the surface-state conduction, using a conventional four-probe method, was obtained for the Si(111)-$\sqrt{21} \times \sqrt{21}$-(Ag + Au) surface, with identifying the surface-state bands contributing to the electrical conduction [11,12], and also on the Si(111)-$\sqrt{3} \times \sqrt{3}$-Ag surface as the effect of carrier doping on the surface-state band [14,18]. The details are described in Sections 5 and 4, respectively.

2.2.3. Conduction through grown atomic layers

If, for example, metallic atomic layers are grown on a semiconductor surface at low temperatures, the layers dominate the electrical conduction above the percolation-threshold coverage. Diffusivity of carrier scattering at the surface and the interface of the atomic layers (or thin films) depends on the morphology of the growing surface, leading to changes in carrier mobility. Therefore, the conductivity is sensitive to the growth modes and kinetics, both of which are dependent on the substrate surface structures. Although conduction through thin films has been extensively studied for the past 50 years [52], our interest lies in the thickness range from sub-ML to a few atomic layers, where the structures of the substrate surface, as well as the growth modes, decisively affect the conductivity [53].

When the grown atomic layers of around ML thick have surface superstructures, as in the case of In layers on Si(111) surface, as described in Section 7, the distinction between the electrical conduction through the surface-state bands $\Delta\sigma_{SS}$ and that through the grown atomic layer $\Delta\sigma_{AL}$ may become unclear; the current passes only through the topmost atomic layers on the surface.

2.2.3.1. Classical size effect. The electrical conductivity is sometimes reported to show oscillatory changes during the growth of atomic layers [53]. The reason is two-fold; one is the classical size effect and the other is the quantum size effect. The former is due to periodic changes in the step density of the surface during the

layer-by-layer growth of the atomic layer. Surface steps scatter the carriers diffusively, so that the mean free paths of the carriers become shorter, when the step density is higher. At the terraces, the carriers are reflected elastically, so that the mean free path is not shorten. In the layer-by-layer growth mode, proceeded by the birth and death of 2D islands on the terraces, the surface step density periodically changes. This type of oscillation in electrical conductivity, with ML period in many cases, due to the changes in step density is called *classical size effect*. These oscillations correspond to the intensity oscillations of the specular beam in *reflection-high-energy electron diffraction* (RHEED) during the growth.

2.2.3.2. Quantum size effect. The quantum size effect arises when the thickness of the conductive atomic layers is just half of the Fermi wavelength of the carriers, which are effectively confined in the layers, so that the carrier scattering at the surface/interface of the layer is reduced, resulting in an enhancement of the electrical conductivity. According to Schulte [59], when the thickness d of the atomic layers is multiples of half of the Fermi wavelength λ_F of the carriers,

$$d = \frac{n}{2}\lambda_F,\ n = 1,2,3,\ldots, \tag{37}$$

a new energy level in the atomic layers is occupied by electrons, so that the electron density at the Fermi level increases, resulting in the increase in conductivity. Since the thickness d of real atomic layers is multiples of monatomic thickness d_0, the requirement of Eq. (37) is rewritten as

$$d_0 n' = \frac{n}{2}\lambda_F,\ n = 1,2,3,\ldots,\ n' = 1,2,3,\ldots. \tag{38}$$

However, this relation is not satisfied exactly, because d_0 and λ_F are independent. The quantum size effect occurs when the difference between $d_0 n'$ and $n\lambda_F/2$ is small compared with λ_F [53].

2.2.3.3. Percolation. Near the percolation threshold coverage, where the islands of the grown atomic layers begin to connect to each other to make conductive paths [54], an interesting question is, what is the unit of percolation, single adatoms or some adatom clusters? Is such an unit metallic or not? These issues for the Ag/Si(111) and In/Si(111) systems are discussed in Sections 4 and 7, respectively.

3. Experimental methods

The experimental techniques we used are now briefly explained, but not in a comprehensive way; the reader should consult the textbooks and monographs on the surface experimental methods for more details [60,61]. For analysis of atomic arrangements on surfaces, we used RHEED, SEM and STM. For analyzing surface electronic structures, ARUPS and XPS were used. For electrical

conductivity measurements, the four-(point-)probe method was combined with a RHEED apparatus in UHV.

3.1. Atomic-structure analysis

3.1.1. RHEED

RHEED [62] is now used as widely as *low-energy electron diffraction* (LEED) for surface structure analysis. A fine collimated electron beam, accelerated up to around 10 keV, irradiates the sample surface with a grazing angle (around several degrees). The forward-scattered electrons produce the diffraction pattern on a fluorescence screen. RHEED has been utilized mainly for the following three purposes, (a) to recognize surface superstructures (or more generally the surface atomic structures) by analyzing the arrangements of (superlattice) reflection spots/streaks in the patterns, (b) to determine atomic arrangements in unit cells by analyzing so-called *rocking curves*, and (c) to monitor atomic-layer growths by detecting the intensity oscillations of specular reflections. Compared to LEED, RHEED has some advantages; a large space opens in front of the sample surface, so that *in-situ} observations during depositions, desorptions, irradiations with energy particles, at high and low temperatures, are easily done. It is suitable for observing dynamical changes of the surface structures.*

Fig. 12 schematically shows the relation between the geometrical arrangement in a RHEED apparatus and the reciprocal (wavevector) space using the *Ewald sphere construction*. An electron beam of wavevector $\mathbf{k}_0$ irradiates the sample surface, and its scattered and diffracted waves have wavevectors $\mathbf{k}_1$,$\mathbf{k}_2$, ..., whose lengths are

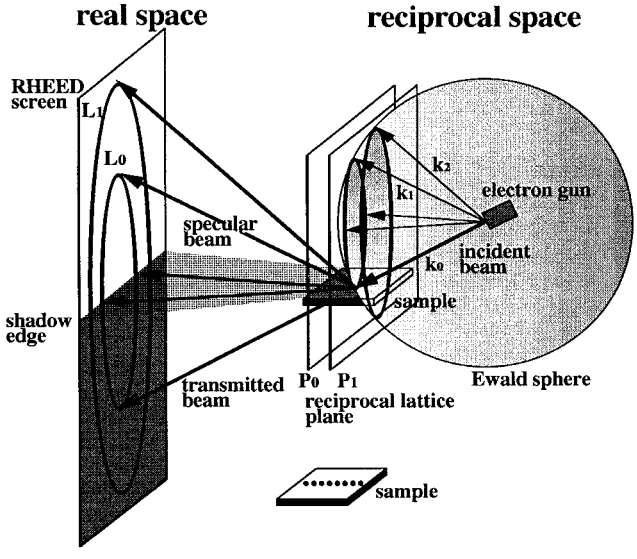

Fig. 12. Direct and reciprocal spaces for RHEED.

the same as $\mathbf{k}_0$, because only elastic scattering is considered. So the end points of the scattered wavevectors are located on the Ewald sphere. We now consider an example of scatters as shown in Fig. 12, linearly arranged atoms with an equal spacing along the incident electron beam. Its Fourier transform is a series of planes (reciprocal lattice planes) P_0,P_1, ... arranged perpendicular to the atomic row. The intersections between these reciprocal lattice planes and the Ewald sphere are circles, as shown in the figure. Only the wavevectors pointing from the center of the Ewald sphere to the intersecting circles emerge as diffracted waves. Therefore, some concentric circles should be observed on the fluorescent screen, though only the upper halves above the shadow edge are actually seen. The smallest (semi)circle is called the 0th *Laue zone* L_0, and the next smallest one is the 1st Laue zone L_1. More strictly, their radii are slightly larger only near the shadow edge, because of the refraction effect of the electron beam.

The surface (i.e., 2D lattice) of a 3D crystal is expressed as a combination of the atomic rows described above and its 90° rotated ones. Its reciprocal lattice is then the intersecting lines between two series of reciprocal lattice planes perpendicular with each other, that is, parallel *reciprocal rods* periodically arranged, standing normal to the sample surface. The intersections between the reciprocal rods and the Ewald sphere are points. These are the diffraction spots observed on the fluorescent screen. Thus, these spots are arranged on the semicircles (Laue zones) mentioned above.

3.1.1.1. RHEED pattern analysis. Fig. 13(a) shows a RHEED pattern taken from the Si(111)-7×7 clean surface at RT. Strong diffraction points E, O, and C appear in the 0th Laue zone L_0, and the points B and D are in the L_1. These spots, called *fundamental reflection spots* or *integral-order reflection spots*, come from the bulk crystal of diamond structure. In addition to these strong spots, many fine spots are also observed on the six concentric circles between L_0 and L_1. Fine spots appear also between the fundamental spots O and E, or O and C, in the L_0 zone. These are called *superlattice reflection spots, super-spots*, or *fractional-order spots*, which indicate the 7×7 superstructure on the surface. These spots appear with 1/7 spacing between the fundamental spots, which means that diffracting gratings of spacing seven times *larger* than the unit cell of the bulk crystal are created in real space.

From the RHEED pattern, we can reduce the 2D reciprocal lattice, which corresponds to a LEED pattern, using the construction drawn in Fig. 13(b). Since the surface observed now is a (111) surface of a diamond-structure crystal, the fundamental spots, corresponding to open circles in Fig. 13(b), make a triangular lattice. Because the RHEED pattern (a) is taken in $[11\bar{2}]$ incidence, the spot C corresponds to the (11) reciprocal point, and B is the (01) point, when the central spot O is the origin (00) of the reciprocal lattice. Since the diffraction spots are the intersecting points between the Ewald sphere and the reciprocal rods, which are perpendicular to the shadow edge as mentioned above, one draws a straight line from each fundamental spot perpendicularly to the shadow edge to reach the corresponding open circle in the figure. The 2D reciprocal lattice thus constructed

from the fundamental spots is used as a reference to plot the superlattice reflections; vertical straight lines are drawn from each super-spots in the same way as for the fundamental spots, and the corresponding fractional-order reciprocal points are plotted. To do this precisely, another RHEED pattern, taken in the $[1\bar{1}0]$ incidence, rotated by 30° from the $[11\bar{2}]$ direction, would be useful; the 0th Laue zone consists of O and B in this incidence, so that the spacing among the super-reflections along the OB line can be correctly evaluated. These constructions to deduce the 2D reciprocal lattice can be directly done, if one use a spherical

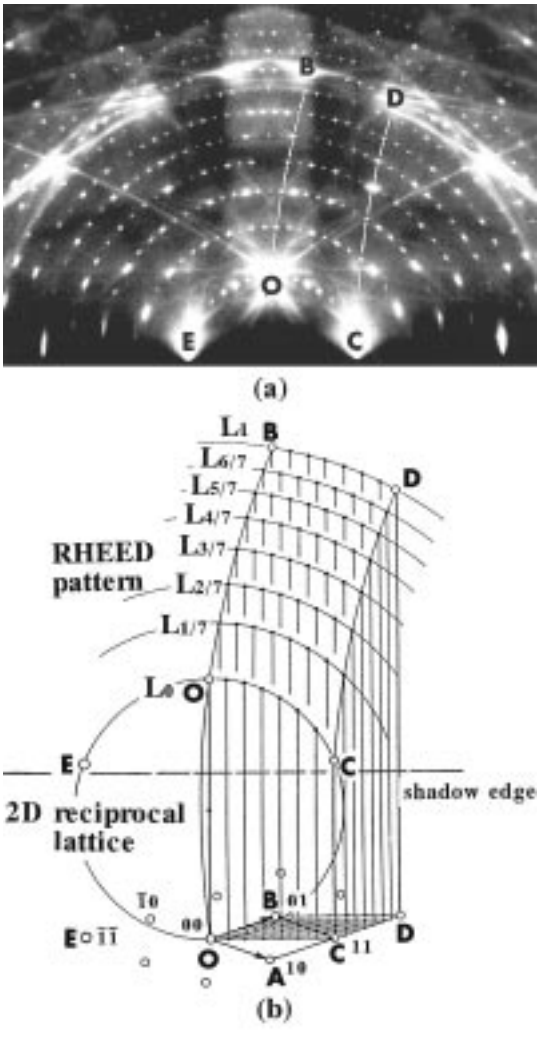

Fig. 13. (a) A RHEED pattern taken from the S(111)-7 × 7 clean surface at RT. The electron beam energy is 15 keV, the glancing angle is 3.1° in $[11\bar{2}]$ incidence. (b) Reduction into two-dimensional reciprocal lattice from the RHEED pattern.

fluorescent screen, whose center coincides with the irradiated point on the sample surface [63]. Other examples of RHEED patterns are shown in the following sections.

3.1.1.2. RHEED intensity oscillations. We should introduce another important application of RHEED, the so-called *RHEED intensity oscillations*. When atomic layers grow in the layer-by-layer mode, proceeded by 2D islands formation, as shown in Fig. 14(a) [64], the surface roughness periodically changes with the growth; the surface is the roughest, i.e., the highest step density, at half of the ML completion, while the surface is smooth at each ML growth completed. During such a growth, the intensity of the specular reflection in RHEED pattern (spot O in Fig. 13) is known to oscillate with a periodicity corresponding to the ML completion [64] (though sometimes corresponding to bilayer growths), as shown in Fig. 14(b). So one can precisely know the number of atomic layers grown on the surface just by counting the oscillation in-situ measured during the growth. Alternatively, one can precisely prepare an atomically smooth or rough surface by interrupting the growth at a particular phase in the RHEED intensity oscillation, e.g., exactly at the completion of a ML or a half ML. The oscillation measurements are used in Section 4 for monitoring Ag-layer growth.

3.1.2. SEM

Scanning electron micrographs are obtained by detecting secondary electrons of energy below about 10 eV that are excited by a fine primary electron beam of around 10 keV energy. The images reflect the spatial variations of the secondary electron yield, when the primary electron beam is scanned over the sample surface. The contrast in SEM images is produced, in general, by two means; one is related to the generation process of the secondary electrons and the other concerns the transfer processes of the secondary electrons from the crystal interior to vacuum through the surface.

On the generation of the secondary electrons, chemical contrast should be mentioned first of all; the generation efficiency of the secondary electrons depends on the elements. Heavier elements generally tend to produce more secondary electrons. But, the more important factor for the contrast generation in SEM is the incidence angle of the primary electron beam; when the primary beam irradiates the sample surface with grazing incidence, the beam can not penetrate into the deep bulk, so that its density and the resulting probability for exciting the secondary electrons increase only near the surface. Therefore, the secondary electrons are efficiently excited only near the surface region, whose depth is shallower than the escape depth of the secondary electrons, around $0.1 \sim 100$ nm, depending on their kinetic energy. As a result, the number of detectable secondary electrons increases, resulting in brighter areas seen in SEM images. So when the sample surface is rough, the areas whose surface is nearly parallel to the primary electron beam are observed brighter, while the surface areas nearly normal to the primary beam are seen darker in SEM images. In this way, the SEM images reflect qualitatively the topography of the sample surface.

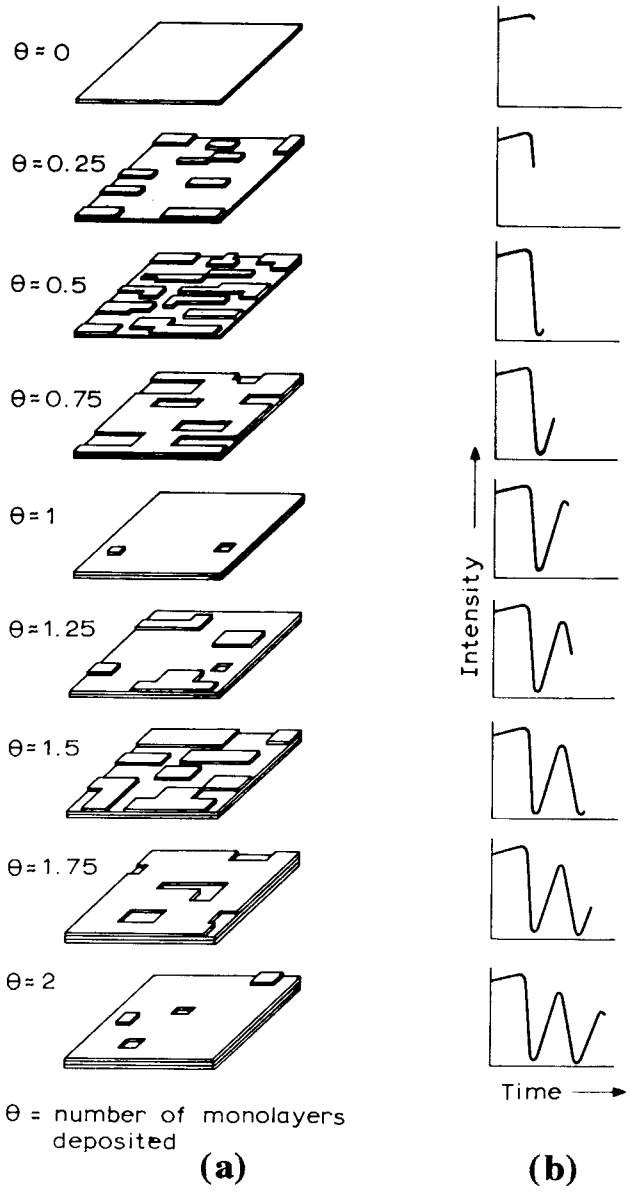

Fig. 14. (a) Schematic illustration of atomic layer growth in layer-by-layer mode. (b) Corresponding oscillatory change of the specular reflection in RHEED pattern. Reproduced with permission from Ref. [64].

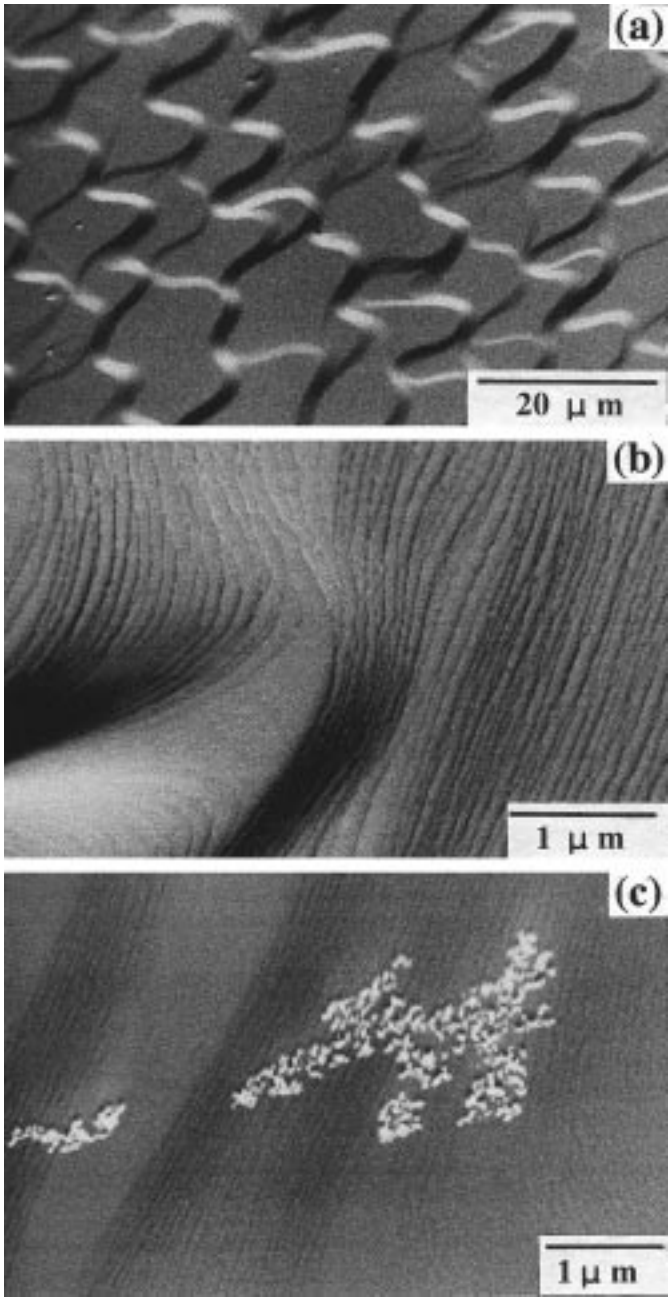

Fig. 15. (a) A grazing-incidence SEM image taken from the clean Si(111)-7 × 7 surface. The energy of primary electron beam is 30 keV, and its glancing angle is 6°. (b) An SEM image taken from the Si(111)-$\sqrt{3} \times \sqrt{3}$-Ag surface in which monatomic steps are seen. (c) When additional Ag of 0.3 ML is deposited on top of the $\sqrt{3} \times \sqrt{3}$-Ag surface maintained at RT, the Ag atoms aggregate into three-dimensional Ag microcrystals which are observed especially brighter.

Fig. 15(a) is an SEM image taken from the clean Si(111)-7 × 7 surface with a glancing angle of about 6°. During heating to 1500 K for cleaning the surface by direct electric current fed through the Si wafer, the atomic steps on the surface migrate (*electromigration*) to produce so-called *step bunching*; the surface separates into two regions, the bunched-step regions, whose average surface is inclined, and flat-terrace regions almost free from steps, so that the surface is like a terraced field on a slope of a mountain. The primary electron beam irradiates the surface with grazing incidence from the bottom in this image, so that the brighter areas are irradiated with a smaller glancing angle. In this way, the image gives us a qualitative *image* of the surface topography; the height difference between the terraces seems to be exaggerated in this grazing-incidence SEM image. As shown in a magnified image of Fig. 15(b), even monatomic steps can produce the observable contrast. For the case of monatomic steps, however, the anisotropy of the secondary electron emission also plays a role in generating the contrast [65].

Fig. 15(c) shows an SEM image of the Si(111)-$\sqrt{3} \times \sqrt{3}$-Ag surface with additionally deposited Ag atoms on top of it at RT. These Ag atoms nucleate into 3D Ag microcrystals, which are observed as brighter particles, while the $\sqrt{3} \times \sqrt{3}$-Ag structure remains on the substrate. This means that the generation efficiency of the detectable secondary electrons in the microcrystals are especially high due to the same reason as in the case of observations of surface topography in Fig. 15(a).

In order to clarify the mechanism for generating the contrast in SEM images concerning the transport and emission processes of the secondary electrons, we should consider several other factors such as the escape depth of the secondary electrons, work function, band-bending (for semiconductors), and the surface electronic states. Fig. 2 shows a growth process of the $\sqrt{3} \times \sqrt{3}$-Ag domains on the Si(111)-7 × 7 clean surface during Ag deposition. The brighter domains are the $\sqrt{3} \times \sqrt{3}$-Ag structure, and the darker ones are the 7 × 7 domains without Ag adsorption. The former surface structure is made by adsorption of monatomic layer of Ag. But the contrast between the respective domains, seen in the images, does not come from the Ag adlayer itself (chemical contrast) nor the difference in work function, but rather from the difference in the band-bending in the Si substrate [65]. For the other surface structures, work-function difference dominates the band-bending difference in making the SEM contrast. The dominant factor for SEM-contrast generation may be different from case to case. There is no example, up to now, in which the surface electronic states dominantly determine the SEM contrast.

3.1.3. STM

STM is completely different from the conventional electron microscopes; instead of a collimated fine electron beam, STM utilizes a fine tip [66,67]. The tip is made close to the sample surface with a spacing of less than 1 nm. When a voltage of around 1 V is applied between the tip and sample, a tunneling current flows between them. The amount of the tunneling current $I(x,y;V)$ detected at a position (x,y) on the surface with a bias voltage V is expressed by

$$I(x,y;V) \propto f(x,y;V) \cdot \mathrm{e}^{-2\kappa(V)d(x,y)}, \tag{39}$$

where $d(x,y)$ is the tip-sample separation, and $f(x,y;V)$ is the tip-sample joint DOS at the position (x,y). In the simplest model, a decay constant $\kappa(V)$ is given by

$$\kappa = \frac{\sqrt{2m\phi}}{\hbar}, \tag{40}$$

where ϕ is an average work function of the tip and sample, and m the electron mass. Then, Eq. (39) tells us two important things. One is concerning the exponential factor $e^{-2\kappa d}$. Since the work functions of most materials are around 4–5 eV, from Eq. (40) we find that a typical 2κ–2Å^{-1}. Thus, since the tunneling current drops by nearly an order of magnitude for every 1 Å separation between the tip and sample, we can trace the roughness of the surface with height resolution of sub-atomic levels, when we measure the current variations during scanning the tip laterally over the surface.

Another point that Eq. (39) indicates concerns the joint DOS $f(x,y;V)$. It is frequently assumed that the tip would consist of a mathematical point source of current (s-wave approximation), or the tip has a constant DOS. In such a case, $f(x,y;V)$ is simply regarded as the local DOS at the Fermi level $\rho(x,y;E_F)$ for the sample surface with a very small bias voltage. With larger bias voltages (but much smaller than the work function ϕ divided by e), it can be written as [68]

$$f(x,y;V) = \int_{E_F}^{E_F+eV} \rho(x,y;E)T(E,V)\mathrm{d}E, \tag{41}$$

where $T(E,V)$ is the barrier transmission coefficient, which describes the tunneling probability of an electron at an energy level E under an applied bias voltage V. The spatial variation of the tunneling current during the tip scanning thus reflects the local DOS of the sample surface, mixed with information on the surface topography. Therefore, for a surface on which the probed electronic states are localized on the surface atoms, as in the case of a dangling-bond surface state on the Si(111)-7 × 7 clean surface, as mentioned in Section 1.2, the protrusions observed in STM images directly correspond to the individual atoms. But when the probed surface electronic states have an extended wavefunction, atomic resolution will not be achieved. In general, STM images probing a surface state described by a 2D Bloch wavefunction Eq. (36) directly show the square of the absolute values of the cell function $u(x,y)$. The plane-wave part of the Bloch wavefunction will, in some cases, play a role in making the STM images, e.g., in imaging so-called *electron standing waves*, as described on the Si(111)-$\sqrt{3} \times \sqrt{3}$-Ag surface in Section 4.

3.2. Electronic-state analysis

The most widely used experimental techniques to obtain information on the occupied electronic states near surfaces are photoemission spectroscopies. The

sample surface is irradiated by mono-energetic photons, and the emitted photoelectrons are analyzed with respect to their kinetic energy. When photons in ultraviolet range are used for the excitation, it is called *ultraviolet photoelectron spectroscopy* (UPS). Unpolarized UV light of He I resonance line (21.22 eV) from a discharge lamp is the most frequently used. With X-ray radiation such as Mg K_α line (1253.6 eV), it is called *X-ray photoelectron spectroscopy* (XPS). With synchrotron radiation, one can cover the whole spectral range from the near-UV to the far X-ray regime. By choosing the photon energy properly, one can change the kinetic energy of the emitted photoelectrons, by which one can select the surface-sensitive mode or bulk-sensitive (surface-insensitive) mode, because the escape depth of the photoelectrons depends on their kinetic energy, as described in Sectiom 3.2.2. We have used UPS in surface-sensitive mode for analyzing the surface-state bands, while the band bendings beneath the surface have been measured by XPS in the bulk-sensitive mode.

3.2.1. ARUPS

In order to investigate the dispersion of electronic surface-state bands $E(k_{/\!/})$, i.e., a relation between the electron binding energy and the surface-parallel component of the wavevector, one has to determine the electron wavevectors. Besides the kinetic energy of the photoelectrons, one needs to know their emission direction. This can be done with an electron energy analyzer having an entrance aperture with a small acceptance solid angle. The analyzer should be rotatable around the sample to detect the photoelectrons emitted in various directions, i.e. ARUPS.

3.2.1.1. Energy and momentum conservations. The essential geometrical parameters in ARUPS [60] are shown in Fig. 16(a). The photons of energy $\hbar\omega$ irradiate the surface with an angle of incidence α with respect to the surface normal, and the emitted photoelectrons are detected in a direction with an angle of θ_e from the normal. In order to get the energy dispersion $E(k_{/\!/})$, the electron detector is rotated to change the detection angle θ_e with the incidence angel α fixed. In usual experiments, the detector is scanned in a plane, so-called a *plane of incidence* (a shadowed plane in Fig. 16(a)), which is defined by the direction of incidence of the exciting light and the detection direction for the emitted electrons. The orientation of the plane of incidence is defined by an angle β with respect to some principal crystal orientation of the sample. The electrons in the valence band, whose binding energy referred to E_F is E_i and its wavevector is k_i, are excited into an energy level E_f with respect to E_F (see Fig. 16(b)). Because of energy conservation,

$$\hbar\omega = E_i + E_f = E_i + \phi + E_{kin}, \tag{42}$$

where ϕ is the work function ($\phi = E_{vac} - E_F$), and E_{kin} is the kinetic energy of the emitted electrons outside the crystal ($E_{kin} = E_f - \phi$). The final-state energy level E_f (having the wavevector k_f) should be above the vacuum level E_{vac} to be detected (or E_{kin} to be positive). One needs to consider only direct transitions with $k_i \sim k_f$, because the wavevector (or momentum) of the photons is so small compared to

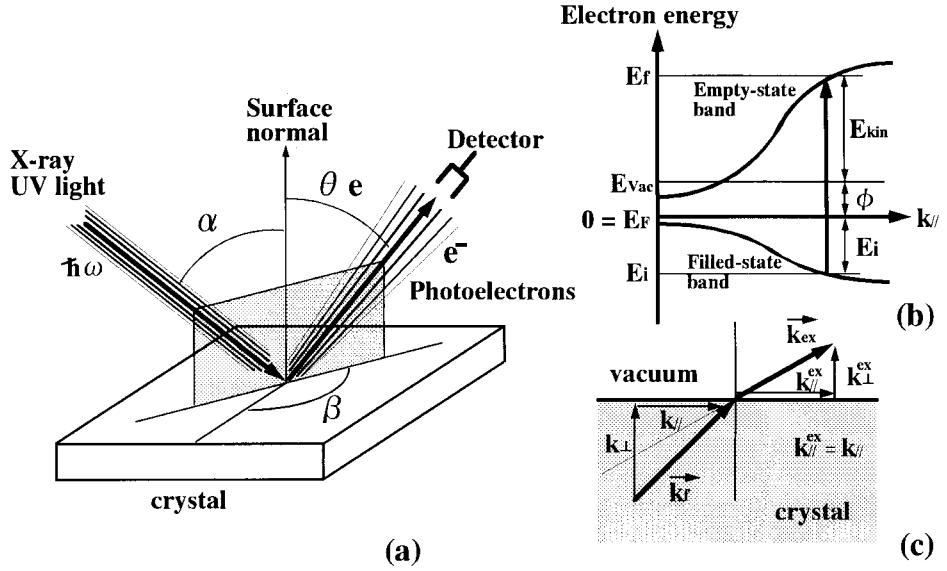

Fig. 16. (a) Definition of angles of incident photons ($\hbar\omega$) and emitted electrons (e^-). (b) Photoexcitation process represented in an electronic band scheme of a semiconductor. (c) Conservation of wavevector component $k_{/\!/}$ of photoelectrons upon transmission through the surface.

the electron's that it can be neglected; $k_f = k_i + \hbar\omega/c \simeq k_i$. The wavevector $\mathbf{k}^{ex}$ of the emitted photoelectrons in the external of the solid is determined by its magnitude (see Fig. 16(c)),

$$k^{ex} = \sqrt{(k_{//}^{ex})^2 + (k_{\perp}^{ex})^2} = \sqrt{\frac{2mE_{kin}}{\hbar}}. \tag{43}$$

Because of the 2D translational symmetry of the crystal surface under investigation, the transmission of the excited electrons through the surface into vacuum requires the conservation of their wavevector component parallel to the surface (Fig. 16),

$$k_{//}^{ex} = k_{//} + G_{//}, \tag{44}$$

where $k_{/\!/}$ is the surface-parallel component of the wavevector inside the crystal, and $G_{/\!/}$ is the 2D reciprocal lattice vector. It should be noted that the component $k_\perp$ normal to the surface is not conserved during the transmission through the surface, because a decelerating force normal to the surface, originating from the inner surface potential, always acts on the electrons during the transmission through the surface (see Fig. 16(c)).

Since $k_{/\!/}^{ex} = k^{ex}\sin\theta_e$, and Eqs. (42) and (43) lead to

$$k_{//}^{\mathrm{ex}} = k_{//} + G_{//} = \sqrt{\frac{2m}{\hbar} E_{\mathrm{kin}}} \cdot \sin\theta_{\mathrm{e}} = \sqrt{\frac{2m}{\hbar}(\hbar\omega - E_{\mathrm{i}} - \phi)} \cdot \sin\theta_{\mathrm{e}}. \tag{45}$$

From this relation, one can directly obtain the internal wavevector component $k_{/\!/}$ when one knows which Brillouin zone is investigated (i.e., $G_{/\!/}$ value).

3.2.1.2. Spectra from Si(111)-$\sqrt{3} \times \sqrt{3}$-Ag surface. Fig. 17(a) shows examples of ARUPS spectra, which are taken from the Si(111)-$\sqrt{3} \times \sqrt{3}$-Ag surface [15]. The UV light (He I resonance line, $\hbar\omega = 21.2$ eV) irradiates the surface with normal incidence, and the detection angle θ_{e} is changed along [10$\bar{1}$] orientation around the $\bar{\Gamma}$ point in the second $\sqrt{3} \times \sqrt{3}$ surface Brillouin zone. The measured kinetic energy E_{kin} of the emitted electrons are converted into the binding energy E_{i} referred to E_{F} using Eq. (42). The Fermi level E_{F} was determined by a sharp rise (Fermi edge) in a spectrum taken from a metal electrode on the sample holder. Three prominent peaks, S_1, S_2, and S_3, are observed in the spectra, which are now assigned as the surface states. Especially, the S_1 peak indicated by arrowheads is observed near E_{F} only at $\theta_{\mathrm{e}} = 28 \sim 34^{\circ}$ with some peak shifts. Fig. 5(c) is a 2D band dispersion diagram constructed from the spectra in Fig. 17(a) [15]. The abscissa is the surface-parallel component of the wavevector $k_{/\!/}$ along $\bar{\Gamma} - \bar{M}$ direction, and the ordinate is the binding energy below E_{F}. Closed circles indicate the peak positions in the spectra Fig. 17(a), and their sizes qualitatively correspond to the intensity of the respective peaks. The symbols $\bar{\Gamma}$ and $\bar{M}$ are symmetric points in the $\sqrt{3} \times \sqrt{3}$ surface Brillouin zone. The solid curve represents the upper edge of the projected bulk valence bands. It is noticed that some of the surface-state bands are located in the projected bulk-bands region, which is called *surface resonance*. The S_1 band, the main part of which lies outside the projected bulk-bands region, is definitely a surface state. The S_1 state indicated by arrowhead on the spectra in Fig. 17(a) shifts with θ_{e} crossing E_{F}, meaning a metallic surface state. But in Fig. 17(b), where the θ_{e} is changed along [11$\bar{2}$] direction, the S_1 peak is not observed near E_{F} at any emission angles, meaning an energy gap opening at this orientation. This is because the probed region in the surface Brillouin zone is along $\bar{K}$-$\bar{M}$-$\bar{K}$ in Fig. 17(b), which does not cross the $\bar{\Gamma}$ point around which the S_1 state exists.

3.2.1.3. Surface Brillouin zone. Here the band structure in bulk electronic states of silicon is introduced with Brillouin zones in bulk and at surface. Fig. 18(a) shows an electronic band structure of 3D silicon crystal, drawn along some principal directions. These directions and symmetric points on them are shown in the 3D Brillouin zone (b). The energy bands distribute three dimensionally in this Brillouin zone; the band diagram (a) only shows its sections along some directions. The *surface Brillouin zone* is constructed by projecting along $<111>$ direction in reciprocal space; the fundamental reciprocal spots should be elongated along $<111>$ direction and their cross points with a plane perpendicular to $<111>$ direction ($k_{/\!/}$ plane) should be marked. The origin on this plane, $\bar{\Gamma}$ point, which is a projection from Γ point in 3D Brillouin zone, should be also marked. The per-

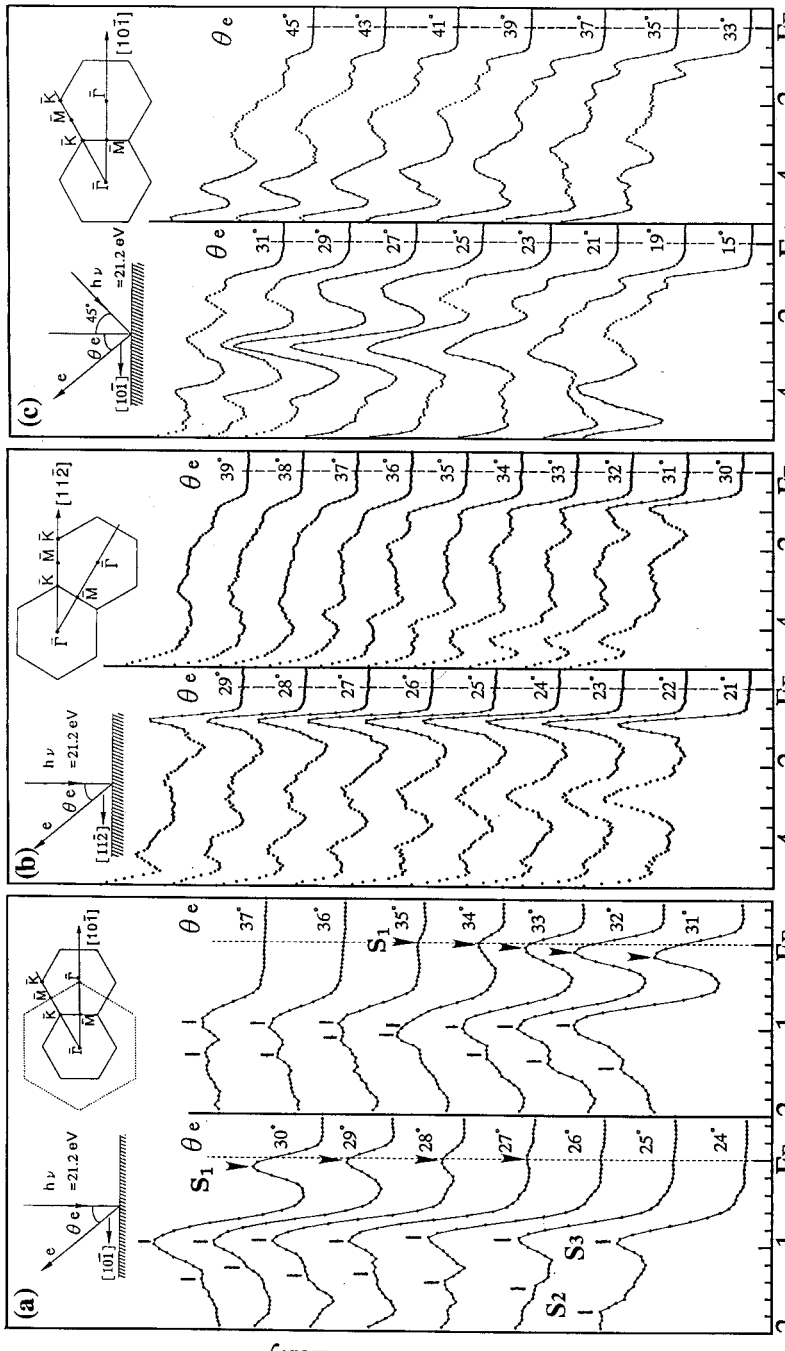

Fig. 17. A series of ARUPS spectra taken from the Si(111)-$\sqrt{3}\times\sqrt{3}$-Ag surface along (a) and (c) [10$\bar{1}$] and (b) [11$\bar{2}$] directions, respectively, with (a) and (b) normal photon incidence, or (c) 45° off incidence. From Ref. [15].

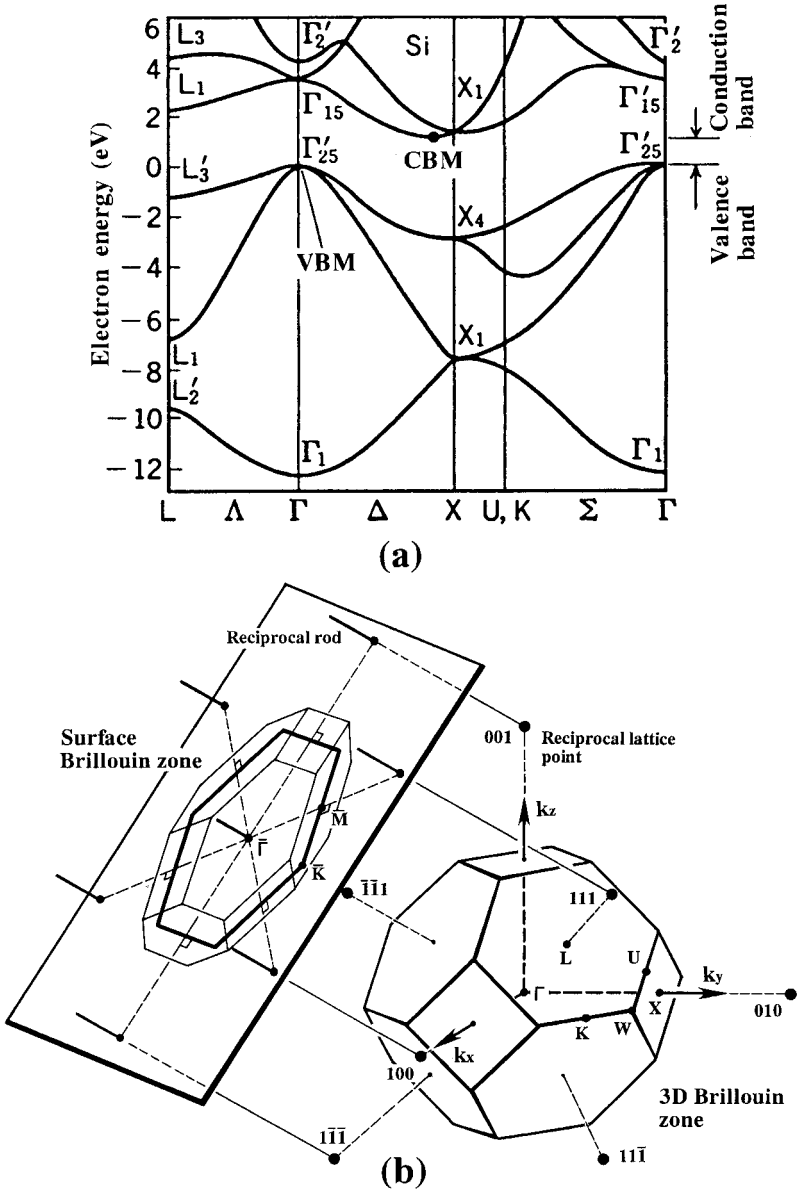

Fig. 18. (a) Band structure of three-dimensional silicon crystal. (b) The first three-dimensional Brillouin zone and its projection along <111> direction, corresponding to the surface Brillouin zone on the Si(111) surface.

pendicular bisector between each reciprocal point and the origin on the $k_{/\!/}$ plane should be drawn; these construct the zone boundary of the surface Brillouin zone. When the energy bands in the 3D Brillouin zone are projected similarly onto the $k_{/\!/}$ plane, some regions are occupied on this plane. This is the projected band structure of bulk states shown by the hatching in Figs. 5(a) and (c)

3.2.1.4. Surface-state emission. Mapping of the band structures on the surface Brillouin zone is straightforward from the measured spectra, but, it is not easy to distinguish between bulk and surface emissions in the spectra. Some criteria can help one to decide whether a particular band arises from surface states or bulk states.

1. Emissions from real surface states must fall into energy gaps of the bulk bands, as the S_1 band on the $\sqrt{3} \times \sqrt{3}$-Ag surface described above. Even if the emissions fall into the projected region of the bulk bands, the emissions can come from surface states (*surface resonance*) according to the following criteria.
2. When the photon energy of the exciting light is changed, a bulk-band emission will vary in energetic position, while a surface-state emission occurs at the same energy in the spectra irrespective of photon energies. This is because no definite $k_\perp$ exists for surface-state bands, so that Eq. (45) is always fulfilled for every possible choice of photon energy, while for a 3D band the $k_\perp$ component plays a role in determining its energy position, due to the momentum conservation.
3. Surface-state emissions are, of course, affected by surface treatments, while the bulk states are insensitive to them. When the emission band changes by surface-structure changes or some adatom adsorptions onto the surface, its origin is likely to be surface states.

3.2.1.5. Symmetry of wavefunctions. We should mention here another important information obtained from photoemission spectroscopies, viz., symmetry of the initial-state wavefunction. The optical excitation of an electron in solids is described in general by the *golden-rule* transition probability;

$$w_{\mathrm{fi}} = \frac{2\pi}{\hbar}|\langle f,\mathbf{k}_{\mathrm{f}}|\mathscr{H}|i,\mathbf{k}_{\mathrm{i}}\rangle|^2\delta\big(E_{\mathrm{f}}(\mathbf{k}_{\mathrm{f}}) - E_{\mathrm{i}}(\mathbf{k}_{\mathrm{i}}) - \hbar\omega\big) \tag{46}$$

$$= \frac{2\pi}{\hbar}m_{\mathrm{fi}}\cdot\delta\big(E_{\mathrm{f}}(\mathbf{k}_{\mathrm{f}}) - E_{\mathrm{i}}(\mathbf{k}_{\mathrm{i}}) - \hbar\omega\big), \tag{47}$$

where the perturbation operator $\mathscr{H}$ is given by the momentum operator $\mathbf{p}(=\hbar\nabla/i)$ and the vector potential $\mathbf{A}$ of the incident light (dipole approximation),

$$\mathscr{H} = \frac{e}{2m}(\mathbf{A}\cdot\mathbf{p} + \mathbf{p}\cdot\mathbf{A}) \simeq \frac{e}{m}\mathbf{A}\cdot\mathbf{p}. \tag{48}$$

In the last equation, $\mathbf{A}$ is assumed to commute with $\mathbf{p}$, since it is nearly constant in the long-wavelength limit. So the matrix elements in Eq. (47) are given by

$$m_{\mathrm{fi}} = \langle f,\mathbf{k}|\frac{e}{m}\mathbf{A}\cdot\mathbf{p}|i,\mathbf{k}\rangle, \tag{49}$$

where direct transitions $\mathbf{k}_{\mathrm{i}} \simeq \mathbf{k}_{\mathrm{f}} \equiv \mathbf{k}$ is assumed. By considering special experimental geometries and the symmetry of the electronic states involved, we can derive from Eq. (49) some *selection rules* for the observability of a particular initial state $|i,\mathbf{k}>$. Consider an experiment in which the exciting (unpolarized) light irradiates the sample surface from the surface-normal direction. Since the vector potential $\mathbf{A}$ is perpendicular to the light propagation direction, it lies on the surface ((x,y) plane), that is, $\mathbf{A}$ has only the (x,y) components. Then, if the initial state $|i,\mathbf{k}>$ to be detected is dominantly composed of a p_z-type orbital oriented along the z-axis, the matrix element Eq. (49) will vanish. Under the normal-incidence irradiation, only the $p_{x,y}$-orbital (and s-orbital) character of the initial-state wavefunction will be detected. This is the case for the S_1 state of the Si(111)-$\sqrt{3}\times\sqrt{3}$-Ag surface. The S_1-state emissions are strongly detected with normal irradiation as shown in Fig. 17(a), while they are negligibly weak, when the surface is irradiated at an incidence angle 45° off from the surface-normal, as shown in Fig. 17(c). This means that the S_1-state wavefunction is strongly anisotropic, lying on the surface ($p_{x,y}$-orbital like). To detect the states of p_z-like character, one needs to irradiate the sample with light at glazing incidence. When one can use polarized light from a synchrotron, more information about the symmetry character (s-,p-,or d-like) of the electronic-state bands will be obtained.

3.2.2. XPS

XPS is frequently used for chemical analysis by detecting core-level emissions. Each element has core levels with definite values of energy levels (though slight shifts occur, due to changes in the chemical environment, including surface chemical shifts). Surface chemical shifts in core-level emissions are used to distinguish the adsorption sites on the surface. When several different adsorption sites exist, one can determine the number of the sites by deconvoluting the emission spectra into different shifted components. This can be done by tuning the incident photon energy to realize the so-called *surface-sensitive* condition. As shown in Fig. 19, the escape depth of the electrons, and thus the mean free path in the solids, strongly varies as a function of their kinetic energy, but it is almost independent of the elements. So a curve showing the general tendency in Fig. 19 is sometimes called a *universal curve*. For photoelectrons from core levels, surface- and bulk-sensitive conditions may thus be achieved by properly adjusting the photon energy.

For example, Fig. 20(a) shows the change in Si $2p$ core-level photoemission spectra during the structural conversion from the 7×7 to the $\sqrt{3}\times\sqrt{3}$-Ag on Si(111) surface [42]. The spectra are excited by photons of $\hbar\omega = 108$ eV, and the binding energy E_{i} of the $2p$ core level is about 99 eV referred to E_{F}, and the work function ϕ of Si is around 4 eV, so that, according to Eq. (42), the kinetic energy of the emitted photoelectrons is $E_{\mathrm{kin}} = \hbar\omega - E_{\mathrm{i}} - \phi \simeq 5$ eV. Then, according to Fig. 19, the escape depth is more than 2 nm, much thicker than a monatomic layer. This is a bulk-sensitive condition. Therefore, the shift in the energy position of the

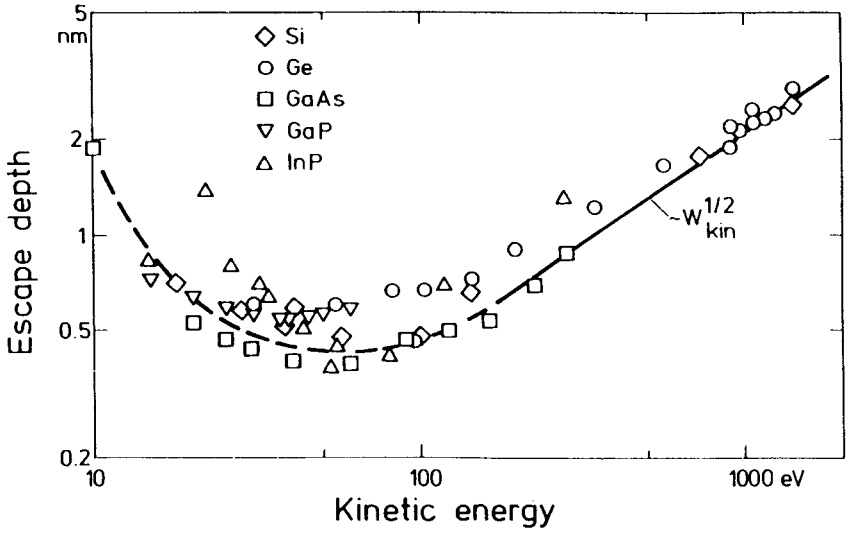

Fig. 19. Electron escape depth as a function of its kinetic energy. Reproduced with permission from Ref. [49].

emission between the 7×7 and the $\sqrt{3} \times \sqrt{3}$-Ag surfaces, observed in Fig. 20(a), does not come from surface chemical shifts, but is due to a change in the band-bending beneath the surface. Since the binding energy is referred to E_F, a larger binding energy of the core level means downward band-bending, while a smaller binding energy means upward band-bending as shown in Fig. 20(c).

In our measurements in XPS, we have used Mg K_α line ($\hbar\omega = 1253.6$ eV) as the exciting light, so that the kinetic energy of the emitted electrons is more than 1100 eV, which is again bulk-sensitive, according to Fig. 19. Even under the bulk-sensitive condition, the escape depth of around 2 nm is much thinner than the band-bending region (or surface space-charge layer) which is more than several hundreds nm in moderately doped Si. Therefore, the core-level shifts can be regarded as directly indicating the E_F shifts in the topmost surface.

Our X-ray is without a monochrometer, so it has a width of about 0.68 eV in energy because of Mg $K_{\alpha 1}$ and $K_{\alpha 2}$ lines with a distance in the energy spectrum of about 0.36 eV [69]. Hence the peaks of Si $2p^{1/2}$ and $2p^{3/2}$ are not resolved in the spectra. However, since the energy resolution of the energy analyzer is about 0.1 eV, the shifts of the convoluted peaks of the core level can be determined by about ± 0.05 eV precision by curve fittings.

In this way, we can estimate the changes in band-bending by using XPS in the bulk-sensitive mode. Since the band bending (or the E_F position at the surface, or u_s in Eqs. (32) and (33)) on the Si(111)-7×7 clean surface is known [30], the surface E_F positions on the other surface superstructures can be determined just by comparing the core-level position with at the 7×7 surface. . Then, we can estimate the carrier concentrations and the resulting conductance $\Delta\sigma_{SC}$ in the

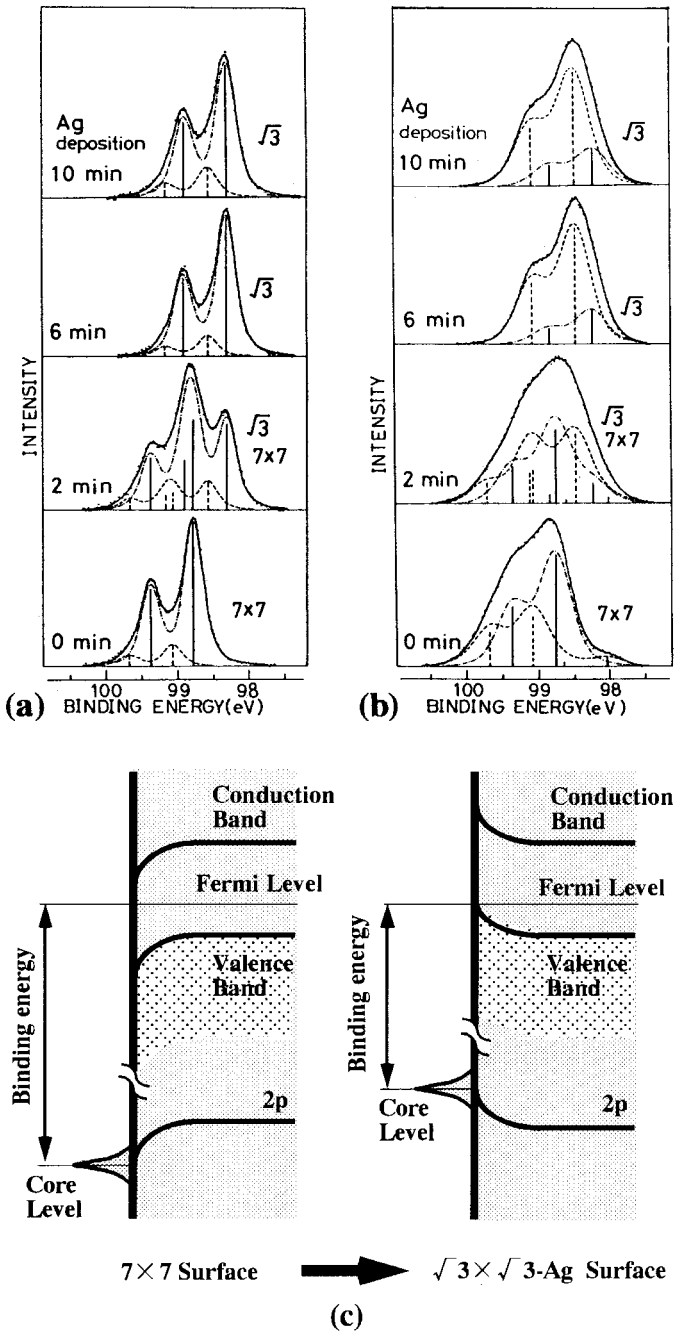

Fig. 20. Si 2*p* core-level photoemission spectra with increase in Ag coverage excited by (a) 108-eV and (b) 130-eV synchrotron radiation, respectively. The surface structure is converted from the Si(111)-7 × 7 clean surface to the $\sqrt{3} \times \sqrt{3}$-Ag surface with coverage increase. Reproduced with permission from Ref. [42]. (c) Schematic illustrations of the band bendings beneath the respective surfaces determined by the core-level shift.

surface space-charge layer according to the calculations mentioned in Section 2.2.1. UPS is sometimes also used to measure band-bending [70]; once an emission peak in UPS spectra is identified as a bulk emission, one only has to trace its shifts. But one has to pay attention to the effects of possible hybridization in UPS.

3.3. Electronic transport measurements

When the atoms rearrange only in one or two atomic layers on the topmost surface, does the electrical conductance of a Si wafer with a macroscopic thickness (0.4–0.5 mm for our samples) actually change by detectable amounts? Measuring the conductance changes of surfaces with superstructures is not straightforward, because the concentration and distribution of dopants in the bulk may change due to the high-temperature heating in vacuum that is necessary for cleaning and preparing the superstructures [71,72]. This may inevitably result in changes in both surface and bulk conductance. To extract the surface contribution from the measured conductance, we made two types of superstructures simultaneously on a single Si wafer (one superstructure on each half of the wafer), and measured the conductivities of the respective surface areas at one time. The bulk beneath the superstructures should have the same heating histories and temperature, meaning the same bulk conductance (at deeper below the surface space-charge layer). So the difference in the measured conductivities can be attributed only to the difference in the surface conductance [7].

3.3.1. Four- or six-probe method

Fig. 21(a) shows a schematic of the sample holder for the conductance measurements and RHEED observations, and (b) is the whole view of the holder with cooling vessels. During metal depositions in the preparation of the surface structures, the half of the wafer is covered by a mask to prevent metal adsorption, while the whole wafer was heated to a uniform temperature. The structure of the other half is changed into metal-induced superstructures, while the masked area remains the clean 7×7 structure on Si(111) surface, for example. The resistance of the respective areas are simultaneously measured by measuring the voltage drops between two pairs of Ta or Mo wire contacts set on the respective surface areas, with direct currents ($1 \sim 200$ μA) flowing through the Ta clamps at both ends of the wafer. By this *six-probe method*, we can measure the conductance difference originating only from the difference of surface superstructures, even if the conductance through the underlying bulk may change, due to impurity redistributions in bulk raised by high-temperature flashings in UHV. (From our experience, since the conductivity of a Si wafer with, e.g., the 7×7 surface did not significantly change, even by repeating the high-temperature flashings many times, the impurity redistribution does not seem to be severe, at least, for lightly doped Si crystals.)

Furthermore, during metal depositions, in-situ and real-time measurements of changes in resistance are possible by the conventional four-probe method combining with RHEED observations. These methods enable one to correlate the

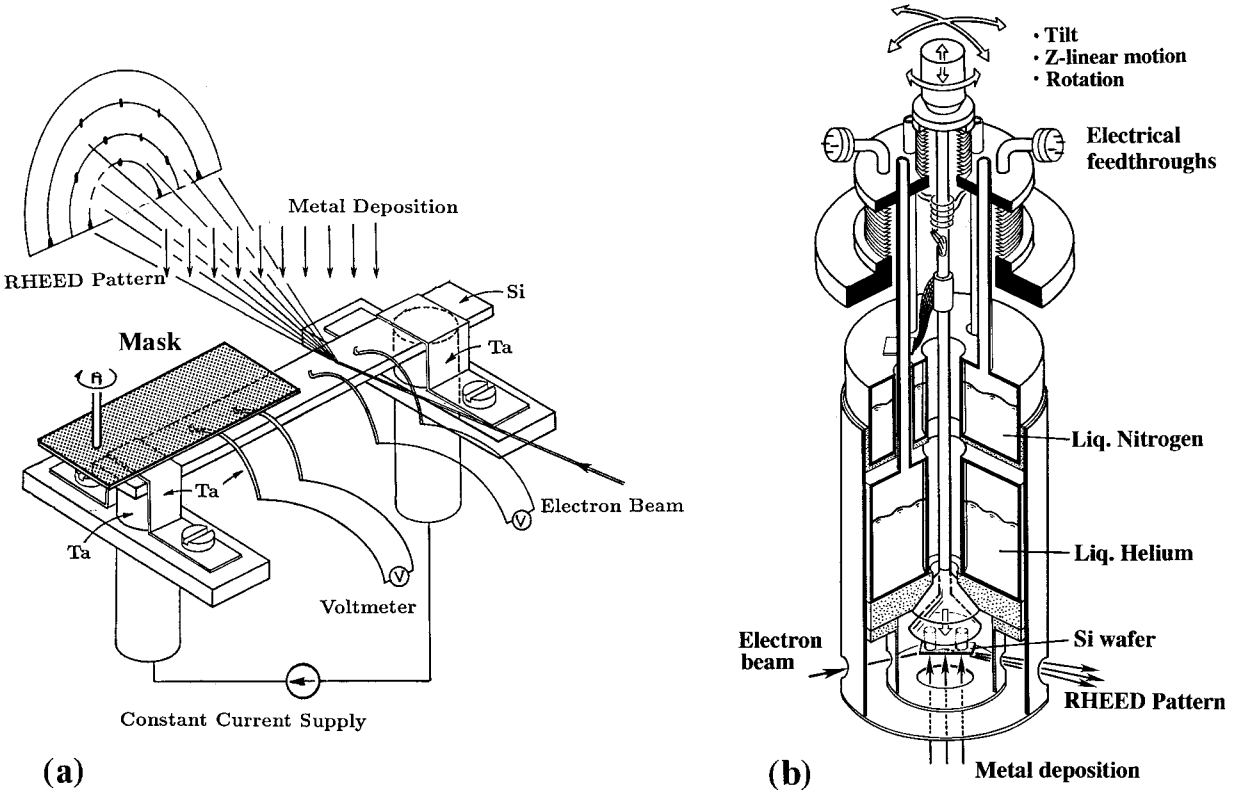

Fig. 21. A RHEED sample holder for the electrical conductivity measurements in UHV using a six-probe method. (a) Only near the sample (drawn upside down), and (b) a cut view of the whole holder. After the surface superstructures are confirmed by using RHEED, the electron beam is always turned off during the subsequent conductivity measurements.

resistance changes with dynamical structural changes, such as growth styles of atomic layers, structural phase transitions, and so on. Since the electron beam of RHEED severely disturbs the resistance measurements, it is always turned off except for intermittent observations of the RHEED pattern to confirm structural changes.

3.3.2. Probe contacts

The contacts between the Ta or Mo wires and the Si surface are sometimes unstable. But the repeated flashing of the Si wafer up to 1500 K, with the metal wires in contact, make their contact resistances small and steady. Though, in principle, the contact resistances at the probe contacts do not affect the measured resistance in the four-probe method (actually the contacts are not ohmic, but rather Schottky contacts), one should carefully check the validity of the measured voltages. A linear relation between the measuring current and the voltage drop should be confirmed first of all. Especially at low temperatures, some additional voltage differences sometimes occur, due to a thermoelectromotive force originating from the temperature difference between the probe contacts, and also due to the photovoltaic effect of light from outside the chamber or from the evaporators. In such cases, the differential resistance should be measured by changing/reversing the measurement current or using AC. All the view ports on the vacuum chamber should be covered to keep the inside dark.

Even in the ambient gas, the surface conductance is successfully measured by a four-probe method with simple mechanical contacts; Petersen et al. measured the conductance changes of Si(111) and Si(100) clean surfaces during dosing oxygen, using four tungsten-carbide pins just pressed against the silicon surface with a constant load [73]. Their four probes are detachable in UHV and are reattached to ensure the reproducibility in the measured voltage drops. From the results, they discuss the early states of the oxidization processes.

Some special methods for obtaining *good* electrical contacts between the metal probes and the Si surface are devised, which should be compatible with high-temperature heatings in UHV for surface preparations. Suurmeijer et al. [74] deposited Nb as contact pads on the Si wafer, on which electrochemically etched W wires were pressed. The group at Hannover University [54] also used predeposited metal pads for the contacts; they made the contact areas by depositing 100-nm-thick Mo and annealing to silicide at 450°C before mounting in UHV. They sometimes dope boron up to as high as 5×10^{20} cm^{-3} concentration only at the contact pad areas before Mo deposition by using ion implantation techniques [75]. Furthermore, 20 ML of Ag were deposited onto the whole surface in UHV and then removed only from the central portion of the sample. By these processes, a *good* electrical contact to the surface (not to the bulk) was expected; in fact, low, stable, and similar contact resistances were obtained for all the four probes, even at liquid-helium temperatures. These metal-predeposited contact areas are sometimes important for measurements with high-resistivity Si wafers, such as above 1000 Ωcm or at low temperatures, while stable contacts can be easily achieved just by pressing the metal wires directly on the bare Si surfaces of

lower resistivity such as 100 Ωcm at RT. Especially, as mentioned above, high-temperature heating up to around 1500 K of the wafer with the metal wires in contact tends to make the contact very stable, probably due to silicide formation at the contacts.

For measuring the conductance through conductive metal atomic layers continuously during their growths, one preferably increases the measurement current, so that the current density per unit thickness of the layer is always kept constant [53].

Instead of a linear four-probe measurement method of Fig. 21(a), the so-called *van der Pauw method* is sometimes used [76] in which a clover-leaf like sample is used. This method is preferable for simultaneous measurements of the Hall effect with conductivity, and for detecting inhomogenuities in the sample.

3.3.3. Surface conductance

The electrical sheet conductance $g[S]$ is defined by

$$g = \frac{L}{W} \cdot \frac{1}{R}, \tag{50}$$

where L and W are the length and width of the measured surface area, and R is the resistance of the area. The resistance measured by the linear four-point probe method is given by $R = V/I$ (in the case that the geometrical factor is unity), where I is a small current supplied through the outer two probes and V is the voltage drop between the inner pair of probes. This conductance g contains both of the bulk conductance and surface conductance, as described by Eq. (21). The surface conductance $\Delta\sigma$ is always measured as a change in the sheet conductance g, i.e.,

$$\Delta\sigma = \frac{L}{W}\left(\frac{1}{R} - \frac{1}{R_0}\right), \tag{52}$$

where R_0 is the resistance under an appropriate reference; for example, when one wants to measure the surface-conductance changes induced by foreign-atom adsorptions, R_0 should be the resistance before adsorption. When one wants to measure the surface-conductance differences among various superstructures, one may take R_0 to be the resistance of the clean 7×7 surface. Often R_0 is taken to be the resistance under flat-band situation.

4. Silver adsorption

4.1. Ag-induced surface superstructures

4.1.1. At elevated temperatures

Phase diagrams are collected from the literature as shown in Fig. 22, showing surface reconstructions on the Ag-covered Si(111) surface observed at temperatures higher than RT [77,78,87]. Three kinds of surface superstructures are

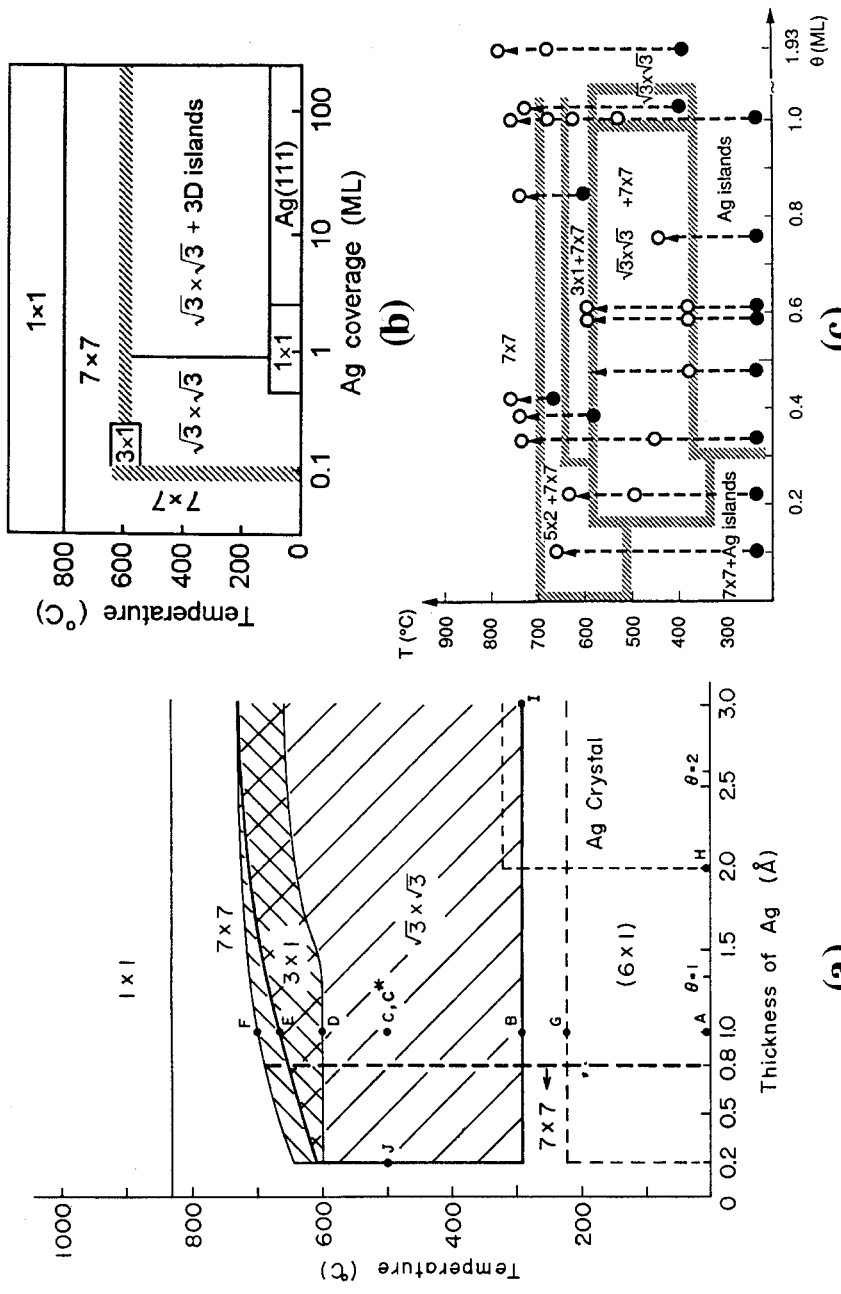

Fig. 22. Phase diagrams showing surface reconstructions vs Ag coverage and annealing/growth temperature; determined by (a) RHEED, (b) LEED-AES, and (c) STM, respectively. Reproduced with permission from Refs. [78], [77], and [87], respectively.

commonly observed in these phase diagrams; $\sqrt{3} \times \sqrt{3}$, 3×1, and 6×1, while a 5×2 structure is reported only in STM observations [87].

4.1.1.1. $\sqrt{3} \times \sqrt{3}$-Ag superstructure. As shown in Figs. 1 and 2, the $\sqrt{3} \times \sqrt{3}$ structure is formed by Ag deposition onto the 7×7 substrate at elevated temperatures (above 250°C). Since the first report on this surface [79], this structure has been considered as a prototypical, nonreactive metal–semiconductor system, and has been a focal subject of almost every surface-science techniques; diffraction and scattering methods, spectroscopies, and microscopies. As a result, many structural models have been proposed (see pp. 55–60 in Ref. [1]). The reader will find the relevant references on this subject also in Refs. [36,80,82]. After a long controversy, a HCT model, shown in Fig. 3(c), first proposed by Takahashi et al. [35], was found to be consistent with most of the reported experimental results and the first-principles calculations [39,40]. The main features of its surface electronic structure are now confirmed, as described in Section 1.2 and Fig. 5(c) and (d). So this surface is now a standard sample and a good platform for comparative studies of various phenomena with the clean 7×7 surface in many ways.

Although, as described in Section 1.2, the surface electronic state of the $\sqrt{3} \times \sqrt{3}$-Ag structure is almost fully clarified, we should point out a discrepancy between the experimental and theoretical results. As shown in Fig. 5(c), ARUPS [38,12,15] shows that a surface-state band, called S_1 crosses E_F, so that the band is partially occupied with electrons, while the first-principles calculations [39,40] reveal the band located above E_F, so that it should be empty (see Fig. 23(a) and (c)); there is an energy-gap around E_F, i.e., semiconductor-like surface electronic structure. Is the partial filling in the surface-state band, observed in photoemission spectroscopy, intrinsic or extrinsic? We present some experimental data in Section 4.3 showing that a small amount of excess Ag adatoms (*2D adatom gas phase*) on top of the $\sqrt{3} \times \sqrt{3}$-Ag substrate donate electrons into the surface-state band S_1. Such an adatom gas phase is considered to exist always as a thermodynamical equilibrium state at RT. It can be these donated electrons that ARUPS detects. So the discrepancy between experiments and calculations seems to come from an extrinsic reason.

4.1.1.2. Electron standing waves. The existence of the free-electron-like surface-state band S_1 on the $\sqrt{3} \times \sqrt{3}$-Ag surface, described in Section 1.2, has been demonstrated by so-called *electron standing waves* observed with low-temperature STM [19]. Fig. 24 shows the STM image of the $\sqrt{3} \times \sqrt{3}$-Ag surface taken at 6 K (though the 7×7 domains partially remain, because of a Ag coverage smaller than 1 ML). In the $\sqrt{3} \times \sqrt{3}$-Ag domains, fine periodic corrugations are seen, which are the same as in Fig. 3(a), corresponding to the $\sqrt{3} \times \sqrt{3}$-periodicity. Additionally, one can see standing wave patterns superimposed near step edges and domain boundaries. In a small domain, surrounded by steps and domain boundaries, a complicated concentric interference pattern is observed, while near the straight step edges and domain boundaries, the interference patterns are parallel to them. There are no standing wave patterns observable in the 7×7 domains.

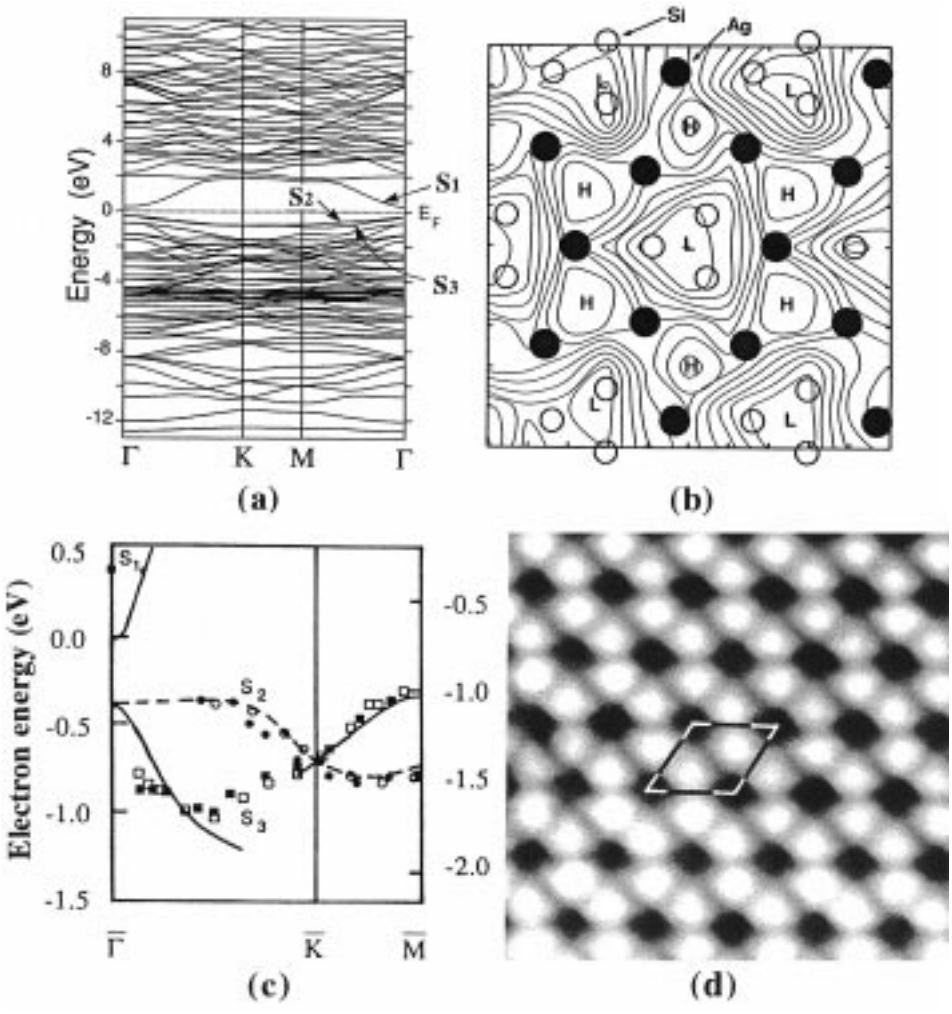

Fig. 23. (a) Energy-band dispersion calculated for the Si(111)-$\sqrt{3} \times \sqrt{3}$-Ag surface. (b) Contour map of the tunneling current in logarithmic scale in empty-state imaging by STM. H and L indicate the maxima and minima, respectively. Reproduced with permission from Ref. [39]. (c) Energy-band dispersion for the same surface. Dashed and solid lines are theoretical calculations for even and odd states, respectively. Open and filled circles and squares are experimental results (from Ref. [38]). The electron energy is referred from the Fermi level for both theory (left axis) and experiment (right axis). Reproduced with permission from Ref. [40]. (d) A magnified empty-state STM image (V_t = -1.0 V, I_t = 0.3 nA, 3.5 × 3.5 nm^2) showing hexagonal protrusions corresponding to the contour pattern (b). The protrusions do not correspond to atoms themselves, but the centers of Ag triangles.

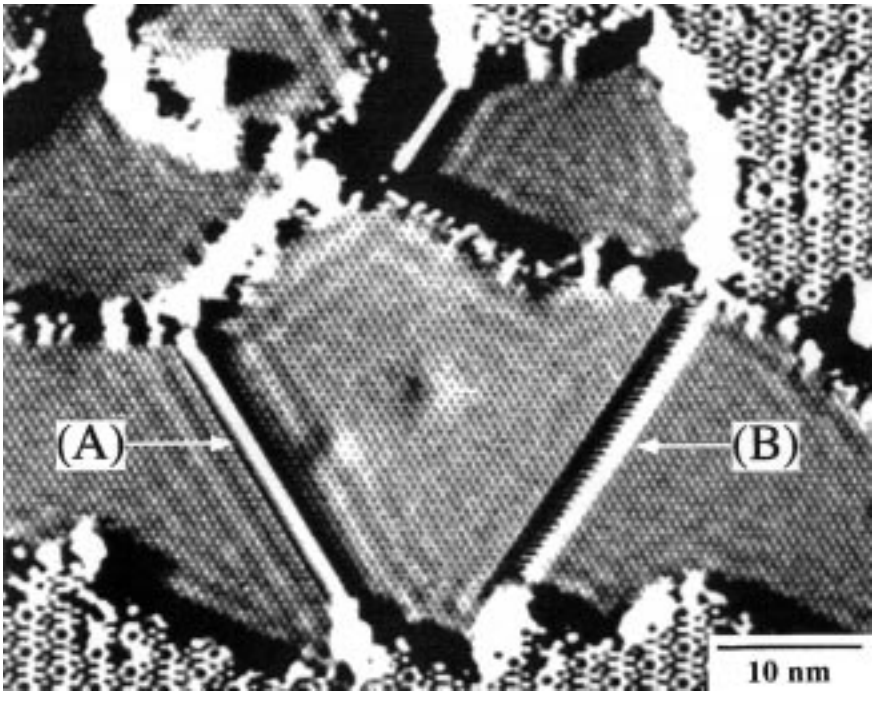

Fig. 24. An empty-state STM image of the Si(111)-$\sqrt{3} \times \sqrt{3}$-Ag surface (partially the 7×7 structure remains) taken at 6 K. The tunneling current is 0.5 nA with sample bias of 0.75 V. From Ref. [19].

These standing waves are interpreted as follows. The electron wavefunction ψ_i in the surface-state band is described by a 2D Bloch wave, i.e., Eqs. (35) and (36) in Section 2.2.2;

$$\psi_i = e^{ik_x x + ik_y y} \cdot u(x,y), \tag{53}$$

$$E = E_0 + \frac{\hbar^2\left(k_x^2 + k_y^2\right)}{2m^*}, \tag{54}$$

where $u(x,y)$ is an appropriate cell function representing the structure within the $\sqrt{3} \times \sqrt{3}$ unit cell, and the z-dependence in Eq. (36) is neglected for simplicity. A step edge or a domain boundary, which is assumed straight along the y-direction, acts as a potential barrier for the surface-state electrons. So the electrons reflected from the barrier are expressed by

$$\psi_r = R \cdot e^{i(-k_x x + k_y y)} \cdot u(x,y), \tag{55}$$

where the reflection coefficient $R = |R| \cdot e^{i\eta}$ with a phase shift η. Then, the 1D local DOS $\rho(E,x)$ along the x-direction (perpendicular to the potential-barrier wall) can be written as

$$\rho(E,x) \propto |\psi_i + \psi_r|^2 \tag{56}$$

$$\propto \left\{1 + |R|^2 + 2|R| \cos(2k_x x - \eta)\right\} \cdot |u(x,y)|^2. \tag{57}$$

Since, as indicated by Eqs. (39) and (41), the STM probes the local DOS of the sample surface more or less, the observed STM image reflects Eq. (56); the standing waves come from the cosine term with a periodicity of π/k_x in real space, while the atomic corrugation originating from the surface superstructure comes from the term $|u(x,y)|^2$. Both are superimposed in the image. By extending this consideration into 2D, the local DOS can be written as

$$\rho(E,x) \propto \left\{1 - J_0(k_{//}x)\right\} \cdot |u(x,y)|^2 \tag{58}$$

$$\simeq \left\{1 - \frac{1}{\sqrt{\pi k_{//} x}} \cdot \cos\left(2k_{//}x - \frac{\pi}{4}\right)\right\} \cdot |u(x,y)|^2, \tag{59}$$

by assuming the step edge as a hard wall (which completely reflects the electron waves) [58], where J_0 is the zero-order Bessel function and its asymptotic formula is used, and $k_{//}$ is the surface-parallel component of the wavevector. In this way, the $\sqrt{3} \times \sqrt{3}$-Ag surface is shown to have an extended surface electronic state, which will contribute to the electrical conduction parallel to the surface, while the carrier scattering by the step edges and domain boundaries is expected to be severe as easily seen from Fig. 24, resulting in low carrier mobilities. These will be discussed in Section 4.3 with the measurements of the conductivity and mobility in the surface-state band. On the 7×7 surface, on the other hand, the dangling-bond state, which mainly contributes to STM images, is not an extended state, but localized on the respective adatoms [81], so that the standing waves are not expected to be observable.

4.1.1.3. Inverse photoemission spectroscopy. The upward-parabolic surface-state band S_1 on the $\sqrt{3} \times \sqrt{3}$-Ag surface, which disperses well above E_F, is detected by *inverse photoemission spectroscopy* (IPES) as well [31]. Fig. 25 shows its spectrum, together with that of the clean 7×7 surface for comparison. The $\sqrt{3} \times \sqrt{3}$-Ag surface shows an approximately constant DOS throughout the band-gap above E_F (a slope around E_F comes from a finite energy resolution in the measurements). This is consistent with the two-dimensionality of the S_1 band, whose DOS is given by Eq. (12), a constant value independent of energy. Since, then, by combining with the band dispersion obtained by ARUPS (Fig. 5(c)), the bulk band-gap is completely filled in by this surface state on the actual $\sqrt{3} \times \sqrt{3}$-Ag surface, the surface can be said to be practically metallic. The theoretical calculations [39] (Fig. 23(a) and (b)) only show the surface-state band structure, which apparently indicates a semiconductor-like nature. But when one includes the bulk states, together with the surface states, there is no energy gap.

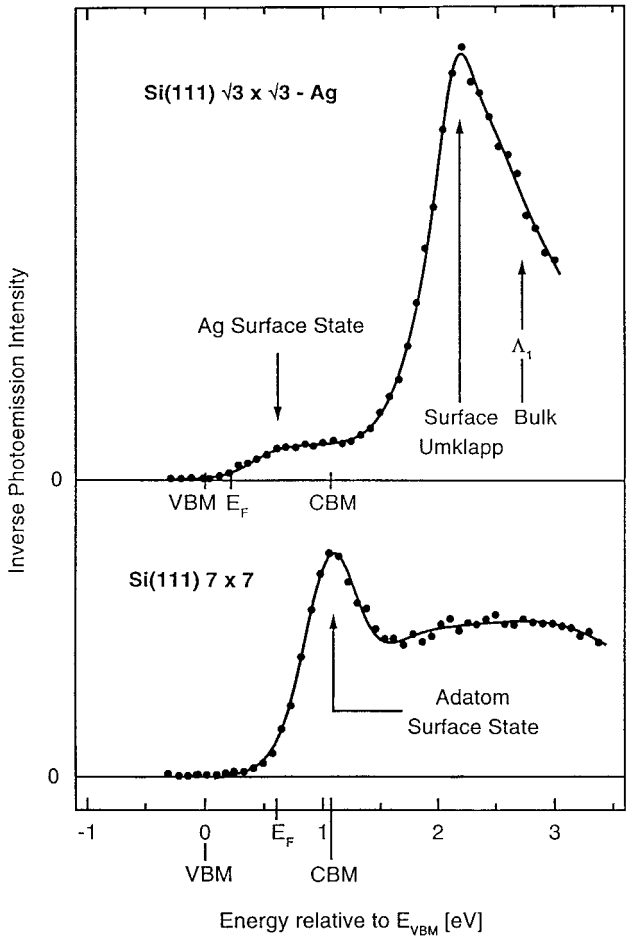

Fig. 25. Inverse photoemission spectra of the clean Si(111)-7 × 7 and -$\sqrt{3} \times \sqrt{3}$-Ag surfaces, taken with electrons incident normal to the surface at an energy of 11 eV above E_F. Reproduced with permission from Ref. [31].

4.1.1.4. 3 × 1 superstructure. On another Ag-induced surface superstructure, 3 × 1, a lot of debate is still going on about its atomic arrangement. A recent paper has proposed a reliable model [83], as shown in Fig. 26(a), where Ag saturation coverage is 1/3 ML. This phase is only formed at high temperatures (above 600°C), where Ag atoms are desorbing from the surface. During cooling the 3 × 1 surface down to RT, a 6 × 1 structure appears below about 200°C. So its atomic arrangement is not significantly different from that of the 3 × 1 structure. In the model [83] (Fig. 26(a)), all Ag atoms in a single 3 × 1 row slightly shift in a direction along [$\bar{1}$10], but in the opposite direction on the every 3 × 1 rows, which shows a $c(6 \times 1)$ periodicity. The 3 × 1 superstructures induced by alkali-metal adsorptions

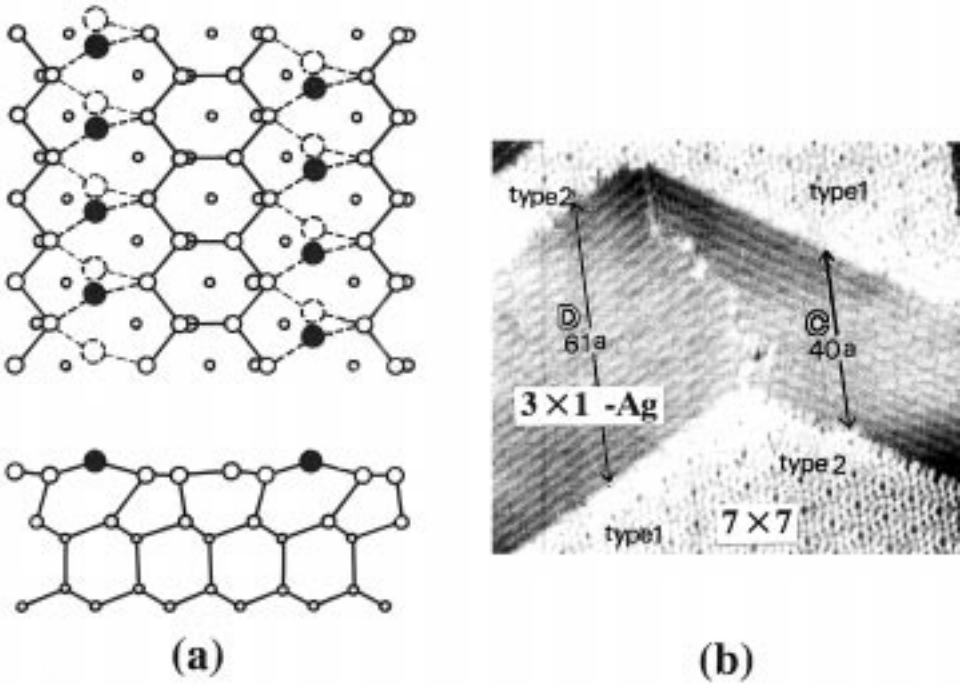

Fig. 26. (a) A structural model of the Si(111)-3 × 1-Ag surface from Ref. [83]. Upper is the plan view, and lower, sectional one. Large solid circles are Ag atoms and the other open circles are Si atoms. Dashed circles indicate equivalent sites for Ag adatoms. (b) Its STM image coexisting with the 7 × 7 domains. Reproduced with permission from Ref. [88].

are suggested to have similar reconstruction structures as that induced by Ag adsorption [84,85] according to similar LEED I–V curves [86], similar STM images [87,89], and similar X-ray and electron-diffraction data [83,84]. But, there are no indications of the 6 × 1 periodicity in the alkali-metal-induced 3 × 1 phases.

4.1.2. At lower temperatures

Most of the reconstructions on silicon surfaces, such as those mentioned above, occur at elevated temperatures above RT. This is because rearrangements and rehybridizations among covalent bonds are prohibited by potential barriers over which the system can ride using thermal energy only at elevated temperatures. In fact, when Ag is deposited onto the Si(111)-7 × 7 surface at temperatures lower than RT, Ag crystals of small sizes grow without breaking the dimer-stacking fault framework of the substrate. Even at RT, as introduced in Section 4.2, Ag grows in a similar way without substrate reconstructions.

However, on the Si(111)-$\sqrt{3} \times \sqrt{3}$-Ag substrate, new superstructures emerge by additional atom depositions onto it, even at temperatures lower than RT [9,10]. As shown below, these surface reconstructions do not involve the substrate reconstructions, but are rather caused by regular arrangements of additionally

adsorbed atoms. The adsorbates interact with each other through the substrate to make superstructures.

4.1.2.1. RHEED observations. As shown in Fig. 27(a)–(d), the RHEED patterns successively change during additional Ag deposition onto (a) the $\sqrt{3} \times \sqrt{3}$-Ag surface at 160 K [10]. The $\sqrt{21} \times \sqrt{21}$ superspots begin to appear from 0.1 ML coverage, and become the sharpest around 0.15 ML (b), corresponding to its saturation coverage. As these spots become weaker above 0.15 ML, faint 6×6 superspots emerge and become the sharpest around 0.19 ML (c) coexisting with the $\sqrt{21} \times \sqrt{21}$ spots. After 0.19 ML, the 6×6 phase disappears, and only the $\sqrt{21} \times \sqrt{21}$ spots remain, gaining the maximum intensity around 0.30 ML coverage, again as shown in (d). Beyond 0.30 ML the $\sqrt{21} \times \sqrt{21}$ spots become weaker to leave only the $\sqrt{3} \times \sqrt{3}$ spots with polycrystalline Ag spots coexisting.

At 100 K, as shown in Fig. 27(e)–(g), compared with the corresponding coverages of additional Ag at 160 K (b)–(d), the spots of the $\sqrt{21} \times \sqrt{21}$ structure are weaker and broader at 0.15 and 0.24 ML (e)–(g), meaning its smaller domain sizes. The single phase of the 6×6 structure with stronger and sharper spots is observed at 0.18 ML (f) at this temperature.

These $\sqrt{21} \times \sqrt{21}$ and 6×6 structures disappear to leave only the $\sqrt{3} \times \sqrt{3}$ spots, when the substrate is warmed up to higher than 250 and 180 K, respectively. Fig. 28 shows a phase diagram for the ranges of temperature and Ag coverage in which the respective surface structures are observed [10]. At RT, any structural changes can not be observed by additional Ag deposition onto the $\sqrt{3} \times \sqrt{3}$-Ag substrate; the $\sqrt{3} \times \sqrt{3}$ spots remain strong coexisting with the transmission diffraction spots from 3D Ag microcrystals, which is exactly the same situation as in Fig. 15(c). At 250 K, the $\sqrt{21} \times \sqrt{21}$ structure is observed only around 0.15 ML coverage. On cooling from 250 down to 180 K, the intensity of the $\sqrt{21} \times \sqrt{21}$ spots at 0.15 ML increases, and the coverage range for its appearance widens. Below 180 K its intensity become weaker. Below 160 K, with more than 0.15 ML coverage, the stable 6×6 superlattice spots coexist with the weak $\sqrt{21} \times \sqrt{21}$ phase, and become the sharpest around 0.18 ML. Only below 100 K, is the 6×6 single phase observed in a restricted range of coverage.

4.1.2.2. STM observations. These processes of structural conversions are also revealed by low temperature STM observations [17]. Fig. 29(a) shows an STM image taken from the $\sqrt{3} \times \sqrt{3}$-Ag surface at 70 K with deposition of a very small amount of additional Ag atoms on it. Some bright protrusions distribute randomly on the $\sqrt{3} \times \sqrt{3}$-Ag substrate. Each bright protrusion corresponds to an adsorbed Ag atom. By counting the average density of the additionally adsorbed Ag atoms at the central parts of terraces, we can estimate the coverage to be about 0.015 ML. At step edges, the Ag adatoms seem to distribute in a regular arrangement with a periodicity of about three unit meshes of the $\sqrt{3} \times \sqrt{3}$. Near these steps, denuded zones are recognized on terraces, where adsorbed monomers do not exist. The width of the denuded zone, around 3 nm, corresponds to the diffusion length of the deposited Ag atoms. It can then be shown that the adsorbed

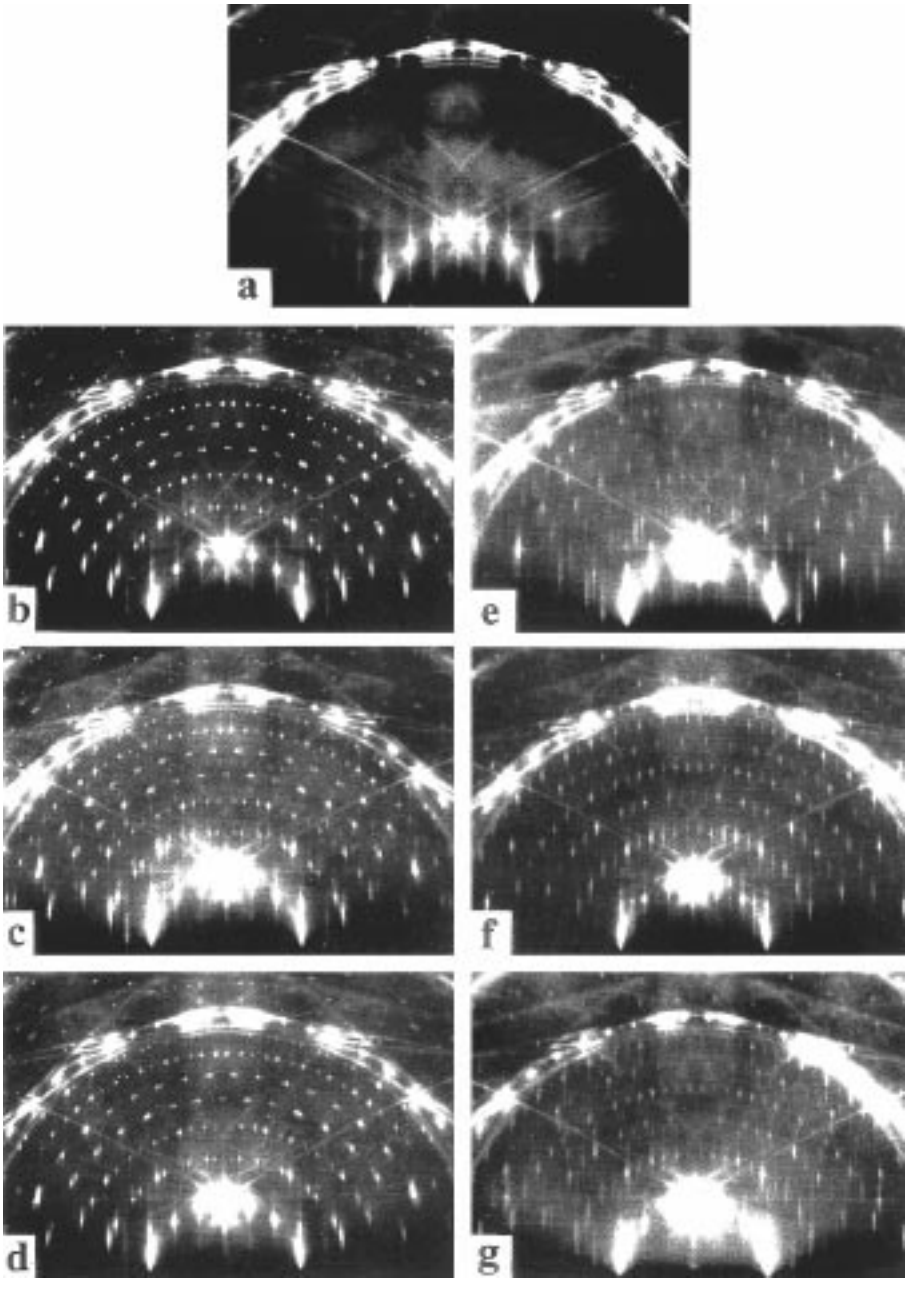

Fig. 27. A series of RHEED patterns taken during additional Ag depositions with a rate of 0.66 ML/min onto the Si(111)-$\sqrt{3} \times \sqrt{3}$-Ag surface (a), at 160 K (b)–(d), and at 100 K (e)–(g), respectively. The additional coverages are (a) 0 ML, (b)(e) 0.1 ML, (c)(f) 0.14 ML, and (d)(g) 0.18 ML, respectively. (b), (d) and (e) the $\sqrt{21} \times \sqrt{21}$ structure, (f) the 6×6 structure, and (c) and (g) their mixtures. From Ref. [10].

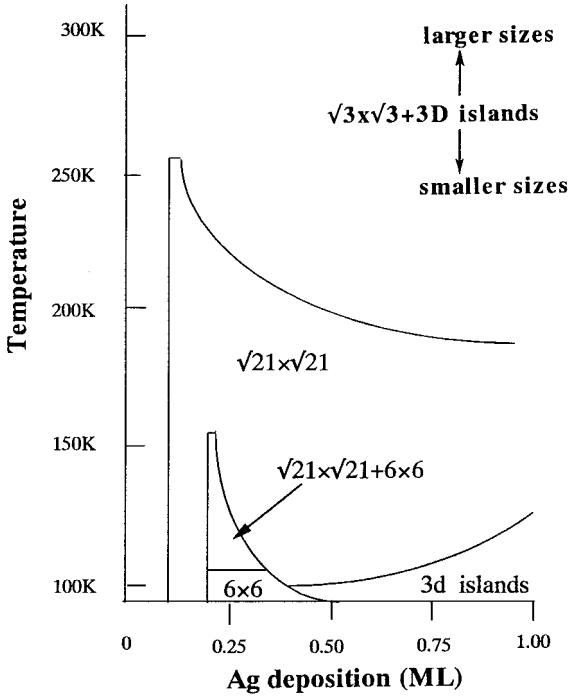

Fig. 28. A phase diagram determined by RHEED observations during Ag deposition with a rate of 0.66 ML/min onto the Si(111)-$\sqrt{3} \times \sqrt{3}$-Ag surface at fixed substrate temperatures. The 1/3-th fractional-order spots are always observed in the ranges covered by this diagram. From Ref. [10].

atoms still migrate with some mobility on the $\sqrt{3} \times \sqrt{3}$-Ag surface, even at 70 K, so that they interact with the steps to be trapped. It should be noted that STM observations at RT never show the indication of additionally deposited Ag atoms with similar amounts on the $\sqrt{3} \times \sqrt{3}$-Ag surface. This is because the adatoms migrate with an extremely high mobility, making a *2D adatom gas* (2DAG) phase [8,14], which cannot be detected by STM; the adatoms move almost freely across the step edges, as well as on the terraces. The 2DAG is discussed in more detail in Section 4.3.4.

On further deposition up to about 0.05 ML of Ag at 70 K, as shown in Fig. 29(b), 2D nuclei are formed at terraces and steps, which is because the monomers observed in Fig. 29(a) still migrate to gather into the nuclei, when the adatom density exceeds some critical value. The density of 2D nuclei at the steps is much higher than that on terraces. They connect with each other to form thin atomic strings along the steps.

When the Ag coverage is increased further, the density of 2D nuclei on the terraces increases, as shown in Fig. 29(c). At this stage, monomers are hardly observed. With further increase of Ag coverage, the arrangements of these 2D nuclei begin to be in order, as shown in Fig. 29(d); we recognize a disordered

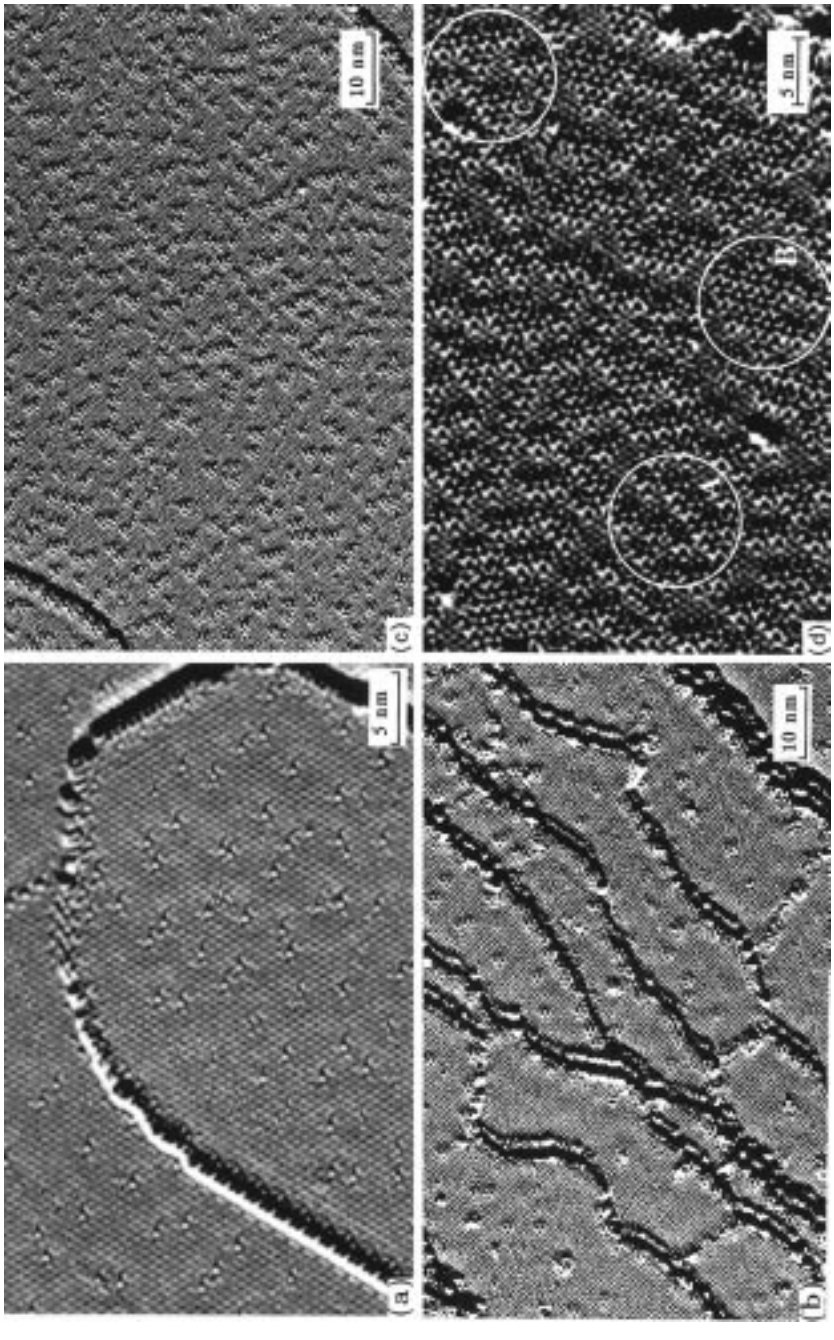

Fig. 29. Occupied-state STM images taken during Ag adsorption on the Si(111)-$\sqrt{3} \times \sqrt{3}$-Ag surface at 70 K with $V_t = 1.0$ V and $I_t = 0.5$ nA. The additional coverages of Ag are (a) 0.015, (b) 0.05, (c) 0.1, (d) 0.12, and (e) 0.15 ML, respectively. From Ref. [17].

region A, a well-ordered regions B, and between them in order as indicated by a region C. Although the degree of ordering in these regions is different, the unit structure of 2D nuclei seems to be the same [17]. Fig. 30(a) is a magnified image of the well-ordered region showing the $\sqrt{21} \times \sqrt{21}$-Ag superstructure with partially remaining $\sqrt{3} \times \sqrt{3}$-Ag domains. By detailed analysis of these STM images [17], Ag adatoms adsorbed on top of the $\sqrt{3} \times \sqrt{3}$-Ag substrate regularly arrange to make the $\sqrt{21} \times \sqrt{21}$ superstructure, without involving the atom rearrangements in the substrate. Fig. 30(b) shows a model of its atomic arrangement; additional Ag atoms sit in the centers of Ag triangles of the HCT framework. The formation of the superstructures, at such low temperatures, is due to a very low potential barrier for adataom migration on top of the surface; the deposited adatoms can migrate even at the lowest temperatures (which might mean nonthermal diffusion on the surface).

4.1.2.3. $\sqrt{21} \times \sqrt{21}$ superstructures. The $\sqrt{21} \times \sqrt{21}$ superstructures are formed, not only by Ag adsorption, but also by adsorptions of other noble metals (Au, Cu) [90–92] and alkali metals (Li, Na, K, Cs) [93] onto the $\sqrt{3} \times \sqrt{3}$-Ag surface (see Section 5). The mechanism operating in the formation of these $\sqrt{21} \times \sqrt{21}$ structures seem to closely related to monovalency of adatoms; in fact the $\sqrt{21} \times \sqrt{21}$ superstructure cannot be induced by Ca, Mg or In adsorption onto the $\sqrt{3} \times \sqrt{3}$-Ag substrate. Furthermore, the $\sqrt{21} \times \sqrt{21}$ superstructures commonly show high electrical conductances, as shown in Sections 4.3 and 5. But we do not have its generally accepted structure model; the adsorption sites of adatoms and its saturation coverage are still controversial [17] (see Section 5.1.1).

4.2. Growth of Ag atomic layers

4.2.1. At elevated temperatures

Above around 200°C of the substrate temperature, Ag growth on the 7×7 surface proceeds in the *Stranski–Krastanov mode*; after completion of an overlayer having the $\sqrt{3} \times \sqrt{3}$-Ag superstructure, nucleation of 3D Ag crystals begins [94]. The distances between the 3D Ag crystals reach nearly 0.1 mm, which means extremely long diffusion lengths of Ag adatoms on the $\sqrt{3} \times \sqrt{3}$-Ag surface at elevated temperatures.

4.2.2. At room temperature

When Ag is deposited onto the 7×7 surface (Fig. 31(b)) below 200°C, streaks (a reflection pattern) from Ag thin crystals appear in RHEED pattern, as shown in Fig. 31(e) (which was taken in the deposition at RT). Thermal energy is not high enough to convert the surface into the $\sqrt{3} \times \sqrt{3}$-Ag structure from the 7×7; the dimer-stacking-fault framework remains beneath the Ag thin crystals, which is revealed by grazing-incidence X-ray diffraction [95]. This Ag layer is known to grow in quasi-layer-by-layer fashion (*quasi-Frank-van der Merwe mode*) up to a few ML, consisting of twining 2D Ag thin crystals in a textured structure [96]. This [111] textured structure has a preferential epitaxial orientation $[01\bar{1}]_{Ag}//[01\bar{1}]_{Si}$

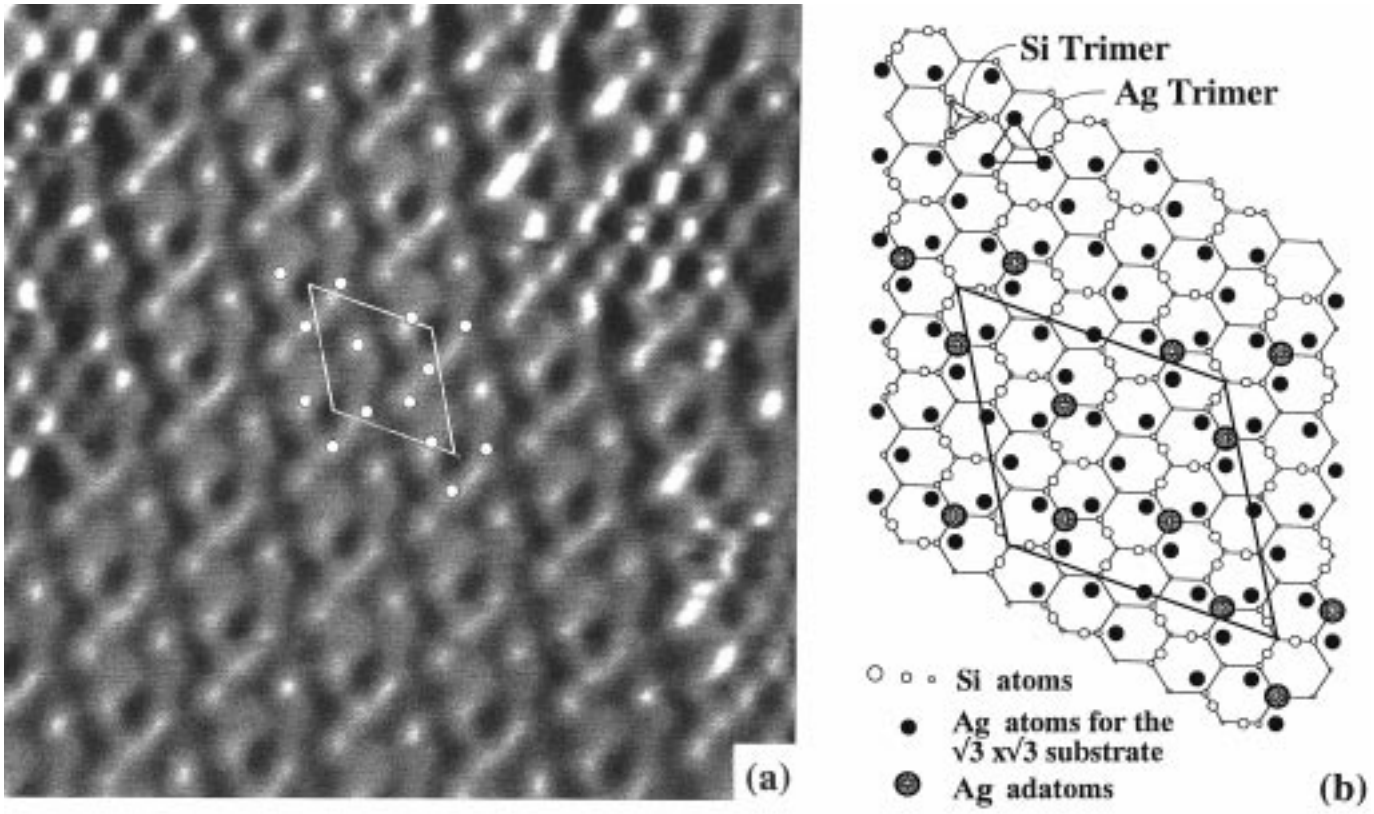

Fig. 30. (a) A magnified empty-state STM image of the Si(111)-$\sqrt{21} \times \sqrt{21}$ superstructure (with the $\sqrt{3} \times \sqrt{3}$-Ag domains partially remained), with $V_t = -1.6$ V and the $I_t = 0.5$ nA (from Ref. [17]). (a) A model of the $\sqrt{21} \times \sqrt{21}$ superstructure.

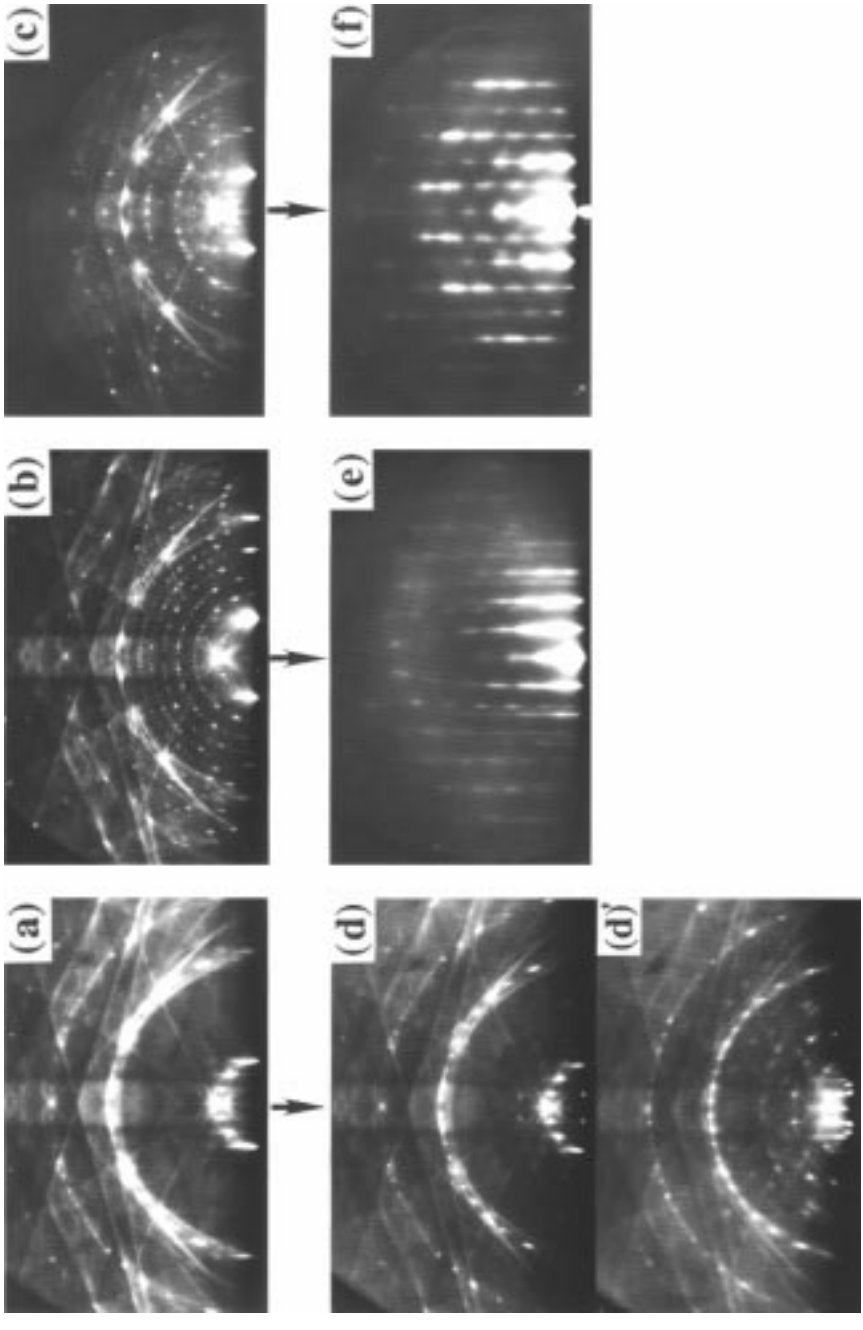

Fig. 31. RHEED patterns showing three different types of substrate surfaces, (a) Si(111)-$\sqrt{3}\times\sqrt{3}$-Ag, (b) the clean Si(111)-7×7, and (c) Si(111)-$(3\times1+6\times1)$-Ag, respectively. After room-temperature deposition of 4.5 ML Ag onto each surface, the Ag grows in different ways (d)–(f). (d′) is a small-glancing-angle observation of (d). From Ref. [5].

on $(111)_{Ag}$ //$(111)_{Si}$. Impact-collision ion-scattering spectroscopy reveals that the epitaxial Ag(111) crystals grown at RT consist of type A and type B crystals, with type B being rotated 180° about the surface normal (in the twin relation) [97].

This Ag-covered Si surface shows SEM pictures as in Figs. 32(a)–(c) [65], indicating small and flat Ag islands growing, as suggested from the RHEED pattern (Fig. 31(e)).

By closer STM observations of the very early stage of Ag condensation onto a near-RT 7×7 surface, the first Ag nuclei are found to be located on the inner adatoms of the 7×7-DAS unit cell, preferentially on the faulted halves, as shown in Fig. 33(a) [98]. Ag atoms are bonded to the inner Si adatoms and also to the dangling bonds of the second atomic layer (rest atoms) of the DAS structure (see Fig. 3(b)). *Scanning tunneling spectroscopy* (STS) reveals the difference in electronic structures between at the Ag-covered and -uncovered areas in Fig. 33(a). The dangling bonds of the clean 7×7 are saturated by Ag atoms, resulting in reduction of the local DOS at E_F with an energy gap opening and converting into a semiconducting character, while the Ag-uncovered parts remain in a metallic character, due to the dangling bonds of the DAS structure. These Ag clusters will grow into the flat Ag islands shown in Figs. 32(a)–(c). The STM also shows deviations from an ideal layer-by-layer growth mode already at 3ML-Ag coverage; the surface roughness is more than two atomic layers as shown in Fig. 33(b) and the line profile in (c) [98].

When the early stage of Ag adsorption is observed by RHEED, the intensity ratios among the 7×7 superspots become different from those of the clean 7×7 structure [99]; the intensities of near-half-order spots ((3/7, 4/7), and so on) decrease, while the weak fractional-order spots along the [10] direction gain in intensity. Such a RHEED pattern corresponds to a so-called δ-7×7 structure, found on H- and alkali-metal-adsorbed 7×7 surface [100,101]; this structure results from the cutting off of the backbonds of Si adatoms by adsorbates.

The incomplete layer-by-layer growth style of Ag on the 7×7 substrate at RT is revealed also by RHEED intensity oscillation measurements [6,102–104]. As shown in Fig. 34(a) [6,102], only a short-lived oscillation is observed at RT on the 7×7 substrate, which means multilayer growth proceeds with increasing the coverage.

In contrast, instead of the oscillatory change, only an abrupt drop in the intensity of the specular spot in RHEED is observed during Ag adsorption on the $\sqrt{3} \times \sqrt{3}$-Ag surface at RT, and the intensity remains a low constant with further deposition (Fig. 34(c)). This means a growth of 3D islands from the beginning (*Volmer–Weber mode*), which is consistent with the SEM observations (Figs. 32(d)–(g) and Fig. 15(c)). This difference in growth mode between on the 7×7 and on the $\sqrt{3} \times \sqrt{3}$-Ag substrates is due to the difference in the surface energy of the substrates; the $\sqrt{3} \times \sqrt{3}$-Ag surface has a much lower surface energy with no dangling bonds remained, resulting in the much longer surface diffusion of the adatoms deposited on it and a strong tendency of aggregation into 3D microcrystals (nonwetting), while the 7×7 surface is wetted by the first Ag layer, because of a higher surface energy with dangling bonds remained.

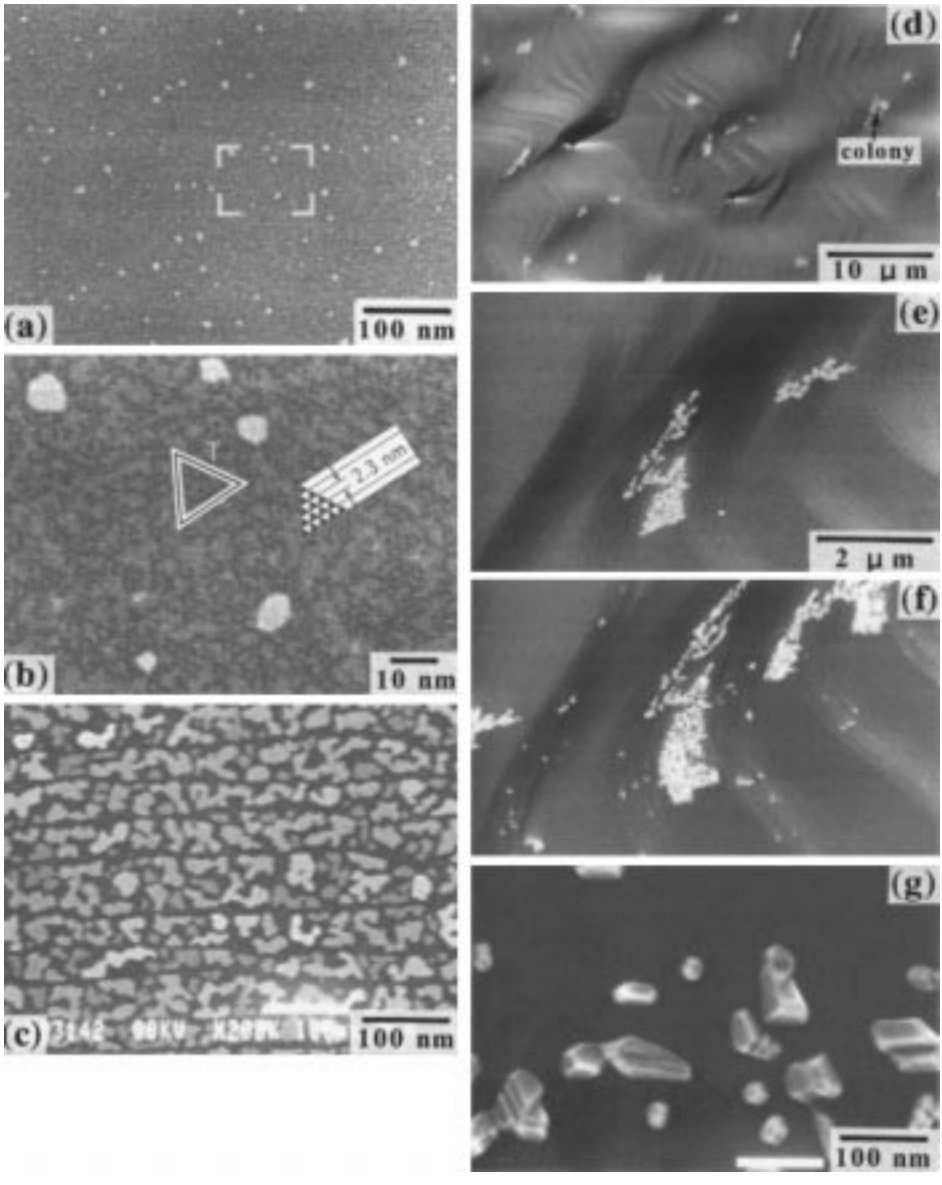

Fig. 32. (a) An UHV–SEM image of the 7×7 surface with ~1 ML Ag adsorbed at RT, and (b) its magnified image (reproduced with permission from Ref. [65]). (c) The same surface with ~3 ML Ag coverage (by courtesy of Dr N. Shimomura). (d) A grazing-incidence UHV–SEM image of the $\sqrt{3} \times \sqrt{3}$-Ag surface after additional 0.2 ML Ag deposition at RT. (e) Its magnified image showing atomic steps and colonies of 3D microcrystals. (f) With further deposition up to around 0.4 ML onto this surface, new additional microcrystals appear. (g) A magnified image of the three-dimensional microcrystals (by courtesy of Dr N. Shimomura).

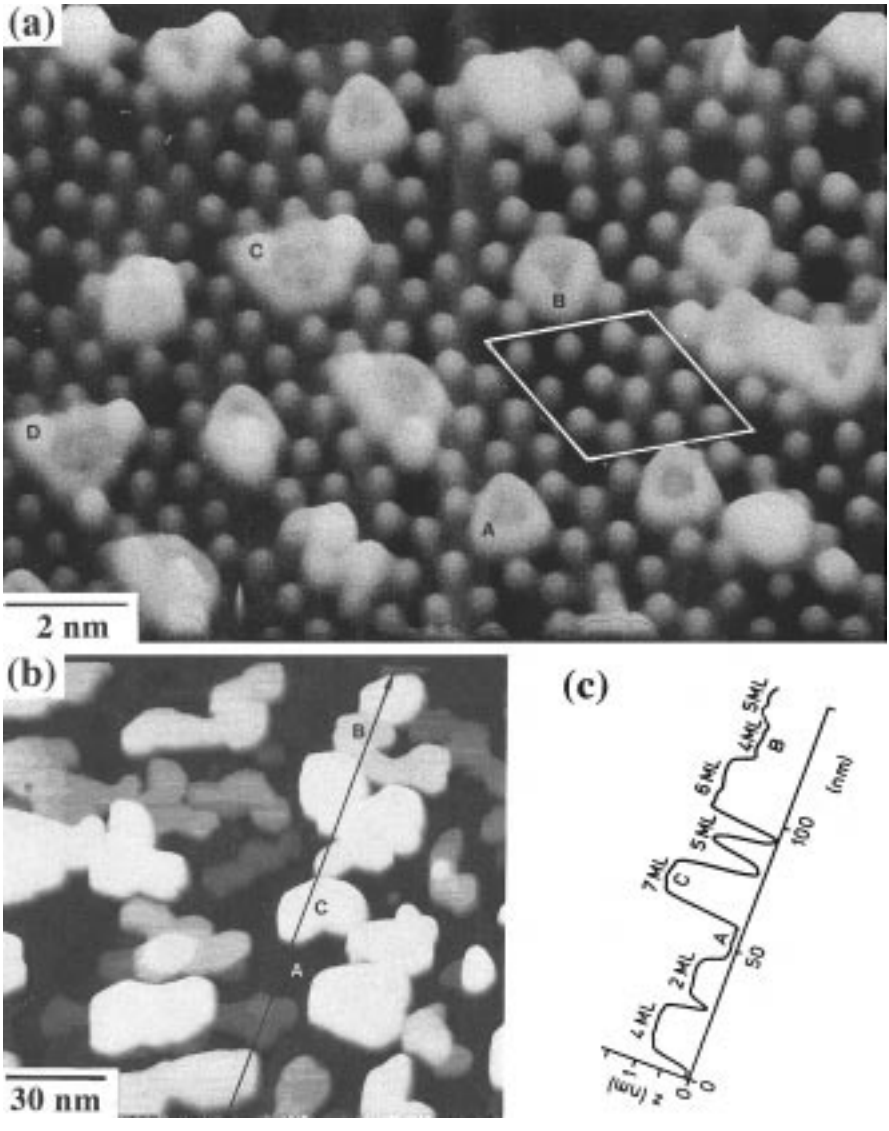

Fig. 33. (a) A topography STM image taken from 1/3 ML Ag-covered Si(111)-7 × 7 surface obtained at the sample bias voltage 2 V and the tunneling current 3 nA. The area is about 12 × 22 nm^2. (b) A topography STM image taken from 3 ML Ag-covered Si(111)-7 × 7 surface of 150 × 150 nm^2. (c) Corrugation of the topography along the line in (b). Reproduced with permission from Ref. [98].

4.2.3. At lower temperatures

By reducing the substrate temperature lower than RT, the tendency of layer-by-layer growth on the 7 × 7 substrate is enhanced, as shown in Fig. 34(b); many oscillations in RHEED intensity are seen during Ag deposition at 160 K. This is

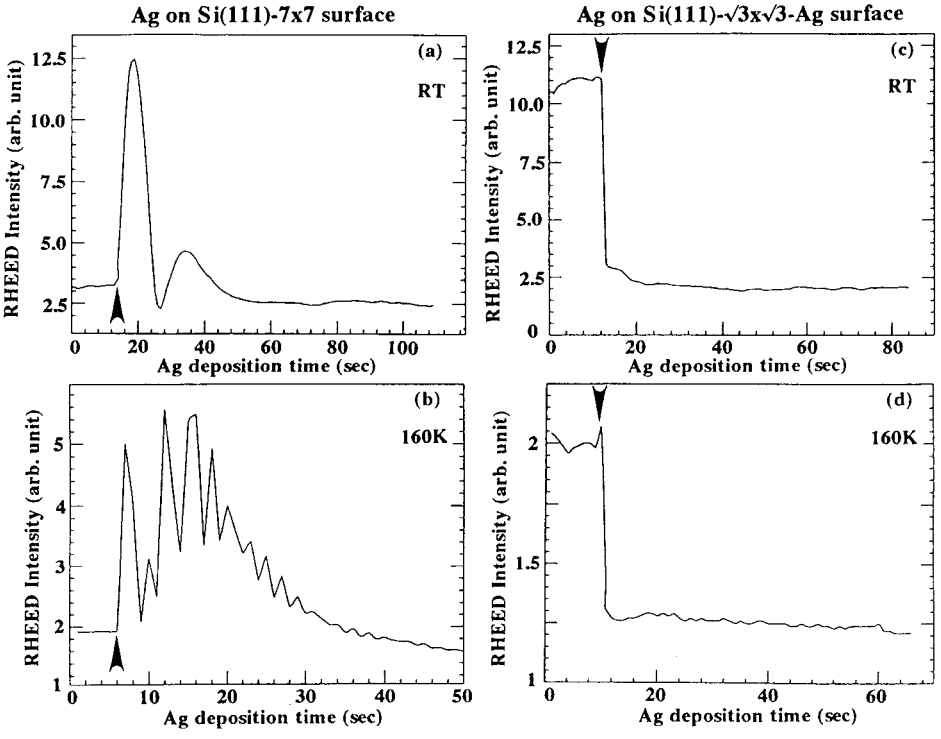

Fig. 34. Changes in intensity of the specular beam in RHEED during Ag deposition onto (a) and (b) Si(111)-7 × 7 clean surface and (c) and (d) Si(111)-$\sqrt{3} \times \sqrt{3}$-Ag surface, (a) and (c) at RT, and (b) and (d) at 160 K. The electron beam of 15keV irradiates the surface in [11$\bar{2}$] incidence with glancing angle of ~0.4°. Arrow heads indicate the opening of the evaporator shutter. From Ref. [6].

because Ag can nucleate with a much higher number density having smaller nuclei sizes on the colder substrates, due to shorter diffusion length and smaller critical sizes for nucleation, so that the Ag growth proceeds nearly 2D by preventing the formation of large multi-layers islands. The situation can be similar, even at RT, by increasing the deposition rate, as shown in Fig. 35(a) [102]; higher deposition rates make the diffusion lengths of adatoms effectively shorter before nucleation, because of enhanced nucleation probability, due to higher adatom density on the surface.

Trigides and co-workers discuss the possible existence of nonthermal diffusion mechanism of the Ag adatoms deposited on the 7 × 7 surface, because their oscillatory changes in the RHEED intensity at 150 K are independent of the deposition rate [103,104]. Fig. 35(b) shows the changes of the normalized peak intensity of the specular beam in RHEED, during Ag deposition with various rates at 150 K, as a function of the normalized deposition time t/τ (τ is the time needed for the first period of the oscillation) [103]. The changes in RHEED intensity almost collapse into a curve by scaling the deposition time, irrespective

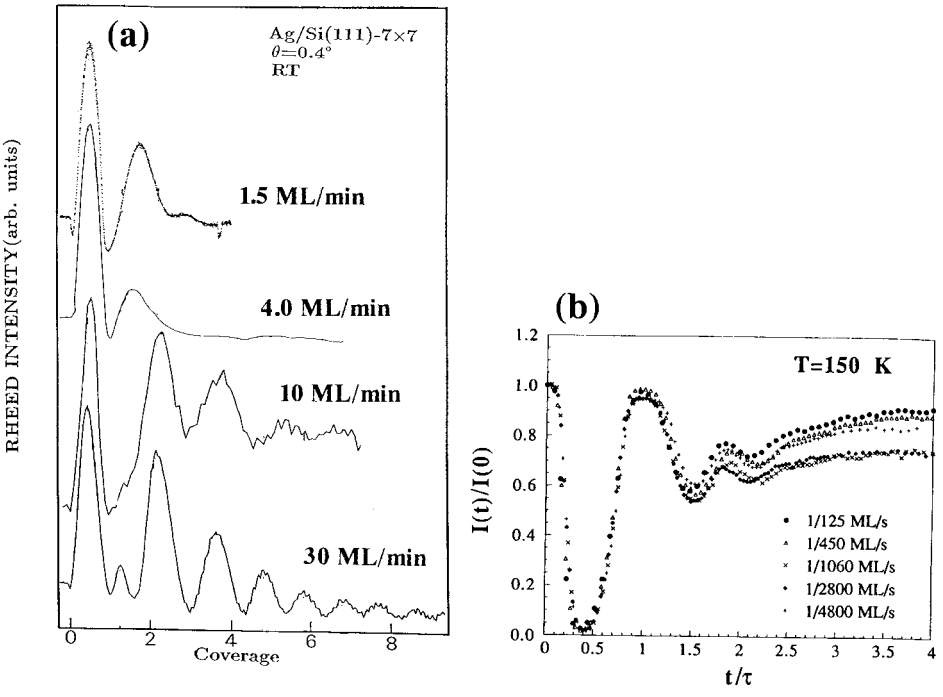

Fig. 35. (a) The RHEED intensity oscillations from the Si(111)-7 × 7 surface during Ag deposition at RT with various deposition rates (from Ref. [102]). (b) Similar measurements at the substrate temperature of 150 K. The abscissa indicates the deposition time scaled with τ, the time needed for the first oscillation. Reproduced with permission from Ref. [103].

of the deposition rate. So we can say that the surface morphology during the growth (quasi-layer-by-layer mode) is flux independent at this temperature, which is in sharp contrast to the RT case in Fig. 35(a). If thermal diffusion of the arriving Ag atoms operates in this system, we should expect the intensity oscillations to depend on the deposition rates as at RT in Fig. 35(a). But the experiments do not show such a tendency. Thermally activated diffusion may not be the main mechanism for the surface diffusion at 150 K [103]. As a possible alternative mechanism for the surface diffusion of the deposited atoms, one can turn to the excess energy of the deposited atoms (kinetic energy and adsorption energy) with respect to the atoms adsorbed at stable sites on the substrate. Such excess energy can be transferred into lateral motion of the arrived atoms, which causes much faster migration of adataoms than by thermally-activated diffusion. Therefore, the adatoms are incorporated into the surface lattice in a much shorter time than the adatom impinging rate, which is the reason for the flux independence of the growth morphology.

Low-temperature adsorption of Ag onto the 7 × 7 surface has been also investigated by STM [105]. Nucleation of Ag occurs in both halves of the 7 × 7 units (though the initial nuclei preferentially appear in the faulted halves at RT as

in Fig. 33 [98]). Corner holes and dimer sites in the 7×7 unit cell are not occupied by Ag initially. The Ag nuclei seem to connect with each other at submonolayer coverage, which corresponds to electrical percolation mentioned in Section 4.3.3 [54,106]. Upon completion of the first ML, 2D-like growth proceeds, which corresponds to the RHEED intensity oscillation in Fig. 34(b).

On the other hand, even at 160 K on the $\sqrt{3} \times \sqrt{3}$-Ag substrate, the change of RHEED intensity indicates a 3D-island growth mode (see Fig. 34(d)) (though the $\sqrt{21} \times \sqrt{21}$-Ag superstructure appears at a submonolayer coverage, as mentioned in the previous subsection). This means that adatom diffusion on the $\sqrt{3} \times \sqrt{3}$-Ag surface is not sufficiently suppressed, even at 160 K, because of a very low activation energy for surface diffusion.

4.3. Electronic transport

4.3.1. Surface conductances

4.3.1.1. Six (four)-probe method. Are the Ag-covered Si(111) surfaces more or less conductive than the clean 7×7 surface? To answer this naive and interesting question, we have used the *six-probe method* described in Fig. 21 in which the conductances at separate surface areas having different superstructures are simultaneously measured, so that the conductance difference due only to the surface structural changes can be extracted. (But, even with the conventional four-probe method, by which only the conductance of a single surface superstructure is measured at one time, we could measure the difference in conductance among the different superstructures with a certain reproducibility. This is because the bulk conductivity of lightly doped Si wafers does not change so much, even with high-temperature heating repeated in UHV, though some redistributions of dopant impurities near surfaces in heavily doped Si wafers are reported [72].) Thus, we have confirmed that the $\sqrt{3} \times \sqrt{3}$-Ag is indeed more conductive than the 7×7 surface by around 115 ± 5 μS/□ for *p*-type wafers [7] or by about 38 ± 8 μS/□ for *n*-type wafers [14];

$$\Delta\sigma = \sigma_{\sqrt{3}\times\sqrt{3}} - \sigma_{7\times7} = 115 \pm 5 \ \mu S/\square \quad \textit{for p-type wafers}, \tag{60}$$

$$= 38 \pm 8 \ \mu S/\square \quad \textit{for n-type wafers}. \tag{61}$$

As described in Section 2.2, this excess conductance $\Delta\sigma$ is a sum of two contributions, from the surface space-charge layer $\Delta\sigma_{SC}$ and from the surface-state bands $\Delta\sigma_{SS}$. The grown-atomic-layer conductance $\Delta\sigma_{AL}$ should be regarded as zero, because the Ag layer forms the surface superstructure by making covalent bonds with Si substrate atoms (Ag atoms do not directly bond with each other), so that it should be regarded neither as a Ag atomic layer nor as a thin-film layer.

4.3.1.2. Calculating $\Delta\sigma_{SC}$. In order to separate the two contributions, $\Delta\sigma_{SC}$ and $\Delta\sigma_{SS}$, from the measured surface conductance $\Delta\sigma$, the $\Delta\sigma_{SC}$ should be evaluated first of all by using the calculation described in Section 2.2.1. The calculated $\Delta\sigma_{SC}$

is shown as the curves for the *n*- and *p*-types in Fig. 36 as a function of surface E_F position. Next we should know the surface E_F positions on the respective surface superstructures. As described in Section 3.2.2, this can be done by measuring the Si 2*p* core-level shifts in XPS with respect to the core-level position on the 7×7 surface. Then, we can evaluate $\Delta\sigma_{SC}$ at the respective surface E_F positions from Fig. 36 and compare them with the measured excess surface conductances.

4.3.1.3. Determining surface E_F positions. The surface E_F position on the 7×7 is located around 0.63 ± 0.05 eV [30] or 0.65 eV [107] above the *valence-band maximum* (VBM) E_{VBM}, around the middle of the bulk-band gap, which means a depletion-layer condition at the surface space-charge layer. On the other hand, the E_F position on the $\sqrt{3} \times \sqrt{3}$-Ag surface lies at 0.10 eV [42], 0.20 eV [38], or 0.08 ± 0.05 eV [14] above E_{VBM}, or between 0.2 and 0.3 eV above E_{VBM} for various dopings throughout *n*- to *p*-types in the substrate [31], while our recent measurements in XPS, shown in Fig. 37, indicate the E_F position at 0.18 ± 0.07 eV above E_{VBM}. Though the values in the literature scatter a little bit, these values mean that the E_F is located near E_{VBM} (the bands bend upwards), so that the surface space-charge layer should be a hole-accumulation layer.

4.3.1.4. Comparing $\Delta\sigma$ with $\Delta\sigma_{SC}$. Therefore, when one considers only the conductance through the surface space-charge layer $\Delta\sigma_{SC}$, the $\sqrt{3} \times \sqrt{3}$-Ag surface should have a higher conductance than the 7×7 clean surface, as shown by the curves in

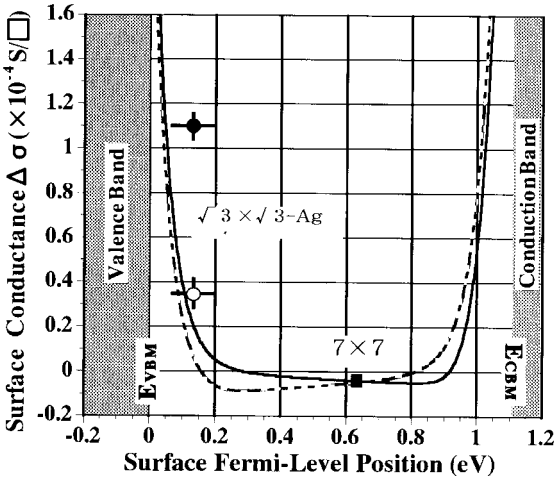

Fig. 36. The curves show the excess electrical conductance through the surface space-charge layer $\Delta\sigma_{SC}$ calculated as a function of surface E_F positions for Si wafers of *p*-type (20 Ωcm resistivity, solid line) and *n*-type (45 Ωcm resistivity, dashed line). Data points indicate the measured excess conductances $\Delta\sigma$ of the $\sqrt{3} \times \sqrt{3}$-Ag surfaces with respect to the 7×7 clean surface for *p*-type (filled circle) and *n*-type (open circle) substrates, respectively. The points are plotted at the experimentally determined surface E_F position.

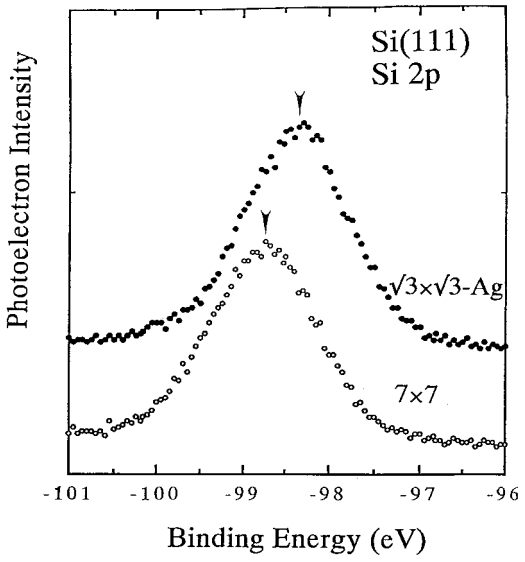

Fig. 37. XPS spectra from Si 2*p* core level on the Si(111)-7 × 7 clean surface and the $\sqrt{3} \times \sqrt{3}$-Ag surface. The peak positions are determined by curve fitting. Nonmonochromatized Mg K_α line ($h\nu = 1253.6$ eV) was used for excitation. This X-ray had a width of about 0.68 eV in energy because of Mg $K_{\alpha 1}$ and $K_{\alpha 2}$ lines with a distance in the energy spectrum of almost 0.3 eV, each having a lifetime broadening of about 0.36 eV [69]. Therefore the peaks of $2p^{1/2}$ and $2p^{3/2}$ are not resolved. However, the energy resolution of our electron analyzer was about 0.1 eV, so the shifts of the convoluted peak in the spectra can be determined by about ± 0.05 eV precision with curve fitting.

Fig. 36. This is in accordance with the measured surface conductance $\Delta\sigma$ described above. But, by quantitatively comparing the *n*-type and *p*-type cases in Fig. 36, one notices that the measured $\Delta\sigma$'s for both of the *p*- and *n*-types locate slightly above the calculated curves. But, by considering the experimental errors, which come both from a finite resolution in photoemission spectroscopy in determining the E_F positions (around ± 0.05 eV) and from the finite reproducibility in measuring the conductances, such slight discrepancy between the calculated curves and the experimental data cannot be conclusive. In other words, the measured excess surface conductance for the $\sqrt{3} \times \sqrt{3}$-Ag surface with respect to the 7 × 7 clean surface seems to come mainly from the difference in the surface-space-charge-layer $\Delta\sigma_{SC}$; the surface-state conductance $\Delta\sigma_{SS}$ through the surface-state band S_1 on the $\sqrt{3} \times \sqrt{3}$-Ag structure cannot be resolved by these measurements. But clear evidence for the surface-state conduction through the S_1-state band has been obtained, as described in Section 4.3.4, by measuring the conductance changes during additional Ag-atom adsorptions onto the $\sqrt{3} \times \sqrt{3}$-Ag surface.

4.3.2. Conductance changes during Ag deposition

In addition to the differences in surface conductance among the different surface superstructures, it is also interesting and informative to measure the conductance

changes during additional Ag atom adsorptions onto the respective surfaces. The adsorbed atoms will make some perturbations on the substrate surfaces, or will induce new order into the surface superstructures, or will grow into ordered atomic layers. Such structural/electronic changes on surfaces will be reflected in the conductance changes in many ways. For these measurements, the four(six)-probe method in UHV, described in Section 3.3, in combined with surface-science techniques, is again useful.

4.3.2.1. On the 7 × 7 surface. Fig. 38(a) shows a change in the resistance of a Si wafer during Ag deposition (rate: 0.45 ML/min) onto the clean Si(111)-7 × 7 surface at RT measured by the four-probe method [2]. The RHEED patterns observed in the course of the separate depositions under the same conditions are indicated at the corresponding coverages. The resistance does not show significant changes until the 7 × 7-RHEED pattern disappears around 2–3 ML coverage, with the exception of a slight increase just after opening the evaporator shutter. This stage corresponds to an SEM image shown in Fig. 32(a) and (b). In response to the subsequent development of a textured structure of the Ag film over 2 ML (Figs. 31(e) and 32(c)), the resistance begins to decrease steeply. After the deposition ceases, the resistance rises slightly.

4.3.2.2. On the $\sqrt{3} \times \sqrt{3}$-Ag surface. However, in the case of Ag deposition onto the Si(111)-$\sqrt{3} \times \sqrt{3}$ -Ag surface at RT under the same conditions, the growth style of the Ag film is quite different, as described in Section 4.2, and accordingly the resistance also changes in a completely different way (Fig. 38(b)) [2]. Though the details are discussed in Section 4.3.4, we describe the conductance change briefly here, for comparison with the case of the 7 × 7 substrate. The resistance abruptly drops at the beginning of deposition (less than 0.1 ML deposition), and then, after making a small overshoot in resistance drop, it turns to decrease at a moderate rate during Ag deposition. As shown in Figs. 31(d) and (d′), in this case, a ring pattern with some preferential-orientation spots from Ag micro-crystals gradually emerge in the RHEED pattern on increasing the amount of deposition, while the clear $\sqrt{3} \times \sqrt{3}$ spots remain to the end. This is due to the high surface diffusivity of Ag adatoms on top of the $\sqrt{3} \times \sqrt{3}$ surface which is enough to nucleate into 3D islands (see the SEM image in Figs. 32(d)–(g)), so that the $\sqrt{3} \times \sqrt{3}$-Ag substrate is scarcely covered by the additional Ag. An abrupt decrease in resistance on opening the evaporator shutter and an abrupt increase at the shutter close are actually caused by Ag-atom adsorption on the substrate, not the influence of radiation from the Ag evaporator. Radiation from the same type of empty evaporator (alumina-coated W baskets), placed near the Ag evaporator, and heated up to the same temperature, scarcely changed the resistance (see Fig. 3 in Ref. [2]). We can safely say, therefore, that it is the adsorbed Ag atoms that cause the resistance changes in Fig. 38(b). As described in Section 4.3.4, the steep drop in resistance at the beginning is due to adatom gas phase of Ag on top of the substrate, and the steep rise in resistance after closing the evaporator shutter corresponds to a process of nucleation in the Ag adatom gas.

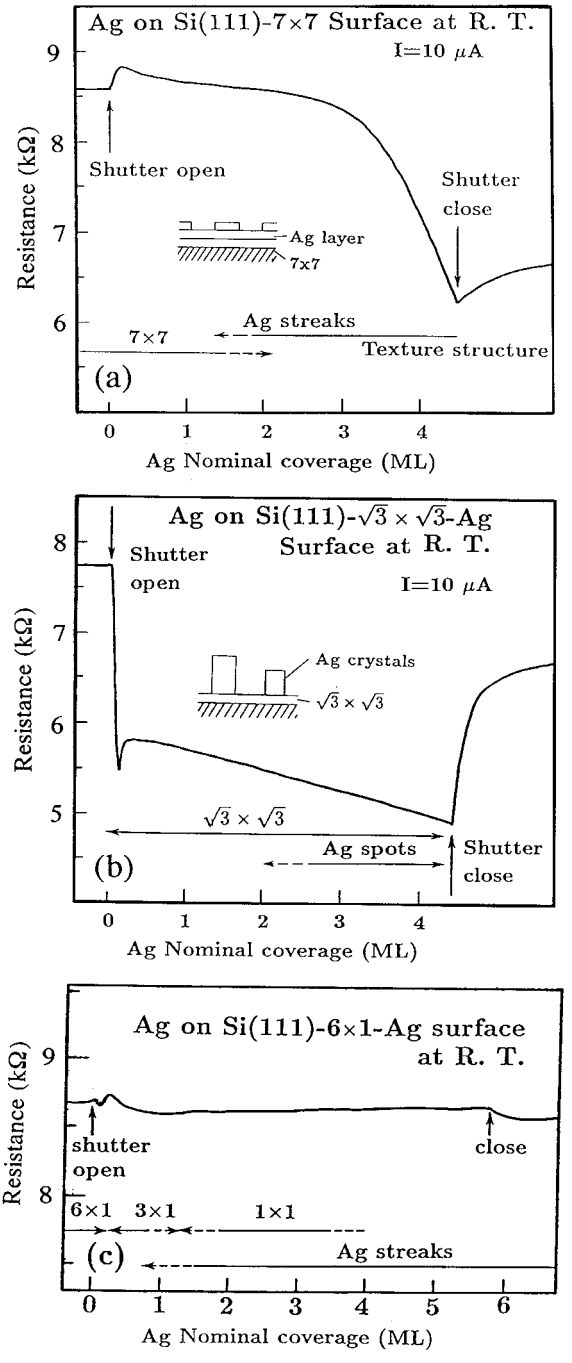

Fig. 38. Changes in resistance of a Si wafer (*n*-type with around 50 Ωcm resistivity) during Ag deposition onto (a) the Si(111)-7 × 7 clean surface, (b) the $\sqrt{3} \times \sqrt{3}$-Ag surface, and (c) the 3 × 1 (6 × 1)-Ag surface at RT, respectively (from Refs. [2,5]). Changes in RHEED patterns observed in the separate runs of depositions under the same conditions are also indicated.

4.3.2.3. On the 3 × 1 (6 × 1)-Ag surface. During Ag deposition onto the Si(111)-3 × 1(6 × 1)-Ag surface at RT, as shown in Fig. 38(c), the resistance changes in quite different way again; it remains almost unchanged to the end (up to about 6 ML coverage). The 6 × 1 RHEED pattern quickly changes into the 3 × 1 pattern only at about 0.2 ML adsorption, and then into a 1 × 1 pattern with further deposition. The RHEED pattern, taken after 5.6 ML deposition (Fig. 31(f)), indicates a similar growth style of the Ag atomic layers as on the 7 × 7 substrate. But the azimuthal rotations of the grown Ag crystals around the texture axis are more restricted, due to the influence of the underlying 3 × 1-anisotropy in the atomic arrangement, and the Ag crystals are more 3D-like compared with those on the 7 × 7 substrate.

In this way, these results show that the resistance of a Si wafer of a macroscopic thickness actually changes by an amount large enough for detection by the four-probe method, even with submonolayer depositions, and what is more interesting is that the resistance changes are quite different, depending on the substrate surface superstructures. In the following subsections, the mechanisms for the observed resistance changes are discussed in detail for the respective surfaces.

4.3.3. On the Si(111)-7 × 7 surface

4.3.3.1. Surface states and band bending. Fig. 39 shows photoemission spectra of (a) the Si 2*p* core-level region and (b) the valence-band region from the Si(111)-7 × 7 surface during Ag adsorption at RT [108]. The valence-band spectra (b) show that adsorption of only about 0.2 ML Ag causes a quick suppression of the dangling-bond state at E_F (S_1 state), converting the surface into semiconducting from metallic. This is consistent with the STS measurements by Tosch and Neddermeyer in which they reveal semiconducting spectra at Ag-covered surface areas and metallic ones at Ag-uncovered areas [98]. Therefore, if the surface-state conductance $\Delta\sigma_{SS}$ exists through the dangling-bond state S_1, the resistance should be increased at the very beginning of the Ag deposition, where the S_1 state dies away. The slight increase in the resistance observed at the beginning in Fig. 38(a) could correspond to this expectation. From this resistance increase, the possible $\Delta\sigma_{SS}$ is estimated to be of the order of 10^{-6} S/□, which is not inconsistent with Henzler's estimation of conductivity via a metallic surface-state band [109], while it seems larger than the conductivity of Hasegawa (Y.) et al. [51] and Heike et al. [29]. Suurmeijer et al. [74] also observed a similar increase in the resistance at the beginning of Pb deposition onto the 7 × 7 surface at RT, but they attributed it to the change in $\Delta\sigma_{SC}$ due to band-bending induced by Pb adsorption. The details of this slight increase in resistance are not yet clear.

The core-level spectra Fig. 39(a) reveal an overall shift of the entire line-shape to lower binding energies, which indicates an upward band-bending ~0.26 eV with 1 ML Ag adsorption. In other words, the Fermi-level is unpinned from the metallic S_1 state of the 7 × 7-DAS surface, and the E_F position is shifted from 0.63 eV (which is the E_F position at the clean 7 × 7 surface) to 0.37 eV above E_{VBM} by the Ag adsorption; the bands in bulk bend upwards slightly. However,

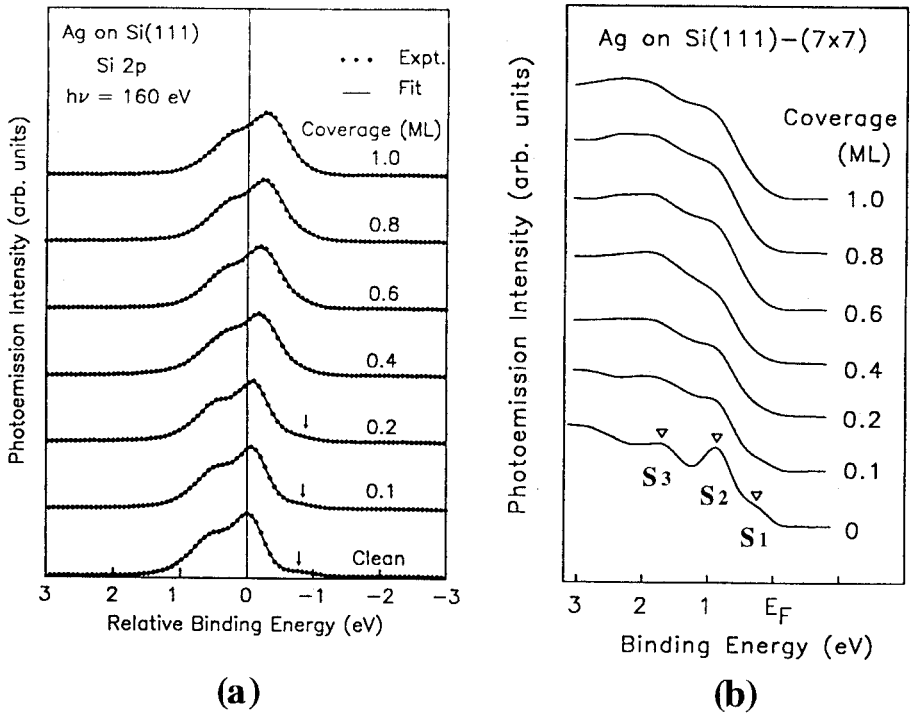

Fig. 39. Photoemission spectra in (a) Si 2*p* core-level region and (b) the valence-band region for the Si(111)-7 × 7 surface at RT covered with various amounts of Ag as indicated. Reproduced with permission from Ref. [108].

as shown by the calculated curve of the surface conductance $\Delta\sigma_{SC}$ versus the surface E_F position (Fig. 36), this E_F shift does not give rise to a significant change in the conductance through the surface space-charge layer; the surface space-charge layer still remains within the depletion-layer condition. This is consistent with the measurement in Fig. 38(a) showing no remarkable changes in the resistance at the initial stage of Ag deposition up to 2.5 ML coverage.

4.3.3.2. Deposition-rate dependence. Now, what is the operating mechanism for the steep drop observed over around 2.5 ML coverage in Fig. 38(a)? One expects naively that with an increase of Ag coverage, Ag layers or Ag thin crystals grow and connect with each other, thus making conducting paths (percolating paths), leading to a conductance increase; the conductance starts through the grown atomic layers $\Delta\sigma_{AL}$. If this is the case, does the substrate (i.e., the surface space-charge layer $\Delta\sigma_{SC}$) play no role in the electronic transport?

Fig. 40 [110] is for measurements similar to those in Fig. 38(a), showing the resistance changes of a Si(111) wafer with the 7 × 7 surface superstructure during Ag deposition with different deposition rates at two different temperatures, RT and 150 K. The main features in Fig. 38(a) are reproduced in Fig. 40(a), namely,

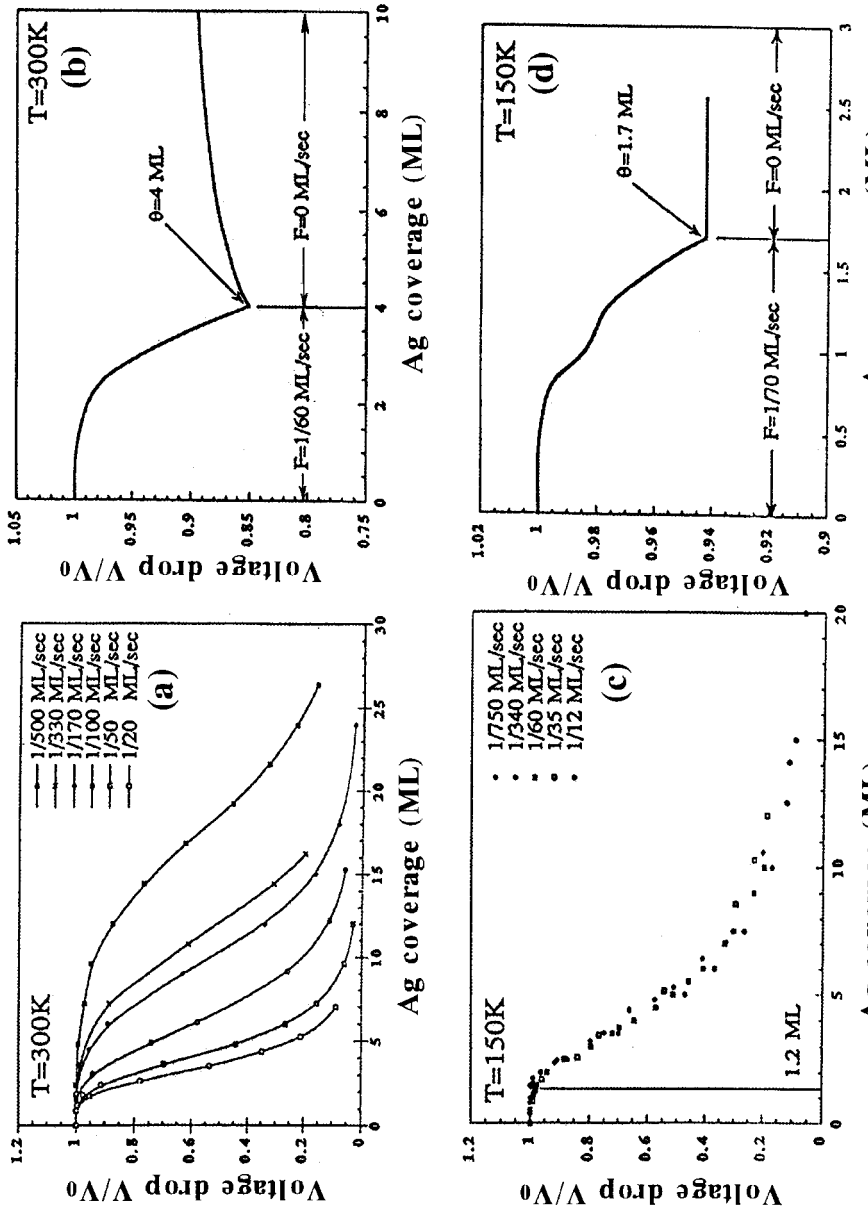

Fig. 40. Changes in the normalized voltage drops, corresponding to the normalized resistance of a Si(111) wafer having the 7×7 superstructure, during Ag deposition at (a) and (b) room temperature, and (c) and (d) 150 K, (a) and (c) with different deposition rates, (b) and (d) Transient measurements showing the resistance changes with time after the Ag evaporator shutter is closed. Reproduced with permission from Ref. [110].

the initial plateau up to a few ML coverage and the following steep drop in resistance with increasing the coverage. But the plateau extends to larger coverages with decreasing deposition rates. When a critical coverage θ_P, a measure of the plateau, is defined as the maximum Ag coverage at which the resistance remains unchanged, θ_P is found to change as a function of the deposition rate F as $\theta_P \propto F^{-0.4}$, which is surprising in a sense [110]. The standard nucleation theory [111] would predict a positive exponent in this relation, since smoother films grow with lower deposition rates, in which the connectivity among the (2D) Ag metal islands would improve and the percolating paths would be created more easily with smaller coverages, which is the opposite to the experimental results. Consequently, Tringides [110] insist that the observed resistance drop should not be attributed simply to the grown Ag overlayers.

Fig. 40(c) shows similar measurements at the substrate temperature of 150 K. The critical coverage θ_P for the initial plateau is always around 1.2 ML at this temperature, independent of the deposition rate, which is a sharp contrast to the RT case (a). This is natural, when one recalls the RHEED intensity oscillations shown in Fig. 35(b), measured under the same conditions [103,104]. The intensity changes of the specular spot, during Ag depositions with different rates onto the 150-K substrate, almost collapse into a similar curve by appropriate scaling in the deposition time, which suggests similar morphologies of the growing surface irrespective of the deposition rates used. However, the RHEED intensity oscillations measured at RT [102] (Fig. 35(a)) indicate that the intensity curves with different deposition rates do not collapse into a curve, even by appropriate scaling in time, meaning different growth morphology depending upon the deposition rates. The difference in growth structure of Ag layers between at RT and 150 K, thus revealed by the RHEED intensity measurements, will raise the difference in resistance changes between Fig. 40(a) and (c). But, we cannot simply say, as mentioned above, that the electronic transport occurs only through the Ag layers. Though we have no data on the changes in electronic state in the Si substrate beneath the Ag overlayers of a few ML thick, we may have to consider a contribution of the transport through the Si substrate ($\Delta\sigma_{SC}$) as well; the electrical conduction via the substrate among the isolated Ag flat islands may play some role, and/or the substrate beneath the Ag islands may become conductive, due to electron transfer from the islands. The details are not yet clear.

The difference in the growth mode of Ag layers between RT and low temperatures is also revealed by transient measurements shown in Fig. 40(b) and (d), in which the resistance changes are monitored with time, after the shutter of the Ag evaporator is closed. At RT (b), the resistance gradually increases towards the initial value, while at 150 K (d), the resistance remains unchanged after the shutter closed. These clearly indicate that the deposited Ag atoms have enough mobility at RT to further roughen the surface by agglomerating into multi-layers (3D) islands present, while at 150 K, such a surface diffusion of the adatoms is suppressed, preventing surface roughening.

4.3.3.3. Percolation. The above-mentioned question—that the resistance decrease seen over a few ML deposition of Ag onto the clean 7×7 surface should be attributed only to the Ag overlayers ($\Delta\sigma_{AL}$) or not—was raised again in the similar measurements at the lowest temperature [106,54]. Fig. 41(a) shows a four-probe voltage measured in van der Pauw geometry, corresponding to the resistance change of a Si(111) wafer during Ag deposition onto the clean 7×7 surface at 83 K [106]. Similar features as in Figs. 38(a) and 40, the initial plateau and the following steep drop in resistance, were again observed, while the critical coverage for the plateau, around 0.9 ML, was smaller than at higher temperatures in Figs. 38(a) and 40(a) and (c). The conductance of the Ag layers, which was derived from the resistance drop in Fig. 41(a), is plotted in (b). Percolation theory [112] predicts that the conductance increase $\Delta\sigma$ near the percolation threshold varies as a function of coverage θ according to

$$\Delta\sigma(\theta) \propto (\theta - \theta_C)^t \quad for\ \theta > \theta_C, \tag{62}$$

with a critical coverage θ_C and an exponent t. The best fit to the measured conductance changes (b) with this equation was obtained with $\theta_C = 0.9$ ML and $t = 1.36 \pm 0.25$, as shown by a straight line on a log–log plot in Fig. 41(c). On the other hand, the percolation theory [173] and Monte Carlo [113, 114] simulations give a value $t \simeq 1.3$ for 2D systems. So the agreement between the theoretically predicted exponent and the experimentally derived value indicates that the observed conductance increase beyond 0.9 ML coverage should be understood in terms of percolation among conductive units. Then, the next question is, what is the unit of percolation?

The theory gives a value for the critical coverage $\theta_C = 0.5$ on a triangular lattice [115]. The measured values for θ_C are always larger than this theoretical prediction, especially at RT. Since, however, the experimental value ($\sim$0.9 ML) for θ_C at 83 K is near the theoretical value (0.5 ML), the units for percolation should be single Ag atoms or clusters with several Ag atoms. However, the question now arises to whether a single-atom chain or a chain with a width of only a few atoms may provide a conducting path. Once again one can speculate that the substrate plays some role in electrical conduction; the percolating paths might be created in the substrate beneath the Ag adsorbates (raising $\Delta\sigma_{SC}$), not through the Ag adsorbates themselves ($\Delta\sigma_{AL}$).

Furthermore, as shown in Fig. 41(d), the critical coverage θ_C is measured to increase with temperature decrease below around 100 K [116], which is a very unexpected tendency. As described in Section 4.2, the Ag growth on the 7×7 surface at RT proceeds in an incomplete layer-by-layer mode; multilayer islands appear with growth. The thermodynamic equilibrium favors the forming of such islands, which becomes larger as the temperature increases. Therefore, a percolation at RT, seen in the conductance measurements (Figs. 38(a) and 40(a)), is observed only after the deposition of several monolayers; the critical coverage θ_C for percolation is as large as several ML. On lowering the temperature, the mobility of the deposited atoms decreases and the nucleation density increases

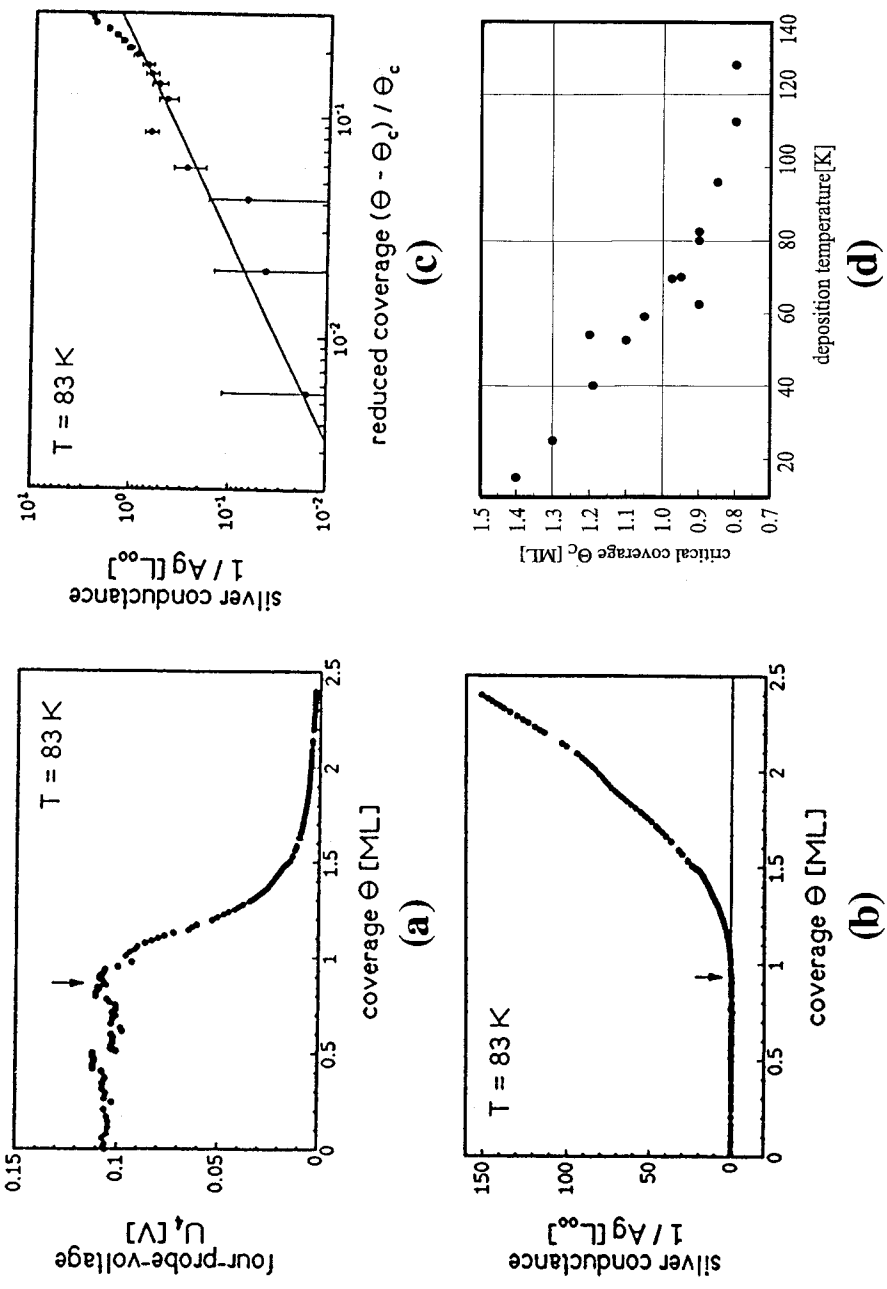

Fig. 41. (a) A change in four-probe voltage, corresponding to the resistance of a Si wafer measured in van der Pauw geometry, during Ag deposition onto the Si(111)-7 × 7 clean surface at 83 K. (b) The conductance of Ag layers (= 1/Ag resistance) determined by resistance drop shown in (a) as a function of Ag coverage. The conductance is given in units of quantum conductance $L_{00} = e^2/2\pi^2\hbar \simeq 1/(81\ \mathrm{k}\Omega)$. (c) A log-log plot of Ag conductance vs reduced coverage $(\theta - \theta_C)/\theta_C$. The straight line indicates the best fit for a power law $\Delta\sigma\ (\theta) \propto (\theta - \theta_C)^t$, with a critical coverage $\theta_C = 0.9$ ML and an exponent $t = 1.23$. Reproduced with permission from Ref. [106]. (d) Substrate-temperature dependence of the critical coverage θ_C for percolating of Ag layers on Si(111)-7 × 7 surface. Reproduced with permission from Ref. [116].

accordingly [111]. At sufficiently low temperatures, the surface mobility of the deposited Ag atoms should be negligible. If all arriving atoms stay at the sites where they impinge, the critical coverage for percolation for random arrangement on a triangular lattice is expected to be the theoretical value $\theta_C = 0.5$. The experimental values of larger θ_C are explained by preferred nucleation of Ag atoms on the triangles of the half unit cells of the 7×7 [105,98]; some mobility of the Ag atoms is needed to agglomerate into the clusters. With a further lowering of the temperature, a further reduction in the migration mobility of Ag atoms is expected, so that θ_C is expected to approach to the theoretical value 0.5 ML. However, the results in Fig. 41(d) indicate the opposite tendency below 100 K. Such an unexpected tendency is speculated to be due to nonthermal diffusion of Ag atoms [116]; when an arriving Ag atom interacts with a Si substrate atom, it can accept the excess energy of the arriving Ag atom (kinetic energy and adsorption energy) only via a displacement, which requires the generation of many phonons. But the lower the substrate temperature is, the less likely should be the excitation of phonons. In this way, the dissipation of the excess energy of the Ag adatoms will be slower and the accommodation of the Ag energy to the substrate temperature is delayed. As a result, the Ag atoms will hop more and more on the surface at lower temperatures until the atoms are captured by clusters, which leads to a tendency of more aggregation into Ag clusters, resulting in larger values of θ_C at lower temperatures below 100 K.

As discussed above, unclear points still remain regarding the mechanism operating in the electrical resistance changes during Ag deposition onto the clean Si(111)-7×7 surface, but they provide interesting insights into the structural evolutions and surface atom behaviors.

4.3.4. On the Si(111)-$\sqrt{3} \times \sqrt{3}$-Ag surface

4.3.4.1. Two-dimensional adatom-gas phase. The mechanism operating in the resistance change observed during Ag deposition on the $\sqrt{3} \times \sqrt{3}$-Ag surface (Fig. 38(b)) is found to be quite different from that on the 7×7 clean surface; the surface-state conductance $\Delta\sigma_{SS}$ plays a main role here.

How do we understand the remarkable resistance drop, as shown in Fig. 38(b), by as much as 20% or more, which is induced by Ag adsorption at a coverage as small as 0.03 ML onto a Si wafer as thick as 0.4 mm? Moreover, when the Ag deposition is terminated at 4.3 ML Ag coverage by closing an evaporator shutter, the resistance swiftly rises towards the initial value. Let us try to clarify such strange changes in the resistance. In Fig. 42(a)–(d), we made similar measurements as in Fig. 38(b), but the depositions were ended at coverages of 4.5, 2.1, 0.52, and 0.081 ML, respectively [14]. The resistances again rise towards the initial values, after the depositions cease. However, in Fig. 42(e)–(g), where the depositions were ended at 0.025, 0.015, and 0.0079 ML coverages, respectively, (which were in the course of the initial steep drop of resistance), the resistances were, surprisingly, almost constant after the depositions! The resistance changes after the depositions are thus revealed to be completely different, depending on whether the Ag

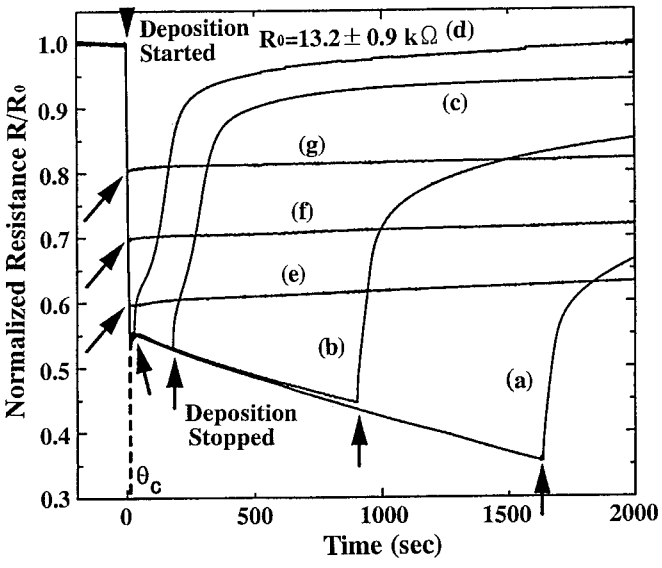

Fig. 42. Resistance changes of a Si wafer with Si(111)-$\sqrt{3} \times \sqrt{3}$-Ag surface at RT during and after additional Ag depositions (rate = 0.16 ML/min). The Si crystal is *n*-type with 100 Ωcm resistivity and 30 $\times$ 4 $\times$ 0.5 mm^3 in size. The depositions were stopped at Ag coverages of (a) 4.5 ML, (b) 2.1 ML, (c) 0.52 ML, (d) 0.081 ML, (e) 0.025 ML, (f) 0.015 ML, and (g) 0.0079 ML, respectively. From Refs. [14,18].

coverage is more or less than the critical coverage θ_C ($\sim$0.03 ML) [14]. θ_C corresponds to Ag coverage at a small overshoot at the initial resistance drop in Figs. 38(b) and 42 (which is a different critical coverage from that defined in percolation phenomena in Section 4.3.3).

Displayed in Fig. 43(a) is the resistance change when Ag is deposited with some interruptions [14]. In this case, the resistance again remains almost constant during the interruption intervals A, B, and C, where the Ag coverage is below the θ_C. But, once the coverage exceeds θ_C, the resistance rises towards the initial value during the interruption intervals D, E, and F.

RHEED and SEM observations in Fig. 31(d)(d′) and Fig. 32(d)–(g) indicate that Ag atoms deposited onto the RT-$\sqrt{3} \times \sqrt{3}$-Ag surface nucleate into 3D microcrystals, so that the surface is scarcely covered with the additional adsorbates. By considering this structural change, the above-mentioned resistance changes are interpreted as follows. In general, in order to initiate nucleation, the density of the deposited atoms should exceed a critical density of adatoms θ_C (*critical supersaturation*). This is similar to the mist that appears only when the water vapor pressure in air exceeds the saturated vapor pressure at a given temperature. In other words, when the Ag coverage is less than θ_C, nucleation does not proceed, and the deposited Ag atoms remain isolated, forming a (supersaturated metastable) *2D adatom gas* (2DAG) phase on top of the surface. Thus, Ag atoms in the 2DAG phase, before they are incorporated into 3D

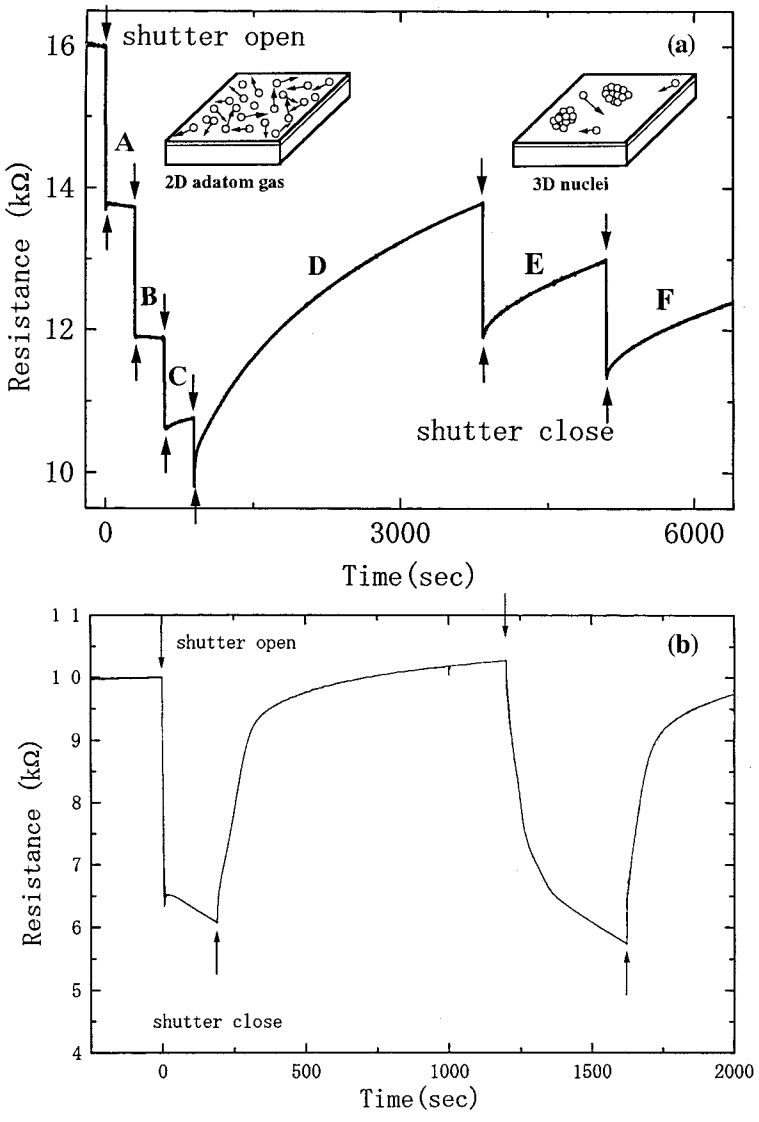

Fig. 43. (a) A resistance change of a Si wafer during intermittent Ag depositions (rate = 0.24 ML/min) onto the Si(111)-$\sqrt{3} \times \sqrt{3}$-Ag surface at RT. The Si wafer is *n*-type of 100 Ωcm resistivity. Downward arrows indicate the starting points of depositions, and upward arrows their end points. Ag atoms of amount of 0.008 ML are deposited during each deposition period (two seconds). A–F indicate the interruption intervals. (b) A resistance change during two successive Ag depositions on the same surface. Ag of 0.5 ML is deposited at the first deposition, and after 17-min interval, 2.2 ML is deposited at the second period. From Ref. [14].

microcrystal nuclei, can make the resistance low, so that the resistance drops at the beginning of the deposition, observed in Figs. 38(b), 42, and 43(a), correspond to increments in the atom density in the 2DAG phase. Actually, as clarified below using photoemission spectroscopy, the Ag adatoms in the 2DAG phase donate carriers into the surface-state band, resulting in an enhancement of the conductance $\Delta\sigma_{SS}$ [14]. Up to the θ_C, the density of 2DAG increases by deposition, resulting in a resistance decrease. Even if the deposition ceases at this stage, the 2DAG remains (meta)stable so as to keep the gas density constant and, therefore, the resistance remains constant. But, once the adatom density exceeds θ_C, nucleation sets in via the stable nuclei capture of the atoms in the 2DAG phase. If the deposition ceases at this stage, the density of 2DAG decreases by nucleation, and will reach a very low gas density equilibrated with the nuclei, which makes the resistance rise towards its initial value. This change of adatom density in the gas phase is revealed by Monte Carlo simulation [117]. But we can not directly observe the individual adatoms in the 2DAG phase by RHEED, SEM, or STM, because they are highly mobile; only the stable nuclei (3D microcrystals) can be observed. As shown in a micrograph of Fig. 32(d)–(g), the 3D microcrystals tend to gather together into *colonies*. The distances among the colonies are ~10 μm, which indicates that the Ag atoms in the 2DAG phase are so mobile that they can easily migrate across atomic steps on the surface to make their surface diffusion lengths very long.

4.3.4.2. Successive depositions. We have found another phenomenon, which supports the scenario that the 2DAG phase reduces the electrical resistance [14]. Fig. 43(b) shows a resistance change during two successive Ag depositions onto the $\sqrt{3} \times \sqrt{3}$-Ag at RT. Ag atoms up to 0.5 ML were deposited during the first deposition period, and after about 17-min interruption, the second deposition was started. The resistance changes observed during and after these two depositions look similar; the initial steep drop, the following gradual decrease, and the steep rise after the depositions cease. But on closer observation, we noticed the difference that the overshoot at the initial steep resistance drop appears around 0.03 ML coverage in the first deposition only, but not in the second deposition, where, instead, a gradual transition from the initial steep drop to the following gradual decrease was observed. Thus, the overshoot in the resistance drop, which occurs only in the first deposition, corresponds to a kinetic overshoot in the adatoms-gas density before the initiation of the nucleation. At the first deposition on a fresh $\sqrt{3} \times \sqrt{3}$-Ag surface (fresh means that there are no stable nuclei in the range of diffusion lengths of deposited Ag atoms, which may act as sinks for the gas-phase Ag adatoms), the density of Ag adatoms kinetically exceeds the critical supersaturation density before their nucleation starts, which was also reproduced by a Monte Carlo simulation [117]. This temporary excess density of adatoms is observed as an overshoot in resistance drop in the first deposition in Fig. 43(b) (and also in Figs. 38(b) and 42). In the second deposition period, on the other hand, there already exist stable nuclei with separations of diffusion lengths of Ag adatoms on the surface, which were formed in the first deposition, so that the

deposited atoms are swiftly captured by the nuclei. This is the reason why the adatom-gas density does not exceed too much beyond the critical supersaturation density, so that no overshoot appears in the resistance curve during the second deposition in Fig. 43(b).

Such an overshoot in resistance drop, observed at the beginning of the depositions, are systematically investigated in Fig. 44(a) and (b) in which the resistance changes are monitored during similar sequences of two successive Ag depositions onto the $\sqrt{3}\times\sqrt{3}$-Ag surface at RT [14]. During the first depositions in Fig. 44(a) (in which the deposited amount is 0.056 ML for all curves) and the following interruption intervals, the resistance changes in the same way as (d) in Fig. 42, i.e., a steep rise in the resistance after the deposition, because the deposited amount is more than the θ_C. Immediately after the start of the second depositions, the resistance drops abruptly again. In the curves (d) and (e) in Fig. 44(a), the resistance decreases slowly after this initial drop in resistance without making an overshoot. By stopping the deposition, the resistance steeply rises making a shoulder. When, as shown in the curves (a) and (b), the second depositions are stopped before reaching the bending point in the curves (d) and (e), the resistance recovers monotonically, but not in a simple exponential way. As discussed above, in the second deposition, there is no kinetic overshoot in the adatom-gas density and also no overshoot in the resistance drop. Therefore, the bending point in curves (d) and (e) corresponds to the critical supersaturation of the adatom gas, and additional nuclei begin to nucleate after this point by continuing the deposition in the curves (d) and (e), but no additional nucleations occur in the curves (a) and (b), because the density of the deposited atoms is less than θ_C.

Fig. 44(b) shows similar measurements during the sequence of two successive depositions, where the amounts of the first depositions are changed in greater than the θ_C, and a constant amount of Ag is deposited at the second stage. When the first-deposition coverage is small, as in curve (f), the resistance drops quickly by starting the second deposition. On the other hand, when the first deposition is prolonged, as in curve (i), the resistance drops slowly at the second-deposition stage.

The change in the adatom density θ_{ad} in the 2DAG phase can be formally described by the rate equation

$$\frac{d\theta_{ad}}{dt} = F - \frac{\theta_{ad}}{\tau}, \tag{63}$$

where F denotes the deposition rate, and τ represents the *life time* of the adatoms in the 2DAG phase against being captured by 3D nuclei. So τ depends on the number density of the sinks (stable nuclei). On the fresh surface, there is no 3D stable nuclei, so that $\tau=\infty$, when $\theta=\theta_{ad}<\theta_C$. Thus, $\theta_{ad}=Ft$ up to θ_C. This corresponds to the steep drop in resistance at the beginning of the first deposition in Fig. 44, and also nearly corresponds to the resistance change at the beginning of the second deposition of (f) in Fig. 44(b), where 3D stable nuclei are very rare

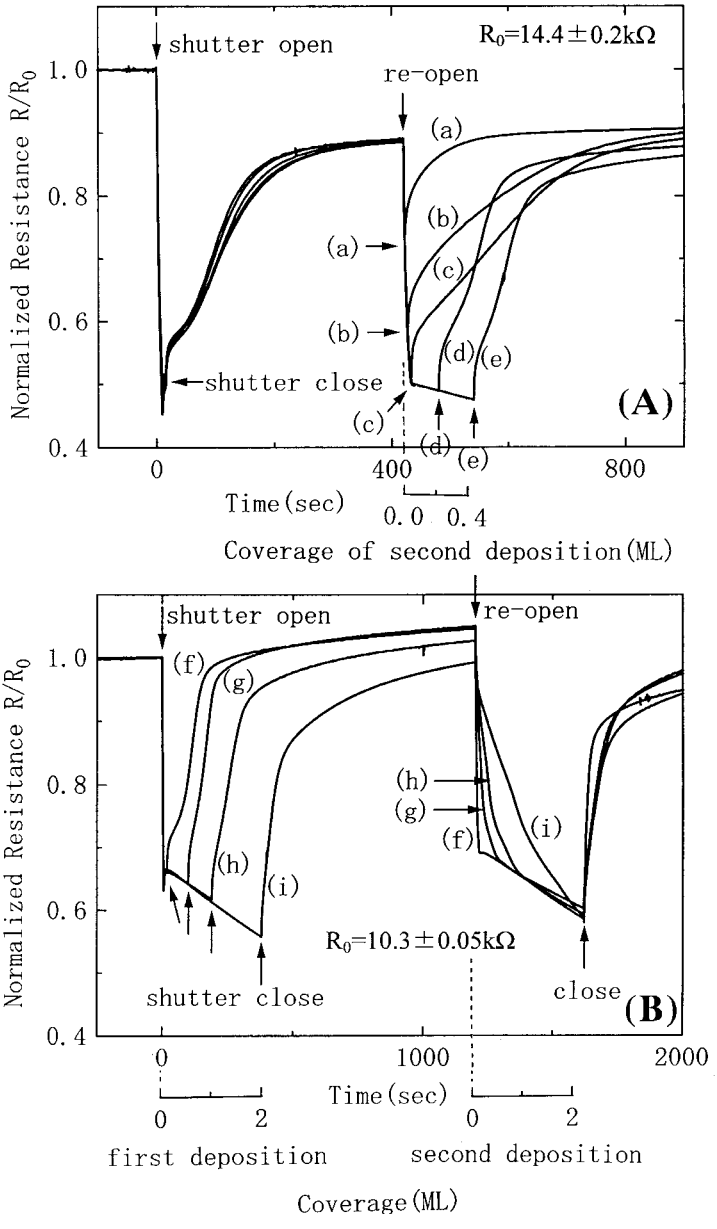

Fig. 44. The resistance changes during the sequence of two successive Ag depositions. (A) The first-deposition coverages are the same 0.056 ML for all curves. The second-deposition coverages are (a) 0.0074 ML (b) 0.026 ML (c) 0.048 ML (d) 0.22 ML (e) 0.44 ML, respectively, with the rate of 0.22 ML/min. (B) The first-deposition coverages are (f) 0.1 ML (g) 0.5 ML (h) 1 ML (i) 2 ML, respectively, with the rate of 0.31 ML/min, while the second-deposition coverages are the same 2.2 ML for all curves. From Ref. [14].

(because of a very small amount of deposition at the first stage). But on increasing the deposited amount in the first deposition, as in curves (g)–(i) in Fig. 44(b), τ will become smaller at the second-deposition stage, because of the already larger density of the stable nuclei. At the beginning of the second deposition, τ should be constant, but different for the respective curves (g)–(i), so that

$$\theta_{ad} = F\tau(1 - e^{-t/\tau}), \tag{64}$$

until the additional new stable nuclei begin to appear. This qualitatively describes the trend of the curves (g)–(i), where the increase rate of the adatom density (which corresponds to the decrease rate in resistance) at the very beginning of the second deposition are almost the same, $\theta_{ad} \approx Ft$, irrespective of τ, while, after that, the increase rate become slower from (f) to (i), because the deposition amounts at the first deposition stage are larger and τ is smaller. Thus, the resistance change can be qualitatively explained by the rate equation of θ_{ad}.

As mentioned so far, the decrease in resistance directly corresponds to the increase in the adatom density in 2DAG phase.

4.3.4.3. Nucleation of 2DAG. Let us carefully look at the resistance recovering process after the deposition is finished. As mentioned above, the curves (d) and (e) in Fig. 44(a) show shoulders during the rise in resistance after the depositions. In these cases, the depositions were stopped after the adatom density θ_{ad} reached the critical supersaturation. Therefore, the Ag adatoms deposited at the second deposition make additionally new stable nuclei. However, the resistance monotonically rises in curves (a) and (b) in Fig. 44(a), where the second depositions are interrupted before the θ_{ad} reaches the critical supersaturation. In these cases, the deposited adataoms are just captured by the stable nuclei already existed on the surface. Therefore, it can be said that the shoulder in the resistance curves (d) and (e) is related to the nucleation of new additional stable nuclei.

Such shoulders are always observed when the deposited amounts are relatively small (but larger than the θ_C) as in curve (d) in Fig. 42. Fig. 45 shows the resistance changes during cycles of Ag deposition onto the Si(111)-$\sqrt{3} \times \sqrt{3}$-Ag surface at RT and its interruption. The amount of Ag deposited during each short period is about 0.07 ML, which is larger than θ_C, so that the resistance rises towards the initial value during the interruption period. By carefully looking at the curve during the interruption periods, one notices that the shoulder indicated by big arrow heads gradually disappears with repeated deposition–interruption cycles. This suggest that the shoulder is observed only when the number of the stable Ag nuclei on top of the surface is relatively smaller. Though the details of the shoulder are still an open question, it is closely related to the atomistic dynamics during the nucleation of the adataom gas.

From these observations and considerations, though unclear points still remain , to measure the resistance changes in real time during depositions (and after depositions) can provide a method for monitoring atomistic dynamics, which can not be observed directly by microscopies and diffractions.

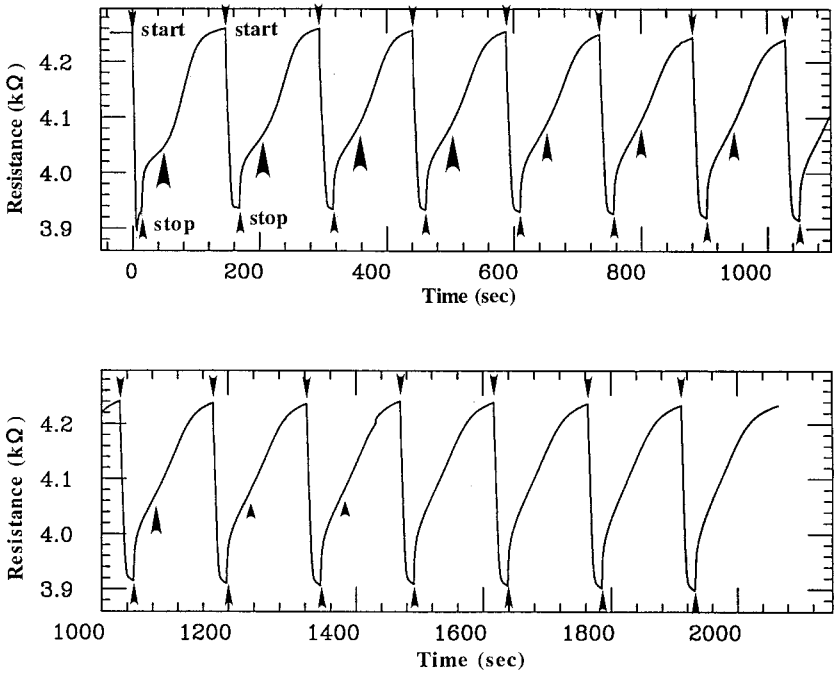

Fig. 45. The resistance changes during cycles of room-temperature Ag deposition onto the Si(111)-$\sqrt{3} \times \sqrt{3}$-Ag surface and its interruption. The amount of Ag deposited during each short period is about 0.07 ML.

4.3.4.4. Carrier doping into a surface-state band. Now we have to face the next question—why do only the Ag atoms in the 2DAG phase reduce the resistance? Why do they lose such a function once they are nucleated into 3D microcrystals? To answer these questions, we have carried out photoemission spectroscopies at RT for three surfaces [14]; (A) the fresh $\sqrt{3} \times \sqrt{3}$-Ag surface (without additional Ag deposition), (B) the same surface with 2DAG on it (after additional Ag deposition of 0.022 ML $< \theta_C$), and (C) the same surface with 3D microcrystals on it (after additional Ag deposition of 0.088 ML $> \theta_C$). We have prepared these surfaces in a following way. Fig. 46(a) shows a conductance change of the Si wafer during the sequence of two successive Ag depositions on the $\sqrt{3} \times \sqrt{3}$-Ag surface at RT. The conductance is calculated by (50) from the measured resistance. When the deposition is interrupted at 0.022 ML coverage, the conductance remains constant, as mentioned in Fig. 42(e)–(g), because the coverage is less than θ_C. Since, as shown in Fig. 42(e)–(g), the 2DAG can remain on the surface for at least one hour, keeping the resistance low, we can measure photoemission spectroscopies during this period. This is the surface (B). When the second deposition (additional 0.066 ML coverage) commences, the conductance begins to rise again. When the deposition is interrupted again at 0.088 ML coverage in total, the conductance decreases steeply down to a lower value, which is due to the nucleation of the

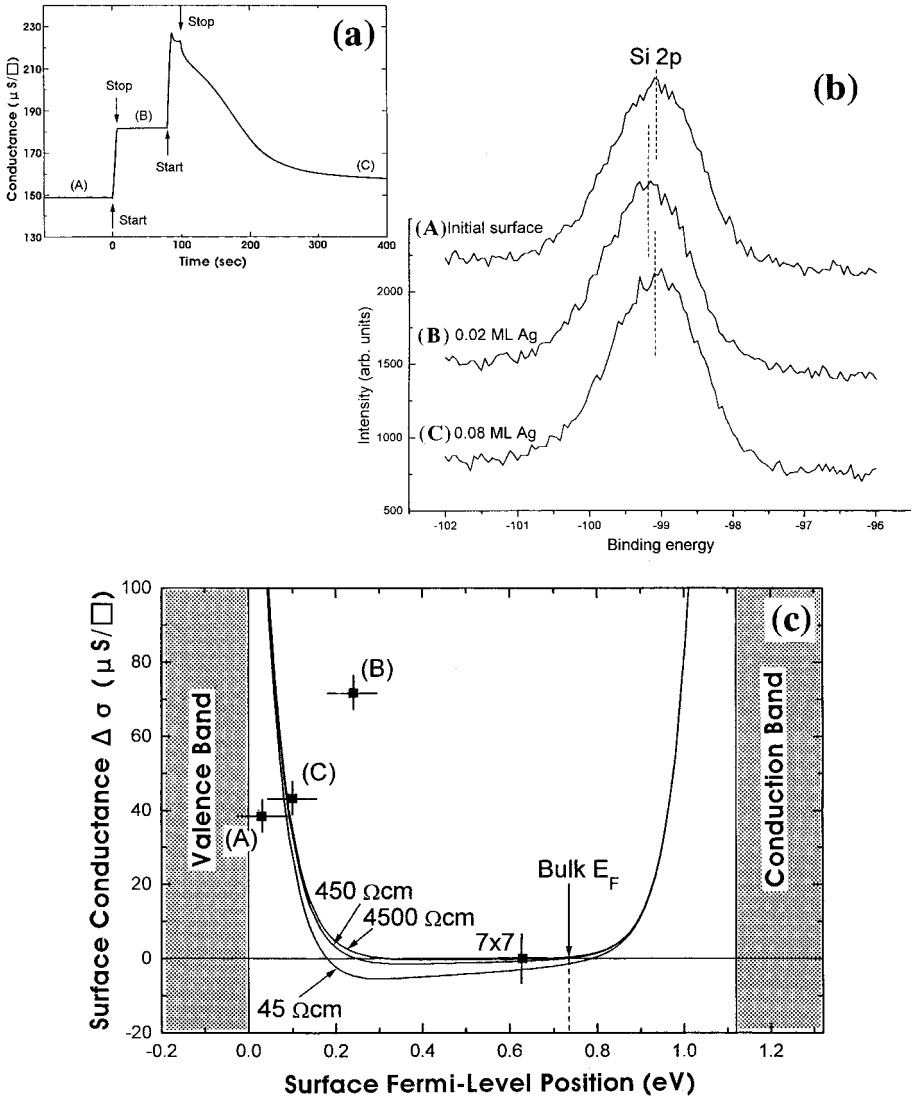

Fig. 46. (a) The conductance change of a Si wafer with the Si(111)-$\sqrt{3} \times \sqrt{3}$-Ag surface at RT during the sequence of two successive additional Ag depositions onto it. The coverage of the first and second depositions were 0.022 ML and 0.066 ML, respectively. (A)–(C) correspond to three samples used in the following photoemission measurements. (b) Si 2*p* core-level emission from the respective surfaces. (c) The differences in conductance among the samples (A)–(C) with respect to that of the 7 × 7 clean surface (measured in (a)) are plotted at the respective surface E_F positions determined in (b). Solid lines show the excess conductances $\Delta\sigma_{SC}$ calculated as a function of the surface E_F position with different bulk resistivities. From Ref. [14].

2DAG phase discussed above. The surface at this stage corresponds to the surface (C).

First of all, as described in Section 3.2, we used XPS to determine the band bendings at the respective surfaces. As shown in Fig. 46(b), the peak of Si 2*p* core level was found to shift towards a larger binding energy by 0.18 eV in going from (A) to (B), while the peak at the surface (C) shifted back, almost to the initial position at the surface (A) [14]. The surface E_F positions, thus determined, are plotted in graph (c) of Fig. 46. As mentioned in Fig. 5(d), the bulk bands below the fresh $\sqrt{3} \times \sqrt{3}$-Ag surface bend upwards, so that the surface space-charge layer is a hole-accumulation one. But, the above XPS results tell us that the 2DAG causes the bands to bend towards the flat-band situation, resulting in a sweeping out of the excess holes accumulated in the surface space-charge layer. Therefore, the 2DAG reduces the conductance $\Delta\sigma_{SC}$ through the surface space-charge layer, as indicated the curves in Fig. 46(c). This is completely opposite to the conductance increase observed in Fig. 46(a) (and the steep resistance drops in Figs. 38(b), 42, 43, and 44); the data point (B) in Fig. 46(c) is significantly deviate from the calculated curves, while the data points (A) and (C) are almost on the curves. We have performed calculations for $\Delta\sigma_{SC}$ using Eq. (34) in Section 2.2.1 with several different bulk resistivities, by assuming possible reductions or redistributions of the dopants in bulk by high-temperature heatings. But such effects, if they exist, do not change the conclusion shown in Fig. 46(c). Therefore, we have to include $\Delta\sigma_{SS}$, the surface-state conduction, at the surface (B), because the additional Ag coverage of 0.022 ML is, of course, too small to form percolation paths.

Next, we measured ARUPS from the respective surfaces. Figs. 47(a)–(c) show the spectra taken from the surfaces (A), (B), and (C) defined above, respectively, scanned in $[10\bar{1}]$ direction around the $\bar{\Gamma}$ point in the second surface Brillouin zone [14]. Three peaks, indicated by arrowheads, correspond to the surface states S_1, S_2, and S_3, mentioned in Figs. 5(c) and 17(a), which exhibit characteristic dispersions, respectively. These features in spectra scarcely change among the respective surfaces (A)–(C), but the binding energies of the respective states shift. The changes are more clearly observed in the 2D band-dispersion diagram of Fig. 48(a) constructed from the spectra in Fig. 47 [14]. The three surface states at the fresh $\sqrt{3} \times \sqrt{3}$-Ag surface (A), of course, disperse in the same ways as in Fig. 5(c). These states at the surface (B), on which the 2DAG sits, shift downward by 0.15 eV compared to at the surface (A), though no significant changes occur in dispersion. Furthermore, when the 2DAG nucleates into 3D microcrystals on the surface (C), these states return to almost the same position as at the surface (A). These shifts in binding energy are consistent with the Si 2*p* core-level shifts observed in Fig. 46(b).

Focusing on the behavior of the S_1-state band crossing E_F, the occupation in this band increases from the surface (A) to (B) and, accordingly, the intensity of its peak in spectra in Fig. 47 increases. That is to say, more electrons are trapped in the surface-state band S_1 by a downward shift of the whole bands as shown in Fig. 48(b), leading to an increase in conductivity. More strictly speaking, as

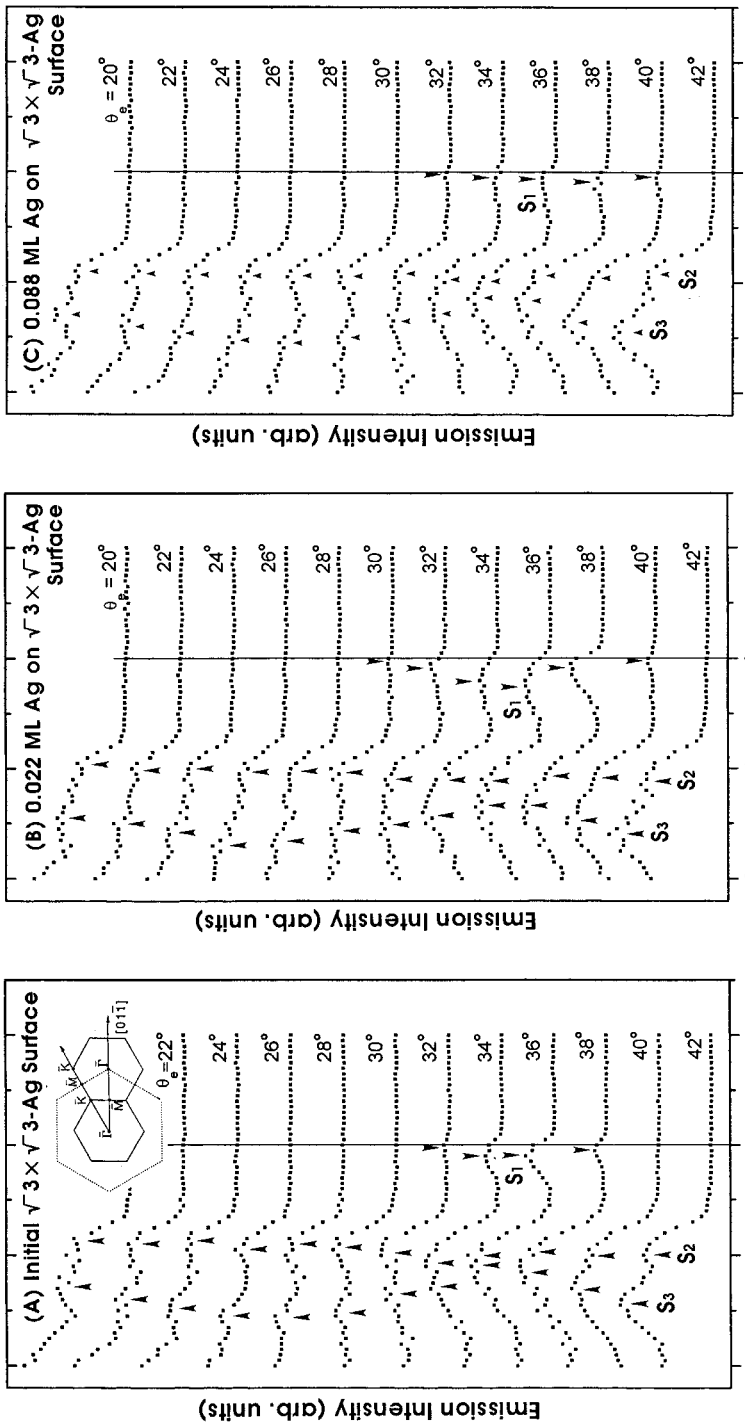

Fig. 47. ARUPS spectra for (A) the "fresh" $\sqrt{3} \times \sqrt{3}$-Ag surface, (B) the same surface with 2DAG on it, and (C) the same surface with 3D Ag nuclei on it, scanned in [01$\bar{1}$] direction. The angle of incidence of the ultraviolet light of 21.2 eV was set 15° off from the surface-normal. The emission angles θ_e presented here, measured from the surface-normal direction, correspond to a range of wave vectors around the $\bar{\Gamma}$ point in the second $\sqrt{3} \times \sqrt{3}$ surface Brillouin zone (see the inset). From Ref. [14].

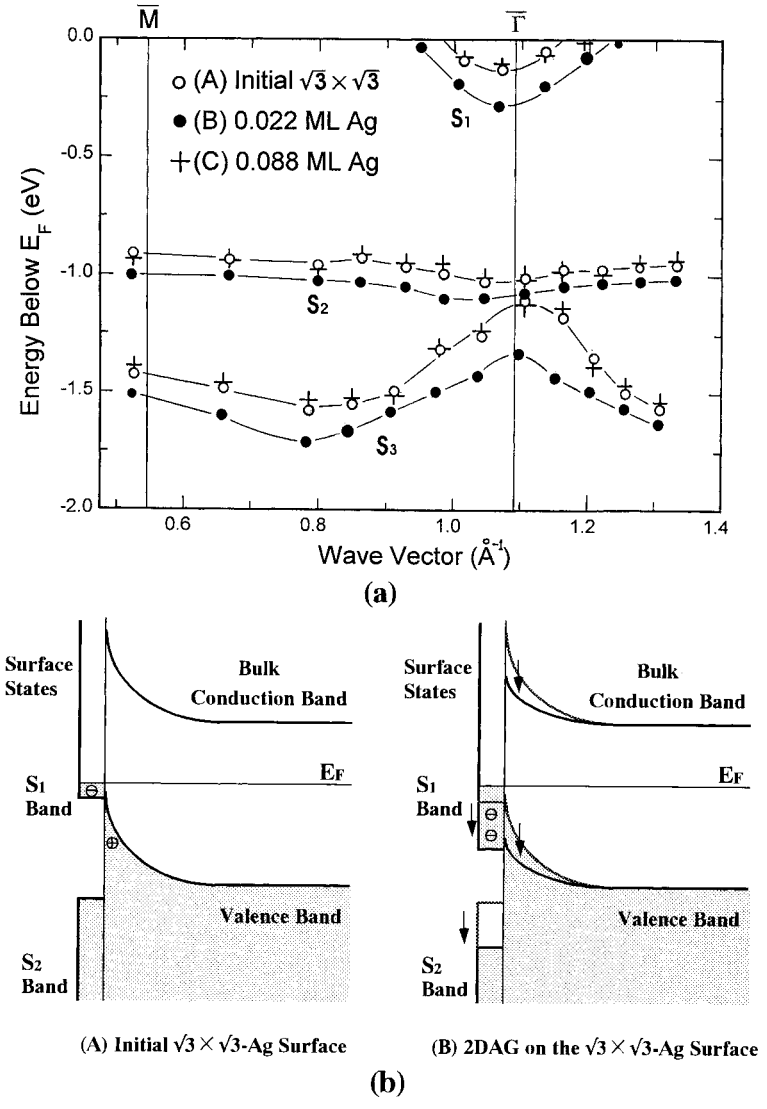

Fig. 48. (a) Two-dimensional band dispersion diagram of the S_1, S_2, and S_3 surface states for the three samples (A)–(C) (defined in Fig. 46) recorded in [01$\bar{1}$] direction, corresponding to the $\bar{\Gamma}$-$\bar{M}$-$\bar{\Gamma}$ direction in the $\sqrt{3} \times \sqrt{3}$-surface Brillouin zone (from Ref. [14]). This is constructed from the spectra in Fig. 47. Thin solid lines are only for eye guide. (b) Schematic illustrations of the surface states and the band bending in the surface space-charge layer at (A) the "fresh" $\sqrt{3} \times \sqrt{3}$-Ag surface, and (B) the same surface covered with 2DAG, respectively. These are obtained from the results of ARUPS and XPS in Figs. 46 and 47.

described in Section 2.1.1, the Fermi wavenumber k_F is approximately 0.1 $Å^{-1}$ at the surface (A), while it increases to be $k_F \approx 0.15$ $Å^{-1}$ at the surface (B) (measured in Fig. 48(a)), so that the Fermi disk becomes larger to increase the number of electrons contributing to conduction (see Eq. (10) in Section 2.1.1) [14]. Therefore, it can be said that Ag adatoms in the 2DAG phase act as donors to provide conduction electrons into the surface-state band S_1. (At the same time, the adatoms donate electrons into the surface space-charge layer, to diminish the excess holes therein, which makes the bulk bands towards flat beneath the surface, as shown in Fig. 48(b).) On the surface (C), the number of electrons in the S_1 band returns to a smaller value as on the surface (A), which brings the conductance down towards the initial lower value.

By estimating the total number of electrons transferred into the S_1 band and into the surface space-charge layer from the Ag adatoms in the 2DAG phase, and by comparing it with the density of the Ag adatoms, it is found that each Ag adatom donates approximately one electron, 97% of which go into the S_1 band and 3% into the surface space-charge layer. Moreover, by comparing the increments of the measured conductance $\Delta\sigma$ and the electron density Δn in the S_1 band, the mobility μ of the conduction electrons in the S_1 band is estimated by $\mu = \Delta\sigma/(e \cdot \Delta n)$ to be around 10 cm^2/V sec [14] (see Eq. (1) in Section 2.1.1). This value of mobility is similar to that on the $\sqrt{21} \times \sqrt{21}$-(Ag + Au) surface discussed in Section 5.1, but is much smaller than the mobility of the conduction electrons in bulk, 1500 cm^2/V sec. This may be because of severe carrier scattering by phonons, due to the two dimensionality of the surface-state band, and also by surface defects, such as atomic steps and domain boundaries as easily seen from the standing-wave pattern in Fig. 24.

Since Ag adatoms in the 2DAG phase act as donors, they are positively charged, which is consistent with the observations of electromigration [33]. As the results of XPS and ARUPS at the surface (C) return to almost the same ones at the surface (A), it can be said that the electron transfer from the adsorbates to the substrate or the donor action of Ag adatoms vanishes once they nucleate into 3D microcrystals, which follows from the fact that the valence electrons of the Ag atoms mainly work for metallic bonding inside the Ag microcrystals, once they are nucleated, whence the surface conductance returns towards the initial lower value. In this way, it experimentally confirmed that the 2D free-electron-like surface-state band S_1 on the $\sqrt{3} \times \sqrt{3}$ surface actually contributes the electrical conduction parallel to the surface.

4.3.4.5. At lower temperatures. At RT, as described so far, the Ag atoms additionally deposited on the Si(111)-$\sqrt{3} \times \sqrt{3}$-Ag surface remain in the 2DAG phase, when the density is below the critical value θ_C, and just nucleate into 3D Ag microcrystals when the density exceeds the θ_C; the surface is not wetted. However, at lower temperatures where the surface migration of Ag adatoms is suppressed, as discussed in Section 4.1.2, the additionally deposited Ag atoms make new superstructures on the $\sqrt{3} \times \sqrt{3}$-Ag substrate, $\sqrt{21} \times \sqrt{21}$ and 6×6. Accordingly,

the changes in surface conductance during the Ag adsorptions are quite different from the cases at RT.

Fig. 49 shows the changes in (a) resistance R (normalized with initial resistance R_0) and (b) the conductance converted from the resistance (a), measured during Ag deposition onto the $\sqrt{3} \times \sqrt{3}$-Ag surface at temperatures lower than RT [10]. We used a *p*-type Si wafer that had $8 \sim 20$ Ω·cm resistivity at RT. At RT, the resistance changes in a similar way as in Fig. 38(b) with an *n*-type Si wafer; steep drop with less than 0.1 ML coverage, a small overshoot, followed by a gradual decrease with further deposition, and a steep increase by stopping the deposition, without any changes in surface superstructures. At lower temperatures, the initial drop tends to be smaller. As described in Section 4.1.2, below 250 K, the $\sqrt{21} \times \sqrt{21}$ superstructure appears around 0.15 ML coverage of additional Ag. When the substrate is cooled, the surface migration of the deposited Ag adatoms is

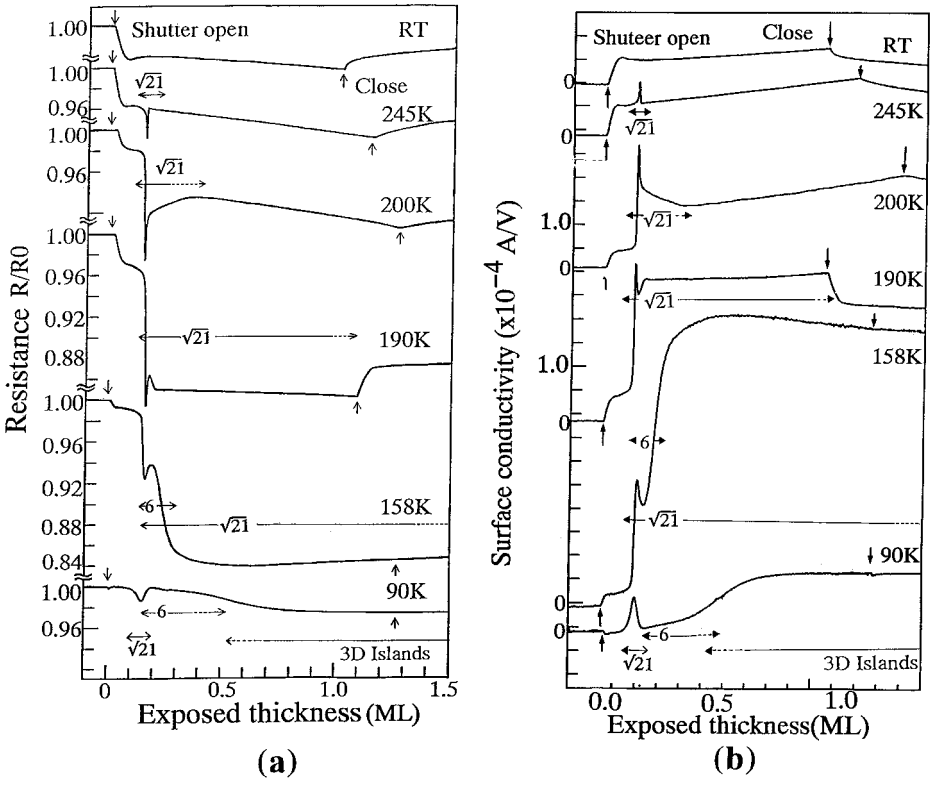

Fig. 49. (a) Changes in (a) resistance and (b) conductance of the Si wafer during Ag depositions with a rate of 0.66 ML/min onto the Si(111)-$\sqrt{3} \times \sqrt{3}$-Ag surface kept at the respective substrate temperatures below RT. (b) The resistance changes are converted into the conductance changes. The structural changes observed by RHEED in separate runs of depositions under the same conditions are also indicated. The $\sqrt{3} \times \sqrt{3}$-superspots are always seen in the ranges of Ag coverage and temperature shown here. From Ref. [10].

suppressed and fixed on particular sites on the surface. In other words, the 2DAG phase observed at RT is *frozen*, resulting in a periodic arrangement of the adatoms making up the $\sqrt{21} \times \sqrt{21}$ superstructure. When the substrate is heated above 250 K, this $\sqrt{21} \times \sqrt{21}$-structure is destroyed, so that it reverts to the initial $\sqrt{3} \times \sqrt{3}$-Ag structure with 3D Ag microcrystals on it; the frozen adatoms are thermally activated to nucleate into 3D nuclei, thus most of the surface reverts to the initial $\sqrt{3} \times \sqrt{3}$-Ag phase. After the initial steep drop, the resistance slowly decreases with gaining spot intensity of the $\sqrt{21} \times \sqrt{21}$ structure, which corresponds to a stage of the $\sqrt{21} \times \sqrt{21}$-domain growth. Coincident with the maximum intensity of the $\sqrt{21} \times \sqrt{21}$ spots around 0.15 ML coverage, the resistance suddenly drops, which corresponds to an electrical connection of the growing $\sqrt{21} \times \sqrt{21}$ domains. The amount of the resistance drop at this coverage increased with cooling from 250 to 180 K, up to about 20%, but decreased with further cooling. Thus, the areal fraction of the $\sqrt{21} \times \sqrt{21}$ domains around 0.15 ML attains its maximum around 180 K. After 0.15 ML at 245 K, the resistance instantly returns, corresponding to the immediate disappearance of the $\sqrt{21} \times \sqrt{21}$ structure. At 200 K, the rise in resistance beyond 0.15 ML coverage becomes slow, which corresponds to the process of the gradual disappearance of the $\sqrt{21} \times \sqrt{21}$ structure. At 190 K, the resistance remains almost unchanged beyond 0.15 ML, because the $\sqrt{21} \times \sqrt{21}$ structure continues to exist throughout the deposition. But after the evaporator shutter is closed, the resistance rises with disappearance of the $\sqrt{21} \times \sqrt{21}$ phase. This phenomenon is not observed below 160 K, where the $\sqrt{21} \times \sqrt{21}$ phase remains, even after the deposition ends. At 158 K, the resistance reaches a small temporal maximum around 0.18 ML, in the course of the drop. This process corresponds to the structural transition that the 6 $\times$ 6 phase temporarily emerges around 0.18 ML with a mixture of the $\sqrt{21} \times \sqrt{21}$ phase. At 90 K, while the resistance shows a small dip around 0.15 ML, corresponding to the short-lived $\sqrt{21} \times \sqrt{21}$ phase, no significant drop in resistance is observed with appearance of the single-phase 6×6 structure. From these series of measurements, we can say that only the $\sqrt{21} \times \sqrt{21}$ phase is highly conductive.

4.3.4.6. Interrupting the deposition. Fig. 50 shows the resistance changes during the sequence of Ag deposition and its interruption at RT (a), 180 K (b), and 140 K (c), respectively. With opening and closing the evaporator shutter, the steep drops and rises in resistance are repeatedly observed in (a) and (b). These are the same as in Fig. 45. However, in (b) these changes precisely correspond to the appearance and disappearance of the $\sqrt{21} \times \sqrt{21}$ superstructure. While no structural changes are observed at RT (a), as described in Fig. 45, the change in resistance corresponds to the process of surface diffusion and nucleation of Ag adatoms; the adatom density in 2DAG phase on the surface decreases by being incorporated into 3D Ag microcrystals during the interruption periods, which has been fully discussed above. But at 180 K (b), such 2DAG makes the $\sqrt{21} \times \sqrt{21}$ superstructure only during deposition, while these adatoms nucleate into 3D microcrystals, again, by interrupting the deposition, resulting in the disappearance of the $\sqrt{21} \times \sqrt{21}$ structure. At 140 K in Fig. 50(c), however, the resistance does not rise by

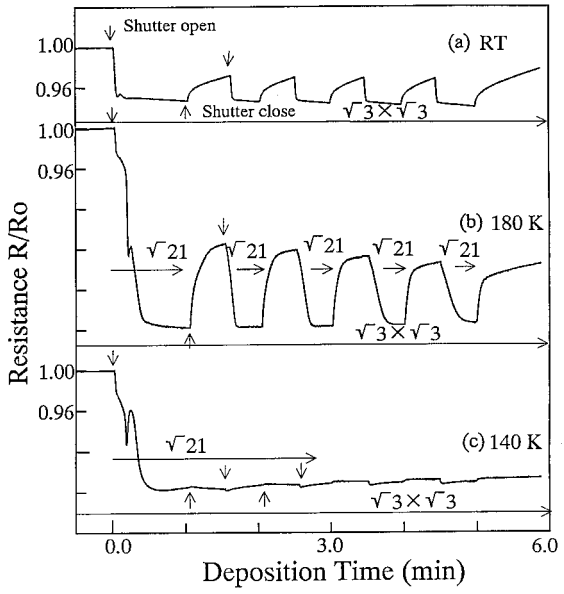

Fig. 50. Changes in resistance of the Si wafer in the sequence of the Ag deposition with a rate of 0.66 ML/min onto the Si(111)-$\sqrt{3} \times \sqrt{3}$-Ag surface and its interruption at (a) RT, (b) 180 K, and (c) 140 K, respectively. The structural changes are also indicated. The $\sqrt{3} \times \sqrt{3}$-superspots are always seen at all temperatures throughout the measurements. From Ref. [10].

stopping the deposition, because the $\sqrt{21} \times \sqrt{21}$ superstructure remains, even during the interruption periods. This is because the surface diffusion of the Ag adatoms is sufficiently suppressed at 140 K, so that the adatoms can not escape from the $\sqrt{21} \times \sqrt{21}$ superstructure by thermal activation, during the interruption periods, once incorporated in the superstructure. From these observations, it can be said, again, that the $\sqrt{21} \times \sqrt{21}$ phase is highly conductive.

4.3.4.7. Structural stability. The $\sqrt{21} \times \sqrt{21}$ and 6×6 phases appear only at low temperatures, which means that these reconstructions do not involve the destruction of the $\sqrt{3} \times \sqrt{3}$ framework of the substrate, as discussed in Section 4.1.2, but are induced by the periodic arrangements of additional Ag adatoms on top of the $\sqrt{3} \times \sqrt{3}$-Ag substrate, as shown in the structural model of Fig. 30(b). The adatoms migrate on the surface with such high mobility at RT that they can not form superstructures. Even at 180 K, as shown in Fig. 50(b), the migration is not completely suppressed, so that the $\sqrt{21} \times \sqrt{21}$ phase can exist only during deposition. The $\sqrt{21} \times \sqrt{21}$ domains at this temperature are formed by the balance of competing processes between the incorporation of Ag adatoms into the $\sqrt{21} \times \sqrt{21}$ domains and their escape from them to nucleate into 3D islands. By switching the deposition off, only the nucleation process proceeds to diminish the $\sqrt{21} \times \sqrt{21}$ domains, resulting in the resistance rise. When the deposition is started again, the $\sqrt{21} \times \sqrt{21}$ domains begin to grow again on top of the almost bare $\sqrt{3} \times \sqrt{3}$-Ag

framework. Since the surface migration is suppressed enough below 160 K, Ag adatoms constituting the $\sqrt{21} \times \sqrt{21}$ structure scarcely escape. So the $\sqrt{21} \times \sqrt{21}$ diffraction spots remain unchanged even when the deposition ends (Fig. 50(c)). By further lowering the temperature, the diffusion length of the Ag adatoms on top of the $\sqrt{21} \times \sqrt{21}$ domains also becomes short enough to form the 6×6 structure in turns. At 100 K, the diffusion is sufficiently suppressed for the 6×6 domains to grow until the $\sqrt{21} \times \sqrt{21}$ domains are completely converted into the 6×6 structure (Fig. 27(f)). The structural stability of the $\sqrt{21} \times \sqrt{21}$-Ag and 6×6-Ag phases, thus depends on the surface diffusion of Ag adatoms, which is determined by the substrate temperature.

When the 6×6 domains are formed, the electronic band structure totally changes from that of the $\sqrt{21} \times \sqrt{21}$ phase, leading to the resistance increase, as shown by the curves at 90 K and 158 K in Fig. 49. When the 6×6 domains disappear to recover the $\sqrt{21} \times \sqrt{21}$ structure, the resistance again drops (at 158 K in Fig. 49(a)). The mechanism of the extremely high electrical conductance of the $\sqrt{21} \times \sqrt{21}$ structure is not clear at the moment, because photoemission spectroscopy data at low temperatures are not available. But, as described in Section 5, a similar $\sqrt{21} \times \sqrt{21}$ structures are known to appear by adsorptions of Au or Cu of the same amount (and also by alkali-metal adsorptions) on top of the $\sqrt{3} \times \sqrt{3}$-Ag surface at RT, which are found to be also highly conductive. Furthermore, by photoemission spectroscopies at RT, these $\sqrt{21} \times \sqrt{21}$ phases induced by Au or Cu adsorptions are found to have metallic surface-state bands crossing E_F, while the surface space-charge layers tend to be depleted. So the metallic surface-state bands are expected to largely contribute to the high surface conductance. Since the $\sqrt{21} \times \sqrt{21}$-Ag structure formed at low temperatures is very similar to the $\sqrt{21} \times \sqrt{21}$-(Ag + Au) structure at RT, as observed by a temperature-variable STM [17], it is most probable that the same mechanism works for the high surface conductance of the $\sqrt{21} \times \sqrt{21}$-Ag superstructure at low temperatures as those for the $\sqrt{21} \times \sqrt{21}$-(Ag + Au), -(Ag + Cu) phases at RT.

4.4. Summary

The results present here thus confirm that the superstructures formed only in one or two of the topmost atomic layers on the surface cause the inherent changes in the electrical conduction of a silicon crystal. The 7×7 surface resists Ag adsorptions below a few ML coverage, showing no significant changes in structure and electrical conductance, while the $\sqrt{3} \times \sqrt{3}$-Ag surface is markedly affected by additional metal adsorptions of much less than 1ML coverage. This is because the dimer-stacking-fault framework in the 7×7 reconstruction is much more persistent, and also because of the differences in the surface electronic structures and the band-bendings beneath the surfaces. Especially on the $\sqrt{3} \times \sqrt{3}$-Ag surface, because the surface-state band has a 2D-free electron-like character, it plays the main role in surface electrical conduction. We have given, as evidence of electrical conduction through the surface-state band, the phenomenon of carrier doping into the surface-state band. Furthermore, the resistance measurements

during Ag adsorptions demonstrate that such measurements can be used for true in-situ and real-time monitoring of dynamical restructuring during growths on surfaces; the information on adatom-gas phase, nucleation, surface diffusion, and so on, is obtained from the resistance changes. Interpretations of the results, that is, the distinction among the contributions from the surface space-charge layer, the surface-state band, and the grown film, of course, need other complementary experiments, such as photoemission spectroscopies and electron microscopies.

5. Monovalent-atom adsorptions on Si(111)-$\sqrt{3} \times \sqrt{3}$-Ag surface

As described in Section 4, the Si(111)-$\sqrt{3} \times \sqrt{3}$-Ag surface is drastically affected by adsorptions of small amounts of additional Ag atoms; new superstructures, $\sqrt{21} \times \sqrt{21}$ and 6×6, are induced and significant changes in surface electrical conductance are observed. The 2DAG phase on top of the $\sqrt{3} \times \sqrt{3}$-Ag surface also raises the conductance increase, due to carrier doping into the surface-state band of the substrate. Such phenomena are commonly observed with monovalent-atom adsorptions, noble metals and alkali metals. In this section, we focus our attention on this interesting surface, $\sqrt{3} \times \sqrt{3}$-Ag, where surface structures and surface electronic transport are considerably affected by adsorptions of small amounts of monovalent atoms.

5.1. Noble-metal adsorptions

5.1.1. Au adsorption

5.1.1.1. $\sqrt{21} \times \sqrt{21}$ superstructure. Fig. 51 shows the RHEED patterns successively taken during Au deposition onto the $\sqrt{3} \times \sqrt{3}$-Ag surface at RT. The pattern begins to change from the initial $\sqrt{3} \times \sqrt{3}$-Ag structure (Fig. 51(a)) to a $\sqrt{21} \times \sqrt{21}$-(Ag + Au) structure from about 0.04 ML Au coverage, and the $\sqrt{21} \times \sqrt{21}$-superspots gain the maximum intensity around 0.15 ML deposition (Fig. 51(b)). On increasing Au coverage further, the pattern returns to a $\sqrt{3} \times \sqrt{3}$ structure around 0.28 ML (Fig. 51(c)). The intensity ratios among the superspots in this $\sqrt{3} \times \sqrt{3}$ phase, however, are different from those in the initial $\sqrt{3} \times \sqrt{3}$-Ag structure (Fig. 51(a)); the (1/3, 1/3) superspots are stronger than the (2/3, 2/3) spots, while the initial $\sqrt{3} \times \sqrt{3}$-Ag pattern has the opposite relative intensity, which means there is a different atomic arrangement in their unit cells in spite of the same periodicity. With more depositions beyond about 0.65 ML, streaks and halos emerge in the $\sqrt{3} \times \sqrt{3}$-(Ag + Au) pattern. Finally, this pattern disappears around 1.2 ML Au deposition, leaving no diffraction spots.

An STM image, showing a domain of the $\sqrt{21} \times \sqrt{21}$-(Ag + Au) structure formed on the Si(111)-$\sqrt{3} \times \sqrt{3}$-Ag surface by RT-deposition of Au, is shown in Fig. 52. The $\sqrt{21} \times \sqrt{21}$ domain nucleates on a terrace, and its domain boundary always fluctuates even at RT. Outside the $\sqrt{21} \times \sqrt{21}$ domain, some mobile atoms are observed as line noise, as indicated by an arrow head on the $\sqrt{3} \times \sqrt{3}$

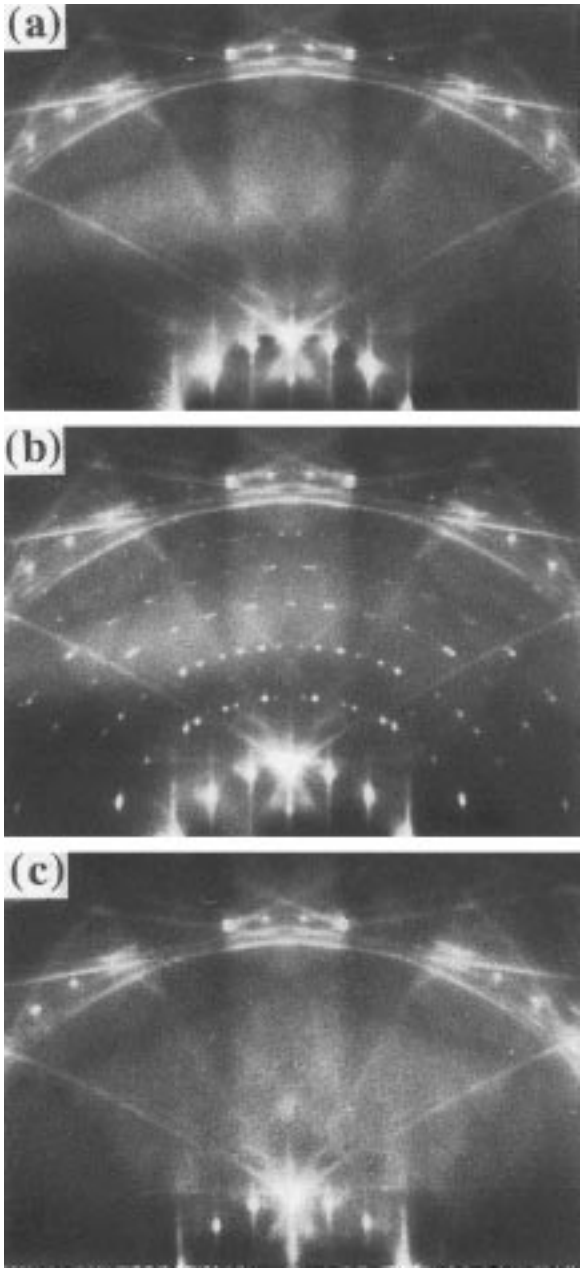

Fig. 51. RHEED patterns taken during Au deposition onto the Si(111)-$\sqrt{3} \times \sqrt{3}$-Ag surface at RT with the electron beam in [$2\overline{11}$] incidence. (a) The initial $\sqrt{3} \times \sqrt{3}$-Ag surface before Au deposition; (b) the $\sqrt{21} \times \sqrt{21}$ surface induced by Au adsorption of about 0.15 ML; and (c) the other $\sqrt{3} \times \sqrt{3}$ surface after 0.5 ML Au deposition. From Ref. [11].

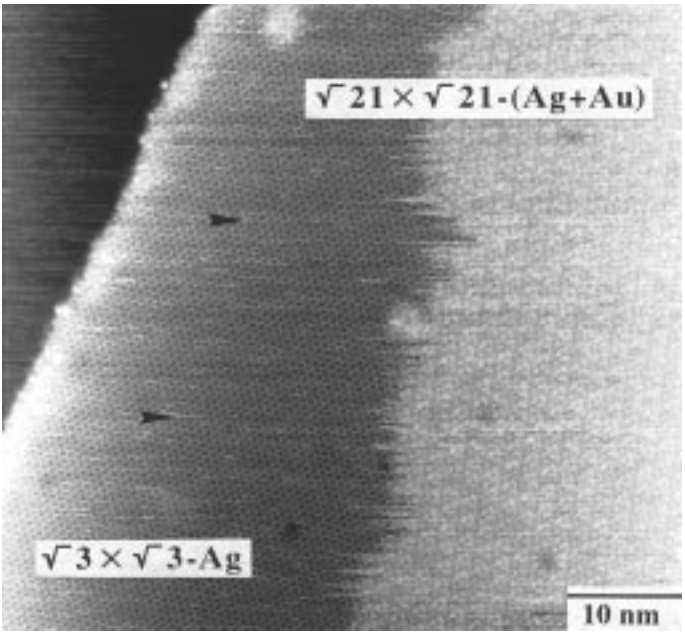

Fig. 52. An STM image of the Si(111)-$\sqrt{3} \times \sqrt{3}$-Ag surface partially covered with the $\sqrt{21} \times \sqrt{21}$-(Ag + Au) superstructure. By courtesy of Mr I. Shiraki.

substrate. With the saturation coverage of Au, the surface is almost wholly covered by this $\sqrt{21} \times \sqrt{21}$-(Ag + Au) phase.

The $\sqrt{21} \times \sqrt{21}$-(Ag + Au) surface superstructure has already been reported to be induced by Au adsorption of submonolayer on the $\sqrt{3} \times \sqrt{3}$-Ag surface at RT [90,91]. Figs. 53(b) and (c) shows the STM images of the $\sqrt{21} \times \sqrt{21}$-(Ag + Au) structure at RT, taken from the literature [90,91], together with the image (a) of the $\sqrt{21} \times \sqrt{21}$-Ag, for comparison, induced by additional Ag adsorption, instead of Au, only at lower temperatures, as described in Section 4.1.2 [17]. The right panels in the figure present models of the atomic arrangement proposed by the respective authors. In the Nogami et al. model of Fig. 53(b), the $\sqrt{21} \times \sqrt{21}$ unit cell contains five Au adatoms sitting at the centers of Ag triangles, while in the Ichimiya et al. model of Fig. 53(c), the unit cell contains three Au adatoms sitting at the centers of Si trimers. These models are different from the model of the low-temperature $\sqrt{21} \times \sqrt{21}$ phase shown in Fig. 53(a), where the unit cell contains four Ag adatoms sitting at the centers of Ag triangles (which is identical to the model shown of Fig. 30 in Section 4.1.2). However, by comparing the respective STM images, they look quite similar to each other, as shown in the left panels of Fig. 53; there are triangular-like protrusions around corner holes of the unit cell, and a prominent protrusion only in the center of one of the half unit-cell triangles. Nogami et al. assumed that the five protrusions observed in the $\sqrt{21} \times \sqrt{21}$ unit cell (though one of them is much weaker than the other four) directly

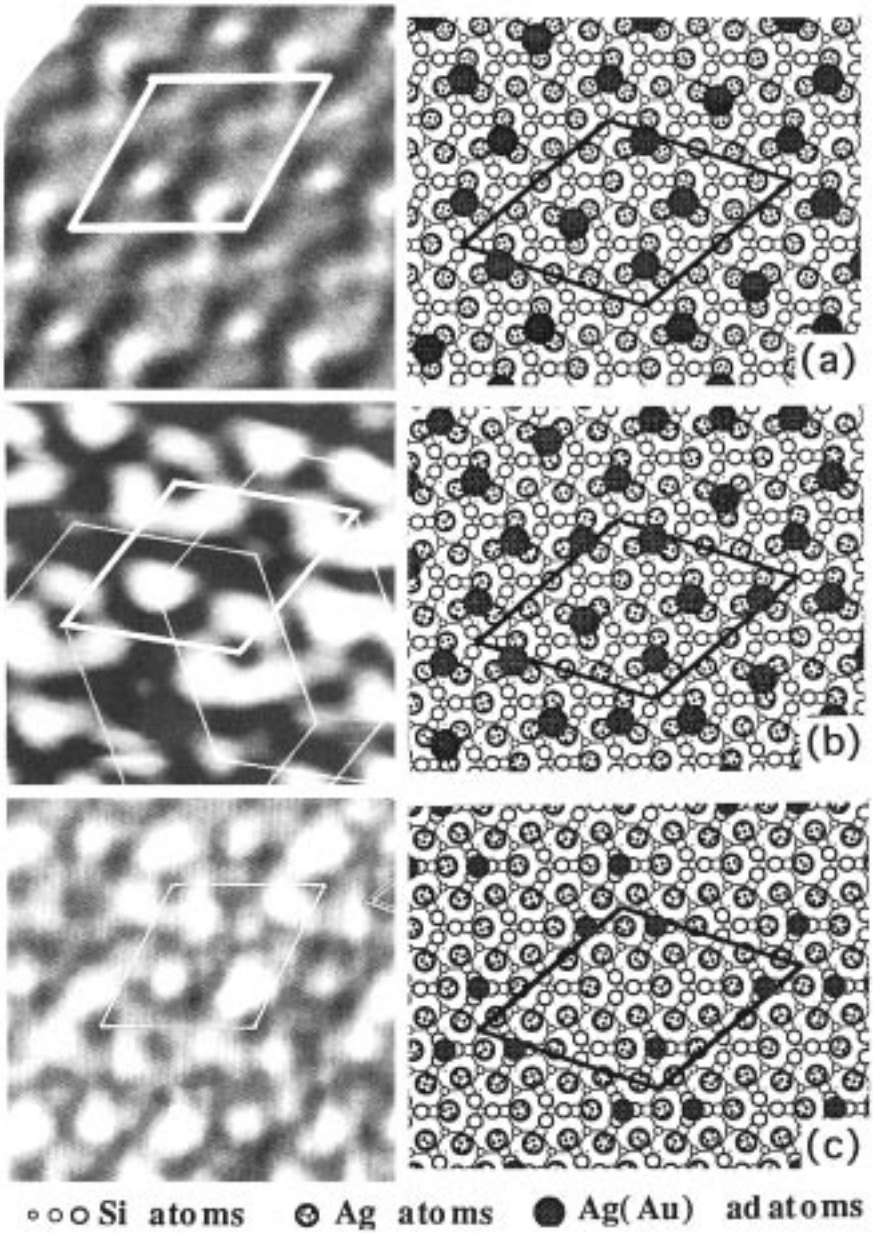

Fig. 53. Comparison of STM images between Ag-induced and Au-induced $\sqrt{21} \times \sqrt{21}$ superstructures. Right panels show the proposed model by the respective authors. (a) Our STM image and model for the Ag-induced $\sqrt{21} \times \sqrt{21}$ phase. (b) Those of Nogami et al. [91] for the Au-induced $\sqrt{21} \times \sqrt{21}$ phase. (c) Those of Ichimiya et al. [90] for the Au-induced $\sqrt{21} \times \sqrt{21}$ phase.

correspond to the adatoms, based on their dual-polarity STM images and the saturation coverage of 5/21 = 0.24 ML. On the other hand, Ichimiya et al. assumed three adatoms in the unit cells, because of its saturation coverage of 3/21 = 0.15 ML. Four protrusions in the unit cell in the images were attributed to some effects of the electronic structures, not directly to the adatoms, by considering the results of rocking-curve measurements in RHEED. Our model for the low-temperature $\sqrt{21} \times \sqrt{21}$-Ag phase is, however, derived by assuming the saturation coverage of 4/21 = 0.19 ML and the four protrusions in the images to be adatoms. This model is derived by analyzing the 2D nuclei at a precursory stage during formation of the $\sqrt{21} \times \sqrt{21}$-Ag structure and the structure at the out-of-phase domain boundaries [17]. Ichimiya et al. measured the RHEED rocking curves for both of the Au- and Ag-induced $\sqrt{21} \times \sqrt{21}$ structures [118]. Since the both curves had similar profiles, it was concluded that Ag adatoms occupied the same sites as the Au adatoms did, which supports an expectation that the atomic arrangement in the Ag-induced and Au-induced $\sqrt{21} \times \sqrt{21}$ superstructures are the same.

5.1.1.2. Electrical conduction. Fig. 54(a) shows the change in resistance of a Si wafer (*p*-type with a resistivity of 20 Ωcm) during Au deposition onto the Si(111)-$\sqrt{3} \times \sqrt{3}$-Ag surface at RT [11]. When the evaporator shutter is opened, the resistance decreases steeply to ~0.15 ML coverage, and then turns to rise at 0.15–0.5 ML coverage. Beyond 0.5 ML, it begins to decrease slowly again, until the deposition is stopped. The initial resistance drop corresponds precisely to the emergence of the $\sqrt{21} \times \sqrt{21}$-(Ag + Au) superstructure. The following rise in resistance corresponds to the disappearance of the $\sqrt{21} \times \sqrt{21}$-phase, leading to the conversion into the $\sqrt{3} \times \sqrt{3}$-(Ag + Au) phase (Fig. 51(c)). The final stage of gradual decrease in resistance corresponds to a degradation of the $\sqrt{3} \times \sqrt{3}$-(Ag + Au) structure.

Fig. 54(b) shows the conductance change $\Delta\sigma$, which is calculated from the resistance data in (a) using (51); $\Delta\sigma = (1/R\text{-}1/R_0)(L/W)$, where R is the resistance at each Au coverage, R_0 is the resistance of the initial $\sqrt{3} \times \sqrt{3}$-Ag surface before Au deposition, L and W are the length and width of the measured area on the Si wafer, 10.2 and 4.0 mm, respectively. From the maximum $\Delta\sigma$ around 0.15 ML Au coverage in Fig. 54(b), the surface conductance $\sigma_{\sqrt{21}\times\sqrt{21}}$ of the $\sqrt{21} \times \sqrt{21}$-(Ag + Au) phase is greater than that of the initial $\sqrt{3} \times \sqrt{3}$-Ag surface $\sigma_{\sqrt{3}\times\sqrt{3}}$ by 2.0×10^{-4} S/□. As described in Section 4.3.1, it is determined that $\sigma_{\sqrt{3}\times\sqrt{3}}$ is greater than the surface conductance of the clean 7×7 phase $\sigma_{7\times7}$ by 1.2×10^{-4} S/□. Then, combining with the result in Fig. 54(b), $\sigma_{\sqrt{21}\times\sqrt{21}}$ is greater than $\sigma_{7\times7}$ by 3.2×10^{-4} S. Does this excess conductance of the $\sqrt{21} \times \sqrt{21}$-(Ag + Au) phase come from $\Delta\sigma_{SC}$ or $\Delta\sigma_{SS}$? ($\Delta\sigma_{AL}$ does not work in this case, because additional Au coverage, less than 0.2 ML, is less than the critical coverage $\theta_C = 0.5$ ML for percolation on a triangular lattice.)

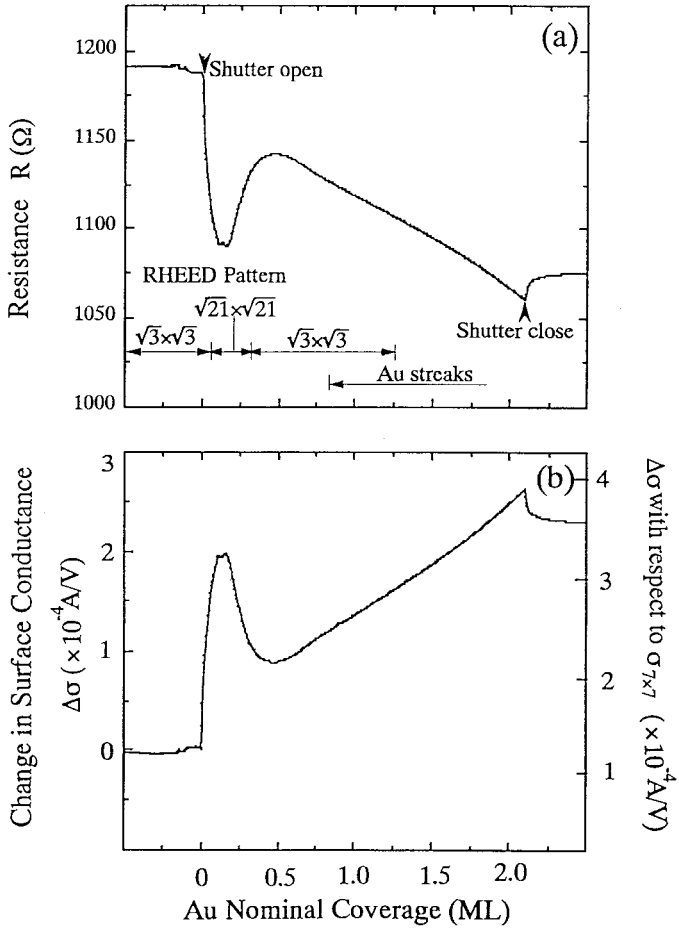

Fig. 54. (a) The change in resistance of the Si wafer during Au deposition onto the Si(111)-$\sqrt{3}\times\sqrt{3}$-Ag surface at RT with a deposition rate of 0.14 ML/min. (b) The change in electrical conductance during this deposition. This is calculated using the data of the resistance change shown in (a). The left-hand ordinate shows the conductance increase from the initial $\sqrt{3}\times\sqrt{3}$-Ag surface, while the right-hand ordinate indicates the conductance increase with respect to the clean 7×7 surface. From Ref. [11].

5.1.1.3. Band bending. When the Au deposition was interrupted at any time during the course of the resistance measurement, as in Fig. 54(a), no significant changes in the resistance or the RHEED pattern were observed during these interruption periods. We then measured the Si 2*p* core-level shifts by XPS and the valence-band states near E_F by ARUPS, during these interruption periods, as a function of Au coverage. As shown in Fig. 55, the Si 2*p* core-level was found to shift to larger binding energies compared to that at the initial $\sqrt{3}\times\sqrt{3}$-Ag surface for Au depositions up to around 0.1 ML, where the $\sqrt{21}\times\sqrt{21}$-(Ag + Au) phase appears. The peak then slightly shifts back to smaller binding energies with further Au de-

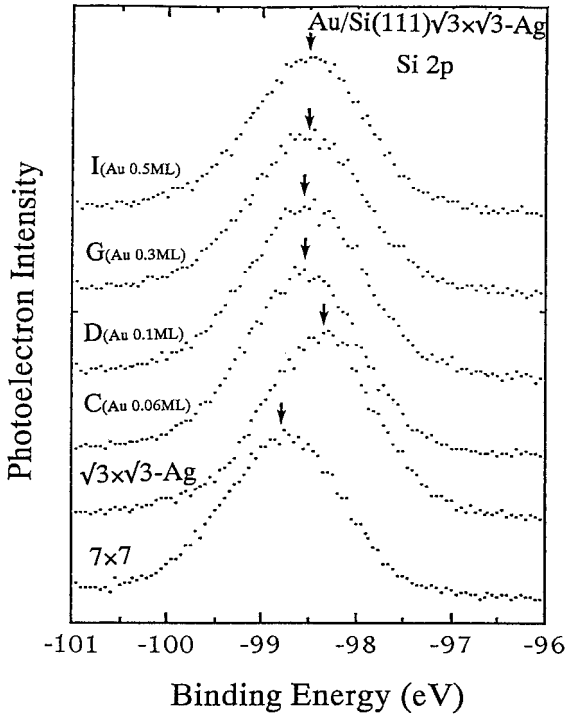

Fig. 55. XPS spectra from Si 2*p* core level of a Si(111) surface with different Au coverages on the $\sqrt{3} \times \sqrt{3}$-Ag structure, together with the spectrum from the clean 7×7 surface for comparison. By courtesy of Dr C.-S. Jiang.

position. In order to confirm the negligible effect of the charging-up in photoemission spectroscopy, we made the measurements with different input power to the X-ray tube. Since, as described in Section 3.2.2, these shifts of the core level are caused by band-bendings in the Si substrate, the changes in surface E_F position can be determined as a function of additional Au coverage, as shown in Fig. 56(a). Here, we adopt the E_F position at the initial $\sqrt{3} \times \sqrt{3}$-Ag surface to be at 0.1 eV above E_{VBM}, which is determined by the difference in binding energy of the core level between that at the $\sqrt{3} \times \sqrt{3}$-Ag surface and that at the 7×7 surface, as shown in Fig. 55. This surface E_F position means that the surface space-charge layer is a hole-accumulation one beneath the initial $\sqrt{3} \times \sqrt{3}$-Ag surface, as described in Fig. 5(d). According to Fig. 56(a), it can be said that the E_F shifts from this initial position towards the bulk E_F position with around 0.1 ML Au adsorption, leading to a conversion of the surface space-charge layer into the flat-band condition. This coverage corresponds to the emergence of the $\sqrt{21} \times \sqrt{21}$-(Ag + Au) phase. With further deposition beyond the saturation coverage of this phase, the E_F returns slightly towards E_{VBM}, but not enough to restore the hole-accumulation condition.

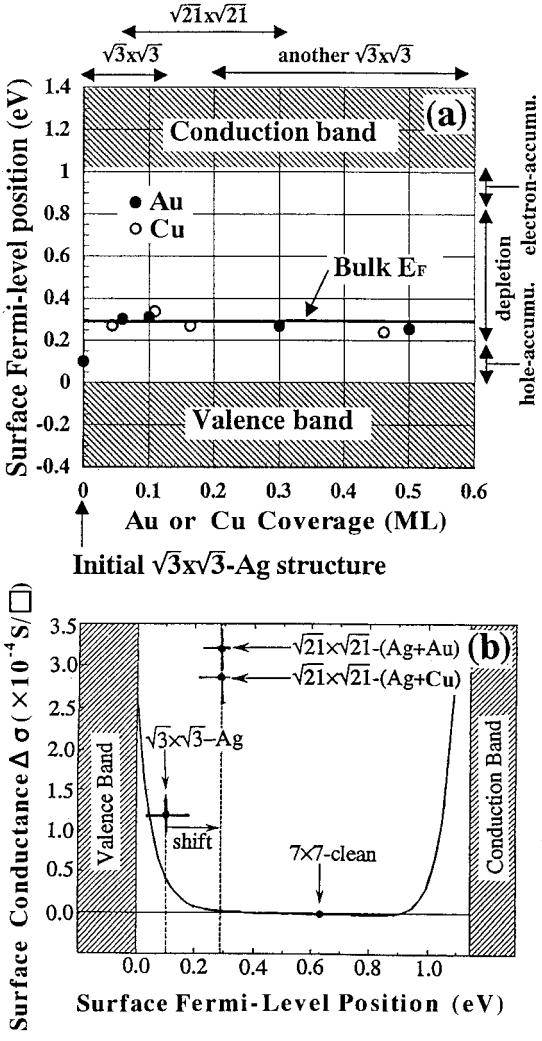

Fig. 56. (a) The shifts of the surface E_F position as a function of Au coverage (solid circles) determined from the peak shifts of Si 2*p* core-level in XPS during Au deposition onto the Si(111)-$\sqrt{3} \times \sqrt{3}$-Ag surface at RT as shown in Fig. 55. Open circles indicate the surface E_F positions during Cu deposition in a similar way, derived from the core-level emission spectra shown in Fig. 62. (b) The excess electrical conductance $\Delta\sigma_{SC}$ through the surface space-charge layer as a function of the surface E_F position, which was calculated using Eq. (34) with the values of the carrier mobilities in the bulk. The electrical conductance under the flat-band condition was defined as the reference. The measured increases in conductance at the $\sqrt{3} \times \sqrt{3}$-Ag surface (see Section 4.3.1 and Fig. 36) and $\sqrt{21} \times \sqrt{21}$ surfaces compared with the clean 7×7 surface (see Fig. 54(b)) are also plotted at the respective surface E_F positions determined in (a).

According to the resistivity of the wafer, the E_F position in the bulk can be estimated to be 0.29 eV above E_{VBM}. Then, if the E_F position at the surface is given, the electric field (band bending), the excess carrier concentration, and the resulting excess conductance $\Delta\sigma_{SC}$ in the surface space-charge layer can be calculated by Eq. (34) in Section 2.2.1. Fig. 56(b) shows the calculated excess surface conductance $\Delta\sigma_{SC}$ through the space-charge layer as a function of the surface E_F position. By tracing the observed shifts of the surface E_F position shown in Fig. 56(a) on this graph, from 0.1 to 0.3 eV above E_{VBM}, it is found that the surface space-charge layer is converted from a hole-accumulation condition at the initial $\sqrt{3}\times\sqrt{3}$-Ag surface into a flat-band condition where the excess holes are depleted in accord with the structural transformation into the $\sqrt{21}\times\sqrt{21}$-(Ag + Au) phase. Then, the electrical conduction through the surface space-charge layer should be suppressed. On the contrary, the measured surface conductance was greatly enhanced by this structure transformation as shown in Fig. 54(b). The data point of the $\sqrt{21}\times\sqrt{21}$-(Ag + Au) phase in Fig. 56(b) is located significantly above the calculated $\Delta\sigma_{SC}$ curve, which means extra conductance in addition to $\Delta\sigma_{SC}$. Therefore, it can be said that $\Delta\sigma_{SC}$ does not play any role for the enhanced surface conduction. We have to include $\Delta\sigma_{SS}$, surface-state conductance.

5.1.1.4. Surface-state bands. Next we investigated the electronic structure near E_F of the $\sqrt{21}\times\sqrt{21}$-(Ag + Au) surface superstructure by ARUPS. In Fig. 57, the spectra in the emission-angle range $\theta_e = 25$–35° exhibit peaks near E_F, indicated by small arrowheads, which is called here S_1' surface state. This state is very similar to the S_1-state band of the initial $\sqrt{3}\times\sqrt{3}$-Ag surface (see Fig. 17(a)). Another surface-state band, inherent in the $\sqrt{21}\times\sqrt{21}$-(Ag + Au) superstructure, is shown by big arrowheads in the spectra of $\theta_e = 30$–40°, called here S^*_1 state, which is not observed at the initial $\sqrt{3}\times\sqrt{3}$-Ag surface. The 2D band-dispersion diagram of Fig. 58 is constructed from these spectra. The S^*_1 and S_1' bands are observed around $\bar{\Gamma}$ point as the initial S_1 band in Fig. 5(c), and all of them are highly upward-dispersive crossing the E_F. The bottom of the S^*_1 band is located as deep as 0.6 eV below E_F, which partially overlaps the projected bulk bands. The Fermi wavenumber k_F is given at a point where the band crosses the E_F. The k_F of the S^*_1 band is then approximately 0.2 Å^{-1}, while that of the S_1 band of the initial $\sqrt{3}\times\sqrt{3}$-Ag surface is about 0.1 Å^{-1} (see Fig. 5(c)). That is to say, the radius of the Fermi disk (not a Fermi sphere, because of two dimensionality) of the surface-state band approximately doubles, so that, according to Eq. (10) in Section 2.1.1, the number of electrons contributing to conduction is also roughly doubled. This increment in the electrons trapped in the surface states is provided by the adsorbed Au atoms, not by the bulk, because the surface space-charge layer is a depletion layer under the $\sqrt{21}\times\sqrt{21}$-(Ag + Au) structure, as shown in Fig. 56. A rough estimation shows that each Au adatoms donates approximately 0.5 electrons to the surface-state band [27]. The adsorbed Au atoms act as donors to provide the conduction electrons into the surface-state band, and also into the surface space-charge layer to diminish the excess holes accumulated therein. This donor-

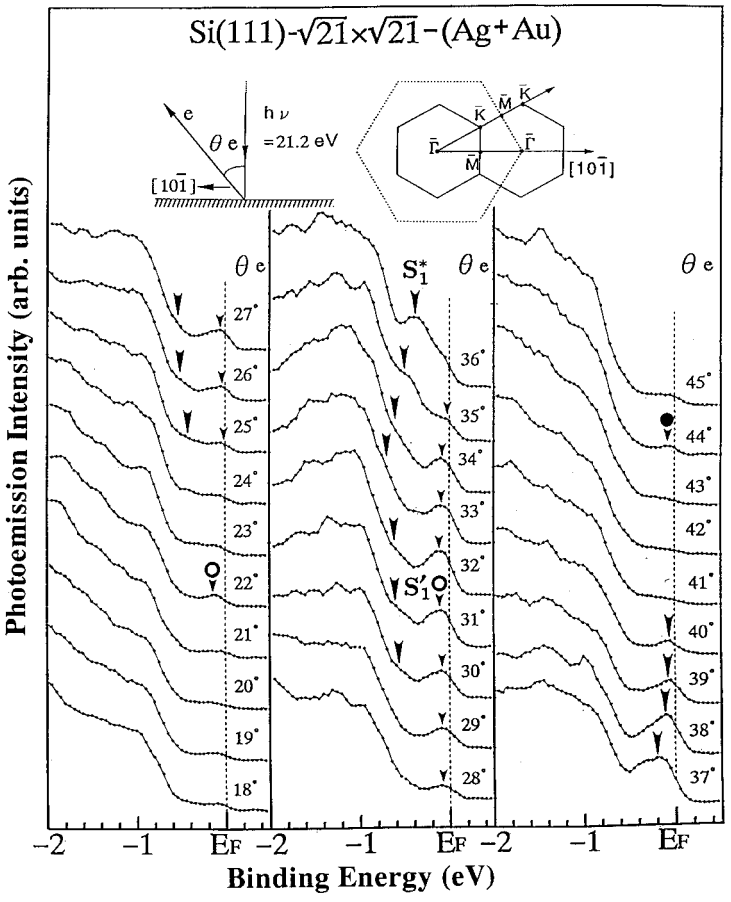

Fig. 57. Angle-resolved ultraviolet photoelectron spectra taken from the Si(111)-$\sqrt{21} \times \sqrt{21}$-(Ag + Au) surface. The electron analyzer was scanned in [10$\bar{1}$] direction, and the electron emission angles θ_e were measured from the surface-normal direction. The range of θ_e shown here correspond to around the $\bar{\Gamma}$ point in the second surface Brillouin zone. He I resonance light (21.2 eV) was used for excitation with irradiation in surface-normal. When the angle of incidence of the UV light was set off from the surface-normal, the peak intensities of the surface states indicated by arrowheads were strongly suppressed, and almost disappeared at 45° incidence. From Refs. [12,15].

type action is similar to the case of Ag atoms in the 2DAG phase on the $\sqrt{3} \times \sqrt{3}$-Ag surface at RT (see Section 4.3.4).

The results of photoemission spectroscopies are summarized as a schematic diagram in Fig. 59(b), showing the surface states and the band-bending at the $\sqrt{21} \times \sqrt{21}$-(Ag + Au) surface; the surface space-charge layer is a depletion layer, contrasting to a hole-accumulation layer beneath the initial $\sqrt{3} \times \sqrt{3}$-Ag surface (Fig. 59(a)), while much more electrons are trapped in the surface-state band, S^*_1.

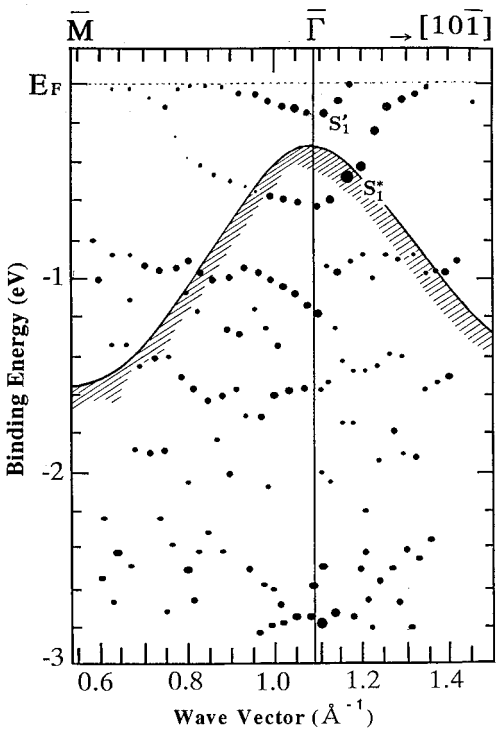

Fig. 58. 2D band-dispersion diagram for the Si(111)-$\sqrt{21} \times \sqrt{21}$-(Ag+Au) surface. $\bar{\Gamma}$ and $\bar{M}$ are symmetric points of the $\sqrt{3} \times \sqrt{3}$ surface Brillouin zone. The projected bulk band structures are also included. The $\sqrt{21} \times \sqrt{21}$ symmetry in S^*_1 and S'_1 surface states are confirmed by scanning in other directions. From Refs. [12,15].

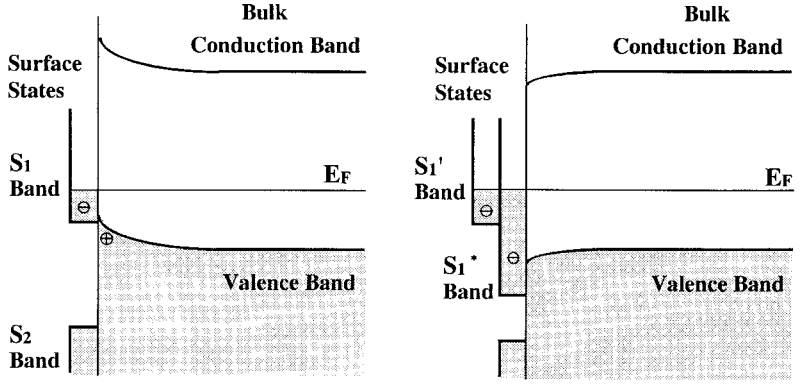

Fig. 59. Schematic illustrations of the surface states and the band bending in the surface space-charge layer at (a) the Si(111)-$\sqrt{3} \times \sqrt{3}$-Ag, and (b) the Si(111)-$\sqrt{3} \times \sqrt{3}$-(Ag+Au) surfaces, respectively. These are obtained from the results of ARUPS and XPS. From Ref. [15].

In this way, we have confirmed that the high electrical conductance of the $\sqrt{21} \times \sqrt{21}$-(Ag + Au) surface is due to the S^*_1-surface-state band [12,15,11]. This is the second example of the experimental confirmation of the electrical conduction through a surface-state band identified; another example was already described in Section 4.3.4, where the electrical conduction through the S_1-surface-state band on the $\sqrt{3} \times \sqrt{3}$-Ag surface was confirmed through a phenomenon of carrier doping into the band. Moreover, we can estimate the carrier mobility μ in the surface-state band from an equation $\Delta\sigma_{SS} = e \cdot \mu \cdot \Delta n$ (see Eq. (1) in Section 2.2.1), where $\Delta\sigma_{SS}$ is the surface-state conductance of the S^*_1 band, given as the observed conductance increase from that of the initial $\sqrt{3} \times \sqrt{3}$-Ag surface (see Fig. 54(a)), and Δn is the difference of the electron density in the surface states between the $\sqrt{21} \times \sqrt{21}$-(Ag + Au) and $\sqrt{3} \times \sqrt{3}$-Ag surfaces, estimated from the band-dispersion diagrams in Figs. 5(c) and 58. Since $\Delta\sigma_{SS} \approx 2 \times 10^{-4}$ S/□ and $\Delta n \approx 7 \times 10^{13}$ cm^{-2}, we obtain $\mu \approx 20$ cm^2/Vsec at RT, which is much smaller than the mobility of conduction electrons in bulk $\mu_{bulk} \approx 1500$ cm^2/Vsec. But this value is similar to that in the S_1 band on the $\sqrt{3} \times \sqrt{3}$-Ag surface (see Section 4.3.4). This may be due to carrier scatterings by surface irregularities and phonons; scattering by phonons, especially, will much more severely affect the mobilities than in bulk, because of the monolayer thickness of the 2D electron system of surface-state bands. Carrier scattering by surface defects are, of course, also severe as is clear from the electron standing waves in Fig. 24; the surface-state electrons are reflected by step edges and domain boundaries. But, in order to fully understand the transport property in the surface-state bands, we have to directly measure the mobilities by the Hall-effect or field-effect measurements to confirm this estimation.

5.1.1.5. Relation between atomic and electronic structures. We now ask, what is the origin of the S^*_1-state band of the $\sqrt{21} \times \sqrt{21}$-(Ag + Au) surface and how is it related to the atomic arrangement? As the atomic structure of the $\sqrt{21} \times \sqrt{21}$-(Ag + Au) is itself not yet solved, it is impossible to answer this question at present. Since, however, this superstructure is expected to consist of periodically arranged Au adatoms, without breaking the underlying $\sqrt{3} \times \sqrt{3}$-Ag framework [90,91] which may be one of the models in Fig. 53, we can make a guess at the answer. It is expected that the S^*_1 and S'_1 bands are originally the S_1 state of the $\sqrt{3} \times \sqrt{3}$-Ag surface, which is partially modulated by electron transfer from Au adatoms. Recalling that the local DOS of the S_1 state has maxima at the centers of Ag triangles of HCT structure (see Fig. 23(b)), it is guessed that some of the Ag triangles are strongly modulated by Au adsorption to become the S^*_1 state, while the remaining Ag triangles are not so influenced by Au adsorption to become the S'_1 state that is very similar to the initial S_1 state; the S'_1-state band can be said to be a remnant of the initial S_1 band, which is plausible by considering the Au coverage to be as small as 0.15 ML. But, of course, we have to await theoretical calculations of the electronic structure, based on a correct model of atomic arrangement, to answer the above question.

5.1.2. Cu adsorption

5.1.2.1. Structure changes. As already reported, Cu adsorption on the $\sqrt{3}\times\sqrt{3}$-Ag surface at RT also induces the $\sqrt{21}\times\sqrt{21}$ superstructure, too [92]. Fig. 60 shows the RHEED patterns during this Cu deposition. As in the case of Au adsorption, shown in Fig. 51, the $\sqrt{21}\times\sqrt{21}$ superstructure (b) appears when Cu of approximately 0.15 ML is adsorbed on the $\sqrt{3}\times\sqrt{3}$-Ag surface at RT. With further Cu deposition, the $\sqrt{21}\times\sqrt{21}$ superstructure converts into the other type of $\sqrt{3}\times\sqrt{3}$ structure (c), as in Fig. 51(c). In this way, the structural changes seem to be quite similar to the case of Au adsorption, described in the previous section, though the $\sqrt{21}\times\sqrt{21}$-superspots in the RHEED pattern of Fig. 60(b) are much weaker and broader than those in the Au-induced $\sqrt{21}\times\sqrt{21}$ pattern in Fig. 51(b).

5.1.2.2. Electrical conductance. Fig. 61 shows the changes in resistance of a Si wafer, during the Cu deposition onto the Si(111)-$\sqrt{3}\times\sqrt{3}$-Ag surface at RT with different deposition rates. These changes are again quite similar to the Au-adsorption case of Fig. 54(a); around 0.1–0.2 ML coverage, the resistance becomes a minimum, corresponding to the appearance of the $\sqrt{21}\times\sqrt{21}$ superstructure, followed by a resistance increase accompanying the disappearance of this structure on further deposition.

5.1.2.3. Band-bending. As shown in the Si 2*p* core-level emission spectra of Fig. 62, the peak follows quite similar shifts, during Cu adsorption, as in Au deposition (Fig. 55). From these measurements, the surface E_F position is determined as a function of Cu coverage as indicated by the open circles in Fig. 56(a). The E_F shifts in a similar way as in the Au case (solid circles). Therefore, the same argument as for Au adsorption is applicable; the band-bending indicates the suppression of the electrical conductance through the surface space-charge layer $\Delta\sigma_{SC}$ beneath the $\sqrt{21}\times\sqrt{21}$ superstructure, although this surface is measured to be highly conductive. Therefore, we have to include the surface-state conductance $\Delta\sigma_{SS}$, again. As shown in Fig. 56(b), the data point of the measured surface conductance for the $\sqrt{21}\times\sqrt{21}$ phase induced by Cu adsorption locates significantly above the calculated curve for $\Delta\sigma_{SC}$. This conclusion is not changed, even if one includes the experimental uncertainty in determining the surface E_F position by XPS.

5.1.2.4. Surface-state band. As expected, the ARUPS spectra taken from the Cu-induced $\sqrt{21}\times\sqrt{21}$ phase, Fig. 63, exhibit surface-state peaks very similar to those for the Au-induced superstructure in Fig. 57; the S^{*}_{1}- and $S^{'}_{1}$-surface-state peaks are observed in a similar way as in Fig. 57. Hence, we can conclude that all the phenomena induced by Cu adsorption on the Si(111)-$\sqrt{3}\times\sqrt{3}$-Ag surface at RT are the same as the Au adsorption case.

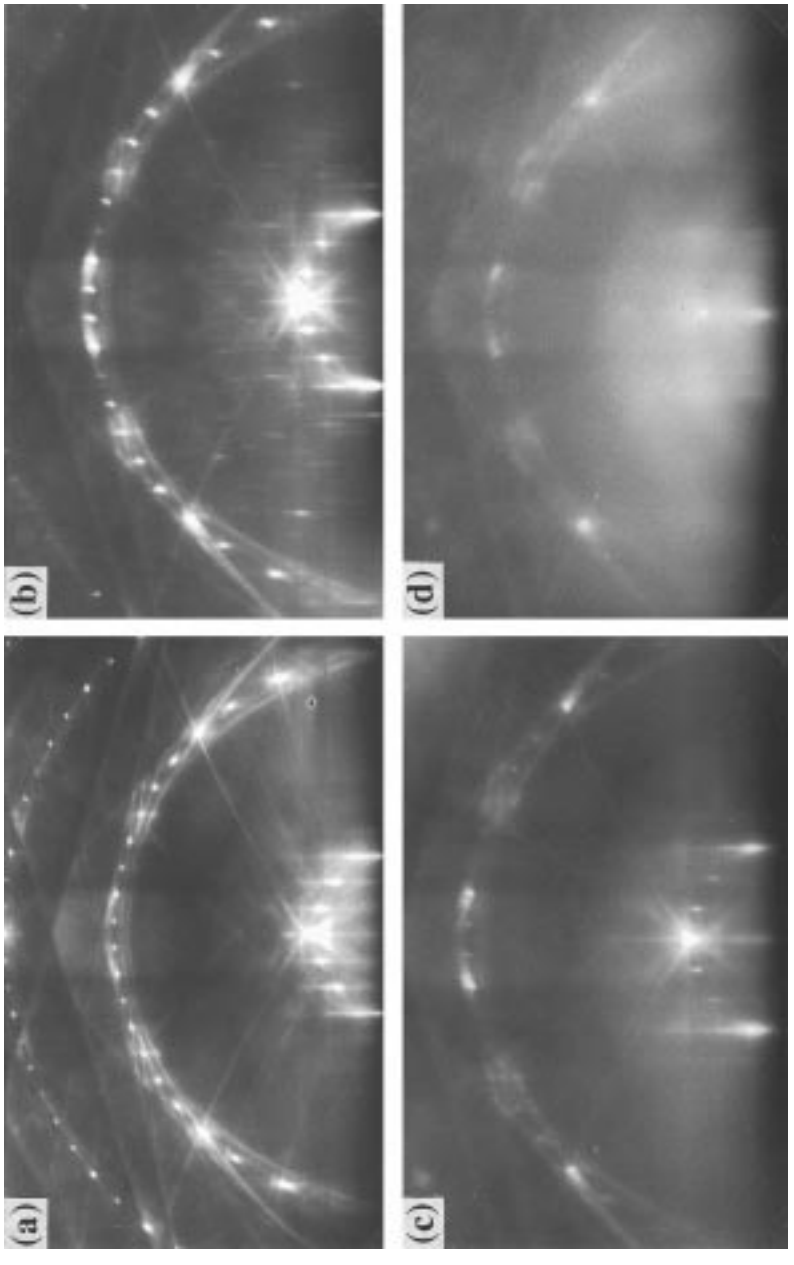

Fig. 60. RHEED patterns of (a) the initial $\sqrt{3}\times\sqrt{3}$-Ag surface, (b) the $\sqrt{21}\times\sqrt{21}$-(Ag+Cu) structure induced by Cu adsorption of about 0.12 ML on the $\sqrt{3}\times\sqrt{3}$-Ag surface at RT, (c) the $\sqrt{3}\times\sqrt{3}$-(Ag+Cu) structure induced by Cu adsorption of about 0.3 ML at RT, and (d) a surface with further adsorption of Cu up to about 1 ML.

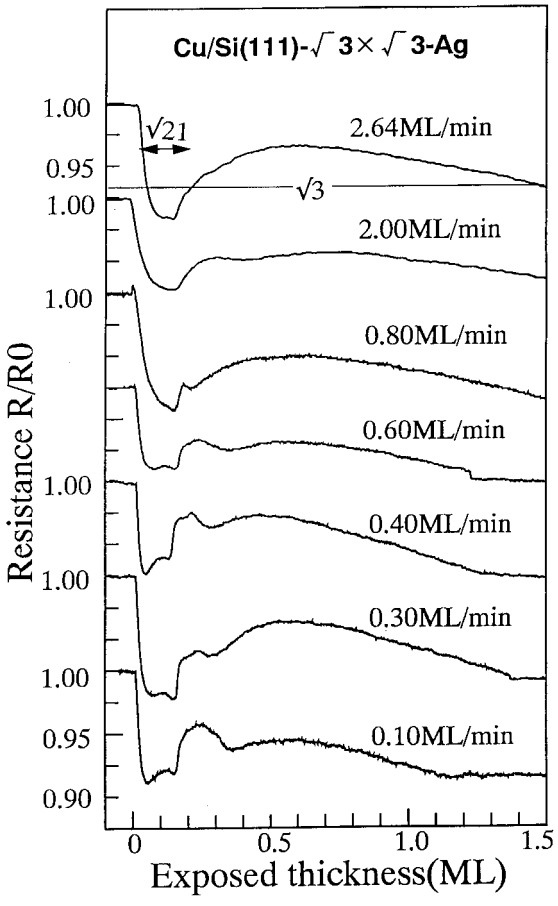

Fig. 61. The change in resistance of the Si wafer during Cu deposition onto the Si(111)-$\sqrt{3} \times \sqrt{3}$-Ag surface at RT with different deposition rates. The structural changes observed by RHEED in separate runs of deposition are also indicated. The $\sqrt{3} \times \sqrt{3}$ superspots were always observed throughout the measurements. From Ref. [20].

5.2. Alkali-metal adsorptions

As described so far, adsorptions of noble-metal atoms onto the Si(111)-$\sqrt{3} \times \sqrt{3}$-Ag surface commonly induce similar changes in the surface superstructures and surface electrical conduction. The noble-metal adsorbates provide electrons to the substrate surface-state band. This is the origin of the observed enhancements in conductance and probably also of the formation of the $\sqrt{21} \times \sqrt{21}$ superstructures. Thus, what happens for adsorptions of the other monovalent atoms such as alkali metals?

Figs. 64(a) and (b) show the changes in the conductance of a Si wafer during K and Cs adsorptions, respectively, onto the Si(111)-$\sqrt{3} \times \sqrt{3}$-Ag surface at RT,

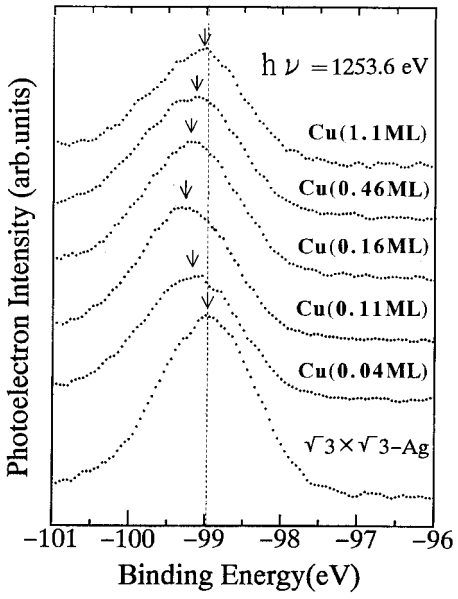

Fig. 62. XPS spectra from Si 2*p*core level of a Si(111) surface with different Cu coverages on the $\sqrt{3} \times \sqrt{3}$-Ag structure. From Ref. [20].

together with changes in RHEED patterns observed in the separate runs of deposition under the same conditions [93]. The alkali-metals were evaporated from commercially available dispensers (from SAES Getters Inc.). The results are shown just as a function of deposition time, because the coverages of alkali-metals were not precisely estimated. The conductances as well as the structures are shown to change in similar ways for both of K and Cs adsorptions; the conductance rises steeply at the beginning to reach a maximum, which corresponds to the appearance of a $\sqrt{21} \times \sqrt{21}$ superstructure. Then, the conductance decreases steeply to a minimum, which is less than the initial value, which corresponds to the disappearance of the $\sqrt{21} \times \sqrt{21}$ superstructure, returning to a $\sqrt{3} \times \sqrt{3}$ structure. Around the conductance minimum, a 6×6 superstructure appears (see Fig. 65(c)). With further adsorptions, the conductance rises again, during which the 6×6 superstructure converts into a $\sqrt{21} \times \sqrt{21}$ structure again (see Fig. 65(a) and (b)). This RHEED pattern continues to be observed with further deposition of Cs, while it changes into a $2\sqrt{3} \times 2\sqrt{3}$ superstructure for the K-adsorption case (Fig. 65(d)). These sequences of the structural changes are very similar to the case of Ag adsorption on the $\sqrt{3} \times \sqrt{3}$-Ag surface at 100 K shown in Fig. 27(e)–(g); the initial $\sqrt{3} \times \sqrt{3} \rightarrow$ (e)$\sqrt{21} \times \sqrt{21} \rightarrow$ (f)$6 \times 6 \rightarrow$ (g) $\sqrt{21} \times \sqrt{21}(+6 \times 6)$. Furthermore, it is also qualitatively similar in that the $\sqrt{21} \times \sqrt{21}$ phases are highly conductive, while the 6×6 phases are not (Compare with the conductance curve at 90 K in Fig. 49(b) for Ag-adsorption case). Although the changes in surface electronic states, during these alkali-metal adsorptions, has not yet been

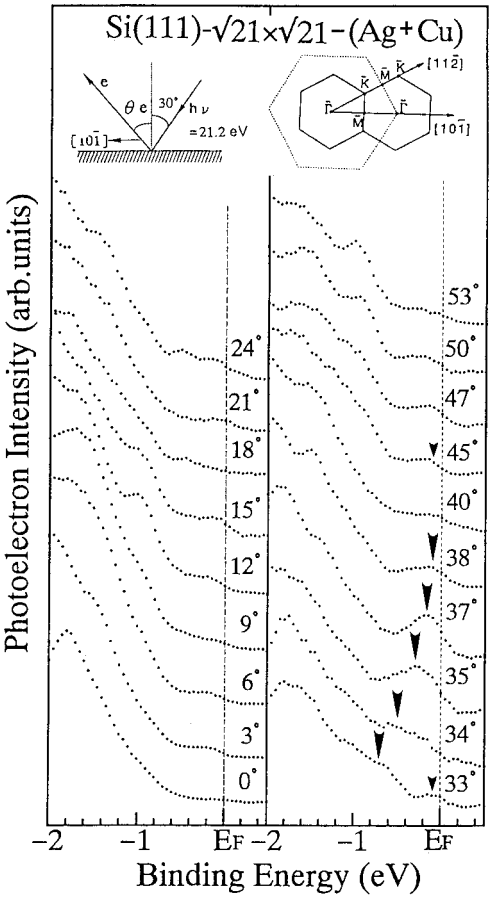

Fig. 63. Angle-resolved ultraviolet photoelectron spectra taken from the Si(111)-$\sqrt{21} \times \sqrt{21}$-(Ag + Cu) surface. The electron analyzer was scanned in [10$\bar{1}$] direction, and the electron emission angles θ_e were measured from the surface-normal direction. The range of θ_e shown here correspond to around the $\bar{\Gamma}$ point in the second surface Brillouin zone. He I resonance light (21.2 eV) was used for excitation with irradiation of incident angle 30° off from the surface-normal. From Refs. [20].

investigated, similar observed behaviors in the atomic structure, as well as the conductance changes, strongly suggest that the common mechanisms, as in the case of noble-metal adsorptions, apply to these phenomena; alkali-metal adatoms arrange periodically on top of the $\sqrt{3} \times \sqrt{3}$-Ag framework without substrate reconstruction to form the $\sqrt{21} \times \sqrt{21}$ superstructure, and also metallic surface-state bands are presumably formed to make the surface highly conductive, as in the case of Au- and Cu-induced $\sqrt{21} \times \sqrt{21}$ superstructures. These phenomena may be raised by the monovalency of the adatoms, which provide the valence electrons to the substrate to modulate the surface-state band of the initial $\sqrt{3} \times \sqrt{3}$-Ag structure.

In fact, none of Ca, Mg, and In adsorptions on the $\sqrt{3} \times \sqrt{3}$-Ag surface induce

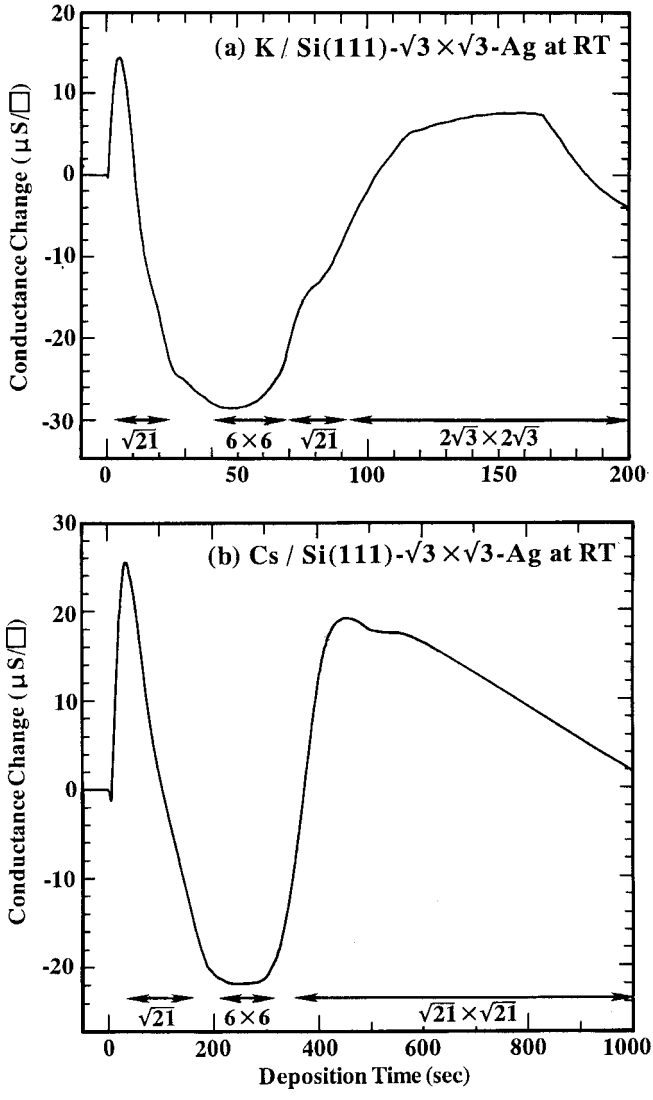

Fig. 64. Changes in electrical conductance of a Si wafer (*n*-type of 10–100 Ωcm resistivity) during adsorptions of (a) K and (b) Cs, respectively, at RT. The RHEED patterns observed in separate runs of depositions are also indicated. The $\sqrt{3} \times \sqrt{3}$ superspots are always observed throughout the measurements. From Ref. [93].

any superstructure or conductance increases; the $\sqrt{3} \times \sqrt{3}$-Ag structure is gradually destroyed as the coverage of the divalent and trivalent atoms increases. Fig. 66 shows the resistance change of a Si wafer during In adsorption on the $\sqrt{3} \times \sqrt{3}$-Ag surface at RT [5]. The resistance monotonically increases from the beginning of the deposition to reach a larger value around 1 ML coverage. The $\sqrt{3} \times \sqrt{3}$-Ag surface structure seems to be destroyed, resulting in a 1×1-RHEED

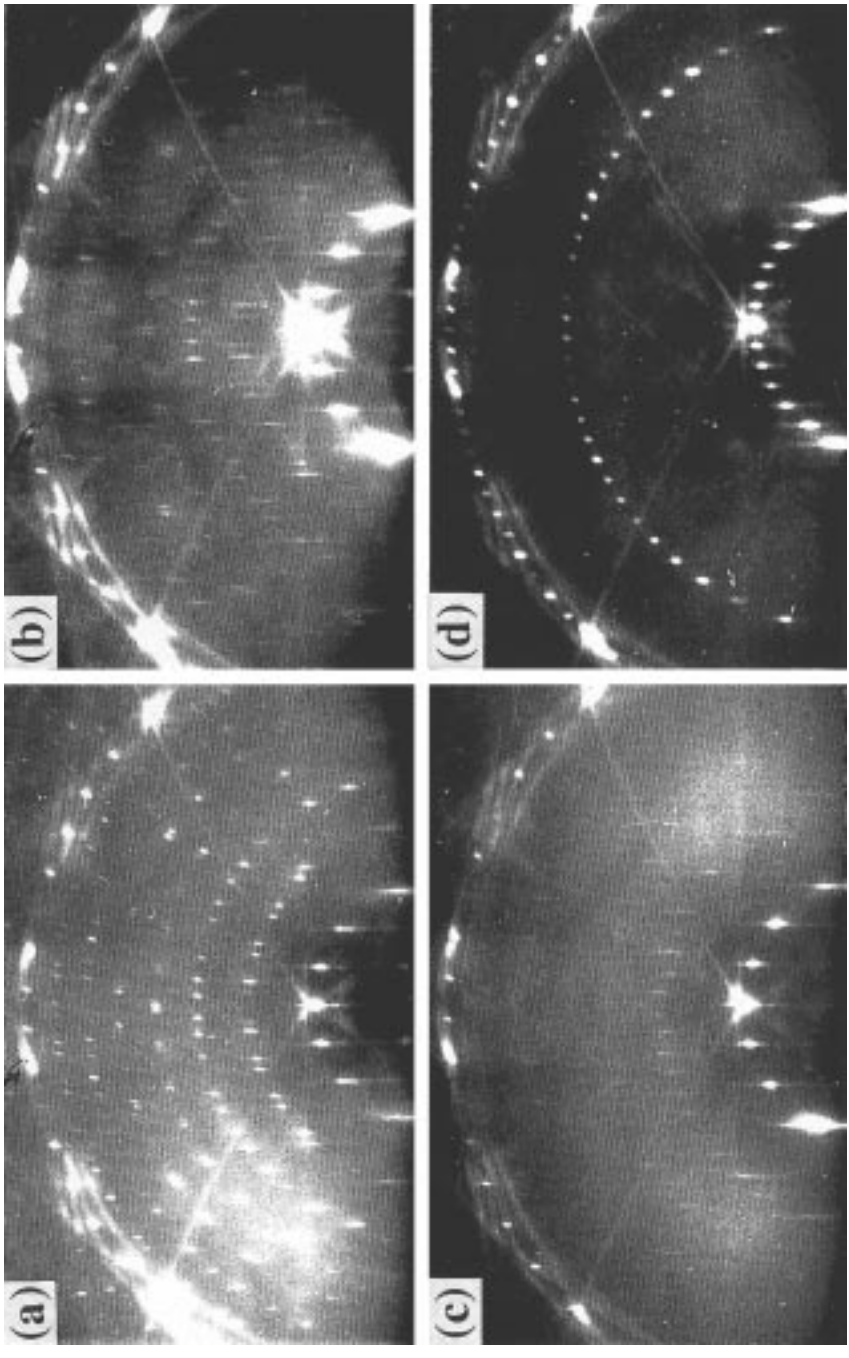

Fig. 65. RHEED patterns observed during K and Cs adsorptions onto the Si(111)-$\sqrt{3} \times \sqrt{3}$-Ag surface at RT. (a) (b) the $\sqrt{21} \times \sqrt{21}$ superstructures induced by Cs and K adsorptions, respectively, with larger coverages than that for the 6×6 superstructures. (c) The 6×6 superstructure induced by Cs adsorption. (d) The $2\sqrt{3} \times 2\sqrt{3}$ superstructure induced by K adsorption. From Ref. [93].

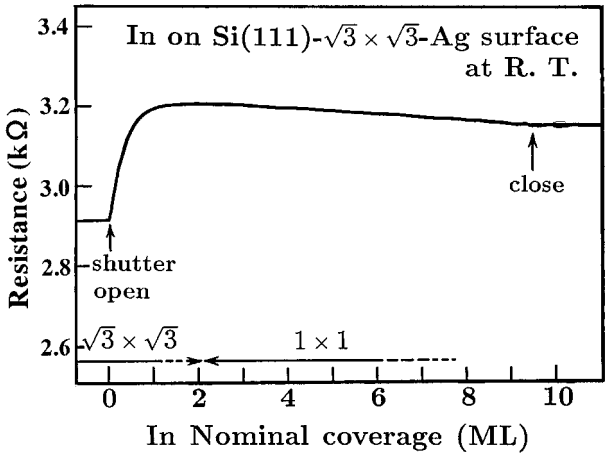

Fig. 66. Change in resistance and RHEED patterns of a Si(111) wafer with the $\sqrt{3} \times \sqrt{3}$-Ag surface during In deposition at RT. From Ref. [5].

pattern. The adsorptions of Ca and Mg also show similar changes. These comparative observations convince us of the importance of monovalency of the adatoms to induce the $\sqrt{21} \times \sqrt{21}$ superstructures and also to raise the surface conductance.

5.3. Summary

Adsorptions of monovalent atoms (noble and alkali metals) of submonolayer coverages (0.1–0.2 ML) on the Si(111)-$\sqrt{3} \times \sqrt{3}$-Ag surface commonly induce similar $\sqrt{21} \times \sqrt{21}$ superstructures, and all of them exhibit high electrical conductances. It is strongly suggested that common processes work among the different adsorbates in making the superstructures and electronic transport properties; metallic surface-state bands inherent in the $\sqrt{21} \times \sqrt{21}$ superstructures raise the surface conductance, as revealed by Au- and Cu-induced $\sqrt{21} \times \sqrt{21}$ phases. These phenomena occur, because the valence electrons of the adatoms are transferred to the substrate surface-state bands, as revealed by Ag adsorption (2D adatom gas phase), which is the carrier doping into the surface-state bands, as described in Section 4.

6. Gold adsorption

6.1. Au-induced surface superstructures

6.1.1. Phase diagram

As in the case of Ag, Au deposition onto the Si(111)-7 × 7 surface at elevated temperatures induces several surface superstructures depending on its coverage

and temperature; 5×2 (or 5×1), $\sqrt{3} \times \sqrt{3}$, and 6×6 structures. Fig. 67 shows phase diagrams showing the ranges of Au coverages and temperatures for formation of each superstructure, determined by (b) LEED-AES [77], (b) RHEED [119,120], and (c) TED [121], and also (d) TED [122], respectively. (e) shows intensities of Au 4*f* and Si 2 *s* lines in XPS and evolution of LEED patterns as a function of Au coverage [123]. After the completion of a 5×2 (or a 5×1) phase around 0.4–0.5 ML coverage, $\sqrt{3} \times \sqrt{3}$ and 6×6 phases develop with further Au adsorptions. The $\sqrt{3} \times \sqrt{3}$ superstructure should be classified into two phases at least as mentioned below.

In spite of numerous investigations on this Au/Si(111) system, its nature is less clearly understood compared with the Ag/Si(111) system. No generally accepted atomic structural models for the superstructures exist at present. Even the saturation coverage for each structure has not yet been confirmed. This may be because Au has higher reactivity with Si than Ag, and they interdiffuse with each other near the surface, although Au and Si are known to form no thermodynamically stable bulk compound [124–126]. According to Molodtsov et al. [126], like Ag, Au atoms have completely filled *d*-levels, which, however, are located closer to the Fermi level than in Ag. In Au/Si(111) system, the *d*-levels shift above E_F with increasing Au concentration due to *d*/*sp* hybridization. This mechanism makes Au resembled to the other *d*-transition metals, which are characterized by unfilled *d*-states and are highly reactive with Si.

Fig. 68 shows the simultaneous measurements of integrated spot intensities of the respective superstructures in RHEED and Au coverages determined by *Rutherford backscattering spectroscopy* (RBS) during Au deposition onto the Si(111)-7×7 surface at elevated temperatures [127]. After the completion of the 5×2 phase around 0.5 ML Au coverage, at which the 7×7-spots disappear completely and the 5×2-spots takes the maximum intensity, $\sqrt{3} \times \sqrt{3}$ phase develops with further Au adsorptions. Around 0.85 ML coverage, the 5×2-spots disappear and instead, the $\sqrt{3} \times \sqrt{3}$-spots become the most intense. These structural conversions are consistent with the phase diagrams in Fig. 67 though Au coverage for each phase are assigned to be different each other.

6.1.2. 5×2-Au superstructure

Fig. 69 shows the (a) STM image and (c) RHEED pattern of the 5×2 superstructure taken at RT after prepared at an elevated temperature. The RHEED pattern (c) consists of superlattice spots of a five-unit-cell periodicity along $<11\bar{2}>$ directions and half-order streaks running between them. These streaks indicate that a two-unit-cell periodicity along $<\bar{1}10>$ directions does not correlate with each other [130–132], although the five-unit-cell periodicity along $<11\bar{2}>$ directions are rigid. The STM image (a) reveals rows oriented along $<\bar{1}10>$ directions with a five-unit-cell separation. Characteristic protrusions are seen on each row; they are spaced at multiples of a two-unit-cell spacing, where a four-unit-cell separation is most common [128,129]. Their number density is about 0.027 ML in average, which seems to be constant at RT irrespective of the total amount of Au deposited [129]. The arrangement of the protrusions are not

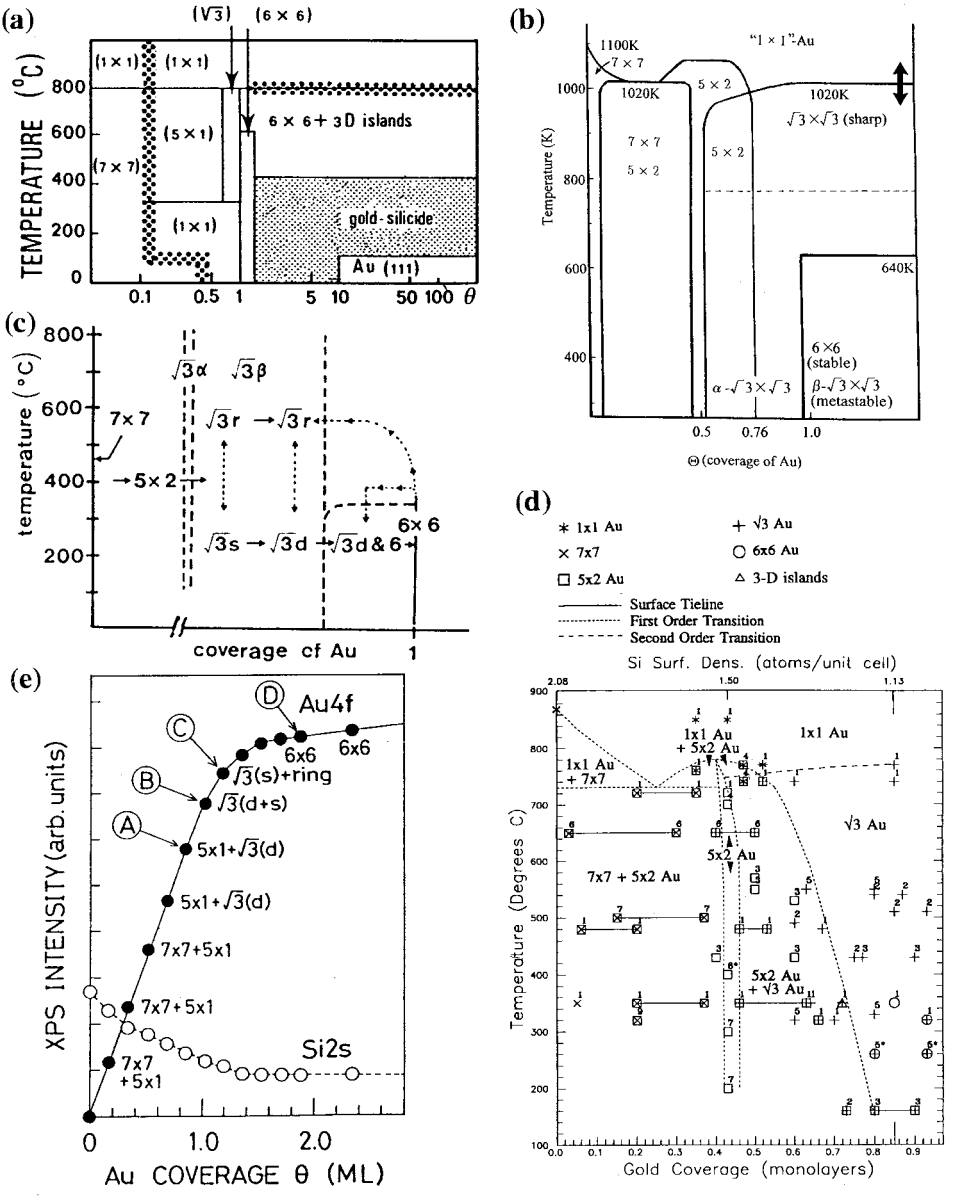

Fig. 67. Phase diagrams showing surface reconstructions of Au/Si (111) system vs Au coverage and annealing/growth temperature; determined by (a) LEED-AES [77], (b) RHEED [119,120], (c) TED [121], and (d) TED [122], respectively. (e) Intensities of Au 4*f* and Si 2*p*X-ray photoemission lines and evolution of LEED patterns as a function of Au coverage after high temperature annealing [123]. The notations and saturation coverages for each phase are not consistent among the investigators. Reproduced with permission.

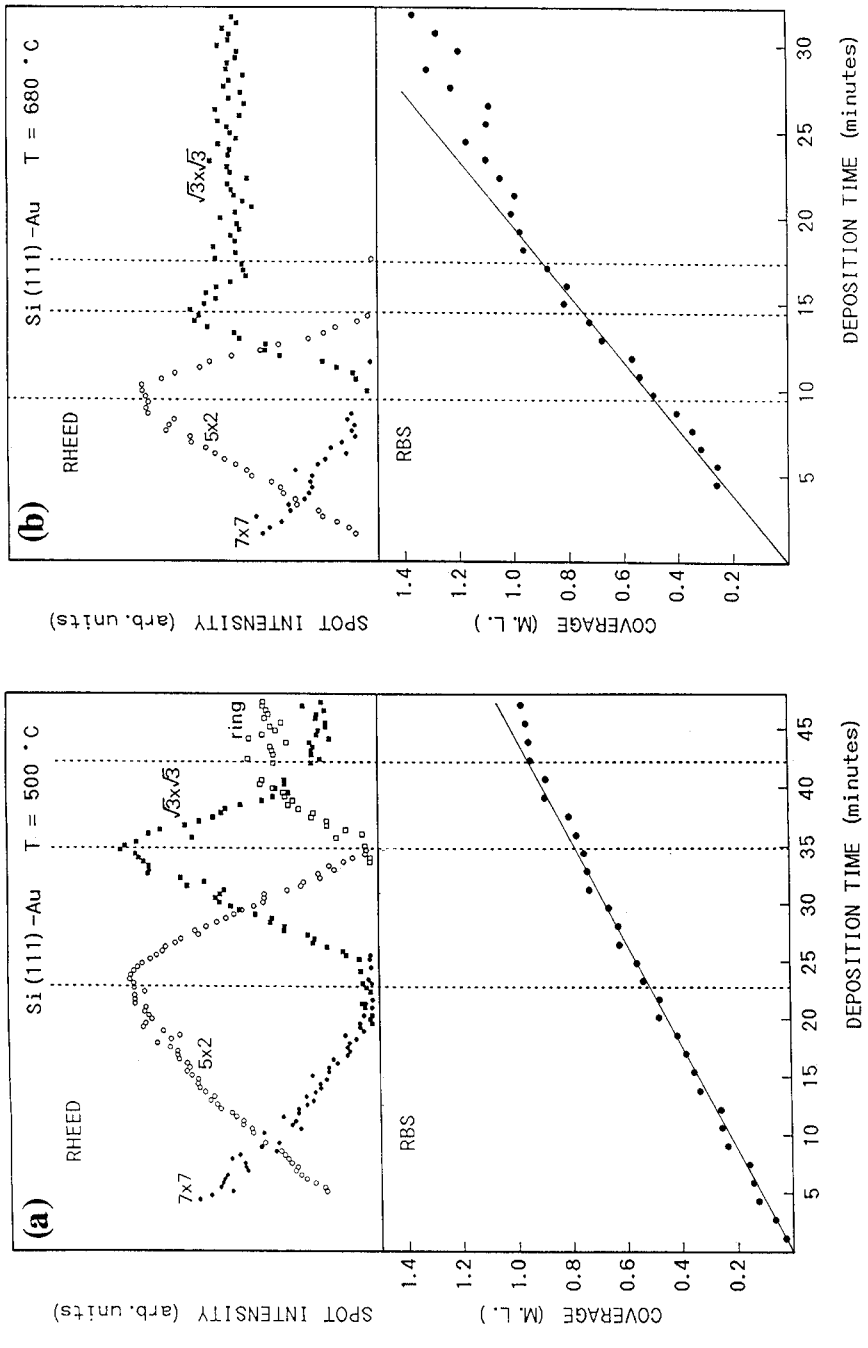

Fig. 68. Upper panels shows the changes of integrated spot intensity of each superstructure in RHEED, measured with a TV camera system, during Au deposition onto the Si(111)-7 × 7 clean surface at (a) 500°C and (b) 680°C. Lower panels shows the changes of Au coverage during this deposition.

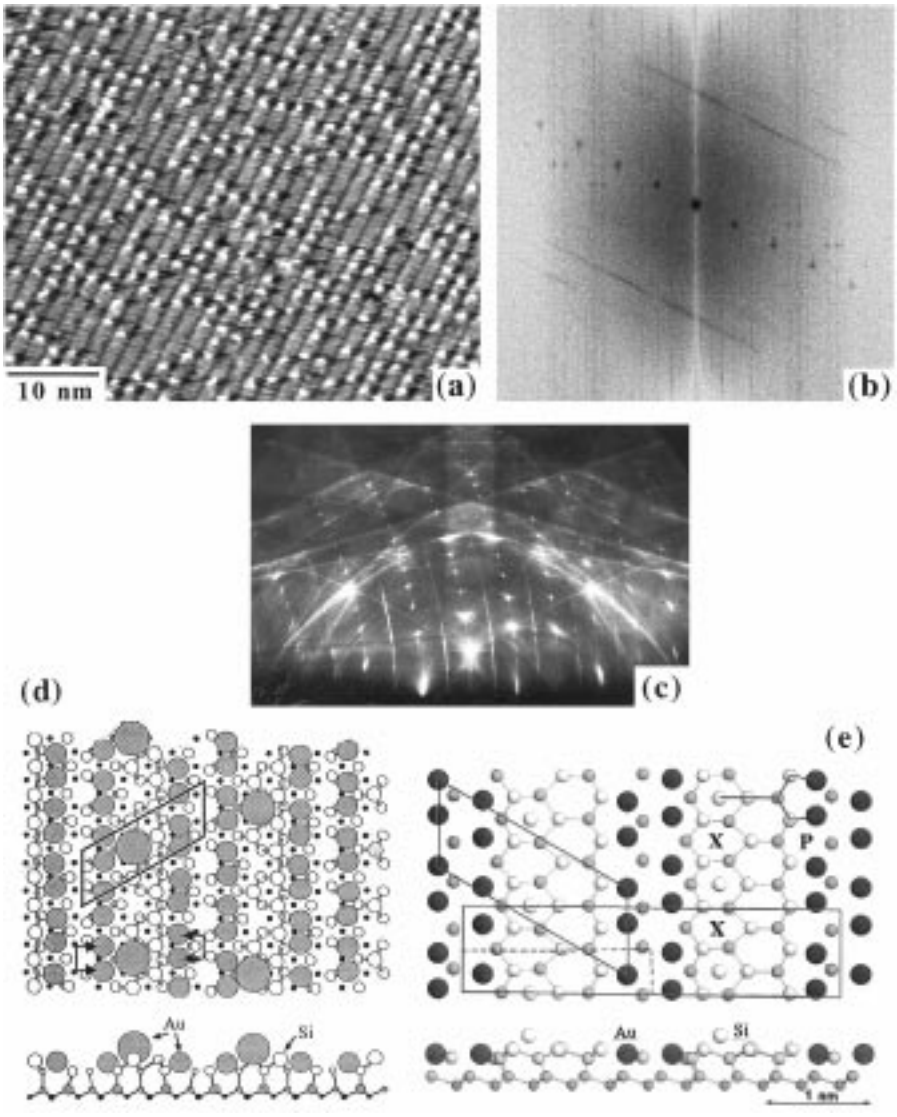

Fig. 69. Si(111)-5 × 2-Au surface. (a) Its filled-state STM image ($V_t = 1$ V), and (b) its Fourier transformed pattern. (c) Its RHEED pattern. Proposed models for this structure by (d) Hasegawa (T.) and Hosoki [134] and (e) Marks and Plass [135,122], respectively, reproduced with permission.

correlated between the neighboring rows. The streaks in the RHEED pattern comes from this lack of long-range ordering of protrusions. In fact, the Fourier-transformed pattern (b) of the STM image (a) shows the half-order streaks. The lack of long-range-ordering is due to stronger adsorbate-substrate interactions compared with adsorbate-adsorbate interactions [132]. The positional correlation function of the bright protrusions are reproduced theoretical by assuming some

repulsive interactions among them [133]. The bright protrusions moves within each row at elevated temperatures [134], so the protrusions are suggested to be Au adatoms.

The atomic structure of the 5×2 phase is not yet fully accepted among the researchers. Figs. 69(d) and (e) show the proposed models for the atomic arrangement in this superstructure [134,135,122]. Both models assume the Au coverage of 0.4 ML in the substrate, forming two Au row in each five-unit-cell-periodicity row, with additional Au atoms for the bright protrusions on the 5×2 framework in (d). Then, the total coverage of Au is about 0.43 ML. The differences between (d) and (e) are inner Au rows, the number and arrangement of Si atoms in the reconstructed layers.

6.1.3. $\sqrt{3} \times \sqrt{3}$-Au superstructure

Fig. 70 shows the RHEED patterns and STM images taken at RT from the $\sqrt{3} \times \sqrt{3}$ surface prepared with different Au coverages at elevated temperatures [120]. The streaky superlattice reflections in (a) and (c) mean small coherent domains of the $\sqrt{3} \times \sqrt{3}$ phase. This is revealed by the STM images (b)(d) in which the $\sqrt{3} \times \sqrt{3}$ domains are separated by a large quantity of out-of-phase domain boundaries seen as wound bright features. The average spacing among the domain walls decreases with increasing Au coverage, i.e., the $\sqrt{3} \times \sqrt{3}$ phase is broken up into sub-10-nm-size domains that decreases in size with increasing Au coverage [136]. STM images of the regular $\sqrt{3} \times \sqrt{3}$ domains shows a centered hexagonal array of bright dots [129,136], as seen in the inset in (b).

In (f), however, the regular array of $\sqrt{3} \times \sqrt{3}$-protrusions are hardly recognized, while its RHEED pattern (e) has sharp superlattice spots accompanying faint complicated streaks. The sharp 1/3-th reflections mean well-defined long-range order though the STM image does not show any order apparently; this is puzzling.

Some in the literature distinguish the phase (a)(b) from (e)(f) by "α-" and "β-" $\sqrt{3} \times \sqrt{3}$ phases, respectively [119,120,3,2]. The difference between these two phases are not only in the domain sizes, but also as described in Section 6.2, in the electronic structure.

The $\sqrt{3} \times \sqrt{3}$-Au phases always have a large quantity of domain boundary as seen in the STM images; this feature is contrasted with the $\sqrt{3} \times \sqrt{3}$ phase induced by Ag where quite large (up to ~1 μm in size) single domains can be prepared under certain conditions. At elevated temperatures, however, large coherent domains of the $\sqrt{3} \times \sqrt{3}$ structure are attained as shown in Fig. 71 [120]. The density of the domain boundary decreases with temperature and the boundaries are completely swept out at 620°C to obtain large single domains (c), so that the RHEED (e) shows very sharp spots of the $\sqrt{3} \times \sqrt{3}$-fractional order. But this surface returns to one shown in (a) and (d) by cooling down to RT having a lot of domain boundaries; large $\sqrt{3} \times \sqrt{3}$ domains at high temperatures are broken up into smaller incoherent domains in the course of cooling. The conversion between Fig. 71(a) and (d) and (c) and (e) is reversible with temperature change. This reversible change should not be understood with a

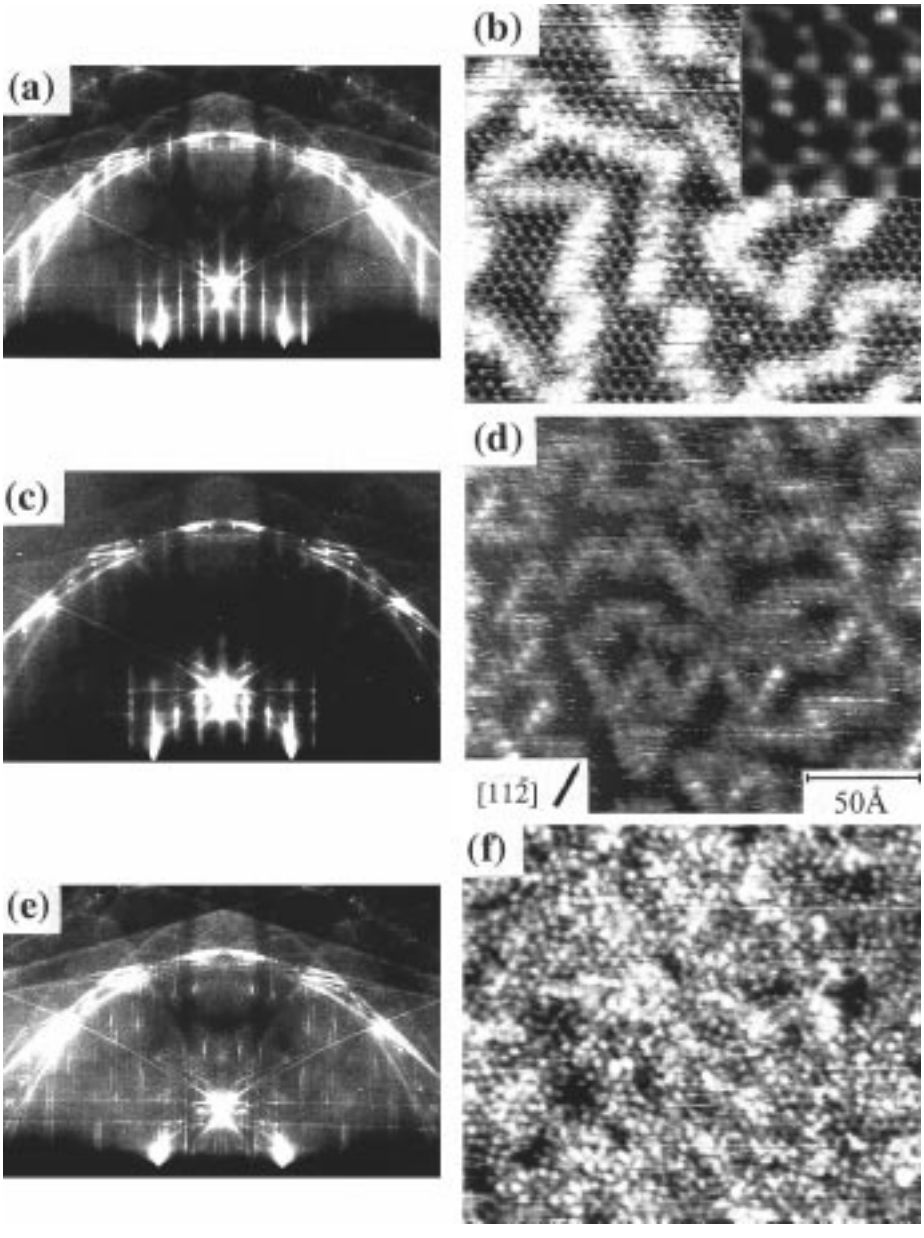

Fig. 70. RHEED patterns and STM images taken from the Si(111)-$\sqrt{3} \times \sqrt{3}$-Au surface at RT, which are prepared at an elevated temperature around 500°C with Au coverages of (a) and (b) 0.76 ML, (c) and (d) 0.83 ML, and (e) and (f) 0.96 ML, respectively [120].

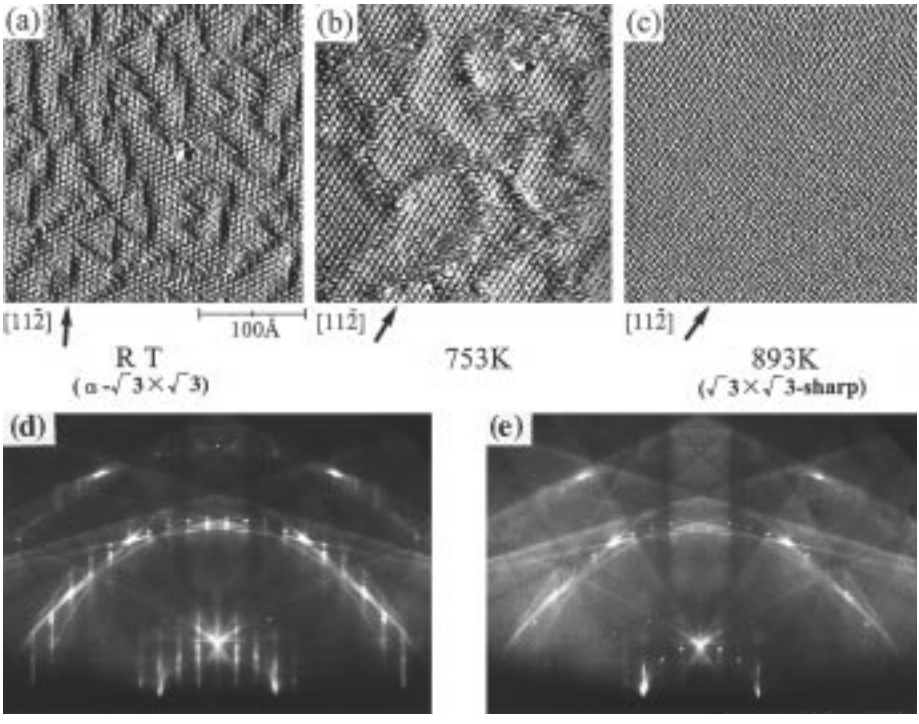

Fig. 71. STM images and RHEED patterns taken from the Si(111)-α-$\sqrt{3}\times\sqrt{3}$-Au surface with Au coverage of 0.76 ML at (a) and (d) RT, (b) 480°C, and (c) and (e) 620°C, respectively [120].

simple domain growth and decay of a single type of $\sqrt{3}\times\sqrt{3}$ phase, rather this phenomenon suggests that the $\sqrt{3}\times\sqrt{3}$ phase at RT and that at higher temperatures are different in structure, and a kind of structural phase transition between them occurs with temperature change.

For the β-$\sqrt{3}\times\sqrt{3}$ phase with 1.0 ML Au coverage shows a similar change with temperature changes as shown in Fig. 72 [120]; its apparently disordered STM image (a) changes into a well ordered $\sqrt{3}\times\sqrt{3}$ pattern (b) at elevated temperatures so that the faint complicated streaks in RHEED pattern (d) disappear, leaving only the sharp 1/3-th fractional-order spots. The surface (b) returns to (a) and (d) by quench cooling down to RT. But when the surface (b) is cooled slowly, it changes into a 6×6 phase (c) and (e). Hence the β-$\sqrt{3}\times\sqrt{3}$-Au phase (a) and (d) is a meta-stable one in a sense; it is considered that domain walls in the β-$\sqrt{3}\times\sqrt{3}$-Au distribute randomly (domain-wall glass) while the walls arrange periodically to make the 6×6-Au phase (domain-wall crystal) [120].

Most plausible models for the atomic arrangement of the regular $\sqrt{3}\times\sqrt{3}$ domains are two, conjugated honeycomb-chained trimer model [137] and missing-top-layer twisted trimer model [138]. Both are consisted of 1 ML Au coverage, though ion scattering spectroscopy indicate the saturation coverage of about 0.85 ML as shown in Fig. 68 [127,139]. The controversy may be raised due to the

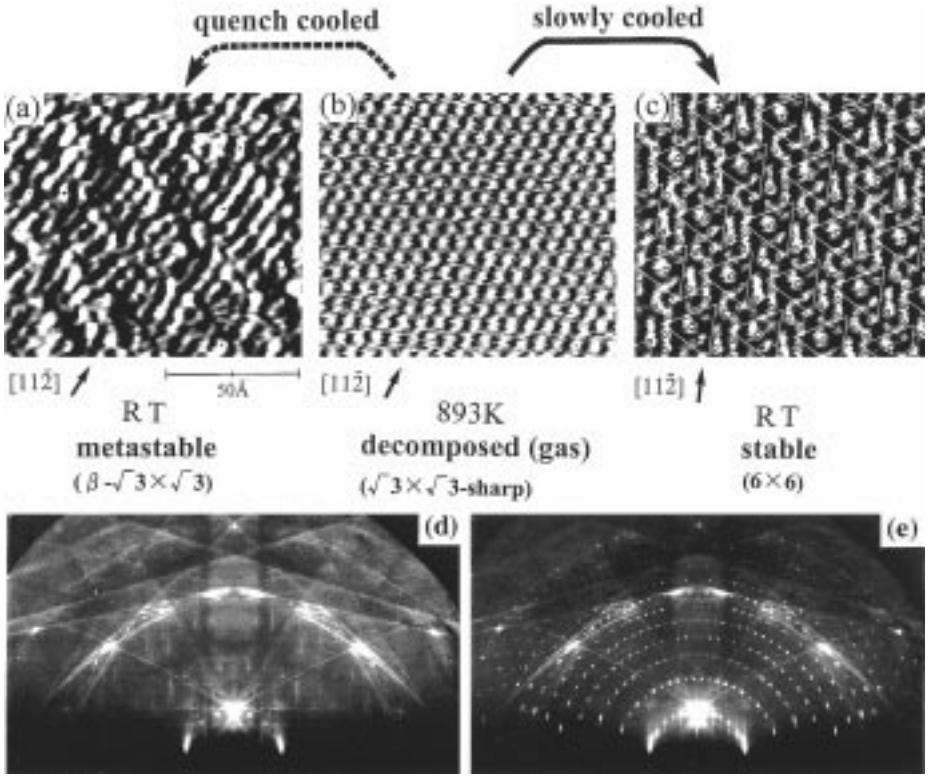

Fig. 72. STM images and RHEED patterns taken from the Si(111)-β-$\sqrt{3} \times \sqrt{3}$-Au surface with Au coverage of 1.0 ML at (a) and (d) RT, (b) 620°C. The surface (b) returns to (a) and (d) by quench cooling, while the surface (b) changes into a 6×6-Au phase (c) and (e) by slow cooling [120].

complicated domain boundaries described above, depending on the Au coverage and temperature. Since the density of domain boundaries increases with Au coverage, the boundaries should be gold excess, while some paper assumes it gold deficient [122].

6.1.4. 6× 6-Au superstructure

As described at Fig. 72, the 6×6 phase is formed by slow cooling of the $\sqrt{3} \times \sqrt{3}$-Au phase with more than 1 ML Au coverages. The apparently same superstructure can be formed also by additional deposition of a small amount of Au (around 0.1 ML) onto the β-$\sqrt{3} \times \sqrt{3}$-Au surface at RT. The 6×6-RHEED pattern (Fig. 72(e)) has an especially high background, meaning a randomness in structure. Since, as described in Section 6.2, the 6×6-Au phase has a very similar electronic structure to that of the β-$\sqrt{3} \times \sqrt{3}$ phase, local atomic arrangements are thought to be quite similar between the two structures. In fact, the β-$\sqrt{3} \times \sqrt{3}$-Au phase is considered to be consisted of minimum-sized domains, having the $\sqrt{3} \times \sqrt{3}$ periodicity, densely random packed to form a short-range order with a

nearest-neighbor distance around $6a_0$, while in the 6×6-Au phase, the minimum-sized domains are arranged in a closed-packed manner to make a long-range order of 6×6 [120].

6.2. Electronic structures

6.2.1. Valence bands

Fig. 73 shows the results of ARPES measurements summarized in 2D band mappings of the (a) 5×2-Au, (b) α-$\sqrt{3} \times \sqrt{3}$-Au, (c) β-$\sqrt{3} \times \sqrt{3}$-Au, and (d) 6×6-Au superstructures, taken by Okuda et al. [182].

The state labeled A without dispersion appears for all superstructures around 4.3 eV below E_F, and is always accompanied with the state B below it by about 0.8 eV. These are assigned to be the nonbonding Au 5 *d* states with spin-orbit splitting. Deeper states labeled C, C′, C″, D, and D′ are suggested to be composed of bonding Au 5 *d* electrons hybridized with Si valence electrons. On every surfaces, there are faint states labeled *s* lying at E_F, especially, on the β-$\sqrt{3} \times \sqrt{3}$-Au and 6×6-Au superstructures; these states are seen in every wave numbers, which implies the metallic characters. The state *s* on the α-$\sqrt{3} \times \sqrt{3}$-Au surface, however, is observed only at several regions in *k* space and its DOS is very small, implying a weak metallic character. If the domain-wall regions, which are the characteristic feature in these $\sqrt{3} \times \sqrt{3}$ and 6×6 phases as described in Section 6.1, have metallic electronic states, the weak metallic character of the α-$\sqrt{3} \times \sqrt{3}$-Au surface is consistent with its smaller density of the domain walls compared with the β-$\sqrt{3} \times \sqrt{3}$-Au and 6×6-Au phase. The features of other observed states E, S, V, are similar among the α- and β-$\sqrt{3} \times \sqrt{3}$-Au and 6×6 phases, especially the latter two surfaces has quite similar bands. These suggest a common local structure in the commensurate domains in these phases.

On the 5×2-Au superstructure, the metallic state *s* is observed only along $[10\bar{1}]$ direction ($\overline{\Gamma K}$), not along $[2\bar{1}\bar{1}]$ direction ($\overline{\Gamma M}$). This results is consistent with a quasi-1D metallic character, which is already suggested by Collins et al. using a single-oriented 5×2-Au surface [184]. Along the stripes observed in STM images like Fig. 69(a), it is metallic, but in the direction perpendicular to the stripes, it is nonmetallic.

6.2.2. Band bending

Fig. 74 shows the Si 2*p* core-level PES spectra taken from the respective superstructures [183]. At a glance, the shapes are quite different from each other. This is because the measured spectra are composed of some components, a bulk one *B* and two surface ones, S_1 and S_2, as shown by dotted and dashed lines, and their intensity ratios are different depending on the structures. But the β-$\sqrt{3} \times \sqrt{3}$-Au and the 6×6-Au superstructures have a quite similar spectra, implying their similarity of local atomic geometry, while the α-$\sqrt{3} \times \sqrt{3}$-Au has a quite different spectra. This may be because the signals come mainly from the dense domain-wall regions in the β-$\sqrt{3} \times \sqrt{3}$-Au and the 6×6-Au superstructures, while they come mainly from the commensurate domains in the α-$\sqrt{3} \times \sqrt{3}$-Au superstructure.

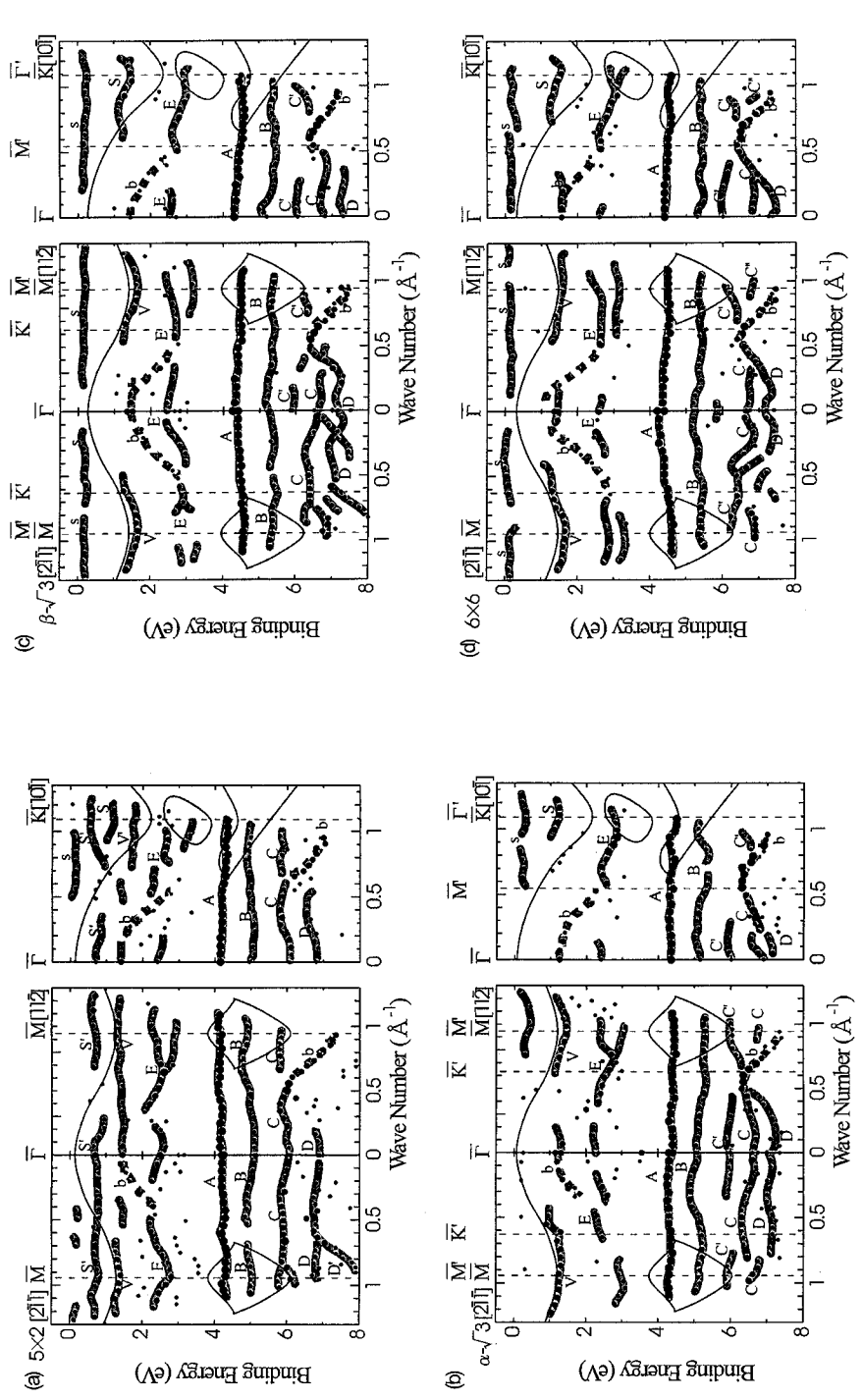

Fig. 73. 2D band maps of the (a) 5×2-Au, (b) α-$\sqrt{3} \times \sqrt{3}$-Au, (c) β-$\sqrt{3} \times \sqrt{3}$-Au, and (d) 6×6-Au superstructures along $[10\bar{1}]$, $[11\bar{2}]$, and $[2\bar{1}\bar{1}]$ directions. Reproduced with permission from Ref. [182].

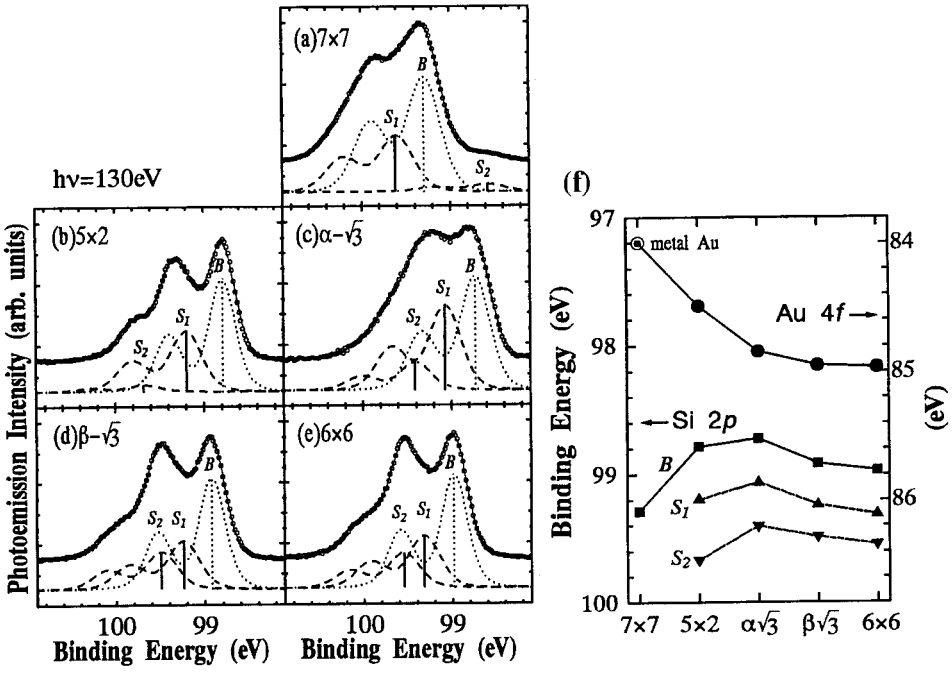

Fig. 74. Si 2*p*core-level spectra in a surface-sensitive mode ($h\nu = 130$ eV) taken from the (b) 5×2-Au, (c) α-$\sqrt{3} \times \sqrt{3}$-Au, (d) β-$\sqrt{3} \times \sqrt{3}$-Au, and (e) 6×6-Au superstructures as well as (a) 7×7 clean surface. (f) Shifts in binding energy of the respective components in Si $2p_{3/2}$ and Au $4f_{7/2}$. Reproduced with permission from Ref. [183].

Another point to be noticed is the shifts in energy position of the respective components. Fig. 74(f) shows the binding energies of the respective components of Si $2p_{3/2}$ and Au $4f_{7/2}$ lines taken from the respective superstructures. One important result is large shifts of the bulk component B towards lower binding energy compared to the 7×7 clean surface; 0.5 eV (5×2), 0.565 eV (α-$\sqrt{3}$), 0.372 eV (β-$\sqrt{3}$), and 0.316 eV (6×6), respectively. These mean upward band bending below the Au-induced superstructures. Especially, the 5×2-Au and α-$\sqrt{3} \times \sqrt{3}$-Au have so strong bending that the surface E_F positions are very close to the VBM, meaning hole-accumulation (*p*-type) layers beneath the surface.

The surface components S_1 and S_2 are always located at higher binding energy compared with the bulk component *B*. This means a charge (electron) transfer from the surface Si atoms to Au atoms, which is reasonable by considering the stronger electronegativity of Au than Si. The shifts of Au 4*f* level towards higher binding energy compared to that of the 7×7 clean surface, which is opposite to the expectation from the charge transfer mentioned above, is explained by an idea of 5 *d* electron depletion and the difference of Coulomb interaction between Au 4*f*–5 *d* and 4*f*-conduction electrons [183].

The α-$\sqrt{3} \times \sqrt{3}$-Au has two surface components S_1 and S_2 as described above,

while the Ag-induced $\sqrt{3} \times \sqrt{3}$ structure has only one surface component as shown in Fig. 20 [42]. Since the signal from the domains walls in the α-$\sqrt{3} \times \sqrt{3}$-Au is considered to be small because of the low density of the walls, the two surface components should come from the commensurate domains. Hence, the Au-induced $\sqrt{3} \times \sqrt{3}$ structure should be quite different from the Ag-induced one.

6.3. Electrical conductance

With an in-situ four-probe method as in Section 4.3.1, the conductance differences between the Au-induced superstructures and the clean 7×7 surface are measured. All of the Au-induced structures shows higher conductance than the clean surface. The results are plotted in Fig. 75 at the surface E_F positions of the respective structures. The E_F positions are determined in Fig. 74. As shown in Fig 75, $\Delta\sigma$ increases with Au coverage (0.5 ML for 5×2, 0.8 ML for α-$\sqrt{3}$, 1 ML for β-$\sqrt{3}$, and 1.2 ML for 6×6 phases), while the surface E_F positions are not located in this sequence; the E_F of the α-$\sqrt{3} \times \sqrt{3}$ phase lies at the nearest to VBM. Comparing the measured $\Delta\sigma$ with the calculated curves of Δ_{SC}, the data points of the 5×2-Au and α-$\sqrt{3} \times \sqrt{3}$-Au surfaces can be roughly said to be consistent with the calculated conductance within the experimental accuracy. But the points for the β-$\sqrt{3} \times \sqrt{3}$-Au and 6×6-Au phases seem to deviate above the curves. This is because their E_F positions are located away from the VBM, i.e., in the depletion-

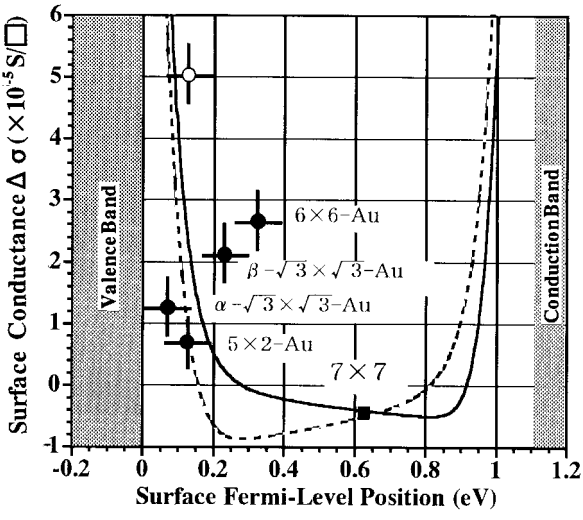

Fig. 75. The curves show the excess electrical conductance through the surface space-charge layer $\Delta\sigma_{SC}$ calculated as a function of surface E_F positions for Si wafers of *p*-type (20 Ωcm resistivity, solid line) and *n*-type (45 Ωcm resistivity, dashed line). Filled circles indicate the measured excess conductances $\Delta\sigma$ of the 5×2-Au, α-$\sqrt{3} \times \sqrt{3}$-Au, β-$\sqrt{3} \times \sqrt{3}$-Au, and 6×6-Au surfaces with respect to the 7×7 clean surface for *n*-type. Open circles indicate the data of the 5×2-Au structure on the *p*-type substrates. The conductance data are plotted at the experimentally determined surface E_F position in Ref. [183].

layer region. This suggest excess conductance other than the conductance through the surface space-charge layer.

As described in Section 6.2 with band maps of the respective surface superstructures in Fig. 73, the β-$\sqrt{3} \times \sqrt{3}$-Au and 6×6-Au surfaces have metallic surface states at almost every wavenumbers, while the 5×2-Au and α-$\sqrt{3} \times \sqrt{3}$-Au surfaces are just weakly metallic. Hence the conductance through the metallic surface states may contribute to the observed excess conductance on the former two surfaces, while the surface space-charge layers dominate the conductance for the latter two surfaces.

6.4. On the 7×7 clean substrate

Fig. 76(a) show a change in resistance of a Si wafer during deposition of Au (rate = 0.21 ML/min) onto the clean 7×7 surface at RT. The changes in RHEED patterns are also indicated. The resistance does not show significant changes at the initial deposition stage, except for a slight increase at the beginning. Above 0.8 ML coverage, the resistance begins to decrease steeply, but the rate of decrease temporarily slows down around 1.5 ML coverage.

In RHEED, with increase of Au coverage, the 7×7-superlattice spots gradually blur up to around 1 ML. But at about 1.5 ML coverage, the superlattice spots temporary regain their intensities, of which relative intensity ratios are different from those of the clean 7×7 surface. For instance, the $(\frac{3}{7}, \frac{3}{7})$-order spots on the 0th Laue zone for the clean 7×7 surface are the most intense, which originates from the adatom array in 2×2 periodicity in the DAS structure [140], while those spots become the weakest in the pattern from a 1.5 ML Au-covered surface, meaning a partial structural change in the 7×7 unit [5]. Over 2 ML coverage, diffraction spots, even the fundamental spots, are hardly observed, remaining diffuse background. This means an amorphous-like surface layer with Au-Si mixture.

According to UHV–SEM observations [141], small islands of a few nanometers in diameter appear at the initial stage of the Au deposition, and then begin to coalesce with increasing Au coverage. Although it is not clear whether the islands are composed of pure Au or Au-silicide, it is natural to expect that the islands are so conductive that the electrical conduction can be set-on above a threshold coverage for percolation paths corresponding to the coalescence among the islands.

According to the measurements of the Si-2*p* core-level shifts using XPS during this deposition, the surface E_F does not shift significantly (Fig. 76(b)), thus remaining in the depleted condition at the surface space-charge layer [7,142]. These surface E_F shifts are similar to the Ag deposition case as shown in the data points in Fig. 76(b). Therefore, the surface space-charge layer is not a reason for the resistance decrease observed in Fig. 76(a). As mentioned above, the Au deposition does not induce any superstructures, so that the surface-state bands do not appear. Then, the resistance decrease should be explained by conduction through conductive islands (Au silicide) grown on the surface. It is shown from

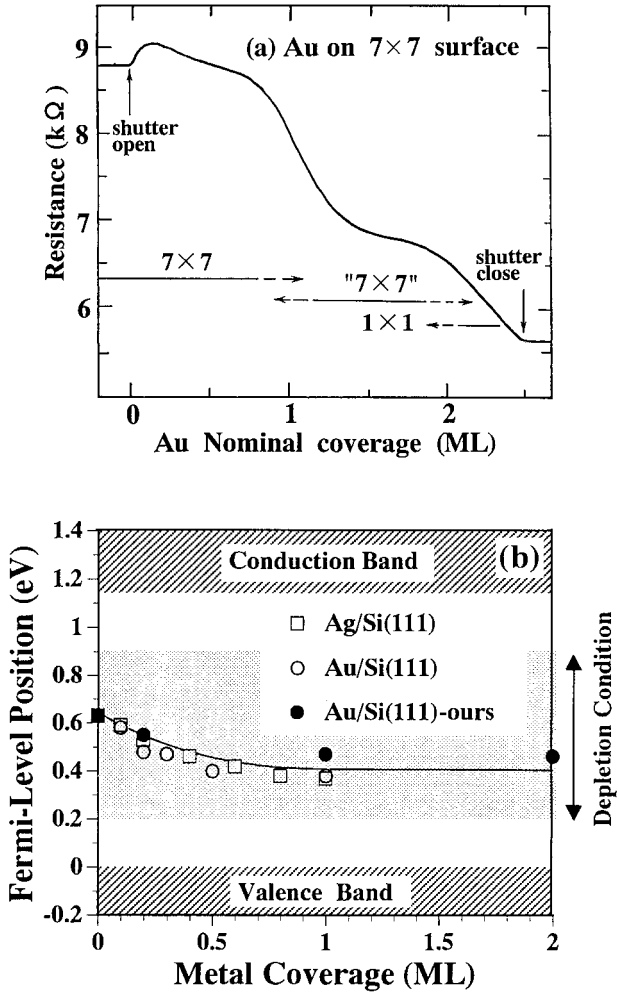

Fig. 76. (a) Resistance change and corresponding RHEED patterns of a Si wafer during RT deposition of Au onto the Si(111)-7 × 7 clean surface. (b) Shifts of the surface E_F position during Au and Ag depositions onto the 7 × 7 surface, determined by Si 2*p*core-level shifts. Open circles and squares are taken from Refs. [142] and [108], and the solid circles are from Ref. [13].

the photoemission analysis of Au 4*f* level that the reaction between Au and Si occur only beyond the Au coverage of around 1 ML [126].

In summary, the conductive metal islands grown densely on the surface have a dominant role in the resistance changes during the Au deposition at RT onto the 7 × 7 clean surface. The surface space-charge layer and the surface-state bands of the substrate seemed to scarcely contribute to the resistance changes in this case.

6.5. On the 5 × 2-Au substrate

Fig. 77 shows the resistance changes during Au and Ag depositions onto the 5 × 2-Au substrate at RT. At a glance, both look quite similar, but quite different from those for the cases of the deposition onto the Si(111)-7 × 7 clean surface (Figs. 76(a) and 38(a)). As soon as the deposition is started, the resistance steeply increases by about 20% with only 0.2 ML coverage of metals in Fig. 77. This coverage range corresponds to a minor change in the RHEED pattern; the half-order streaks in the 5 × 2 pattern (see Fig. 69(c)) disappears, converting into a 5 × 1 structure. Passing through the maximum, the resistance begins to drop, and the 5 × 1 structure disappears with further deposition.

Fig. 78(a) shows the resistance change during cycles of Au deposition onto the 5 × 2-Au surface at RT and the interruption of deposition. The resistance changes during deposition periods are similar to those shown in Fig. 77(a). During the interruption periods, the resistance remains almost constant. During these interruption periods, XPS spectra from Si 2*p* core level are measured at each coverage. With an additional Au coverage of 0.2 ML, corresponding to the resistance maximum in Fig. 77(a), the core level shifts to a larger binding energy by 0.15 eV from that at the initial 5 × 2-Au surface, and returns almost to the initial position at 1 ML coverage. As shown in Fig. 78b), this means that the E_F position at the surface shifts upwards by 0.15 eV from its initial position, and then returns to its initial position with further increase of Au coverage. By tracing these

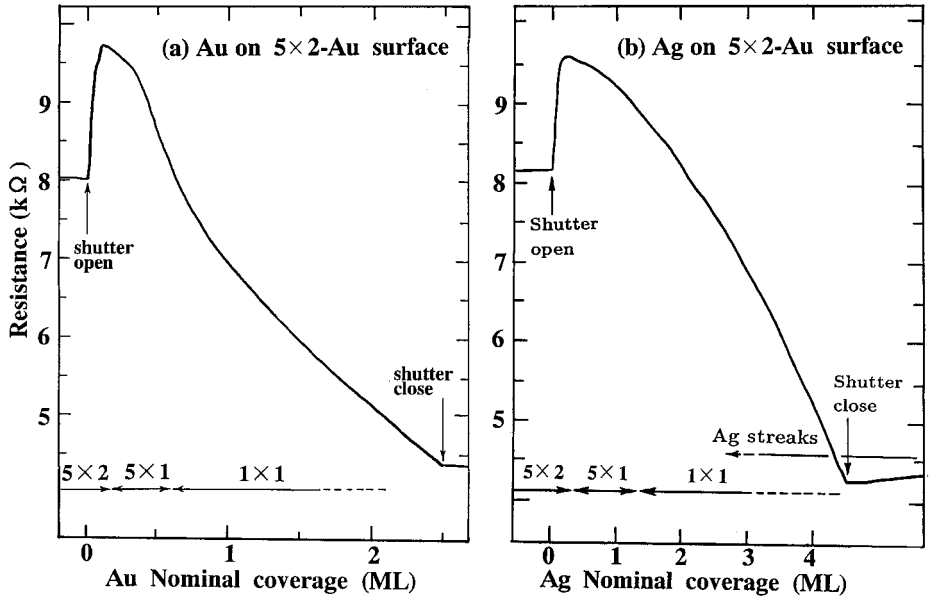

Fig. 77. Resistance changes of a Si wafer and corresponding RHEED patterns during RT depositions of (a) Au and (b) Ag onto the Si(111)-5 × 2-Au surface. From Ref. [13].

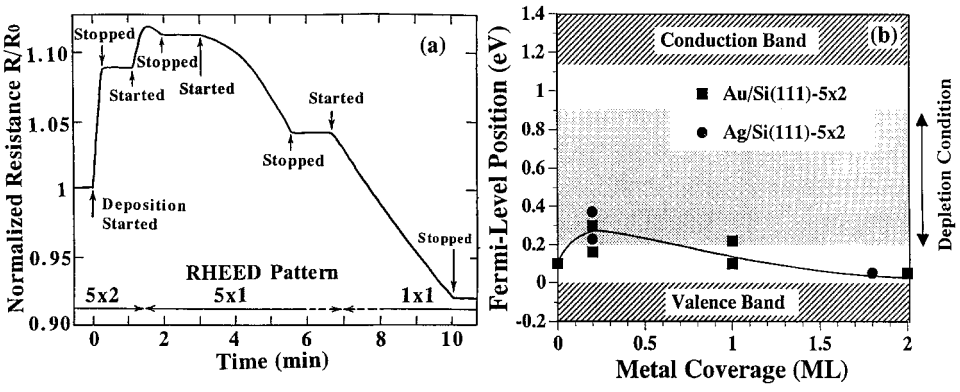

Fig. 78. (a) Resistance changes of a Si wafer with a 5×2-Au surface during a cycle of deposition and interruption of additional Au at RT. (b) Shifts of the surface E_F position during the Au deposition, measured by XPS. From Ref. [13].

shifts in the surface-E_F position in Fig. 75, the measured change in conductance $\Delta\sigma$ can be understood in terms of changes in the surface-space-charge-layer conductance $\Delta\sigma_{SC}$. The hole-accumulation situation at the initial 5×2-Au surface is converted into a depletion-layer condition by 0.2 ML-Au adsorption, resulting in an resistance increase. When the observed resistance rise in Fig. 77(a) is converted to the conductance decrease, $\Delta\sigma \sim -2 \times 10^{-5}$ S/□. This value is nearly expected one from the calculated curve in Fig. 75 when the E_F shifts to a position at the conductance minimum, around 0.25 eV above the VBM from the initial position at 0.13 eV.

This direction of the E_F shift means that additional Au atoms create donor-like surface electronic states to diminish the holes in the surface space-charge layer, in other words, to flatten the band. The same mechanism occurs in the resistance changes for the Ag adsorption on the 5×2 surface (Fig. 77(b)). With further adsorption of Au, the surface space-charge layer returns to a hole-accumulation layer as seen in Fig. 78(b), and simultaneously a metallic Au-silicide layer is formed, resulting in the steep decrease in resistance after the peak at 0.2 ML in Fig. 77(a).

In summary, in the early stages of both the Au and Ag depositions onto the Si(111)-5×2-Au surface at RT, the resistance changes can be explained by the surface space-charge layers; the initial hole-accumulation condition converts into the depletion condition by adsorption of only 0.2 ML of the additional metals, and then returns to a hole-accumulation condition by their further depositions.

6.6. On the other substrates

Also during Au depositions onto the α-$\sqrt{3} \times \sqrt{3}$-Au, β-$\sqrt{3} \times \sqrt{3}$-Au, and 6×6-Au surfaces at RT, the resistance changes are measured as a function of the additional Au coverage as shown in Fig. 79 [3]. Remarkable increases in resistance

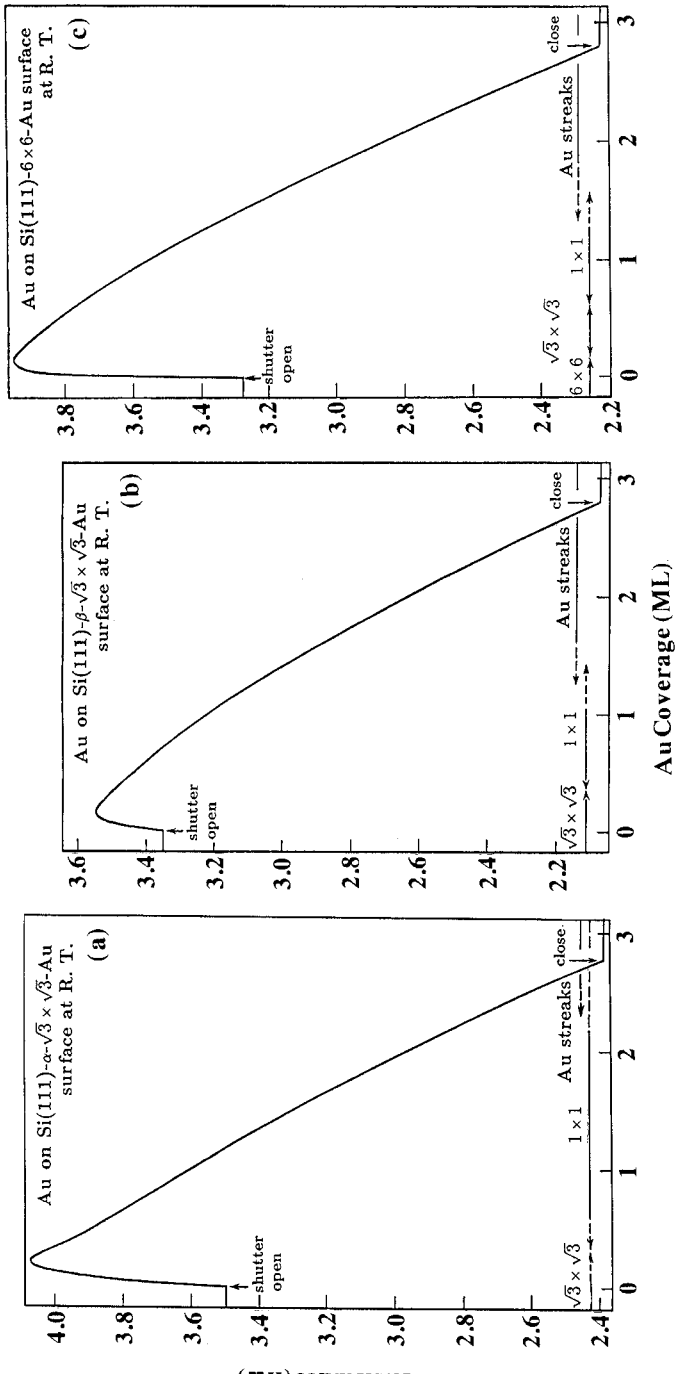

Fig. 79. Resistance changes of a Si wafer and corresponding RHEED patterns during RT depositions of additional Au onto the (a) Si(111)-α-$\sqrt{3} \times \sqrt{3}$-Au, (b) β-$\sqrt{3} \times \sqrt{3}$-Au, and (c) 6×6-Au surfaces, respectively. From Ref. [3].

are observed just after starting the deposition for all of the surfaces. After reaching the maxima, the resistances steeply drops with increase of Au coverage. These features are quite similar to the case on the 5×2-Au surface in Fig. 77(a). The RHEED patterns of the initial superstructures disappear with less than 1 ML depositions for all cases, resulting in similar patterns with only 1×1 fundamental spots. The decrease rates of the resistance beyond 1 ML coverages are also similar for all the surfaces, which suggests that the resulting surface layers, probably Au silicide [126], have similar structures irrespective of the initial surface structures. This is contrasted to the Ag (Section 4) and In (Section 7) cases in which the initial surface superstructures of the substrate strongly affect the nature of the metal layers grown on them at RT. This difference between Au and Ag/In cases may originate from the difference in reactivity with Si.

Since photoemission data for band-bending measurements are lacking for these surfaces, the mechanism of the observed resistance changes can not be discussed at the moment. But, it is likely that for the α-$\sqrt{3} \times \sqrt{3}$-Au surface in Fig. 79(a), the resistance change may be governed by the changes of the band bending as in the case of the 5×2-Au surface in Section 6.5, because the surface E_F position of the initial α-$\sqrt{3} \times \sqrt{3}$-Au surface is located so near the VBM that its surface space-charge layer is a hole-accumulation layer having higher conductance, which will change into a depletion layer by additional Au adsorption, as in the case on the 5×2-Au surface. This may be the reason for the initial remarkable resistance rise, which should be confirmed by band-bending measurements with photoemission.

On the other hand, such a mechanism of band bending can not be applied for the β-$\sqrt{3} \times \sqrt{3}$-Au and 6×6-Au surface in Fig. 79(b) and (c), because their surface space-charge layers are depletion layers as indicated by their E_F positions in Fig. 75. As suggested in Section 6.3, these two surfaces have excess conductances because of their metallic surface-state bands. Hence, it is speculated that the initial resistance rises observed in Fig. 79(b) and (c) is due to a killing of the surface-state bands by the additional Au adsorptions.

6.7. Summary

Au/Si(111) system exhibits several well-defined surface superstructures which have different surface conductances higher than the 7×7 clean surface. The reason for the higher surface conductance is mainly the band bending below the surface for the 5×2-Au and α-$\sqrt{3} \times \sqrt{3}$-Au surfaces, while metallic surface states make the conductance higher on the β-$\sqrt{3} \times \sqrt{3}$-Au and 6×6-Au surfaces. Additional Au adsorptions onto these Au-induced superstructures show characteristic conductance changes which are common for all of the superstructure, but quite different from on the 7×7 clean surface. These phenomena comes from the difference of the surface electronic structures and band bending in the subsurface region. Beyond monolayer coverage of additional Au, the nature of the grown atomic layers (Au silicide) are similar irrespective of the starting substrate superstructure. This should be contrasted to the depositions

of nonreactive species such as Ag and In in which the growth styles of atomic layers are quite sensitive to the substrate surface structures.

7. Indium adsorption

7.1. In-induced surface superstructures

Since the first report by Lander and Morrison [143], group-III metal (Al, In, Ga)-adsorbed Si(111) surfaces have been investigated as intensively as noble-metal/Si(111) systems because of their wide variety of surface phases appearing [1]. Three kinds of superstructures, $\sqrt{3} \times \sqrt{3}$, $\sqrt{31} \times \sqrt{31}$, and 4×1, which appear by In adsorption onto the Si(111)-7×7 surface with heat treatments [144,145], are most frequently investigated in the literature, though other surface phases such as $\sqrt{7} \times \sqrt{3}$, 2×2, and 1×1 ($R30^\circ$) are known to appear with special preparation procedures as described in Section 7.3. Fig. 80 shows a surface-phase diagram on Si(111) as functions of In coverage and substrate temperature [144]. RHEED patterns and STM images of the respective superstructures are shown in Fig. 81.

Of these phases, the nature of the $\sqrt{3} \times \sqrt{3}$-In has been studied in most detail. Its saturation coverage of In is determined to be 1/3 ML, i.e., one In adatom in the $\sqrt{3} \times \sqrt{3}$-unit cell, so that only one protrusion is observed in the $\sqrt{3} \times \sqrt{3}$ unit cell in STM images (Fig. 81(b)). Then, this trivalent atom can entirely satisfy all the dangling bonds of the substrate Si atoms. Al- and Ga-induced $\sqrt{3} \times \sqrt{3}$ phases are also considered to be the same structure. From a first-principles calculation of the total energy, Northrup [148] found two atomic sites for Al to be in the lowest

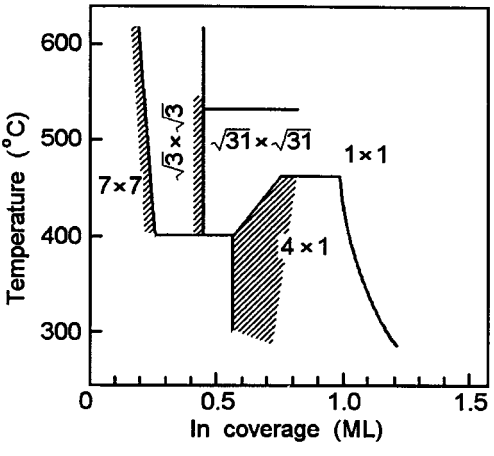

Fig. 80. A phase diagram of In/Si(111) system determined by RHEED. The shaded areas are transition regions between neighboring two superstructures at which the superspots of both coexist in RHEED. These superstructures do not change by cooling down to RT once they are formed at high temperatures indicated. Reproduced with permission from Ref. [144].

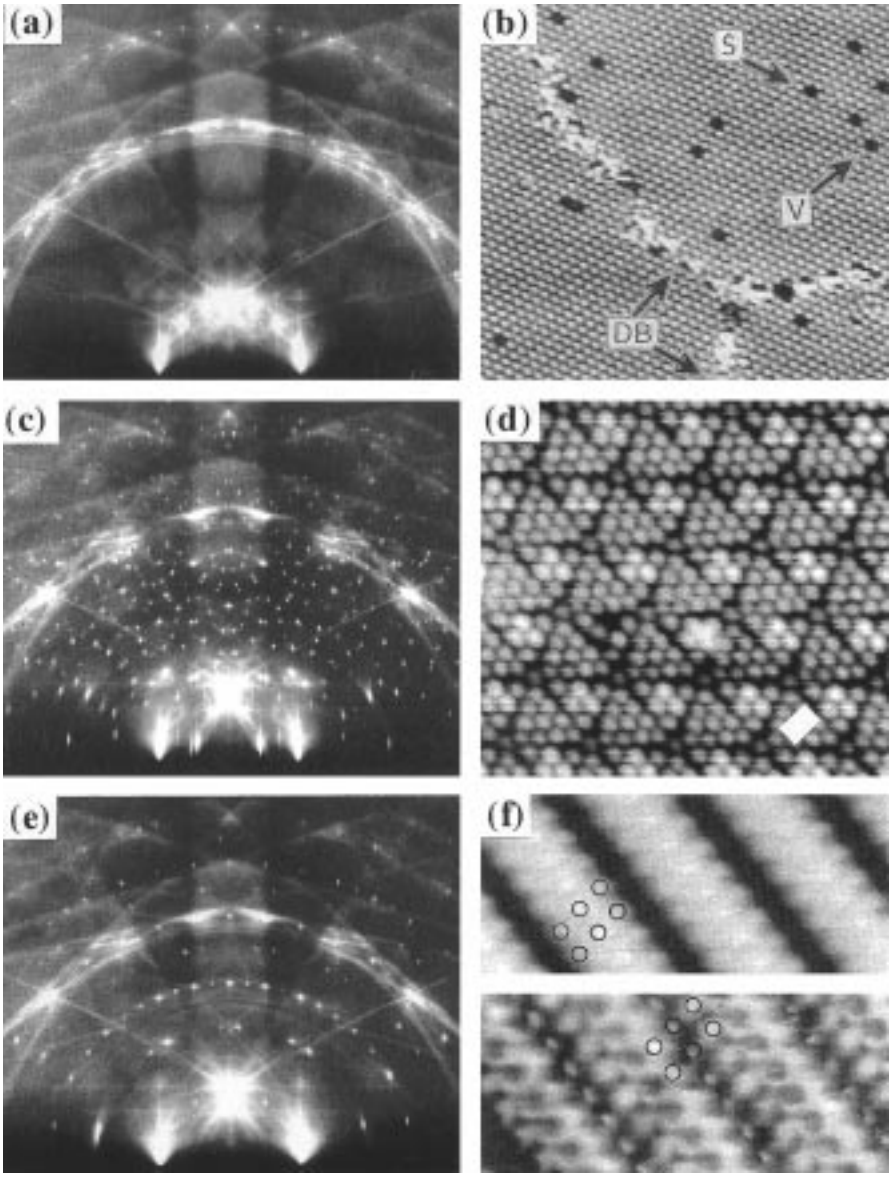

Fig. 81. RHEED patterns and STM images of (a) and (b) $\sqrt{3}\times\sqrt{3}$, (c) and (d) $\sqrt{31}\times\sqrt{31}$, and (e) and (f) 4×1 superstructures on In/Si(111) surface. (b) An empty-state image ($V_t=-2.28$ V, $I=0.06$ nA, 25 $\times$ 20 nm), (d) an empty-state image ($V_t=-1.85$ V, $I=0.42$ nA, 10×10 nm), (f) upper panel; a filled-state image ($V_t=0.1$ V, $I=0.7$ nA, 5×2.5 nm), lower panel; an empty-state image ($V_t=-0.04$ V, $I=0.08$ nA, 5×2 nm). The STM images are reproduced with permission from Refs. [179,180,147].

energy states; threefold hollow site (H_3 model) and threefold on-top site of the second-layer Si atom (T_4 site). Since the both models lead to similar electronic states, *angle-resolved photo-emission spectroscopy (ARPES)* [149,150] could not differentiate between them. STM observations revealed no evidence of coadsorption on H_3 and T_4 sites on different areas of any single images [151]. Ion scattering spectroscopy experiments suggest the T_4 model for the $\sqrt{3} \times \sqrt{3}$-In to be more plausible [152]. The Si(111)-$\sqrt{3} \times \sqrt{3}$-Ga structure is also determined as T_4 geometry by LEED analysis [153]. Northrup's energy-minimization calculations for the $\sqrt{3} \times \sqrt{3}$-Al also favor the T_4 structure by 0.3 eV/adatom compared with the H_3 arrangement if including the completely relaxed geometries. Thus the $\sqrt{3} \times \sqrt{3}$ structures on Si(111) surface induced by the group-III metals are now believed to be in the T_4 arrangement. The most positive confirmation of the T_4-bonding site was given in an STM examination of a phase boundary between the 7×7 clean and $\sqrt{3} \times \sqrt{3}$-In regions at a lower In coverage [154].

Surface-state bands for the $\sqrt{3} \times \sqrt{3}$-In surface are plotted as a 2D dispersion mapping in Fig. 82, together with Al- and Ga-induced $\sqrt{3} \times \sqrt{3}$ structures [155]. All of the three surfaces have similar electronic structures, a semiconducting feature with energy gaps of 1–2 eV between an empty state S_1' and filled state S_2. A dispersionless state S_1 near E_F is attributed to a defect of Si adatoms substituting for metal adatoms [146] which are actually observed as dark dots in Fig. 81(b). In terms of atomic orbitals, the two occupied bands S_2 and S_3 correspond to p_z orbitals on the Si atoms (which comes from the dangling bonds), which are coupled with p_x and p_y orbitals on the group III atoms. In this way, all the dangling bonds are saturated, resulting in a semiconducting surface.

Around 0.5 ML and 0.7–1 ML coverages, the $\sqrt{31} \times \sqrt{31}$ and 4×1 structures are completed, respectively, as shown in Fig. 80. But unfortunately there are no generally-accepted structural models for these phases, though plausible models

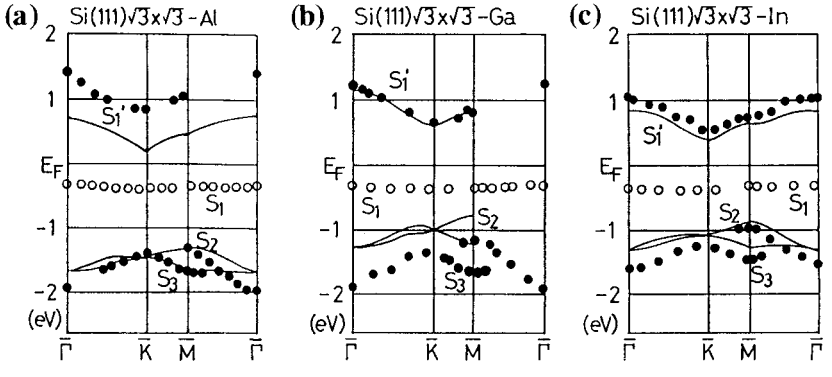

Fig. 82. 2D dispersions of the surface-state bands of (a) S(111)-$\sqrt{3} \times \sqrt{3}$-Al, (b) $\sqrt{31} \times \sqrt{31}$-Ga, and (c) $\sqrt{31} \times \sqrt{31}$-In surfaces. Solid curves are for theoretical calculations by Northrup [148]. The energy distance E_F-E_{VBM} is assumed to be 0.8, 0.5, and 0.5 eV for the respective surfaces. Reproduced with permission from Ref. [155].

have been proposed recently for the 4×1-In phase [156,157]. Although the arguments on the atomic arrangement is not yet settled down on the 4×1-In phase, its electronic structure is known to have a peculiar feature; ARUPS [158] and angle-resolved IPES [159] have revealed its 1D metallic character along the stripes in its STM image (Fig. 81(f)). It is insulating in the direction perpendicular to the stripes. Furthermore, by cooling the 4×1-In phase, it is found to undergo a phase transition into a 8×2 superstructure around 130 K [160]. This transition is clarified to be a Peierls transition due to the one-dimensional metallic character of the surface; the nesting vector and metal–nonmetal transition are confirmed by ARUPS.

After the completion of the 4×1 structure, epitaxial growth of ordered In islands is observed at still higher coverages [151]; the In adatoms on top of this phase easily moves as revealed in electromigration studies [161].

7.2. On the 7×7 clean substrate

During In deposition onto Si(111) surfaces, the atomic and electronic structural evolutions, and accordingly the change in electrical conductance are quite different depending on the substrate surface structures, which are comparatively shown with the 7×7-clean substrate in this subsection and with the $\sqrt{3} \times \sqrt{3}$-In substrate in the next subsection.

7.2.1. Atomic structural evolutions

7.2.1.1. At RT. Fig. 83 shows a series of RHEED patterns with continuous In deposition onto the clean 7×7 surface at RT. Around 0.3 ML coverage of In (Fig. 83(b)), the relative intensities among the 7×7 superlattice reflections change from those of the clean 7×7 surface (Fig. 83(a)); for example, similar intensities of the superlattice spots on the 0th Laue zone in (b) should be compared with those in (a) where the $\frac{3}{7}$ th and $\frac{4}{7}$ th spots are especially strong. With further adsorption of In, the 7×7 super-reflections gradually blur (Figs. 83(c)–(e)), and finally disappear around 4 ML coverage.

This process is revealed in more detail as changes in integrated intensities of the 7×7 superlattice spots as a function of In deposition time (Fig. 84). The blurring processes of the spots are not simple. Some superlattice spots temporarily increase their intensities during In adsorption, while other spots monotonically fade out. The temporal intensity maxima of the spots occur at two different coverages; about 0.2 ML (95-sec deposition time, indicated by "A") and 0.3 ML (145 sec, indicated by "B"). The changes of the relative intensities among the superlattice spots mean some structural modifications in the 7×7-unit cell. Fig. 85 shows qualitatively estimated intensity of each superlattice spot in the $[11\bar{2}]$-incidence RHEED pattern from (a) a clean 7×7, and (b) and (c) are with In adsorption of coverages indicated by "A" and "B", respectively, in Fig. 84. For the clean 7×7 surface, the $(\frac{3}{7},\frac{3}{7})$-th and $(\frac{4}{7},\frac{4}{7})$-th fractional-order reflections show extra intensities, which originate from the adatom array in a 2×2 periodicity in the DAS structure

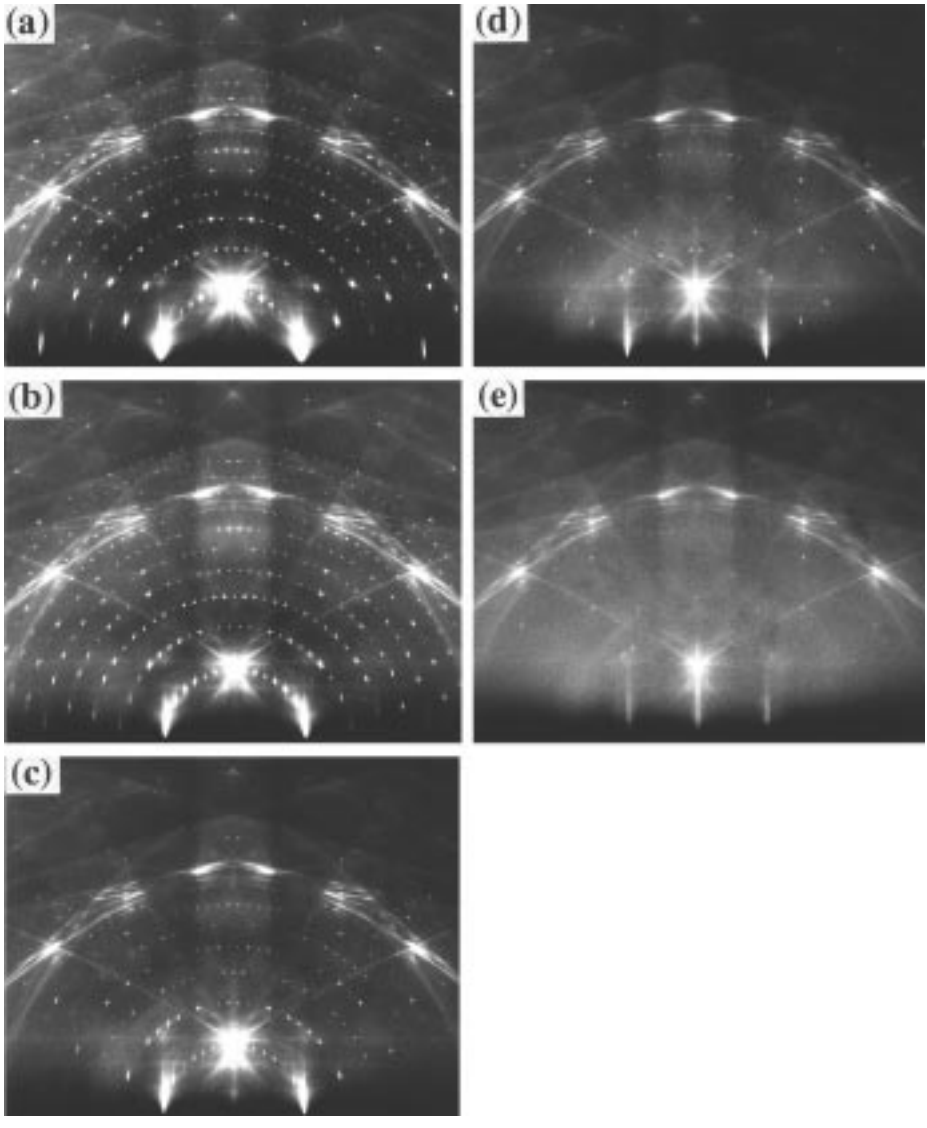

Fig. 83. A series of RHEED patterns during In deposition onto the clean Si(111)-7 × 7 surface (a) at RT. In coverages are around (b) 0.3 ML, (c) 0.7 ML, (d) 1.2 ML, and (e) 3 ML. In the 7 × 7 superlattice spots blurring out, the relative-intensity ratios among them changes with coverage increase [162].

[140]. This feature is reproduced by a kinematical calculation with atomic coordinates determined by Horio and Ichimiya [163] based on the DAS structure, as shown in Fig. 85(d). This intensity distribution totally changes by In adsorption of sub-monolayer coverage. The distribution in Fig. 85(c), in which the $(\frac{3}{7},\frac{4}{7})$ spot

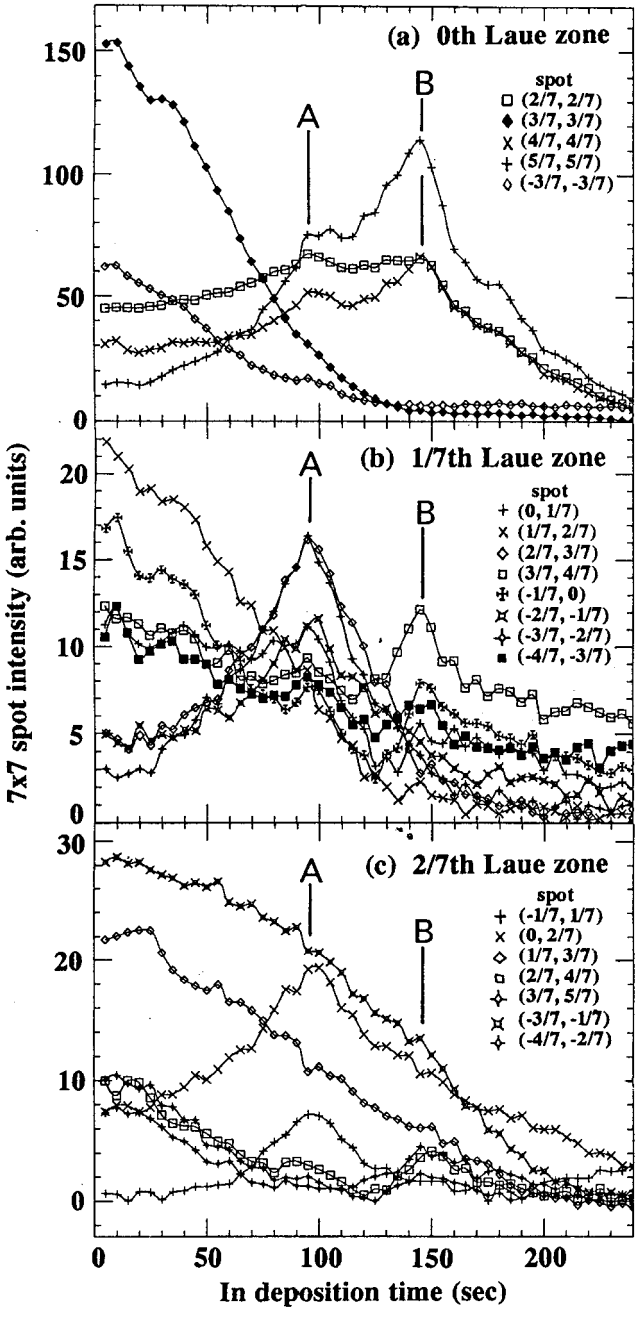

Fig. 84. Changes in the integrated intensities of the superlattice spots on the (a) 0-th, (b) $\frac{1}{7}$ th, and (c) $\frac{2}{7}$ th Laue zones, respectively, in the [11$\bar{2}$]-incidence RHEED patterns during the In deposition onto the clean Si(111)-7 × 7 surface at RT. The deposition rate was around 0.13 ML/min [162].

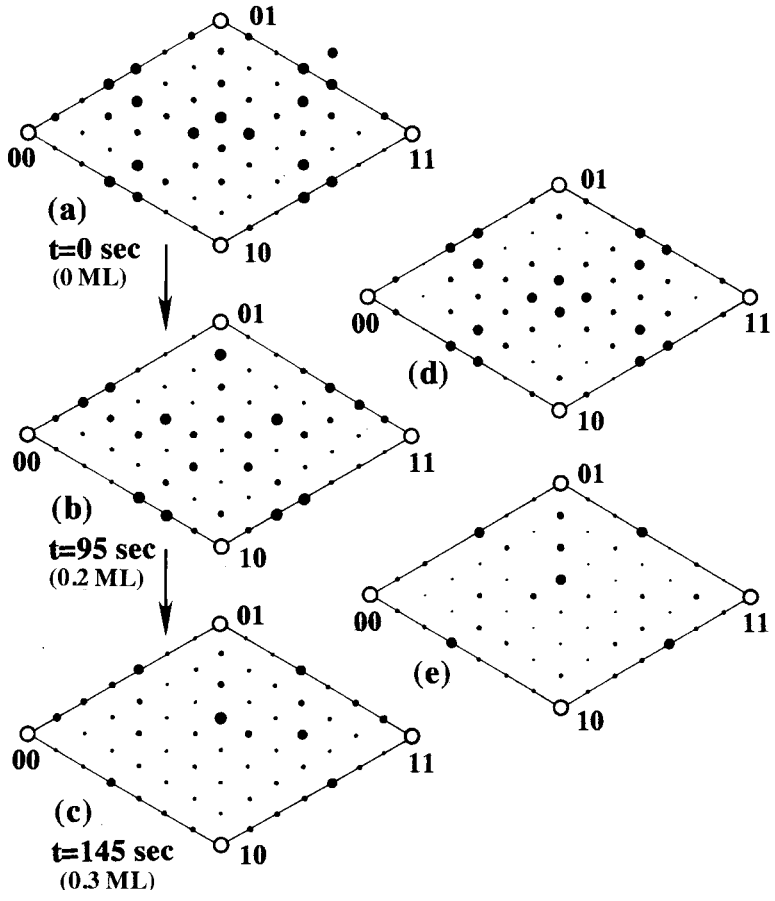

Fig. 85. Two-dimensional reciprocal lattices presenting qualitatively estimated relative intensities of the 7×7 superlattice spots during In adsorption at RT. (a) is for the clean Si(111)-7×7 surface. (b) and (c) are for the surface with In adsorption of coverages indicated by "A" and "B" in Fig. 84, respectively. (d) and (e) are kinematically calculated ones for the clean 7×7-DAS surface and for the 7×7 without adatoms, respectively [162].

is especially strong and the ($\frac{3}{7}$,*smallfrac*17) spot is weakened, is well simulated by a similar kinematical calculation as shown in Fig. 85(e) if adatoms are neglected from the 7×7-DAS structure in the calculation. Then it is concluded that In adsorption of submonolayer coverage makes the 2×2-adatom array in the DAS unit cell random, remaining a 7×7 periodicity with only the dimer-stacking-fault framework. The transient structure corresponding to an intensity distribution in Fig. 85(b) with smaller In coverage is not yet characterized.

With further deposition of In onto the RT substrate, extra streak-like spots appear just outside the Si bulk fundamental spots in RHEED [16]. These extra spots indicate the growth of In islands whose surfaces have a hexagonal structure

with lattice constant 3.4 Å and have the same orientation with respect to the substrate. The structure of bulk In has a face-centered tetragonal structure and its (111) face has a distorted hexagonal structure with lattice constants 3.25 and 3.38 Å. So the surface structure of the In islands is regarded as a pseudomorphic structure very similar to the (111) face of bulk indium.

Indium on the 7×7 surface at RT is known to grow in the Stranski–Krastanov growth mode [164,165]; the first (sub)monolayer of In covers the whole surface (with randomization of the Si adatoms in the DAS structure as mentioned above), and then 3D In islands begin to grow. STM observations [164,165] show that the large In islands sparsely distribute on the wetting layer and that the surface of these islands has hexagonal structure with lattice constant 3.29 Å with standard deviation 0.22 Å, which is consistent with the RHEED observations mentioned above.

7.2.1.2. At low temperatures. At the initial stage of In adsorption at a substrate temperature below 150 K, the 7×7 fractional-order spots in the RHEED patterns are weakened gradually with In coverage, and disappear around 2 or 3 ML, just leaving the Si fundamental 1×1 spots, which is a similar behavior at RT described above. With further deposition at 100 K, broad streaks come out in RHEED, which are typical patterns from a mosaic structure [16]. This pattern indicates that In islands become much smaller in size and higher in their number density, compared with the RT case. The small islands are observed by low-temperature STM to be nanometer-sized flat islands [172], while at RT large In islands having flat pseudomorphic (111) face of In crystal distribute sparsely on the first In layer [164,165]. As described in Section 7.2.3, the critical coverages for electrical percolation are quite different between at RT and 100 K due to the differences in the island density.

7.2.1.3. At elevated temperatures. At elevated temperatures, completely different restructurings proceed during continuous In deposition onto the 7×7 clean surface. As shown in the phase diagram of Fig. 80, the $\sqrt{3} \times \sqrt{3}$, $\sqrt{31} \times \sqrt{31}$, and 4×1 superlattice structures are successively formed with coverage increase. Sequences of domain conversions among these surface superstructures sensitively depend on the substrate temperatures. Fig. 86 shows the intensity changes of each superlattice spot in RHEED as a function of nominal In coverage at various substrate temperatures [162]. The abscissa, In coverage, is calibrated in a way that the maximum intensity of the $\sqrt{3} \times \sqrt{3}$ spot corresponds to $\frac{1}{3}$ ML coverage. This is based on a plausible assumption that the sticking probability of In atoms in forming the $\sqrt{3} \times \sqrt{3}$-In phase is always unity at every temperatures (though it is not always unity after the completion of the $\sqrt{3} \times \sqrt{3}$-In phase). The 7×7 phase converts to the 4×1 through a 1×1 phase at 400°C (a), or $7 \times 7 \rightarrow \sqrt{3} \times \sqrt{3} \rightarrow \sqrt{31} \times \sqrt{31} \rightarrow 4 \times 1$ at 450°C (b), while the 4×1 structure does not appear at higher temperatures. This is consistent with the phase diagram of Fig. 80. At 520°C (d), a newly found phase, a $\sqrt{43} \times 4$, appears in a narrow range of coverage between the $\sqrt{3} \times \sqrt{3}$ and the $\sqrt{31} \times \sqrt{31}$ phases. At still higher temperatures, 570°C (e), only the

$\sqrt{3} \times \sqrt{3}$ phase is found. By carefully examining this figure, some points are noticed:

1. A simple expectation is that the maximum intensity of each superlattice structure corresponds to its saturation coverage; the whole surface is covered

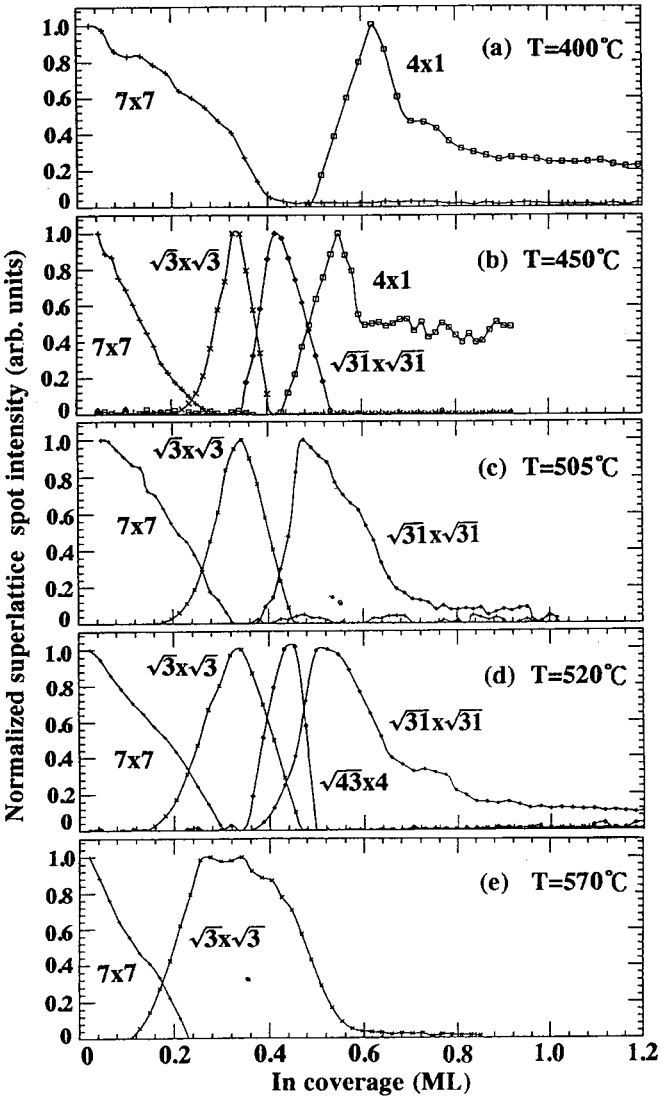

Fig. 86. Growth and decay in the integrated normalized intensity of each superlattice spot appearing during In deposition onto the clean Si(111)-7 × 7 surface at various temperatures as a function of In coverage [162].

with the superstructure. But the maximum-intensity coverage changes depending on the temperature; for the 4×1 spot, the intensity peak is at 0.62 ML at 400°C (a), while it is 0.55 ML at 450°C (b). For the $\sqrt{31} \times \sqrt{31}$ spot, the intensity maximum appears at 0.42 ML at 450°C (b), 0.48 ML at 505°C (c), and 0.52 ML at 520°C (d). These temperature dependences of the nominal saturation coverages are caused by changes in the sticking probability of the deposited In atoms and/or changes in the domain sizes of each superlattice structure; sticking probability of In atoms on top of the $\sqrt{3} \times \sqrt{3}$-In surface can be reduced at higher temperatures.

2. For the 4×1 spots in (a) and (b), their intensity does not drop down to zero, rather remains a smaller constant, after passing through the intensity maximum, while the spots of the $\sqrt{31} \times \sqrt{31}$ (c) and $\sqrt{3} \times \sqrt{3}$ (e) swiftly completely disappear to become a 1×1 with coverage increase. This means a formation of 3D islands on top of the 4×1 layer in (a) and (b), which scarcely cover the surface, while 2D In layers grow on the $\sqrt{31} \times \sqrt{31}$ and $\sqrt{3} \times \sqrt{3}$ phases in (c) and (e), destroying the superlattices.
3. The areal fractions of domains of the respective superstructures, $\sqrt{3} \times \sqrt{3}$, $\sqrt{31} \times \sqrt{31}$, and 4×1, in (b) seem to change linearly with increase of In coverage; the sum of the normalized intensities of the two interchanging structures is always almost unity and the intensity curves intersect with each other around the middle. But the transition from the 7×7 to the $\sqrt{3} \times \sqrt{3}$ phases is not the case; the $\sqrt{3} \times \sqrt{3}$ spot emerges only after that the intensity of the 7×7 spot decreases down to *smallfrac*15–$\frac{1}{10}$ of the initial intensity. This phenomenon is seen also at high temperatures (c)–(e). This means that the 7×7 domain does not directly convert to the $\sqrt{3} \times \sqrt{3}$ domain; a transient 1×1 phase is created, and more than a critical coverage is necessary for the formation of the $\sqrt{3} \times \sqrt{3}$ domains to be detectable by RHEED.

The average size of the $\sqrt{3} \times \sqrt{3}$ domain can be estimated from its spot sharpness [166]. Figs. 87(a) and (b) show the profiles of the $\sqrt{3} \times \sqrt{3}$-superlattice spot during its growth with In adsorption at the substrate temperatures of (a) 430°C and (b) 570°C, respectively [162]. The spot in (b) is evidently sharper, meaning larger $\sqrt{3} \times \sqrt{3}$ domains. These spot profiles are fitted with a Lorentzian function, and the *full width of half maximum* (FWHM) of each spot is deduced. Fig. 87(c) shows the changes of the FWHM as a function of In coverage at various substrate temperatures. While the spot width remains a small constant at 570°C, at lower temperatures (410, 430, and 510°C), the broader peaks at smaller coverages become sharper with coverage increase. This means that the domains of the $\sqrt{3} \times \sqrt{3}$, of which size is larger than the coherence length of the electron beam, is formed from the beginning at 570°C, whereas domain growths of smaller ones proceed at lower temperatures. This is caused by elongation of the diffusion length of impinging In atoms and also by decrease of their nucleation probability on the surface with temperature increase.

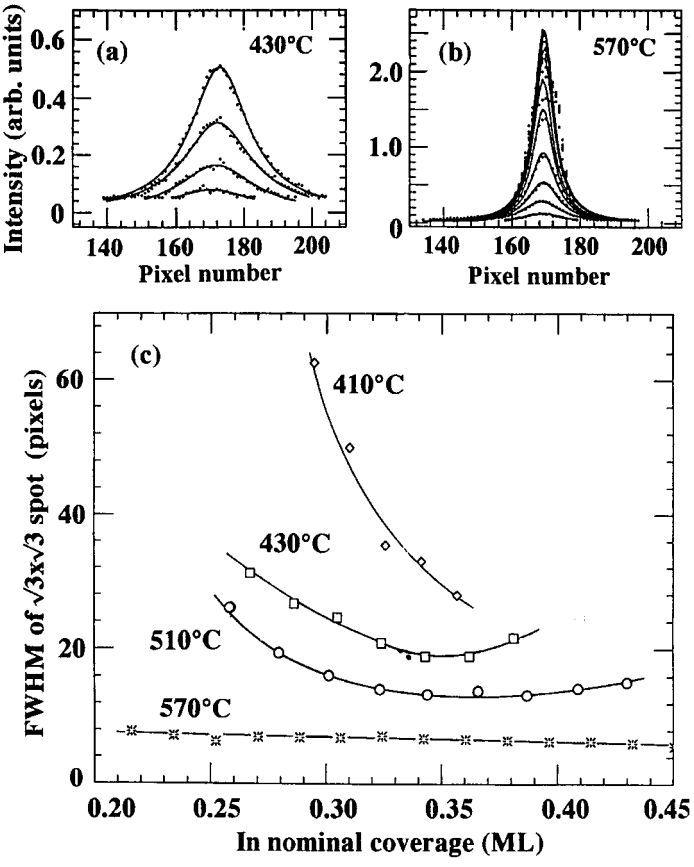

Fig. 87. (a) and (b) are the changes in profiles of the $\sqrt{3} \times \sqrt{3}$ spot along a vertical direction in [11$\bar{2}$]-incidence RHEED pattern during growth by In deposition at 430°C and 570°C, respectively. (c) The In-coverage dependence of the full width of the half maximum (FWHM) of the $\sqrt{3} \times \sqrt{3}$ superlattice spots at various substrate temperatures [162].

7.2.2. Electronic-state evolutions

Fig. 88(a) shows UPS spectra taken from the clean Si(111)-7×7 surface (dashed curve), and the surfaces with In deposition (solid lines) of different coverages onto the 7×7 at RT [167]. The E_F position is determined by linear interpolation of the photoelectric edge of a tantalum sheet in contact to the sample. Since the peak lying 4.8–5 eV below E_F originates from a feature of the bulk silicon [168,169], all the curves in the figure are plotted keeping this peak position constant. From these spectra, two facts are noticed. The first is that the distance between the bulk-silicon peak and E_F decreases with In coverage. This indicates a change in the relative position of E_F at the surface, which is shown in Fig. 88(b). This means that some band bending occurs (see Fig. 20). Fig. 88(b) indicates that E_F at the surface shifts from at 0.63 eV to at 0.26 eV above the VBM with about 2 ML In

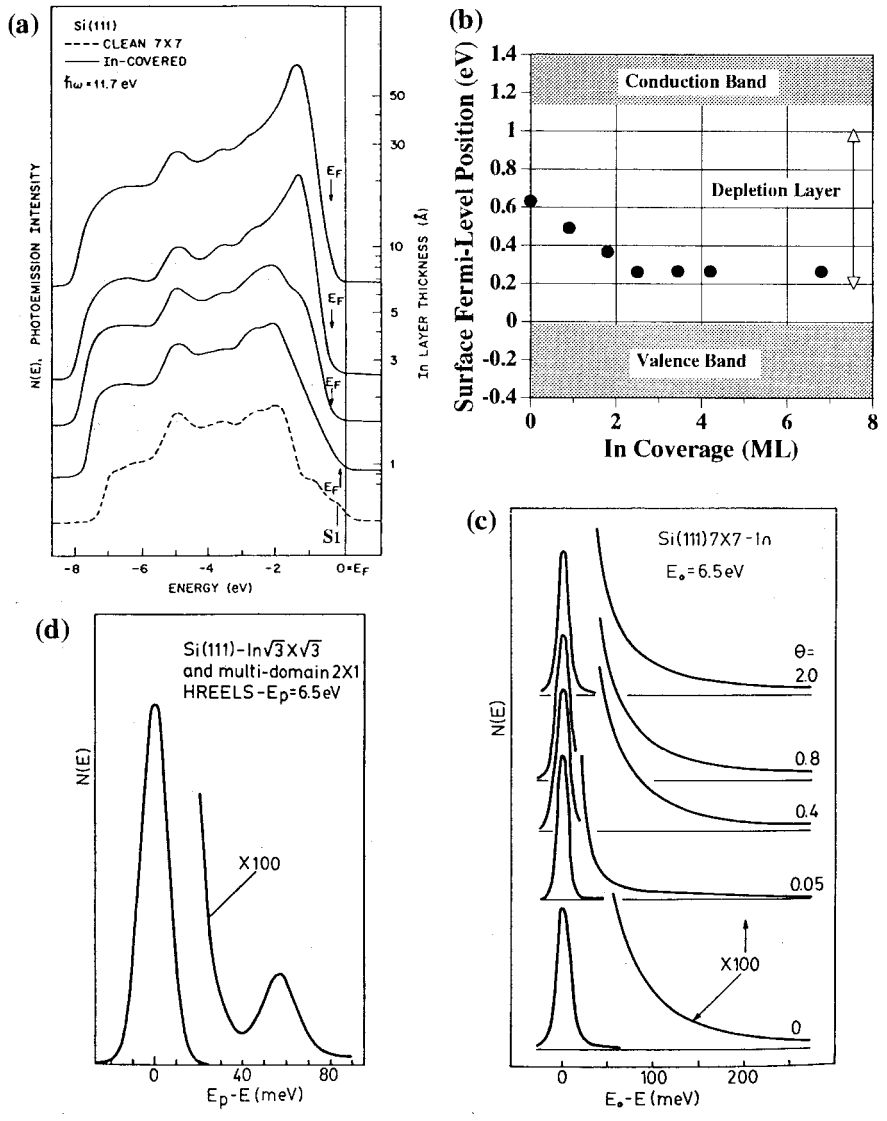

Fig. 88. (a) UPS spectra from the clean Si(111)-7 × 7 surface (dashed curve) and In-covered surfaces (solid curves) with different coverages [167]. (b) Energy positions of the surface Fermi level E_F as a function of In coverage, determined by UPS [167]. (c) High-resolution electron-energy-loss spectra taken in sequence of In adsorption onto the clean Si(111)-7 × 7 surface [170], and (d) that for the Si(111)-$\sqrt{3} \times \sqrt{3}$-In surface [171]. Reproduced with permission from the respective references.

adsorption. According to Fig. 8, then, these E_F positions indicate that the surface space-charge layer remains within the depletion situation. Even when the In coverage increases up to 10 ML, the space-charge layer still remans the same as that at 2 ML coverage; the E_F is located around 0.26 eV above the VBM.

Another phenomenon to be noticed in the spectra in Fig. 88(a) is that In of less than 1 ML coverage causes a marked reduction of the density of S_1 state near E_F on the 7×7 surface (see also Fig. 5(a)). As suggested by the intensity analysis of RHEED spots in Fig. 85, the adsorbed In atoms remove the Si adatoms in the DAS structure, so that the dangling-bond state S_1 of the adatoms disappears. Indium-induced interface states grow in the valence-band energy region, well below E_F. This process is common to other simple-metal adsorption such as shown in Fig. 39(b) for Ag case. This observation leads to a simplistic model of Schottky–Barrier formation that a large DOS exist at E_F for pinning throughout the formation process. The nature of these states change from clean-surface to metal-induced type.

Figs. 88(c) and (d) show high-resolution electron-energy-loss spectra taken in sequence of In adsorption onto the clean Si(111)-7×7 surface at RT(c) [170] and Si(111)-$\sqrt{3} \times \sqrt{3}$-In surface (d) [171]. The spectrum of the clean 7×7 surface has the characteristic tail on the right-hand side of the primary peak in (c), which means metallic nature of the surface. This is contrasted to the spectrum of the $\sqrt{3} \times \sqrt{3}$-In surface in Fig. 88(d) where little elastic tail is observed. The metallic tail of the 7×7 surface is quickly suppressed by only 0.05 ML In adsorption, corresponding to the removal of the adatoms' dangling bonds of the 7×7 surface. But the metallic character is recovered by further In adsorption of 0.4 ML. This comes from In metallic crystal islands of nanometer-sized, which are revealed by STM observations [172]; after completion of a wetting layer of a submonolayer In coverage, around 100 nm-sized flat 3D islands appear with increase of In coverage. Such islands are formed sparsely and scarcely cover the surface.

7.2.3. Electrical conduction

Fig. 89(a) shows the conductance changes $\Delta\sigma$ during In deposition onto the Si(111)-7×7 clean surface at RT and 100 K. At RT, there is no conductance change up to In coverage of 40 ML, while at 100 K, the conductance steeply rises up from around 2.5 ML (see inset in Fig. 89(a)) and increases monotonically.

As described in Section 7.2.1, indium grows in the Stranski–Krastanov mode, though the 3D islands on top of the wetting layer differ in size and density depending on the temperature; fine In islands grow densely at 100 K, while large ones are distributed sparsely at RT. It is then expected that the conductance rise from around 2.5 ML at 100 K is due to the In fine islands connecting to each other to form conducting paths on the surface. This path-forming process may be described by the percolation theory [173] which predicts the conductance increase $\Delta\sigma$ as a function of coverage θ in the form of Eq. (61) in Section 4.3.3, $\Delta\sigma \propto (\theta - \theta_c)/\theta_c\}^t$, where θ_c is a critical coverage and t a critical exponent. The exponent t for 2D system is obtained to be 1.3 by Monte Carlo simulations [173]. The early stage of the conductance increase observed at 100 K can be fitted to this form

using the reduced coverage $(\theta\text{-}\theta_c)/\theta_c$ with t and θ_c as fitting parameters, as shown in Fig. 89(b), giving the critical coverage $\theta_c = 2.33(\pm 0.06)$ ML and the critical exponent $t = 1.29 \pm 0.02$. The agreement of this t value with that obtained by the

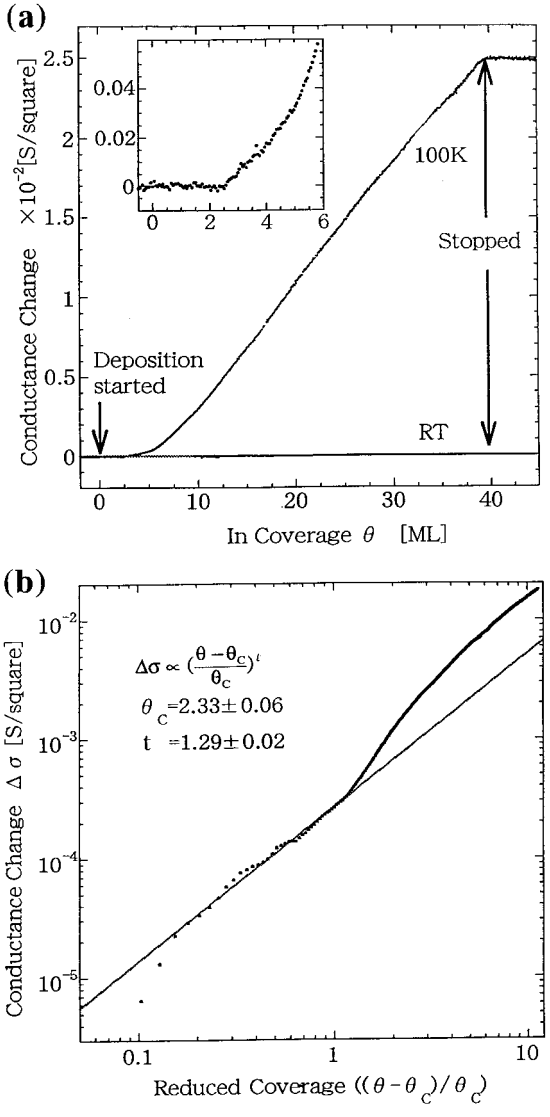

Fig. 89. (a) Conductance changes $\Delta\sigma$ measured during In depositions onto the Si(111)-7 × 7 substrate at RT and 100 K. The inset shows a magnified curve around a critical coverage of 2.3 ML for 100 K measurement. (b) The same data at 100 K in (a), plotted as a function of reduced coverage of In. The straight line in the log-log plot presents a fitting to a form $\Delta\sigma \propto (\theta\text{-}\theta_c)/\theta_c$. From Ref. [16].

simulations insists that the observed conductance increase is a set-on of a 2D percolation among In fine islands.

After the islands are percolated, the conductance monotonically increases until the deposition is stopped at 40 ML coverage at 100 K. This increase can be attributed to the conductance through a continuous In film because the surface space-charge layer in the Si substrate remains in a depletion-layer condition as shown in Fig. 88(b). The increase above about 10 ML coverage can be fitted to a straight line $\Delta\sigma = a \cdot d - b$, where d is the film thickness and a and b are constants. The coefficient a can be regarded as a conductivity. Then, from a gradient of the straight part in the conductance curve of Fig. 89(a), the conductivity of the film is estimated to be 8×10^{-4} S/ML, or 4×10^{4} S·cm^{-1}. This value is an order of magnitude smaller than the bulk value at 100 K. Assuming the Drude model, Eqs. (1) and (2) in Section 2.1.1, the mean free path $\ell = v_F \cdot < \tau >$ is estimated to be approximately 2 nm, because the carrier (holes) concentration $n \sim 3 \times 10^{22}$ cm^{-3}, and the Fermi velocity $v_F \sim 1.7 \times 10^{8}$ cm/s for indium. Since this length remains constant with increase of film thickness from 10 to 40 ML, it can be said that the mean free path is not restricted by the carrier scattering at surface/interface, but scattering at grain boundaries or defects in the films whose separations are constant during the growth.

No change in conductance up to 40 ML of In deposition at RT is explained by the fact that In islands grow in a 3D way with a large separation among them, so the critical coverage is too large to make the percolation paths. The first monolayer in the Stranski–Krastanov growth scarcely contributes to the measured conductance either at RT and at 100 K, which is consistent with two reports that band bending during In deposition onto the Si(111)-7 × 7 surface means a depletion in the substrate as described in Section 7.2.2 [167] and that the first monolayer is not a continuous monatomic layer but an ensemble of small In agglomerates uniformly spread over the 7 × 7 framework [164].

The changes in electrical conductance during In adsorption at elevated temperatures will also be interesting because, as described in Section 7.2.1, many structural conversions take place depending on the substrate temperatures. But, we have not yet succeeded to measure them because of some technical difficulties.

7.3. On the $\sqrt{3} \times \sqrt{3}$-In substrate

Quite different phenomena are observed in changes of structures and electrical conductance during In adsorption onto the pre-deposited substrate, Si(111)-$\sqrt{3} \times \sqrt{3}$-In surface.

7.3.1. Atomic structural evolutions

A series of RHEED patterns taken during the In deposition onto the $\sqrt{3} \times \sqrt{3}$-In surface at RT are shown in Fig. 90. Starting from the initial $\sqrt{3} \times \sqrt{3}$ structure (Fig. 90(a)), 2 × 2 (b) and $\sqrt{\{7\}} \times \sqrt{3}$ (c) phases are successively appear, which are completed around 1 and 2 ML coverages of In, respectively. With further deposition, superlattice spots disappear and only the fundamental spots with

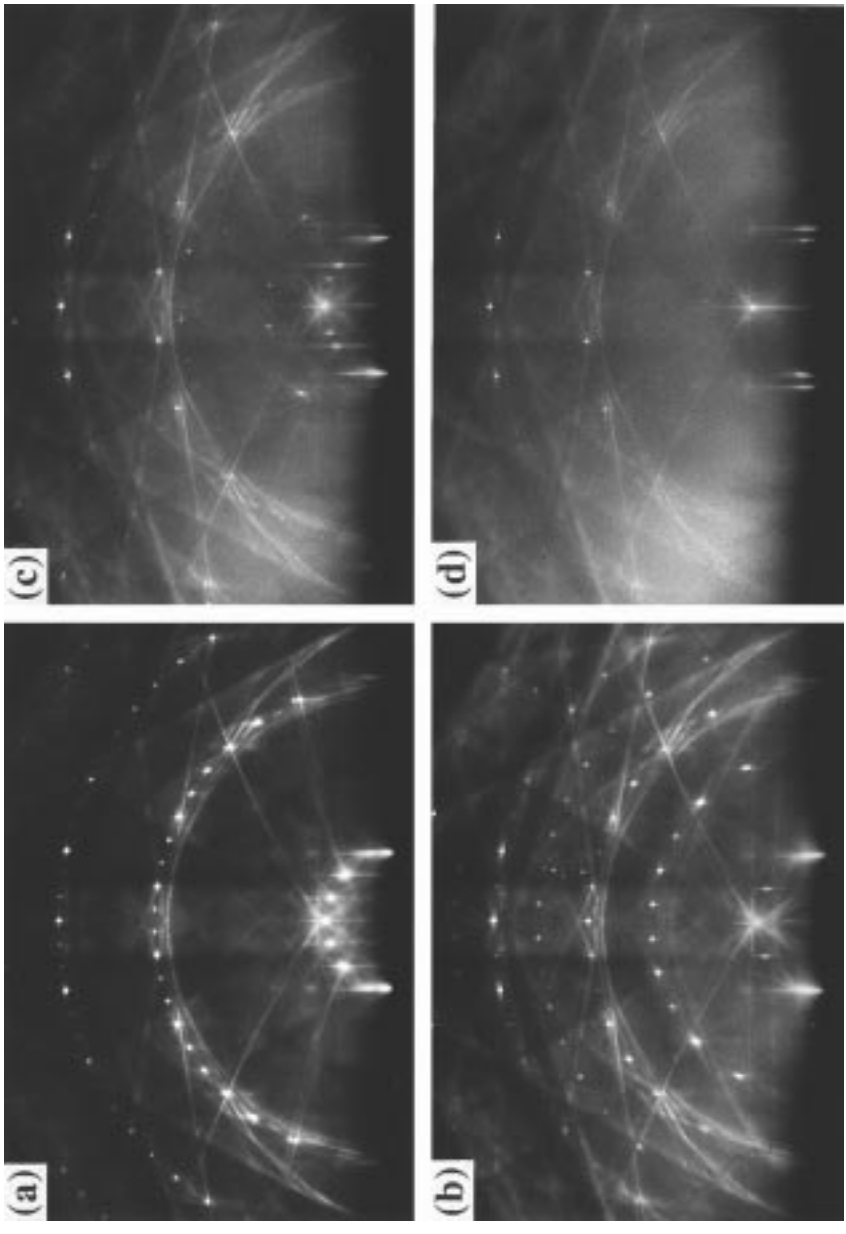

Fig. 90. A series of RHEED patterns during additional In deposition onto the pre-deposited Si(111)-$\sqrt{3} \times \sqrt{3}$-In surface at RT; (a) the initial substrate surface, (b) a 2×2, (c) a $\sqrt{7} \times \sqrt{3}$, and (d) a 1×1+In streaks, respectively [162].

streaks from epitaxial In flat islands are observed in (d). In the $\sqrt{\{7\}} \times \sqrt{\{3\}}$ pattern (c), some superlattice points are observed in a limited range of the electron-beam glancing angle, meaning that this phase is composed of several atomic layers.

The sequence of these structural conversions are revealed as intensity changes of the respective superlattice spots as shown in Fig. 91. In place of the $\sqrt{3} \times \sqrt{3}$ spot, the 2×2 spot becomes stronger almost linearly with In coverage increase. After passing its maximum intensity, it linearly goes down to zero, and in turn, the $\sqrt{7} \times \sqrt{3}$ spot begins to grow. The saturation coverage of the $\sqrt{7} \times \sqrt{3}$ phase is exactly twice that of the 2×2 phase, measured from the deposition times for the intensity peaks of the respective spots.

It is quite surprising that these structural changes occur even at RT and that each phase has a very nice long-range ordering, judged from the sharp spots in RHEED. These are due to high mobility of arriving In atoms on top of the substrate.

The difference in adsorption process of In layers between on the Si(111)-7×7 (see Section 7.2.1) and on the Si(111)-$\sqrt{3} \times \sqrt{3}$-In substrates may originate from the presence or absence of the remains of the DAS framework on the topmost layers of the Si substrate. It is interesting to recall the experiment of In adsorption at RT on top of the UHV-cleaved Si(111)-2×1 surface at RT [174]. This surface is known to have no stacking fault layer. In this case, the surface structure successively changes in a similar way as for the case of the Si(111)-$\sqrt{3} \times \sqrt{3}$-In substrate described above; from 2×1 into $\sqrt{3} \times \sqrt{3}$, and then 2×2. Thus In

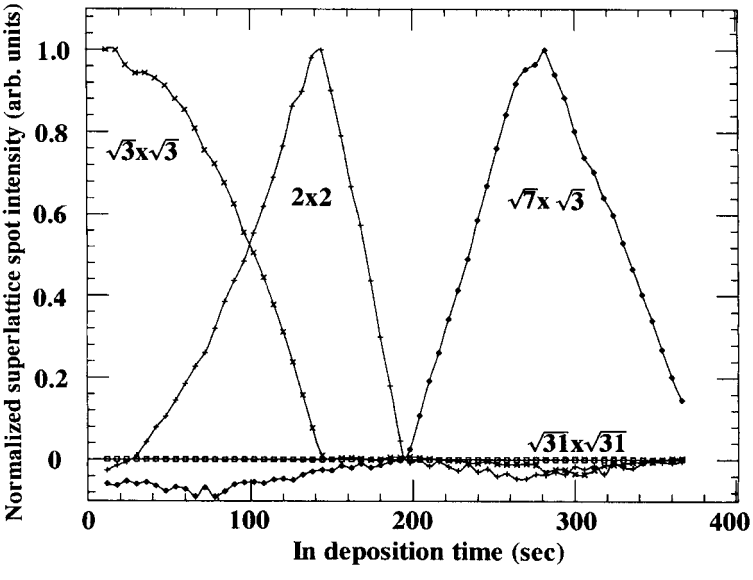

Fig. 91. Changes in the integrated intensities of each superlattice spot appearing during In deposition onto the Si(111)-$\sqrt{3} \times \sqrt{3}$-In surface at RT as a function of deposition duration time [162].

adatoms are considered to move relatively easily to attain a new ordering on the normal-stacking Si substrate even at RT, whereas the remain of the DAS structure, the dimer-stacking fault framework, on the 7×7 substrate is not broken by In adsorption (though the Si adatoms are removed), and prevents the surface from converting to a new superlattice at RT.

A surface showing a $\sqrt{7} \times \sqrt{3}$ periodicity is known to appear not only by In deposition onto the $\sqrt{3} \times \sqrt{3}$-In substrate at RT, as described above, but also onto the 7×7 clean surface at elevated temperatures (670–820 K) with complicated procedures [164,165,171,175–178]. Hereafter, we call the former structure $\sqrt{7} \times \sqrt{3}$(RT), and the latter structure $\sqrt{7} \times \sqrt{3}$(HT). There is no general consensus until now whether the both are the same or not. According to a report [175], there are two types of atomic arrangements for the $\sqrt{7} \times \sqrt{3}$(HT) phase which are designated $\sqrt{7} \times \sqrt{3}$-hex. and $\sqrt{7} \times \sqrt{3}$-rect. whose coverages are 1.0 and 1.2 ML, respectively. They also reported, using STM and optical microscopy, that further deposition of In on the $\sqrt{7} \times \sqrt{3}$(HT) surface at 400°C causes a formation of very large islands sparsely distributed on the surface. This is because of the large mobility of the arriving In atoms. The formation of In layer on top of the $\sqrt{7} \times \sqrt{3}$(HT) surface occurred only when the surface was exposed by oxygen, followed with In deposition at RT. This high mobility of indium atoms on the $\sqrt{7} \times \sqrt{3}$(HT) without oxygen is quite similar to that on the $\sqrt{7} \times \sqrt{3}$(RT).

As for the $\sqrt{7} \times \sqrt{3}$(RT) structure, only a few studies have been reported [5,179]. Very recently, Saranin et al. [179] have studied this surface by AES and STM. Their results show that each structural transformation ($\sqrt{3} \times \sqrt{3} \rightarrow 2 \times 2 \rightarrow \sqrt{7} \times \sqrt{3}$) occurs at In coverage smaller than that described above.

7.3.2. Electrical conduction

7.3.2.1. At RT. Fig. 92(a) shows the conductance changes during In depositions onto the Si(111)-$\sqrt{3} \times \sqrt{3}$-In surface at RT [16]. When the deposition is started, the conductance increases up to 3 ML coverage with characteristic inflections (indicated by A, B, and C in the figure). Similar phenomena had been reported by Baba et al., but without notice of structural transformations [181]. These inflections are almost coincident to points of the surface structural transformations, $\sqrt{3} \times \sqrt{3} \rightarrow 2 \times 2 \rightarrow 1 \times 1 \rightarrow \sqrt{7} \times \sqrt{3}$, which are already explained in Figs. 90 and 91. "1×1" means that there are no superspots other than the fundamental spots in RHEED. The conductance increase stops at around 3 ML coverage (point D) and no significant increase is observed even with further deposition, where the $\sqrt{7} \times \sqrt{3}$ superspots gradually fade to leave the fundamental spots and streaks from In crystals. These In streaks gradually appear at around 2.5 ML coverage, and indicate the growth of In 3D flat islands. This is the same as on the 7×7 surface at RT. When the deposition is stopped, the $\sqrt{7} \times \sqrt{3}$ superspots gradually appear again, and simultaneously the conductance starts to decrease as shown in Fig. 92(b). The deposition is stopped at the point E in the figure. The conductance begins to decrease soon after that and then reaches a smaller constant value which is almost the same as that at 2 ML coverage during the deposition (point C in

(a)). When the deposition is restarted, the conductance increases to a higher constant value again (not shown here). These changes in conductance are similar with various deposition rates (0.045–1.125 ML/min), and the inflections in the conductance curve appear in the same way.

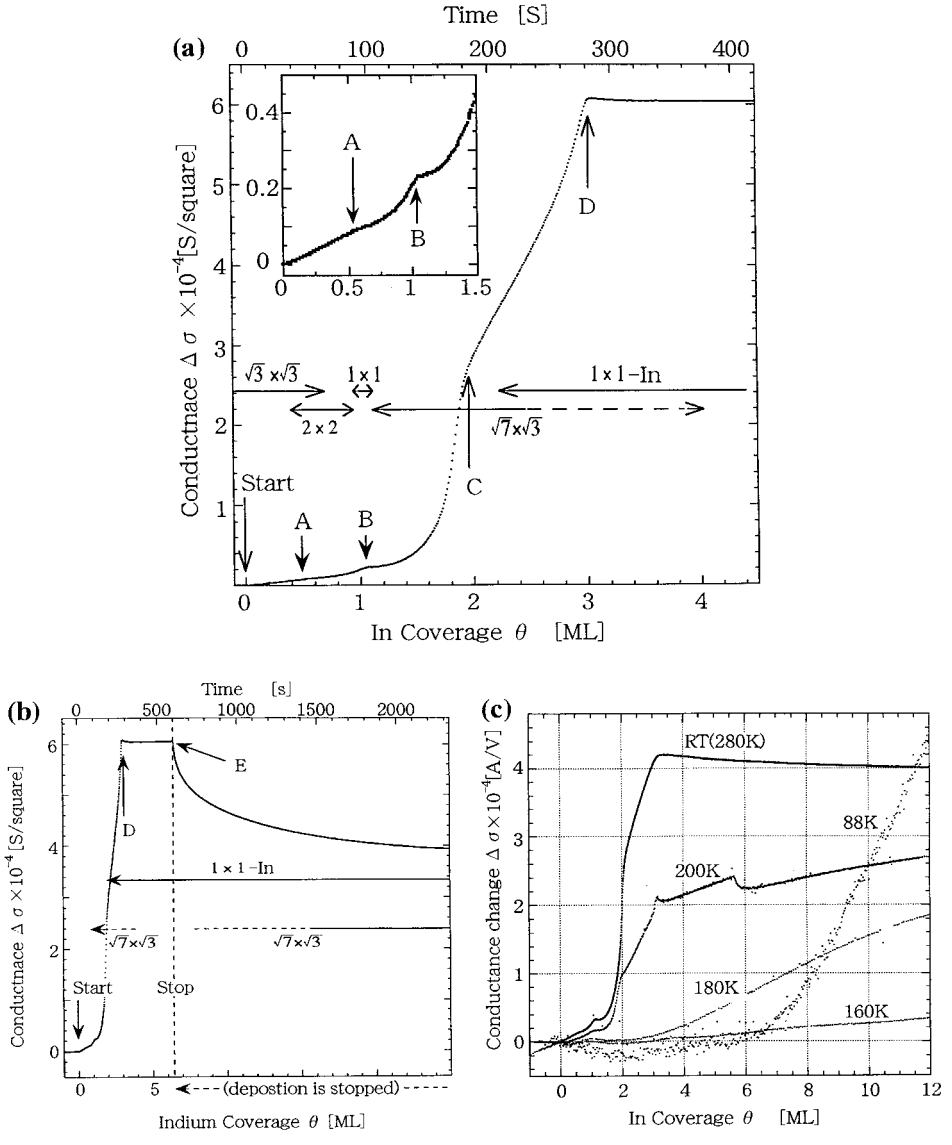

Fig. 92. (a) Conductance change $\Delta\sigma$ during In deposition onto the Si(111)-$\sqrt{3}\times\sqrt{3}$-In surface at RT. (b) The same as in (a) also showing after the deposition off. (c) Conduction changes $\Delta\sigma$ during In depositions onto the Si(111)-$\sqrt{3}\times\sqrt{3}$-In surface at various substrate temperatures. From Ref. [16].

7.3.2.2. At low temperatures. At lower substrate temperatures, the surface structural transformations differ from the RT case. The 2×2 spots are weak on the substrate at 200 K, and not observed below 200 K; the fundamental spots are just seen in the coverage range where the 2×2 pattern is observed at RT. The $\sqrt{7} \times \sqrt{3}$ pattern also does not appear below 160 K. At 100 K the initial $\sqrt{3} \times \sqrt{3}$ spots just disappear around 0.8 ML In coverage without any other superspots appearing, and broad streaks slowly appear around 8 ML. These streaks are the same as those observed on the 7×7 surface at 100 K, which show the growth of In islands of a mosaic structure. The conductance curves for these low temperatures are shown in Fig. 92(c). The inflections on the curves at RT and 200 K clearly correspond to the appearance of the 2×2 and $\sqrt{7} \times \sqrt{3}$ structures. These inflections are not seen below 200 K where no structural transformations are observed. Hence, it is obvious that the characteristic conductance changes at RT are associated with the formations of the 2×2 and $\sqrt{7} \times \sqrt{3}$ superstructures. At 88 K, the increase in conductance looks similar to the case of the 7×7 substrate shown in Fig. 89, which indicates the percolation mechanism for the conductance increase, though the critical coverage seems slightly larger.

7.3.2.3. Band bending. In order to characterize the observed conductance changes at RT shown in Fig. 92(a), the band bending below the surface in the Si substrate is measured. As described in Section 3.2.2, the band bending can be measured by XPS under proper conditions. Fig. 93 shows XPS spectra for the Si $2p$ core level obtained from (a) 7×7, (b) $\sqrt{3} \times \sqrt{3}$-In, (c) 2×2-In (at additional 0.7 ML In coverage on the $\sqrt{3} \times \sqrt{3}$-In surface), (d) $\sqrt{7} \times \sqrt{3}$-In (at additional 3 ML), and (e) 1×1 (at additional 5 ML) structures at RT, respectively. It should be noted that the spectrum (e) for the 1×1 surface is measured for the surface after 5 ML In deposition; but this surface returns to the $\sqrt{7} \times \sqrt{3}$ structure by stopping the deposition as mentioned in Fig. 92(b), where the XPS measurements were carried out. The binding energy in the spectra is referred to E_F. As seen at (b)–(e), the energy of the Si $2p$ level shifts towards E_F with In coverage. This indicates that the bands bend upward. The shifts of the core level relative to at the $\sqrt{3} \times \sqrt{3}$-In surface are (c) 0.28 ± 0.05 eV, (d) 0.47 ± 0.05 eV, and (e) 0.50 ± 0.05 eV, respectively.

The Si $2p$ peak of the $\sqrt{3} \times \sqrt{3}$-In surface is located at a position slightly deeper than that of the 7×7 surface by 0.03 ± 0.05 eV (compare (a) and (b) in Fig. 93). Then, it is simply obtained from the XPS results that the $E_F - E_{VBM}$ for the respective surface structures are (b) 0.66 ± 0.05 eV, (c) 0.38 ± 0.05 eV, (d) 0.19 ± 0.05 eV, and (e) 0.16 ± 0.05 eV, because the energy distance $E_F - E_{VBM}$ is measured to be 0.63 eV for the 7×7 surface [30,31]. Since, at (d) and (e), E_F's are located near E_{VBM}, the surface space-charge layer becomes a hole-accumulation layer. On the other hand, the layers at (b) and (c) are depletion layers as in the case of the 7×7 surface.

7.3.2.4. Conductance through the surface space-charge layer. We now discuss the mechanism of the conductance changes in Fig. 92(a) accompanied with the structural transformations. As described in Section 2.2, there are in general three possi-

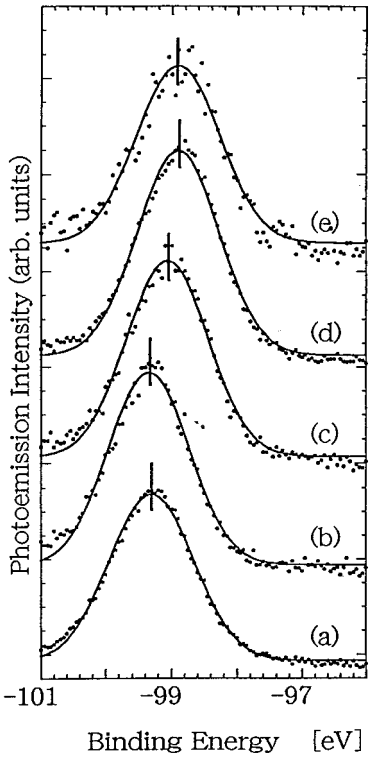

Fig. 93. X-ray photoemission spectra from Si 2*p*core level of the (a) 7×7 clean and (b) $\sqrt{3} \times \sqrt{3}$-In surfaces, and (c) 2×2, (d) $\sqrt{7} \times \sqrt{3}$, (e) 1×1 surfaces which were prepared by depositing In of 0.7, 3, and 5 ML onto the $\sqrt{3} \times \sqrt{3}$ surface at RT, respectively. The peak positions were determined by Gaussian fits. From Ref. [16].

bilities to account for the conductance change; conductances through the surface-state band, through the grown metal atomic layers, and through the surface space-charge layer of the substrate. The distinction between the former two types of conductance will be obscure when the metal overlayers make surface superstructures like the present case of the In layers.

The above XPS results show that the band bendings occur for the respective structures. So we first estimate the conductance increase $\Delta\sigma_{SC}$ induced by the band bending in the surface space-charge layer according to Eq. (34) in Section 2.2.1. The curves in Fig. 94 show $\Delta\sigma_{SC}$ calculated as a function of the surface E_F position [16]. The four curves are calculated by assuming different resistivities of Si crystals, corresponding to different E_F positions in bulk. This is for later discussions on possible changes in impurity concentration in the bulk (subsurface region) due to heat treatments. Then, we can estimate the conductance increases through the surface space-charge layer at the respective surface structures because each surface E_F position is already determined by XPS measurements as described

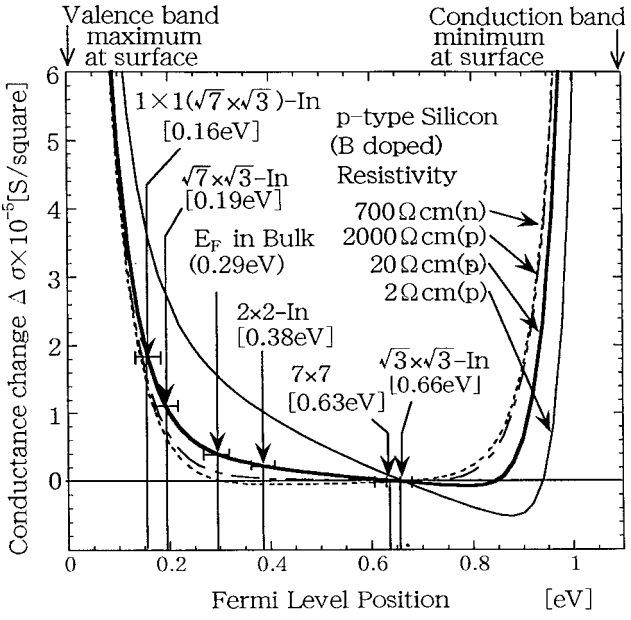

Fig. 94. The excess conductance $\Delta\sigma_{SC}$ through the surface space-charge layer in the substrate, calculated as a function of the surface E_F position measured from E_{VBM}, using the bulk value for the mobilities of holes and electrons, 496 cm^2/Vsec and 1330 cm^2/Vsec, respectively. The conductance at the $\sqrt{3} \times \sqrt{3}$-In surface is defined as a reference. The E_F positions at the respective superstructures determined by XPS measurements are indicated. The energy in square brackets has an error of $\pm$ 0.05 eV. Thin-solid, thick-solid, dash, and dot-dash lines show the calculations for 2 Ωcm (p-type), 20 Ωcm (p-type), 2000 Ωcm (p-type), and 700 Ωcm (n-type) samples, respectively. These resistances correspond to the E_F positions in the bulk at 0.02, 0.29, 0.40, and 0.66 eV above E_{VBM}, respectively. From Ref. [16].

above. From the calculated curve for 20 Ωcm resistivity, the increases in conductance for the 2×2 and $\sqrt{7} \times \sqrt{3}$ surfaces with respect to at the $\sqrt{3} \times \sqrt{3}$ surface (designated as $\Delta\sigma_{SC}^{2\times2}$ and $\Delta\sigma_{SC}^{\sqrt{7}\times\sqrt{3}}$ here after) are estimated to be $\Delta\sigma_{SC}^{2\times2} = 2.3\ (\pm0.3) \times 10^{-6}$ S/□ and $\Delta\sigma_{SC}^{\sqrt{7}\times\sqrt{3}} = 1.2(\pm0.4) \times 10^{-5}$ S/□ (or $\Delta\sigma_{SC}^{\sqrt{7}\times\sqrt{3}} = 1.9(\pm0.4) \times 10^{-5}$ S/□ if one takes the E_F position at the 1×1-In surface in Fig. 94), respectively. On the other hand, the measured conductance increases for the respective surfaces in comparison to the conductance of the initial $\sqrt{3} \times \sqrt{3}$-In surface are $\Delta\sigma_{2\times2} = 2.3(\pm0.1) \times 10^{-5}$ S/□ (see Fig. 92(a)) and $\Delta\sigma_{\sqrt{7}\times\sqrt{3}} = 3.8(\pm0.2) \times 10^{-4}$ S/□, respectively (we take the value of $\Delta\sigma_{\sqrt{7}\times\sqrt{3}}$ as a smaller constant value after the deposition off in Fig. 92(b), so that we can consistently compare the conductance increase with the XPS results). The measured $\Delta\sigma_{2\times2}$ is about 10 times larger than the space-charge-layer contribution $\Delta_{SC}^{2\times2}$, and $\Delta_{\sqrt{7}\times\sqrt{3}}$ is about 20–30 times larger than $\Delta\sigma_{SC}^{\sqrt{7}\times\sqrt{3}}$. These discrepancies seem to suggest that mechanisms other than the surface space-charge layer are responsible for the observed conductance increases.

If one takes into account that the mobilities of carriers in the surface space-

charge layer can be smaller than the bulk values due to carrier scattering at the surface in the case of steep band bending, the discrepancy between the respective $\Delta\sigma$ and $\Delta\sigma_{SC}$ described above will become more serious. Furthermore, the possibility that some changes in the dopant concentration near the surface region, which may be caused by high-temperature flashings and anealings in vacuum [71,72], must be considered. For such a case, we calculate the changes of $\Delta\sigma_{SC}$ assuming samples of different resistivities. The results are shown in Fig. 94 by four curves. As seen in the figure, the calculated $\Delta\sigma_{SC}$ changes by a factor of less than three at most even if the resistivity changes from a nominal value (20 Ωcm) by two orders of magnitude. This means that the observed conductance increase is not explained by space-charge-layer conduction even if assuming some changes in the dopant concentration in the Si substrate. From these considerations, it can be said that the band bending is not a major reason for the observed conductance increases. The conduction through In atomic layers or through the surface-state band should be considered.

The correspondence between the characteristic changes in conductance (indicated A and B in Fig. 92(a)) and the structure transformations suggests that the surface states inherent in the respective superstructures govern the conductance. The stop of the conductance increase at 3 ML (marked D in Fig. 92(a)) and the following constant conductance in spite of further deposition seem to indicate the occurrence of 3D island growth from this coverage. The highest conductance is achieved only during the deposition where the RHEED shows almost only the 1×1 fundamental spots and the In streaks beyond 4 ML coverages. The $\sqrt{7} \times \sqrt{3}$ spots are seen only up to about 3 ML, but fade out with another 1 ML deposition. When the deposition is interrupted, the conductance begin to decrease gradually down to a lower value which corresponds to the value around 2 ML coverage during deposition, and the $\sqrt{7} \times \sqrt{3}$ spots gradually appear again, as shown in Fig. 92(b).

From these observations, the following mechanism may be plausible. The deposited In atoms on top of the $\sqrt{3} \times \sqrt{3}$-In surface grow in the Stranski–Krastanov mode; the first 3 ML grow in layer-by-layer mode, and then followed by 3D islanding. The first 2 ML are pseudomorphic films; the first layer has a 2×2 superstructure and the second layer has a $\sqrt{7} \times \sqrt{3}$ superstructure. The third layer showing the 1×1 structure, which is an intermediate layer between the underlying 2D layer and the 3D islands, is kinetically meta-stable only during the deposition. Once the deposition is interrupted, the third layer aggregates into 3D islands, remaining the underlying 2D layer of the $\sqrt{7} \times \sqrt{3}$ structure. When the deposition is restarted, the metastable 1×1 layer is formed again on top of the $\sqrt{7} \times \sqrt{3}$ 2D phase. The 1×1 phase is more conductive than the stable $\sqrt{7} \times \sqrt{3}$ phase. Hence the disappearance and reappearance of the $\sqrt{7} \times \sqrt{3}$ spots correspond to the formation and the destruction of the meta-stable third layer.

The conductance of three atomic layers of In calculated from the conductivity of its bulk value at RT is 7.5×10^{-3} S/□. This is about 12 times larger than our measured value $6.0(\pm 0.3) \times 10^{-4}$ S/□ (see Fig. 92(a)). From this value, the carrier mean free path in the present 3 ML of In on the $\sqrt{3} \times \sqrt{3}$-In surface is estimated

to be only 5 Å. Although these are rough estimations, 5 Å is too small as a distance among scatters, so the surface scattering is considered to give a severe effect on the conductance in the present 3 ML film. The atomic structure in the film, which is different from the bulk In, would be another reason for the lower conductance. In Section 7.2.3, it is shown that the In film grown on the 7×7 substrate also has a lower conductance compared with the bulk value. This was due to carrier scattering by defects such as grain boundaries. But for the films on the $\sqrt{3} \times \sqrt{3}$-In substrate, the surface scattering may dominate over the defect scattering.

7.4. On the other substrates

When In is deposited onto the Si(111)-4 × 1-In or -$\sqrt{31} \times \sqrt{31}$-In surface, no significant changes in structures and electrical conductance are observed at RT. This is because the initial surfaces are so stable that 3D In islands are just formed very sparsely on the surface from the beginning of additional deposition, due to a high mobility of the deposited In atoms, resulting in the lack of electrical connection among the islands. By lowering the substrate temperature, the small In islands are formed closer to each other due to the suppression of the In-atom migration. So a set-on of the percolation conduction is observed as in the case of the 7×7 and $\sqrt{3} \times \sqrt{3}$-In substrates at 100 K.

7.5. Summary

Indium adsorption on the Si(111)-$\sqrt{3} \times \sqrt{3}$-In surface is unique in its successive structure transformations with coverage increases. Accordingly, the electrical conduction through the grown In layers with superstructures rises. In this case, the distinction between the electrical conductions through the surface-state bands of the surface superstructures and through the grown atomic layers may become vague; the electrical current flows through the In atomic layers having atomic arrangements different from the bulk. More detailed discussions will be possible when the photoemission data on the respective superstructures are available.

On the 7×7 clean surface, on the other hand, the deposited In atoms just aggregate into fine clusters or 3D islands depending on the substrate temperatures, which are revealed by electrical percolation among the In islands; the 7×7 framework is just buried under the In islands without restructuring into new superstructures.

Characteristic phenomena described so far comes from a high mobility of In atoms on the surface which is strongly dependent on the temperature. At the present stage, the conductance measurements are restricted only at RT and lower temperatures. But it will be also interesting at higher temperatures where another series of structural conversions occur as shown in Fig. 86, though the measurements will be more difficult, because of larger contribution from the bulk conductance at elevated temperatures.

8. Concluding remarks

We have discussed the close relation between the surface structures of the topmost atomic layers of silicon and the electrical conduction phenomena. In particular, we have shown the electrical conduction through the surface-state bands, inherent in the surface superstructures. Direct experimental evidence for this type of electrical conduction has been given for several systems (2D adatom-gas phase and $\sqrt{21} \times \sqrt{21}$ phases induced by monovalent-atom adsorptions, Au- and In-adsorbed surfaces).

Although this review article focuses only on the Si(111) surfaces, the surface conductance differences among the different surface superstructures are confirmed also on Si(100) surfaces [185]; Si(100)-$c(8 \times 2)$-Au and -$\sqrt{26} \times 3$-Au surfaces have higher surface conductance than the clean Si(100)-2×1 surface by 6×10^{-5} S/□ and 1.1×10^{-4} S/□, respectively. These investigations show that each surface phase has its own electrical conductance, which is directly measured with four-point probe method of macroscopic probe distances even with Si crystals of macroscopic thicknesses. This fact was not recognized before our studies.

However, our studies are only in the initial stage of systematic investigations of the electronic transport properties of such surface phases, especially, properties of ultimate 2D electron systems created by surface-state bands, where the correlation with the atomic arrangements on surfaces is of essential importance. In order to characterize the fundamental properties, measurements of temperature dependences of the conductances are indispensable. In-situ measurements at low temperatures under a magnetic field in UHV with atomically controlled sample surfaces are also strongly desired to clarify the fundamental properties of the surface-state transport. Another direction for further study is conductance measurements of micro- or nanoscopic areas on the surface. In order to elucidate the effcets of surface defects such as steps and domain boundaries on the transport properties, we have to measure the conductance on a single terrace or a single domain without steps. For that we need microscopic four-point probes combined with microscopy for probe positioning, using, e.g., a multi-tip STM-like apparatus.

By utilizing the variety of surface superstructures, which is not exhibited in bulk, and also by combining the technology to manipulate the atomic-scale structures on surfaces, we should be able to control the transport properties in novel ways. In addition to the expectation from the view point of fundamental physics of nanometer-scale systems, the transport properties of surface-state bands will be one of the most important subjects in nanoscale device performance. As the electronic devices become samller, the current is forced to flow through thinner region near surfaces where surface-state bands will play main roles. In the near future, the huge amount of knowledge on the atomic and electronic structures of silicon surfaces accumulated so far, will fructify a new and rich field of research on surface electronic transport properties.

Acknowledgements

Some of the results presented here were obtained under collaboration with the former and present students in our research group, Dr Zhi Hong Zhang, Dr Naoharu Shimomura, Dr Chun-Sheng Jiang, Mr Yuji Nakajima, Mr Kotaro Horikoshi, Mr Keinosuke Toriyama, Mr Koji Tsuchie, Mr Ichiro Shiraki, Mr Takaaki Matsumoto, and Mr Takeharu Sekiguchi. The former research associates, Dr Tomohide Takami and Mr Fumio Shimokoshi are acknowledged for their experimental assistance and stimulating discussions. We thank Professor Martin Henzler of Hannover University and Professor Shozo Ino of Utsunomiya University for their valuable advice. Professors Masaru Tsukada and Satoshi Watanabe of University of Tokyo are also acknowledged for their helpful discussions from theoretical points of view. This work was started under PRESTO (Precursory Research for Embryonic Science and Technology) Project of the Japan Science and Technology Corporation (JST). We are now supported in part by Grants-In-Aid from the Ministry of Education, Science, Culture, and Sports of Japan, especially through Grants-In-Aid for Creative Basic Research Project (No. 09NP1201) conducted by Professor Katsumichi Yagi of Tokyo Institute of Technology. We are supported also by CREST(Core Research for Evolutional Science and Technology) Project of JST conducted by Professor Masakazu Aono of Osaka University and RIKEN.

References

[1] V.G. Lifshits, A.A. Saranin, A.V. Zotov, Surface Phases on Silicon, Wiley, Chichester, 1994.
[2] S. Hasegawa, S. Ino, Phys. Rev. Lett 68 (1992) 1192.
[3] S. Hasegawa, S. Ino, Surf. Sci 283 (1993) 438.
[4] S. Hasegawa, S. Ino, Thin Solid Films 228 (1993) 113.
[5] S. Hasegawa, S. Ino, Int. J. Mod. Phys B7 (1993) 3817.
[6] S. Hasegawa, Z.H. Zhang, C.S. Jiang, S. Ino, in: H. Sakaki, H. Noge (Eds.), Nanostructures and Quantum Effects, Springer, Berlin, 1994, p. 104.
[7] C-S. Jiang, S. Hasegawa, S. Ino, Phys. Rev B54 (1996) 10 389.
[8] Y. Nakajima, G. Uchida, T. Nagao, S. Hasegawa, Phys. Rev B54 (1996) 14 134.
[9] Z.H. Zhang, S. Hasegawa, S. Ino, Phys. Rev B52 (1995) 10 760.
[10] X. Tong, S. Hasegawa, S. Ino, Phys. Rev B55 (1997) 1310.
[11] C-S. Jiang, X. Tong, S. Hasegawa, S. Ino, Surf. Sci 376 (1997) 69.
[12] S. Hasegawa, X. Tong, C-S. Jiang, Y. Nakajima, T. Nagao, Surf. Sci 386 (1997) 322.
[13] S. Hasegawa, C-S. Jiang, X. Tong, Y. Nakajima, Adv. Colloid and Int. Sci 71/72 (1997) 125.
[14] Y. Nakajima, S. Takeda, T. Nagao, S. Hasegawa, X. Tong, Phys. Rev B56 (1997) 6782.
[15] X. Tong, C-S. Jiang, S. Hasegawa, Phys. Rev B57 (1998) 9015.
[16] S. Takeda, X. Tong, S. Ino, S. Hasegawa, Surf. Sci 415 (1998) 264.
[17] X. Tong, Y. Sugiura, T. Nagao, T. Takami, S. Takeda, S. Ino, S. Hasegawa, Surf. Sci 408 (1998) 146.
[18] S. Hasegawa, C-S. Jiang, Y. Nakajima, T. Nagao, X. Tong, Surf. Rev. Lett 3/4 (1998) 803.
[19] N. Sato, T. Nagao, S. Takeda, S. Hasegawa, Phys. Rev B59 (1999) 2035.
[20] X. Tong, K. Horikoshi, S. Hasegawa, Jap. J. Appl. Phys (1999) (submitted).
[21] X. Tong, K. Horikoshi, S. Hasegawa, Phys. Rev. B (1999) (submitted).
[22] K. Horikoshi, X. Tong, T. Nagao, S. Hasegawa, Phys. Rev. B (1999) (submitted).

[23] K. Horikoshi, X. Tong, T. Nagao, S. Hasegawa, Phys. Rev. B (1999) (submitted).
[24] M. Kikuchi, Buturi 51 (1996) 21 (in Japanese).
[25] T. Sato, T. Sueyoshi 1992 JEOL Application Note, Scanning Tunneling Microscope TM03 (in Japanese).
[26] K. Takayanagi, Y. Tanishiro, M. Takahashi, S. Takahashi, Surf. Sci 164 (1985) 367.
[27] V.A. Gasparov, K.R. Nikolaev, Phys. Low-Dim. Struct 1/2 (1996) 53.
[28] Ph Avouris, I-W. Lyo, Y. Hasegawa, in: R. Rosei (Ed.), Chemical, Structural and Electronic Analysis of Hetrogeneous Surfaces on Nanometer Scale, Kluwer, Dordrecht, 1997, p. 1.
[29] S. Heike, S. Watanabe, Y. Wada, T. Hashizume, Phys. Rev. Lett 81 (1998) 890.
[30] F.J. Himpsel, G. Hollinger, R.A. Pollak, Phys. Rev B28 (1983) 7014.
[31] J. Viernow, M. Henzler, W.L. O'Brien, F.K. Men, F.M. Leibsle, D.Y. Petrovykh, J.L. Lin, F.J. Himpsel, Phys. Rev B57 (1998) 2321.
[32] D. Haneman Rep. Prog. Phys. 50 1987 1045; Adv. Phys. 31 (1982) 165.
[33] G.X. Qian, D.J. Chadi, J. Vac. Sci. Technol B4 (1986) 1079.
[34] G.X. Qian, D.J. Chadi, Phys. Rev B35 (1987) 1288.
[35] T. Takahashi, S. Nakatani, N. Okamoto, T. Ishikawa, S. Kikuta Jpn. J. Appl. Phys. 27 1988 L753; Surf. Sci. 242 (1991) 54; T. Takahashiand S. Nakatani, Surf. Sci. 282 (1993) 17, and references therein.
[36] M. Katayama, R.S. Williams, M. Kato, E. Nomura, M. Aono, Phys. Rev. Lett 66 (1991) 2762.
[37] T. Yokotsuka, S. Kono, S. Suzuki, T. Sagawa, Surf. Sci 127 (1983) 35.
[38] L.S.O. Johansson, E. Landemark, C.J. Karlsson, R.I.G. Uhrberg Phys. Rev. Lett. 63 1989 2092; *ibid.* 69 (1992) 2451.
[39] S. Watanabe, M. Aono, M. Tsukada, Phys. Rev B44 (1991) 8330.
[40] Y.G. Ding, C.T. Chan, K.M. Ho Phys. Rev. Lett. 67 1991 1454; *ibid.* 69 (1992) 2452.
[41] K.J. Wan, X.F. Lin, J. Nogami, Phys. Rev B45 (1992) 9509.
[42] S. Kono, K. Higashiyama, T. Kinoshita, T. Miyahara, H. Kato, H. Ohsawa, Y. Enta, F. Maeda, Y. Yaegashi, Phys. Rev. Lett 58 (1987) 1555.
[43] C. Kittel, Introduciton to Solid State Physics, Wiley, New York, 1976.
[44] S.M. Sze, Physics of Semiconductor Devices, Wiley, New York, 1981.
[45] K. Seeger, Semiconductor Physics: An introduction, Springer, Berlin, 1996.
[46] D.R. Frankl, Electrical Properties of Semiconductor Surfaces, Pergamon, Oxford, 1967.
[47] A. Many, Y. Goldstein, N.B. Grover, Semiconductor Surfaces, North-Holland, Amsterdam, 1965.
[48] C.E. Young, J. Appl. Phys 32 (1961) 329.
[49] W. Mönch, Semiconductor Surfaces and Interfaces, Springer, Berlin, 1995.
[50] B.N.J. Persson, J.E. Demuth Phys. Rev. B30 1984 5968; B. N. J. Persson, Phys. Rev. B34 (1986) 5916.
[51] Y. Hasegawa, I-W. Lyo, Ph Avouris Ultimate Limits of Fabrication and Measurement, Welland ME, Gimzewski JK (Eds), Kluwer, Dordrecht, 147; Surf. Sci. 358 (1996) 32.
[52] J.T. Coutts, Electrical Conduction in Thin Metal Films, Elsevier, Amsterdam, 1974.
[53] M. Jalochowski, E. Bauer Phys. Rev. B37 1988 8622; Phys. Rev. B38 (1988) 5272; Surf. Sci. 213 (1989) 556; M. Jaløchowski, E. Bauer, H. Knoppe, G. Lilienkamp, Phys. Rev. B45 (1992) 13 607.
[54] R. Schad, S. Heun, T. Heidenblut, M. Henzler Appl. Phys. A55 1992 231; Phys. Rev. B45 (1992) 11430.
[55] S.D. Kevan, R.H. Gaylord Phys. Rev. B36 1987 5809; P. Heimann, J. Hermanson, H. Miosga, H. Neddermeyer, Surf. Sci. 85 (1979) 263; P. Heimann, H. Neddermayer, H. F. Roloff, J. Phys. C10 (1977) L17.
[56] T. Ando, A.B. Fowler, F. Stern Rev. Mod. Phys. 54 1982 437, and the proceedings of the biennial conference on Electronic Properties of Two-Dimensional Systems which are regularly published in Surface Science 73 (1978); 98 (1980); 113 (1982); 142 (1984); 170 (1986); 196 (1988); 229 (1990).
[57] S. Datta, Electronic Transport in Mesoscopic Systems, Cambridge Univ. Press, Cambridge, 1995.

[58] Ph Avouris, I-W. Lyo, R.E. Walkup, J. Vac. Sci. Technol B12 (1994) 1447.
[59] F.K. Schulte, Surf. Sci 55 (1976) 427.
[60] H. Lüth, Surfaces and Interfaces of Solids, Springer, Berlin, 1993.
[61] J.C. Riviere, Surface Analytical Techniques, Clarendon, Oxford, 1990.
[62] P.K. Larson, P.J. Dobson (Eds.), Reflection High-Energy Electron Diffraction and Reflection Electron Imaging of Surfaces, Plenum, New York, 1988.
[63] S. Ino, Japan. J. Appl. Phys 16 (1977) 891.
[64] B.A. Joyce, P.J. Dobson, J.H. Neave, K. Woodbridge, J. Zhang, P.K. Larsen, B. Boelger, Surf. Sci 168 (1986) 423.
[65] A. Endo, S. Ino, Surf. Sci 293 (1993) 165.
[66] J.A. Stroscio, W.J. Kaiser (Eds.), Sanning Tunneling Microscopy, Academic Press, San Diego, 1993.
[67] N.J. DiNardo, Nanoscale Characterization of Surfaces and Interfaces, VCH, Weinheim, 1994.
[68] J. Tersoff, D.R. Hamann, Phys. Rev B31 (1985) 805.
[69] M.O. Krause, J.H. Oliver, J. Phys. Chem. Data 8 (1979) 329.
[70] H.H. Weitering, A.R.H.F. Ettema, T. Hibma, Phys. Rev B45 (1992) 9126.
[71] L. He, H. Yasunaga, Japan. J. Appl. Phys 24 (1985) 928.
[72] M. Liehr, M. Renier, R.A. Wachnik, G.S. Scilla, J. Appl. Phys 61 (1987) 4619.
[73] C.L. Petersen, F. Grey, M. Aono, Surf. Sci 377 (1997) 676.
[74] E.P.Th Suurmeijer, R. Benedictus, A. der Stadt, T.M. Klapwijk, Appl. Surf. Sci 70/71 (1993) 452.
[75] F. Jentzsch, H. Froitzheim, R. Theile, J. Appl. Phys 66 (1989) 5901.
[76] L.J. van der Pauw, Phillips Tech. Rev 13 (1958) 1.
[77] G. LeLay, Surf. Sci 132 (1983) 169.
[78] Y. Goto, S. Ino, Jap. J. Appl. Phys 17 (1978) 2097.
[79] K. Spiegel, Surf. Sci 7 (1967) 125.
[80] E.L. Bullock, G.S. Herman, M. Yamada, D.J. Friedman, C.S. Fadley, Phys. Rev B41 (1990) 1703.
[81] H. Lim, K. Cho, I. Park, J.D. Joannopoulos, E. Kaxiras, Phys. Rev B52 (1995) 17 231.
[82] E.J. van Loanen, J.E. Demuth, R.M. Tromp, R.J. Hamers, Phys. Rev. Lett 58 (1987) 373.
[83] C. Collazo-Davila, D. Grozea, L.D. Marks, Phys. Rev. Lett 80 (1998) 1678.
[84] L. Lottermoser, E. Landemark, D-M. Smilgies, M. Nielsen, R. Feidenhans'l, G. Falkenberg, R.L. Johnson, M. Gierer, A.P. Seitsonen, H. Kleine, H. Bludau, H. Over, S.K. Kim, F. Jona, Phys. Rev. Lett 80 (1998) 3980.
[85] S.C. Erwin, Phys. Rev. Lett 75 (1995) 1973.
[86] W.C. Fan, A. Ignatiev, Phys. Rev B41 (1990) 3592.
[87] K.J. Wan, X.F. Lin, J. Nogami Phys. Rev. B46 1992 13635; B47 (1993) 13700.
[88] H. Ohnishi, I. Katayama, Y. Ohba, K. Oura, Jpn. J. Appl. Phys 33 (1994) 3683.
[89] M-H. Kang, J-H. Kang, S. Jeong, Phys. Rev B58 (1998) R13359.
[90] A. Ichimiya, H. Nomura, Y. Horio, T. Sato, T. Sueyoshi, M. Iwatsuki, Surf. Rev. Lett 1 (1994) 1.
[91] J. Nogami, K.J. Wan, X.F. Lin, Surf. Sci 306 (1994) 81.
[92] I. Homma, Y. Tanishiro, K. Yagi, in: S.Y. Tong, M.A. Van Hove, K. Takayanagi, X.D. Xie (Eds.), The Structure of Surfaces 3, Springer, Berlin, 1991, p. 610.
[93] X. Tong, K. Toriyama, S. Hasegawa to be published.
[94] S. Hasegawa, H. Daimon, S. Ino, Surf. Sci 186 (1987) 138.
[95] H. Hong, R.D. Aburano, D.S. Lin, H. Chen, T.S. Chiang, Phys. Rev. Lett 68 (1992) 507.
[96] Y. Goto, S. Ino Japan. J. Appl. Phys. 17 1978 2097; Thin Solid Films 109 (1983) 255; Y. Gotoh, S. Ino, and H. Komatsu, J. Crystal Growth 56 (1982) 498.
[97] K. Sumitomo, K. Tanaka, Y. Izawa, I. Katayama, F. Shoji, K. Oura, T. Hanawa, Appl. Surf. Sci 41 (42) (1989) 112.
[98] St Tosch, H. Neddermeyer Phys. Rev. Lett. 61 1988 349; H. Neddermeyer, Crit. Rev. Sol. State Mat. Sci., 16 (1990) 309.
[99] S. Kohmoto, A. Ichimiya, Appl. Surf. Sci 33 (34) (1988) 45.

[100] A. Ichimiya, S. Mizuno, Surf. Sci 191 (1987) L765.
[101] H. Daimon, S. Ino, Surf. Sci 164 (1985) 320.
[102] Z.H. Zhang, S. Hasegawa, S. Ino, Phys. Rev B55 (1997) 9983.
[103] K.R. Roos, M.C. Tringides Phys. Rev. B47 1993 12705; Europhys. Lett. 23 (1993) 257.
[104] R. Biswas, K. Roos, M.C. Tringides, Phys. Rev B50 (1994) 10 932.
[105] G. Meyer, K.H. Rieder Surf. Sci. 331–333 1995 600; Appl. Phys. Lett. 64 (1994) 3560.
[106] S. Heun, J. Brange, R. Schad, M. Henzler, J. Phys. Condens. Matter 5 (1993) 2913.
[107] F.J. Himpsel, B.S. Meyerson, F.R. McFeely, J.F. Morar, A. Taleb-Ibrahimi, J.A. Yarmoff, M. Campagna, R. Rosei (Eds.), Proc. of the Enrico Fermi School on Photoemission and Absorption Spectroscopy of Solids and Interfaces with Synchrotron Radiation, North Holland, Amsterdam, 1990, p. 203.
[108] A. Samsavar, T. Miller, T.C. Chiang, Phys. Rev B42 (1990) 9245.
[109] M. Henzler, in: J.M. Blakely (Ed.), Surface Physics of Materials I, Academic Press, New York, 1975, p. 241.
[110] M.C. Tringides Morphological Organizations in Epitaxial Growth and Removal, Z. Zheng, M.G. Lagally, (Eds.), World Scientific 1998 K.R. Kimberlin and M.C. Tringides, J. Vac. Sci. Technol. A13 (1995) 462.
[111] J.A. Venables, G.D.T. Spiller, M. Hanbücken, Rep. Prog. Phys 47 (1984) 399.
[112] D. Stauffer, A. Aharony, Introduction to Percolation Theory, Taylor and Francis, London, 1992.
[113] M. Sahimi, J. Phys. A: Math. Gen 17 (1984) L601.
[114] K.G. Watson, J. Kougut Phys. Rep. 12 1974 75; J. M. Youmans and R. B. Stinchcombe, J. Phys. C: Solid State Phys. 11 (1978) 4098.
[115] N.E. Cusack, The Physics of Structurally Disordered Matter, Adam Hilger, Bristol, 1987.
[116] M. Henzler, T. Lüer, A. Burdach, Phys. Rev B58 (1998) 10 046.
[117] A. Natori, M. Murayama, H. Yasunaga, Surf. Sci 357/358 (1996) 47.
[118] M. Lijadi, H. Iwashige, A. Ichimiya, Surf. Sci 357/358 (1996) 51.
[119] S. Ino, in: P.K. Larson, P.J. Dobson (Eds.), Reflection High-Energy Electron Diffraction and Reflection Electron Imaging of Surfaces, Plenum, New York, 1988, p. 3.
[120] T. Nagao, S. Hasegawa, K. Tsuchie, S. Ino, C. Voges, G. Klos, H. Pfnür, M. Henzler Phys. Rev. B57 1998 10 100; Appl. Surf. Sci. 130/132 (1998) 47.
[121] S. Takahashi, Y. Tanishiro, K. Takayanagi, Surf. Sci 242 (1991) 73.
[122] R. Plass, L.D. Marks, Surf. Sci 380 (1997) 497.
[123] K. Higashiyama, S. Kono, T. Sagawa, Jap. J. Appl. Phys 25 (1986) L117.
[124] L. Braicovich, I. Abbati, J.N. Miller, I. Lindau, S. Schwarz, P.R. Skeath, C.Y. Su, W.E. Spicer, J. Vac. Sci. Technol 17 (1980) 1005.
[125] A. Hiraki, Surf. Sci. Rep 3 (1984) 357.
[126] S.L. Molodtsov, C. Laubschat, A.M. Shikin, V.K. Adamchuk, Surf. Sci 269/270 (1992) 988.
[127] T. Tsuno, Doctor Thesis (University of Tokyo, 1989), unpublished, 1989.
[128] A.A. Baski, J. Nogami, C.F. Quate, Phys. Rev 41 (1990) 10 247.
[129] T. Hasegawa, K. Takata, S. Hosaka, S. Hosoki, J. Vac. Sci. Technol A8 (1990) 241.
[130] H. Lipson, K.E. Singer, J. Phys C7 (1974) 12.
[131] H. Daimon, C. Chung, S. Ino, Y. Watanabe, Surf. Sci 235 (1990) 142.
[132] E. Bauer, Surf. Sci. Lett 250 (1991) L379.
[133] Y. Yagi, K. Kakitani, A. Yoshimori, Surf. Sci 356 (1996) 47.
[134] T. Hasegawa, S. Hosoki Phys. Rev. B54 1996 10 300; T. Hasegawa, S. Hosaka, and S. Hosoki, Surf. Sci. 357 (1996) 858.
[135] L.D. Marks, R. Plass, Phys. Rev. Lett 75 (1995) 2172.
[136] J. Nogami, A.A. Baski, C.F. Quate, Phys. Rev. Lett 65 (1990) 1611.
[137] Y.G. Ding, C.T. Chan, K.M. Ho, Surf. Sci 275 (1992) L691.
[138] M. Chester, T. Gustafsson, Surf. Sci 256 (1991) 135.
[139] J. Yuhara, M. Inoue, K. Morita, J. Vac. Sci. Technol A10 (1992) 334, 3486.
[140] S. Ino, Jap. J. Appl. Phys 19 (1980) L61, 1277.
[141] A. Endo, S. Ino, Jap. J. Appl. Phys 32 (1993) 4718.

[142] J-J. Yeh, J. Hwang, K. Bertness, D.J. Friedman, R. Cao, I. Lindau, Phys. Rev. Lett 70 (1993) 3768.
[143] J.J. Lander, J. Morrison, Surf. Sci 2 (1964) 553.
[144] H. Hirayama, S. Baba, A. Kinbara Appl. Surf. Sci. 33/34 1988 193; Jap. J. Appl. Phys. 25 (1986) L452; S. Baba, M. Kawaji, and A. Kinbara, Surf. Sci. 85 (1979) 29.
[145] T. Aiyama, S. Ino, Surf. Sci 82 (1979) L585.
[146] H. Hibino, T. Ogino, Phys. Rev B54 (1996) 5763.
[147] A.A. Saranin, A.V. Zotov, V.G. Lifshits, T. Numata, O. Kubo, H. Tani, M. Katayama, K. Oura, Surf. Sci 398 (1998) 60.
[148] J.E. Northrup, Phys. Rev. Lett 53 (1984) 683.
[149] J.M. Nicholls, P. Mårtensson, G.V. Hansson, J.E. Northrup, Phys. Rev 32 (1985) 1333.
[150] G.V. Hansson, J.M. Nicholls, P. Mårtensson, R.I.G. Uhrberg, Surf. Sci 168 (1986) 105.
[151] J. Nogami, S. Park, C.F. Quate, Phys. Rev B36 (1987) 6221.
[152] K. Izumi, T. Takahashi, S. Kikuta, Jap. J. Appl. Phys 28 (1989) 1742.
[153] A. Kawazu, H. Sakama, Phys. Rev B37 (1988) 2704.
[154] J. Nogami, S-il Park, C.F. Quate, J. Vac. Sci. Technol B6 (1988) 1479.
[155] T. Kinoshita, H. Ohta, Y. Enta, Y. Yaegashi, S. Suzuki, S. Kono, J. Phys. Soc. Jap 56 (1987) 4015.
[156] A.A. Saranin, A.V. Zotov, K.V. Ignatovich, V.G. Lifshits, T. Numata, O. Kubo, H. Tani, M. Katayama, K. Oura, Phys. Rev 56 (1997) 1017.
[157] C. Collazo-Davila, L.D. Marks, K. Nishii, Y. Tanishiro, Surf. Rev. Lett 4 (1997) 65.
[158] T. Abukawa, M. Sasaki, F. Hisamatsu, T. Goto, T. Kinoshita, A. Kakizaki, S. Kono, Surf. Sci 325 (1995) 33.
[159] I.G. Hill, A.B. McLean, Phys. Rev 56 (1997) 15 725.
[160] H.W. Yeom, S. Takeda, E. Rotenberg, I. Matsuda, K. Horikoshi, J. Schaefer, C.M. Lee, S.D. Kevan, T. Ohta, T. Nagao, S. Hasegawa, Science (submitted).
[161] H. Yasunaga, Y. Kubo, N. Okuyama, Jap. J. Appl. Phys 25 (1986) L400.
[162] S. Hasegawa, Y. Nagai, T. Oonishi, N. Kobayashi, T. Miyake, S. Murakami, Y. Ishii, D. Hanawa, S. Ino, Phase Transition 53 (1995) 87.
[163] Y. Horio, A. Ichimiya, Surf. Sci 219 (1989) 128.
[164] S.L. Surnev, J. Kraft, F.P. Netzer, J. Vac. Sci. Technol A13 (1995) 1389.
[165] H. Öfner, S.L. Surnev, Y. Shapira, F.P. Netzer, Phys. Rev B48 (1993) 10 940.
[166] J.K. Zuo, J.F. Wendelken, Appl. Surf. Sci 48/49 (1991) 366.
[167] G. Margaritondo, J.E. Rowe, S.B. Christman, Phys. Rev B14 (1976) 5396.
[168] J.E. Rowe, H. Ibach, Phys. Rev. Lett 32 (1974) 421.
[169] E.O. Kane, Phys. Rev 146 (1966) 558.
[170] M.K. Kelly, E. Colavita, G. Margaritondo, J. Anderson, L. Papagno, D.J. Frankel, G.J. Lapeyre, Phys. Rev B32 (1985) 2693.
[171] M.K. Kelly, G. Margaritondo, J. Anderson, D.J. Frankel, D.J. Lapeyre, J. Vac. Sci. Technol A4 (1986) 1396.
[172] S. Takeda, T. Nagao, S. Hasegawa to be published.
[173] M. Sahimi, J. Phys. A, Math. Gen 17 (1984) L601.
[174] D. Bolmont, P. Chen, C.A. Sébenne, F. Proix, Surf. Sci 137 (1984) 280.
[175] J. Kraft, M.G. Ramsey, F.P. Netzer Phys. Rev. B55 1997 5384; Surf. Sci. 55 (1997) L271; J. Kraft, S. L. Surnev, F. P. Netzer, Surf. Sci. 340 (1995) 36.
[176] M.S. Finney, C. Norris, P.B. Howes, E. Vlieg, Surf. Sci 277 (1992) 330.
[177] M. Kawaji, S. Baba, A. Kinbara, Appl. Phys. Lett 34 (1979) 748.
[178] S. Park, J. Nogami, C.F. Quate, J. Microsc 152 (1988) 727.
[179] A.A. Saranin, A.V. Zotov, T. Numata, O. Kubo, K.V. Ignatovich, V.G. Lifshits, M. Katayama, K. Oura, Surf. Sci 388 (1997) 299.
[180] A.A. Saranin, T. Numata, O. Kubo, H. Tani, M. Katayama, K. Oura, Jap. J. Appl. Phys 36 (1997) 3814.
[181] S. Baba, J.M. Zhou, A. Kinbara, Jap. J. Appl. Phys 19 (1980) L571.
[182] T. Okuda, H. Daimon, S. Suga, Y. Tezuka, S. Ino, Appl. Surf. Sci 121/122 (1997) 89.

[183] T. Okuda, H. Daimon, H. Shigeoka, S. Suga, T. Kinoshita, A. Kakizaki, J. Electron Spectrosc. Rel. Phen 80 (1996) 229.
[184] I.R. Collins, J.T. Moran, P.T. Andrews, R. Cosso, J.D. O'Mahony, J.F. McGilp, G. Margaritondo, Surf. Sci 325 (1995) 45.
[185] S.V. Ryzhkov, D.A. Tsukanov, V.G. Lifshits Phys. Low-Dim. Struct. 7/8 1998 1; S. V. Ryzhkov, D. A. Tsukanov, D. V. Gruznev, and V. G. Lifshits, Phys. Low-Dim. Struct. 7/8 (1998) 109.